PETROPHYSICS

The SPWLA Journal of Formation Evaluation and Reservoir Description

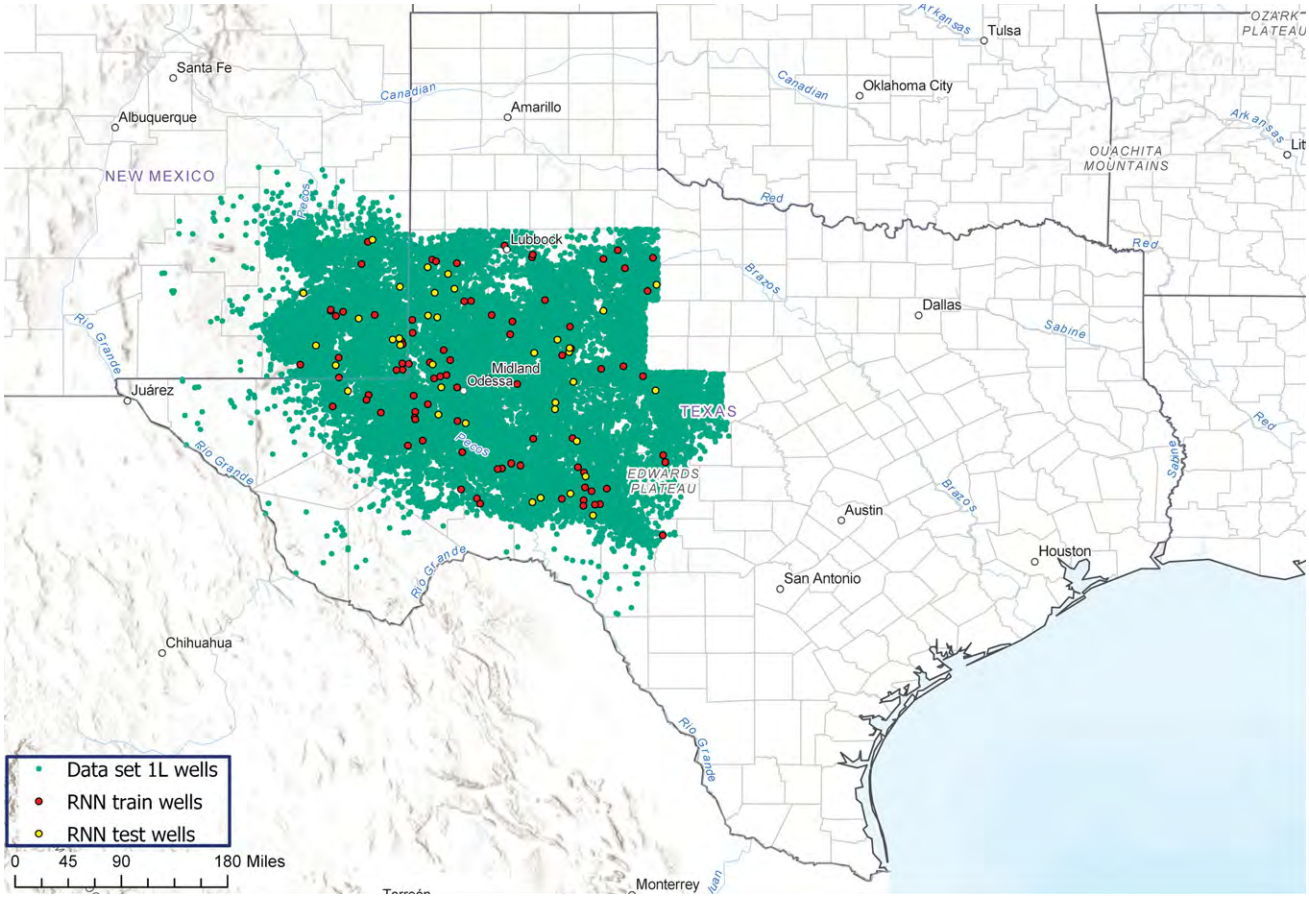

Vol. 61, No. 5

October 2020

PETROPHYSICS

October Vol. 61, No. 5

Contents

Full-color versions of all technical articles are available in the digital edition of PETROPHYSICS, which is free to SPWLA members and can be found at https://www.spwla.org/SPWLA/Publications/Journals/Recent_Petrophysics_Journals.aspx.

The Society of Petrophysicists and Well Log Analysts

8866 Gulf Freeway, Suite 320
Houston, TX 77017, USA
P: +1-713-947-8727
F: +1-713-947-7181
Email: Sharon@spwla.org
Membership@spwla.org
www.SPWLA.org

SPWLA Foundation. This fund supports scholarships in higher education and research in formation evaluation. Please send donations to: SPWLA, 8866 Gulf Freeway, Suite 320, Houston, TX 77017, USA

ISSN 1529-9074

PETROPHYSICS is published bimonthly by the Society of Petrophysicists and Well Log Analysts (SPWLA). Subscription is included in annual dues for members. Library Subscription cost is $250 (6-issues, Feb, April, June, Aug, Oct, Dec) Send Subscription and member address changes to the SPWLA business office. Back issues if available are $35 each to members and $45 each to library subscribers.

ADVERTISING RATES: *(based on one-time, full color)* Full Page: $1500, Half Page: $1200, Quarter Page: $1000. Additional fee for printing on covers. Media kits are available by contacting the SPWLA business office or by visiting the SPWLA website www.spwla.org.

About the Cover

In this issue, Sen et al. explore a novel workflow for automatically identifying and flagging wellbore cave-ins using an unsupervised clustering algorithm for depth-series data. This workflow, which was applied to a set of 3,762 Permian Basin wells, may be used to efficiently preprocess well-log data by removing erroneous measurements resulting from wellbore cave-ins. The resulting data set can be used for a variety of purposes, such as well-log interpolation using a supervised learning algorithm.

PRINTED IN USA ON ACID FREE PAPER

The Society of Petrophysicists and Well Log Analysts is dedicated to the advancement of the science of formation evaluation through well logging and other formation evaluation techniques. SPWLA is dedicated to the application of these techniques, to the exploration and exploitation of gas, oil and other minerals. PETROPHYSICS publishes original contributions on theoretical and applied aspects of formation evaluation; particularly well logging and petrophysics.

As of Vol. 46 (1) 2005, PETROPHYSICS [ISSN: 1529-9074] is indexed and abstracted in Thomson Reuters:
Scientific Citation Index Expanded
Journal Citation Report–Science
Current Contents–Physical, Chemical, and Earth Sciences

PETROPHYSICS

Editor

Mayank Malik
Chevron
VP-Publications@spwla.org
(+1) 713-927-7493

Associate Editors

Acoustics and Rock Physics
Alexei Bolshakov, *Chevron*


Core Analysis and Laboratory Petrophyiscs
William Richardson, *Chevron*
S. Mark Ma, *Saudi Aramco*

Electromagnetics
Hui Xie, *Schlumberger*

Formation Testing
Melton Hows, *Shell*


Integrated Formation Evaluation
Chengbing Liu, *Saudi Aramco*
Haijing Wang, *Chevron*

Integrated Formation Evaluation and Case Studies
Hesham El-Sobky, *ConocoPhillips*


Magnetic Resonance
Lalitha Venkataramanan, *Schlumberger*
Wim Looyestijn, *Shell*

Nuclear
Pingjun Guo, *ExxonMobil*

Petroleum Geochemistry
Drew Pomerantz, *Schlumberger*

Well and Reservoir Surveillance
Dale Fitz, *Consultant*

Data-Driven Analytics
Chicheng Xu, *Aramco Services*

The Society of Petrophysicists and Well Log Analysts Board of Directors 2020–2021

President
James Hemingway
Consultant
Manitou Springs, CO, USA
(+1) 281-433-5170
President@spwla.org

President-Elect
Katerina Yared
SM Energy
Highlands Ranch, CO, USA
(+1) 720-431-7482
President-Elect@spwla.org

VP Technology
Tegwyn Perkins
Lloyd's Register
Houston, TX, USA
(+1) 713-670-4976
VP-Technology@spwla.org

VP Education
Fransiska Goenawan
Halliburton
Houston, TX, USA
(+1) 346-401-8201
VP-Education@spwla.org

VP Finance, Secretary, and Administration
Doug Patterson
Baker Hughes, a GE Company
Houston, TX, USA
(+1) 713-879-4056
VP-Finance@spwla.org

VP Publications
Mayank Malik
Chevron
Houston, TX, USA
(+1) 713-927-7493
VP-Publications@spwla.org

VP IT
Lin Liang
Schlumberger-Doll Research
Cambridge, MA, USA
(+1) 617-335-4469
VP-InfoTech@spwla.org

REGIONAL DIRECTORS

N. America 1
Robin Slocombe
Schlumberger
Houston, TX, USA
(+1) 281-690-0837
Director-NA1@spwla.org

N. America 2
Kelly Skuce
Core Petrophysical Consulting
Calgary, Canada
(+1) 587-228-0203
Director-NA2@spwla.org

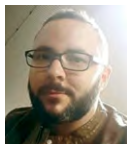

Latin America
Fernando Maia Jr.
Petrobras
Rio de Janeiro, Brazil
(+55) 2196-7767-084
Director-LA@spwla.org

Europe
Craig Lindsay
Core Specialist Services Ltd.
Aberdeenshire, United Kingdom
(+44) 7530-040117
Director-Europe@spwla.org

Middle East/Africa
Nelson Suarez
Dubai Petroleum Establishment
Dubai, UAE
(+971) 504-528576
Director-MEA@spwla.org

Asia and Australia
Jennifer Market
MPC Kinetic
Perth, Australia
(+61) 417-598-269
Director-Asia-Aus@spwla.org

Executive Director
Sharon Johnson
SPWLA
Houston, TX 77017
(+1) 713-947-8727
sharon@spwla.org

Managing Editor
Elizabeth Naggar
(+1) 713-444-3495
editor@spwla.org

Publication Manager
Anna Tarlton
InkSpot Printing
2301 S. Shaver
Pasadena, TX 77502, USA
(+1) 713-472-1100
orders@inkspotprinting.com

FROM THE EDITOR

Welcome to the October 2020 issue of *Petrophysics*. This issue is traditionally dedicated to publishing the "Best Papers" presented at the SPWLA Annual Symposium, but we had delays in ranking papers with the online symposium spread over 6 weeks. As I write this article, it's been 6 months of working from home in Houston. Progress is being made on a vaccine for COVID-19, with research being done in many countries in over two dozen trials. Advances in technology have allowed for the acceleration of the vaccine development process. In fact, much of what has been learned from work on HIV has provided the science that is helping in this pandemic. However, a public rollout is still a long way off. When a vaccine is approved, the manufacture, distribution, and application will take significant time. And, because of all that time, there is a strong desire to hurry the process along. It's gratifying to know that the greater scientific community is taking time to do it right, just as we do through our peer-review process.

Due to low commodity prices and a decline in demand, the oil industry continues to hemorrhage itself with layoffs across all major companies. The myth that machine learning is a replacement for people has taken over in company boards. Business is business, but loyalty is a two-way street. It's a challenging time to convince young university students that there is a bright future ahead for oil and gas. All we can do is continue to hold ourselves and others accountable, assure safeguards are in place and functioning, and we will eventually put this pandemic behind us. It may take time, but as we know from our long history, the right behaviors will produce positive outcomes.

SPWLA recently sent out a call for *Petrophysics* tutorials to our members. Tutorials are valuable scientific literature as they provide a comprehensive overview and summary, and integrate the findings of existing literature. They allow readers to form an idea about the knowledge on a topic without having to read all the published works in the field. Well-written tutorials are popular, have a high impact, and receive a lot of citations. Tutorials are submitted using the SPWLA Editorial Manager system and go through a peer-review process. If the tutorial is selected for publishing (after review), SPWLA will waive the editorial fee ($1,200 for SPWLA members; $1,800 for nonmembers; $600 for authors employed by nonprofit or academic institutions). Additionally, SPWLA will also offer a one-year complimentary membership to the lead author. This is a small token of appreciation for the effort our members put into writing high-quality tutorials. There isn't any specific deadline to submit the tutorial as the submissions are reviewed continuously.

In this issue, there are seven excellent papers on topics pertinent to unconventional Wolfcamp shale, carbonate reservoirs in the Middle East, and clastic sand/shale reservoirs. *Petrophysics* is your journal and should meet your needs, so, as always, I welcome your feedback.

Mayank Malik
Vice President Publications

PETROPHYSICS, VOL. 61, NO. 5 (OCTOBER 2020); PAGES 404–416; 12 FIGURES. DOI: PJV61N5-2020a1

Nanoindentation of Shale Cuttings and Its Application to Core Measurements

Erica Esatyana[1], A. Sakhaee-Pour[1]*, Fadhil N. Sadooni[2], and Hamad Al-Saad Al-Kuwari[2]

ABSTRACT

Large samples (~1 in.) required for standard tests are often unavailable in shale formations due to various reasons. They are not usually recovered in horizontal drilling, which is a common practice in hydraulic fracturing. They also delaminate and are difficult to process in core analysis. Hence, common characterization techniques face challenges and lead to uncertainties. A new method is needed that can be applied to small pieces, such as drill cuttings, which are often the only available sources, especially in real-time conditions. The present study proposes a new method applicable to the cuttings to determine the geomechanical properties of shale formations at the core scale from nanoindentations. In particular, the Young's moduli have been determined from cuttings, and the results are compared with those of the core plugs. Nanoindentation and the required sample preparation are reviewed. The results are promising, and the methodology has applications in characterizing formation heterogeneity in the petroleum industry.

INTRODUCTION

Hydraulic fracturing has increased energy recovery from shale formations within the last decade. Although increased production has played a dominant role, the full potential of such resources is yet to be realized. One of the key challenges is evaluating formations that encounter difficulties due to the lack of large samples.

Large samples, such as core plugs (~1 in.) or blocks that are an important part of formation characterization, are not usually available, as recovering them is difficult and expensive. Large-scale tests are also time consuming and expensive. Thus, the data required for detailed analysis are scarce, leading to uncertainties in predicting the performance of a formation. The lack of large samples is relevant, especially to shale formations, as they delaminate and are hard to process in core analysis.

Drill cuttings are often the only sources available and provide useful information for formation evaluation (Tutuncu et al., 2005), and predicting the relevant properties from drill cuttings is a known problem (Tutuncu et al., 2004) One appealing test for analyzing cuttings is nanoindentation because it can be done on small samples. Nanoindentation is based on contact mechanics, which was founded by Hertz (1896). He recognized that the mathematics of contact between two elastic bodies resembles common problems in electricity and proposed five key assumptions that were adopted later but did not derive from the stress field (Huber, 1904).

Indentation has a wide range of applications because it can be performed easily, and the results provide useful information about Young's modulus (Sneddon, 1965; Velez et al., 2001), hardness (Bobji and Biswas, 1998), cracking (Lawn et al., 1980), creep (Li et al., 2008), and fracture toughness (Laugier, 1987; Volinsky et al., 2003). The main idea is that the features of the load-displacement curve are related to the specimen deformation. Researchers have applied nanoindentation to heterogeneous media, characterizing cement (Constantinides et al., 2003; Constantinides and Ulm, 2004; Jennings et al., 2005), shale (Ulm et al., 2007; Shukla et al., 2013), and even bone (Tai et al., 2006), based on conceptual models that have enabled them to interpret nano- to microscale deformations of forming phases (Ulm and Abousleiman, 2006; Ortega et al., 2007; Abedi et al., 2016a; Abedi et al., 2016b). They have also used nanoindentation to investigate carbonate properties (De Paula et al., 2010; Vialle and Lebedev, 2015; Uribe et al., 2016). Research using nanoindentations has

Manuscript received by the Editor February 23, 2020; revised manuscript received May 25, 2020; manuscript accepted June 26, 2020.
[1]University of Houston, Cullen College of Engineering, Department of Petroleum Engineering, UH Technology Bridge, 5000 Gulf Freeway Bldg 9, Room 219, Houston, TX 77204-0945
[2]Environmental Science Center, Qatar University, P. O. Box 2713, Doha, Qatar
*Corresponding author: asakhaee@central.uh.edu

focused mainly on the local properties (Deirieh et al., 2012; Abedi et al., 2016a; Abedi et al., 2016b).

Nanoindentation has also been used to predict the large-scale properties (Bobko et al., 2011; Li and Sakhaee-Pour, 2016; Abdolhosseini Qomi et al., 2017; Monfared et al., 2018). Abdolhosseini Qomi et al. (2017) used statistical mechanics to determine the microscale properties from nanoscale measurements. Recent investigations (Bobko et al., 2011; Abdolhosseini Qomi et al., 2017; Monfared et al., 2018) based on the multiscale approach provide new insights into the interplay of texture and effective bulk properties, but they are computationally intensive and hard to implement.

In the present study, we propose a new method using cuttings to determine the geomechanical properties of a shale formation at the core scale. In particular, the Young's moduli of the cuttings are investigated. A review of nanoindentation and the required sample preparation are also provided.

NANOINDENTATION

Nanoindentation consists of touching a material whose mechanical properties are unknown with another material with known properties. The goal is to extract the unknown property from readings of the indenter load and penetration depth. The term "indenter" refers to the body to which the load is applied, and the "specimen" refers to the penetrated medium. The shale sample, whose properties are of interest in the present study, is the specimen.

In nanoindentation, the load is increased from zero to some maximum and then decreased to zero. The variation of force with displacement provides a useful tool for characterizing various properties, but here we focus on those that are related to the present study. The penetration depth is recorded as the load is decreased (Fig. 1) and is used as follows (Pharr et al., 1992):

$$M = \frac{S}{2\alpha}\sqrt{\frac{\pi}{A_c}} \tag{1a}$$

$$H = \frac{p_{max}}{A_c} \tag{1b}$$

where M is the indentation modulus, S is the slope of load-displacement at the beginning of unloading, α is the shape factor, A_c is a projected area, H is the specimen hardness, and p_{max} is the maximum applied load. The shape factor (α), which is a geometric parameter, is equal to 1.03 for the Berkovitch tip used in this study. The shape factors for other geometries are available in the literature (Riester et al., 2000).

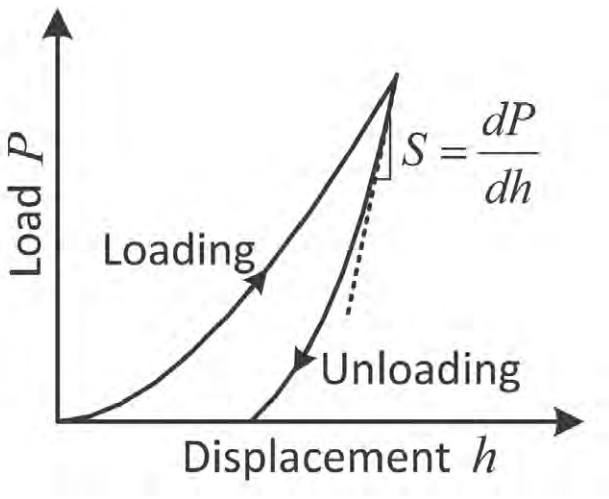

Fig. 1—Schematic of nanoindentation load-displacement where the unloading is used to determine the modulus (Eq. 1a).

The indentation modulus (M) is related to the specimen modulus as follows:

$$\frac{1}{M} = \frac{1-\nu_s^2}{E_S} + \frac{1-\nu_i^2}{E_i} \tag{2}$$

Where ν_s is the specimen Poisson's ratio, E_s is the specimen modulus, ν_i is the indenter Poisson's ratio, and E_i is the indenter modulus. The effect of the second term on the right side is negligible because E_i is usually much larger than E_s.

The indentation modulus is related to the effective modulus ($= E_S/(1-\nu_S^2)$) and not the Young's modulus ($= E_s$), but this does not have a significant impact on the interpreted results because the Poisson's ratio is usually between 0.25 and 0.3 for most types of rock. More importantly, changing the Poisson's ratio by 0.1 would alter the results by less than 1%:

$$\Delta E_s \approx M(1-\Delta\nu_s^2) \tag{3}$$

where ΔE_s shows the change in the interpreted Young's modulus due to the changes in the Poisson's ratio ($\Delta\nu_s$).

CUTTING SCALE

Nanoindentation was originally developed based on Sneddon's solution to the stress field in an infinite half-space (Sneddon, 1965), but is usually applied to finite-size samples with the justification that the sample size is larger than the indented (stimulated) volume. Sneddon's assumptions are often overlooked, as recent interpretations have focused

on the local properties of porous media (Ulm et al., 2007; Shukla et al., 2013; Tai et al., 2006).

Our assumption in the present study, which is compatible with the Sneddon solution, is that nanoindentation captures a bulk property (as opposed to a local property) relevant to a volume smaller than the core volume. The rationale is that a solid medium undergoes deformations in various locations when loaded, even if they are small. The corresponding plastic-size zone (Fig. 2) can be approximated as follows (Johnson, 1970):

$$\frac{c}{a} = \left[\frac{1}{6(1-\nu)}\left(\frac{E}{\sigma_{yield}}\tan\left(\frac{\pi}{2}-\theta\right)+4(1-2\nu)\right)\right]^{\frac{1}{3}} \quad (4)$$

where c is the plastic-zone radius, a is the projected-area radius, ν is the Poisson's ratio, E is the Young's modulus, σ_{yield} is the yield strength, and θ is a geometrical parameter.

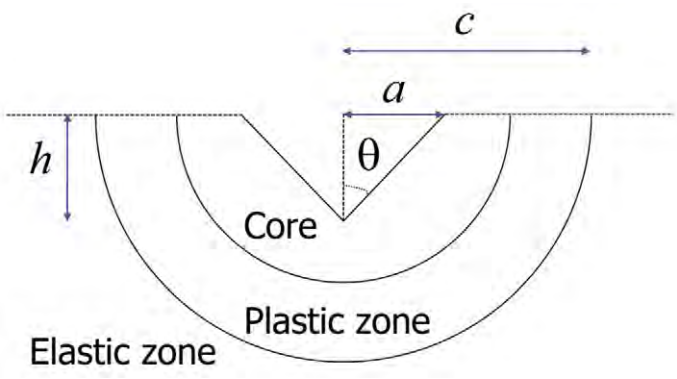

Fig. 2—Schematic of the plastic zone characterized in Eq. 4. The minimum distance between nanoindentations will be larger than the plastic-size zone to avoid interference (spacing > 2*c*).

We assume that the geomechanical properties at a centimeter-sized scale are equal to the average values obtained from nanoindentations at a regularly spaced distance if the average value does not change significantly when decreasing the distance between the indentations. This assumption is based on the notion that each nanoindentation characterizes a zone (volume) larger than the plastic zone. The corresponding distance is equal to the representative-elementary-volume (REV) size (Hill, 1963) shown by the red square in Fig. 3a, whose repetition creates the bulk volume at the large scale (Fig. 3b). The assumption implies that there is a scale smaller than the core scale, which controls the core-scale properties.

We refer to the smaller scale as a cutting scale, which is not necessarily equal in different formations. In practice, it may not be possible to accurately determine the cutting scale for each formation, as only small pieces (cuttings) may be available. Nevertheless, measuring the geomechanical properties for a sample whose size is close to this scale should provide an estimate for the geomechanical properties at the core scale.

Our objective is to propose a method that can be applied to shale cuttings, as opposed to core plugs. The spacing between indentations is restricted by the plastic-zone and core sizes. The plastic-zone size is the lower limit, and the core size is the upper limit. The spacing between nanoindentations has to be larger than the plastic-zone size to avoid interference between the stimulated regions. The sample is damaged significantly in the plastic zone, where its properties are not really realistic.

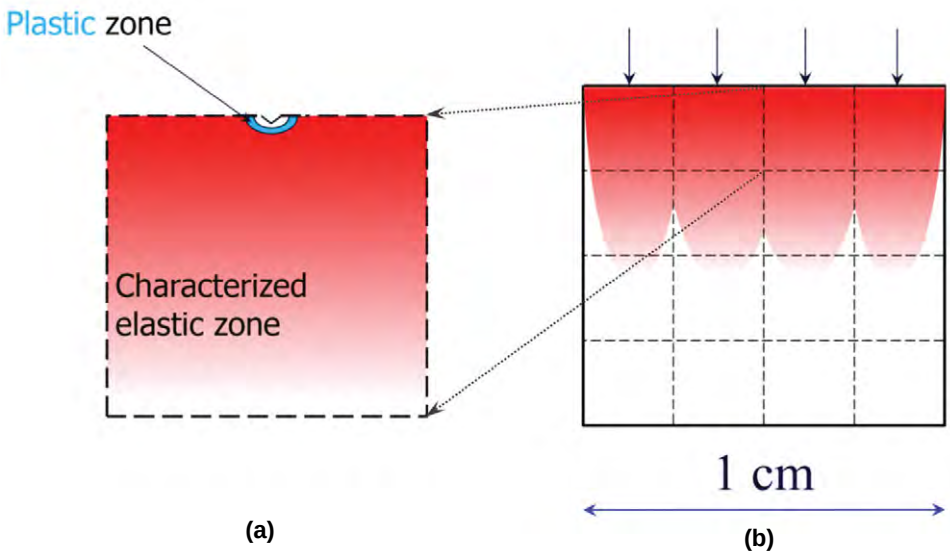

Fig. 3—(a) A conceptual illustration of the representative elementary volume (REV) whose repetition creates (b) the shale bulk volume.

Next, we turn to the determination of the plastic-zone size. The nanoindentation force in this study is 500 mN because results obtained with smaller force (< 100 mN) are usually influenced by the surface roughness (Miller et al., 2008). Our study on a variety of shale samples shows that the penetration depth is close to 3.5 μm for this range of force. This leads to the plastic-zone size (= 2*c*) being close to 85 μm (Eq. 4), as the semi-angle for an equivalent Berkovich indenter is 70.3°. The calculation is based on Poisson's ratio being 0.25, Young's modulus being 20 GPa, and the yield strength being 20 MPa (Wang et al., 2001; Zhu et al., 2009; Mavko et al., 2009; Gao et al., 2015). Figure 4 shows the variation of the plastic-zone size with the Young's modulus and yield strength when the Poisson's ratio is equal to 0.25. The data provide an estimate for the lower limit for different shales.

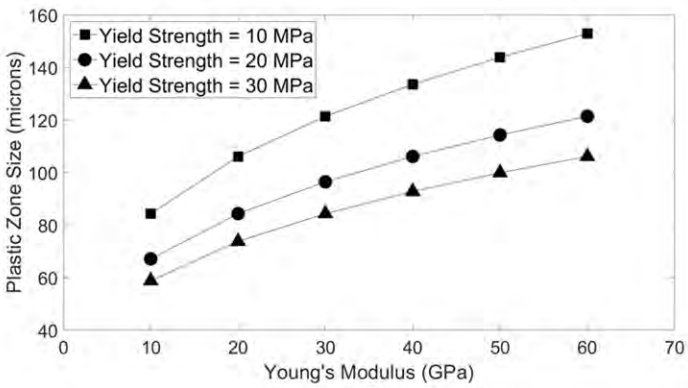

Fig. 4—Variation of the plastic-zone size with Young's modulus at different yield-strength values. Poisson's ratio is equal to 0.25, and Young's modulus and the yield-strength values are taken to be representative of shale formations (Sayers, 2013; Sone and Zoback, 2013; Rybacki et al., 2015).

SAMPLE PREPARATION

The nanoindenter tip that applies the load to the surface is much smaller than the core size. The small tip size and small penetration depth suggest that the rock surface has to be prepared to obtain reliable results. Otherwise, the interpreted results may characterize small fractures on the rock surface, which show lower resistance than the intact medium, or the surface roughness.

Sample preparation, in general, is easier for core samples that are common in rock mechanics because the actuator size is larger and less sensitive to local defects. This task may also be easier in other fields, such as materials science and mechanical engineering, because they are focused on materials such as fused silica and aluminum that usually have fewer defects than do shales.

Core samples were collected from the Wolfcamp Formation. Figure 5 shows the shale surface at different stages of preparation. The nanoindentation is envisaged as characterizing the bulk properties, as opposed to those of the local defects, when the rock surface is more polished. The sensitivity of the results to the surface preparation is discussed later in this paper. Achieving a high-quality surface that reflects the light is not an easy task when dealing with cuttings. The small pieces have irregular shapes and sometimes break during polishing, especially when the sample is brittle. The surface roughness (often shortened to "roughness") is quantified in materials science and engineering, and there are even standards for it, such as *ISO 4287* (1997). The quantitative characterization of surface roughness is beyond the scope of this study.

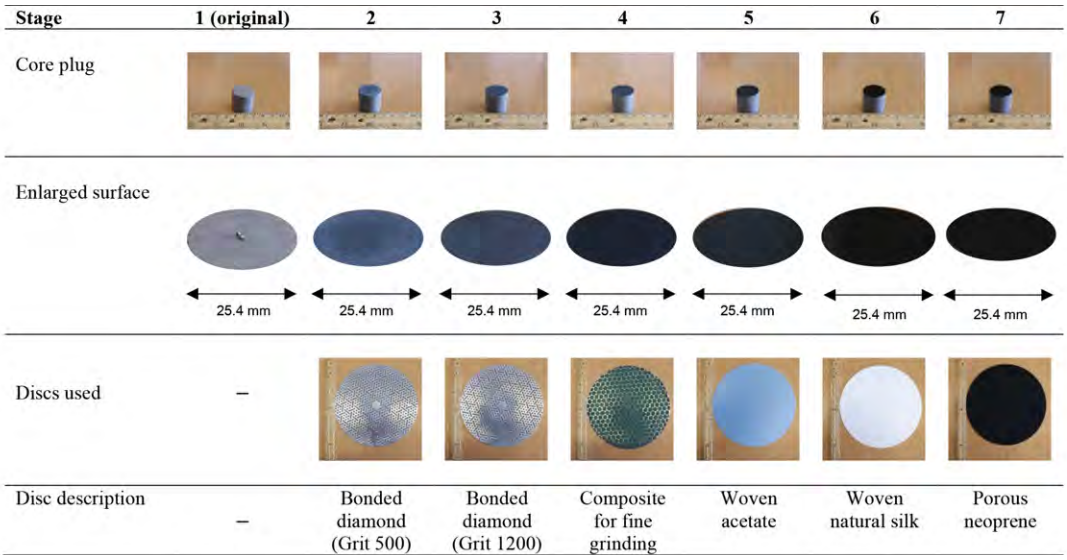

Fig. 5—Shale surface with the discs used for preparation at different stages. The surface roughness decreases at higher stages and is more reflective of light. A nanoindenter tip is placed on the rock surface in the first stage for the size comparison.

The first three stages of preparation (Stages 2 to 4 in Fig. 5) are grinding, and the last three (Stages 5 to 7) are polishing (Bhushan and Gupta, 1991). The process starts with a rough abrasive in grinding and uses a finer abrasive at subsequent stages. The rough abrasive removes imperfections like pits, nicks, lines, and scratches, and the finer abrasives leave progressively finer lines that are not visible to the naked eye.

RESULTS

We determine the geomechanical properties of the shale formation at the core scale here. To do so, we first determine the sensitivity of the results to sample preparation. We then determine the cutting scale for different samples whose core plugs are available. Subsequently, this scale is used to obtain the pertinent properties at the core scale. The main focus will be on Young's moduli, which are fundamental.

Sensitivity to Sample Preparation

Shale samples were collected from the Wolfcamp Formation to determine the sensitivity of the results to the preparation. The cross section is divided into equal areas (Squares 1 to 16 in Fig. 6), and each square is indented at its center. The shale sample is first indented as received (Stage 1 in Fig. 5). It is then prepared for the subsequent stage and tested until the rock surface at all the stages is studied. The removed length of the shale sample perpendicular to the circular cross section is chosen to be larger than the plastic-size zone to avoid interference between the tests.

The average Young's moduli of the shale samples at different conditions are investigated to better understand the effects of sample preparation. Figure 6 shows the results. It is apparent that the outcome is very sensitive to the first preparation step, which is grinding, as it removes small-scale features such as microcracks. Other preparation steps slightly alter the results. For instance, the average modulus in the first preparation increases 83% in Sample A, 52% in Sample B, and 64% in Sample C. The average modulus changes less than 10% during the last three stages for all the samples.

With the importance of the sample preparation in mind, we report and analyze the measurements after completing all the preparation stages. The finished surface of a core plug reaches a higher level of smoothness than that of a cutting due to the high level of irregularity in the cutting.

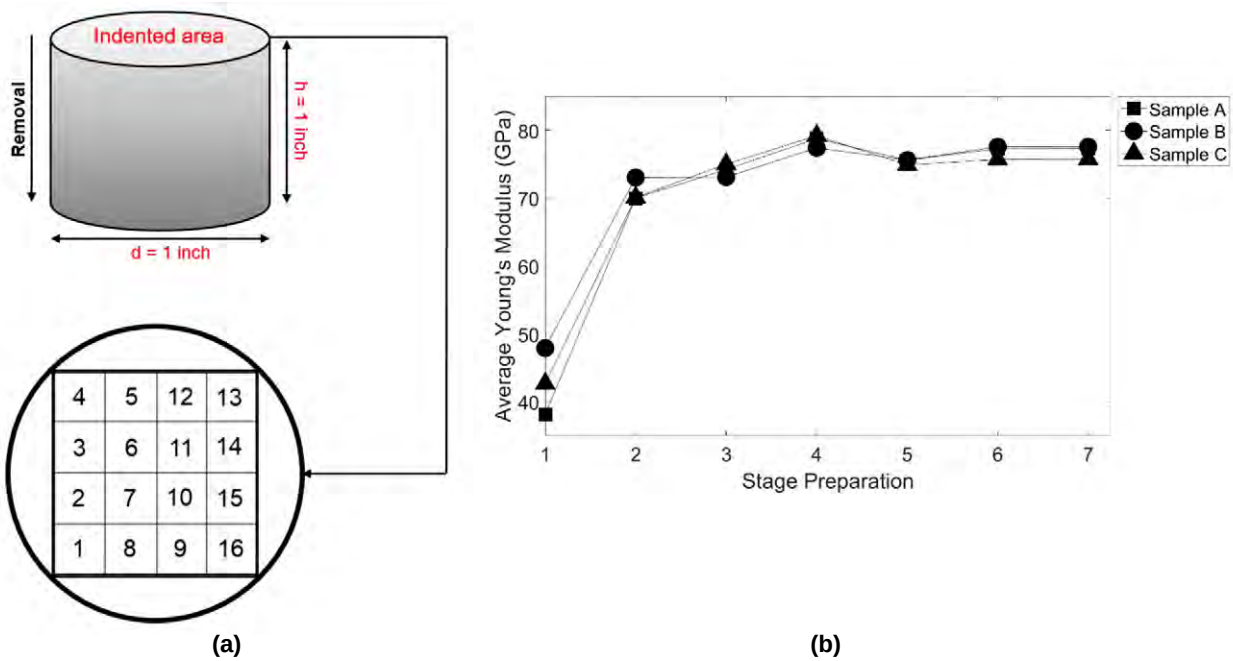

Fig. 6—(a) The shale cross section is divided into equal areas and indented at the center. (b) Variation of the average Young's modulus, which is obtained from nanoindentation, of the shale samples at each preparation stage.

Determining the Cutting Scale

We apply nanoindentation with regular spacings on the polished surface of a core plug to determine the cutting scale. Figure 7 shows the divisions and the spatial locations of the indentations at each step. Our objective in determining the cutting scale is to find the smallest size possible to be used in place of the core size (~1 in.). The smallest size allows us to use small cuttings, which are more easily accessible.

Figure 8 shows the variation of the Young's modulus with the indentation number. The nanoindentation allows us to investigate the shale surface regularly at different locations based on the pattern shown in Fig. 7. The penetration depth remains close to a few microns when the applied load is 500 mN. Thus, the regular spacings of the loads are crucial for characterizing the shale surface, and the outcome is related to the bulk properties, depending on the penetration depth of each sample.

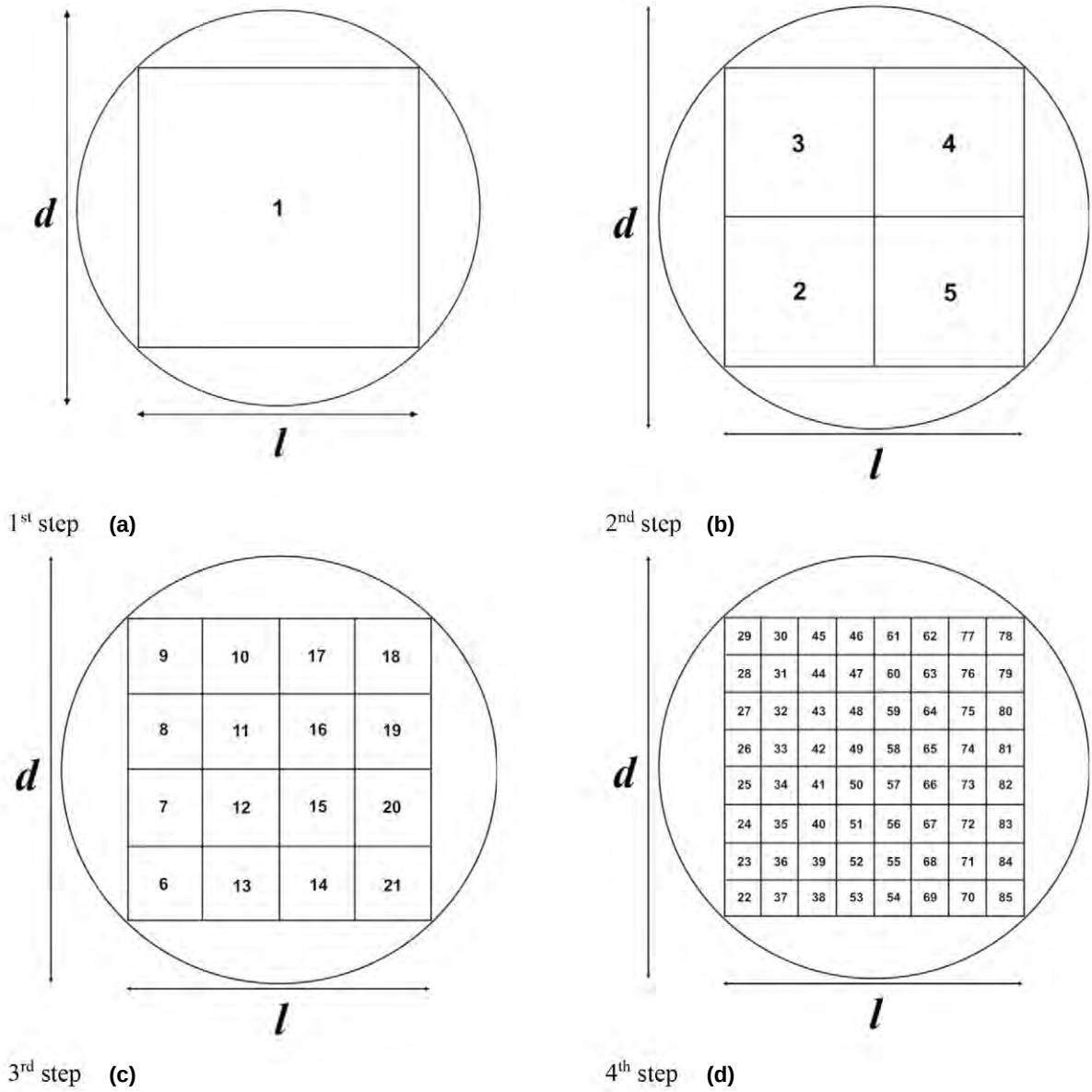

Fig. 7—(a, b, c, d) Spatial locations of nanoindentations in four steps on a core plug (d = 25.4 mm, l = 17.6 mm) with regular spacing. The area is equally divided in each step, and the process stops when the distance between the nearest indentations is close to the plastic-zone size.

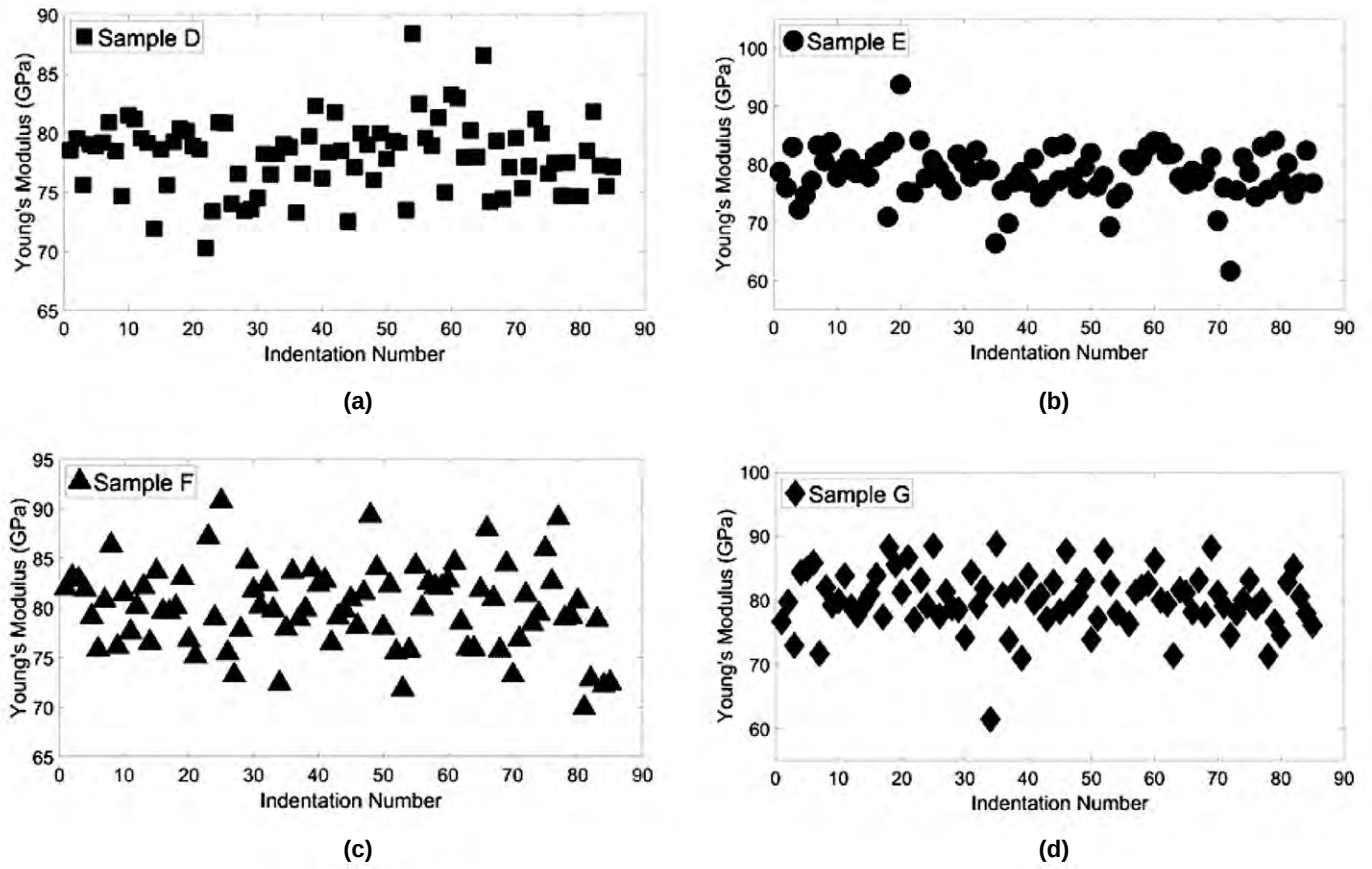

Fig. 8—The variation of Young's modulus with indentation number for shale Samples (a) D, (b) E, (c) F, and (d) G. The spatial locations of the nanoindentations are shown in Fig. 7.

Young's modulus and hardness are the primary parameters available from nanoindentations (Eq. 1). Young's modulus, which is of the main interest here, is used to determine the cutting scale. To evaluate the cutting scale, the average of the difference between Young's moduli at each step and those of the four nearest indentations are determined. The process is conducted for different shale samples whose results are shown in Fig. 9. It is apparent that the average difference between the Young's moduli is smaller than 6% when the regular spacing is equal to 2.2 mm.

The small difference associated with 8.8-mm spacing, which is close to 4% in Fig. 9, indicates that the moduli obtained with 17.6-mm spacings are close to those obtained with 8.8-mm spacings; thus, an 8.8-mm sample can replace a 17.6-mm sample. Following the same logic, a 4.4-mm sample can be used in place of an 8.8-mm sample, and a 2.2-mm sample can be used in place of a 4.4-mm sample. Our conclusion is that the cutting scale can be set close to 2.2 mm, and samples with this size or nanoindentations with this spacing can be used in place of core-scale measurements.

It is desirable to define the cutting scale as small as possible to be able to use small cuttings. This scale should be larger than the plastic-size zone, which is close to 0.1 mm when the applied load is equal to 500 mN, but it is unclear whether the cutting scale can be determined accurately. In our analysis, we halved the spacing between the indentations at each step, which is depicted in Fig. 7, but other division schemes can be tried, which are likely to yield other answers.

The cutting scale may vary in different formations and even for different samples from the same formation. In practice, it may not be possible to determine the cutting scale due to the lack of large samples. The existing limitations prevent us from accurately assigning the scale to all the shale samples. Thus, we consider a millimeter as an acceptable range for the cutting scale, and in the present study, we determined the accuracy of the results by comparing them with independent laboratory measurements.

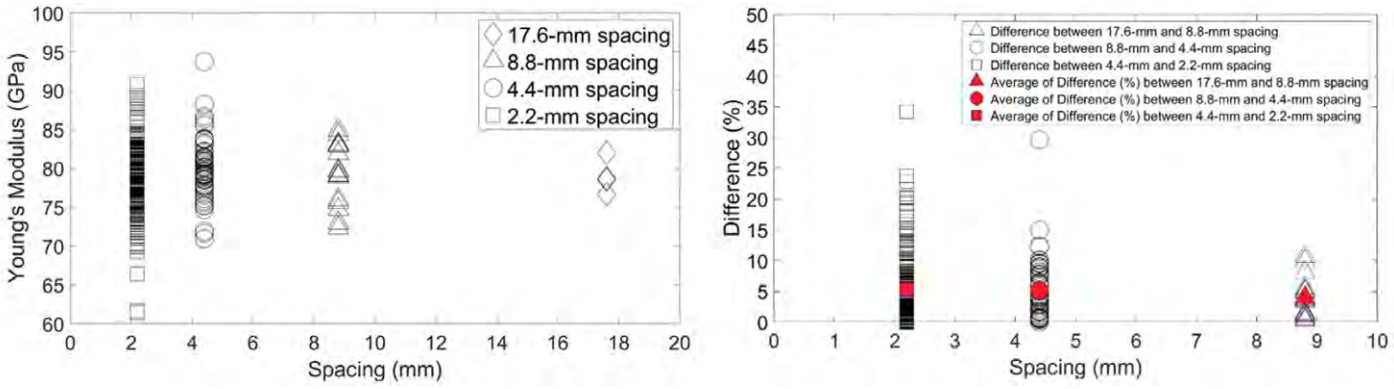

(a) (b)

Fig. 9—(a) Young's moduli of shale samples obtained from nanoindentations with regular spacings. (b) Difference between the Young's modulus at each step and those of the four nearest at the subsequent step. The difference is presented with the spacing between the indentations, and the average value is smaller than 6% when the spacing is 2.2 mm.

Next, we tested the accuracy of the cutting scale in determining the geomechanical properties at the core scale. Core plugs were extracted from a shale formation in the US, and their properties were measured using triaxial tests prior to conducting nanoindentations. The core plug was broken under compression as it was loaded to characterize the yield strength. The small pieces obtained after compression were used in nanoindentations. It was not easy to accurately determine the bedding orientation in pieces, which is also true in practice when we deal with cuttings.

Figure 10 shows the small pieces. Figure 10a shows the pieces, which are used as a proxy for cuttings, prior to preparation, and Fig. 10b shows them when they are prepared. The sample size is also shown using a scale ruler in Fig. 10. The sample size varies but is consistent with the data reported for cutting size in the literature (Ortega and Aguilera, 2014).

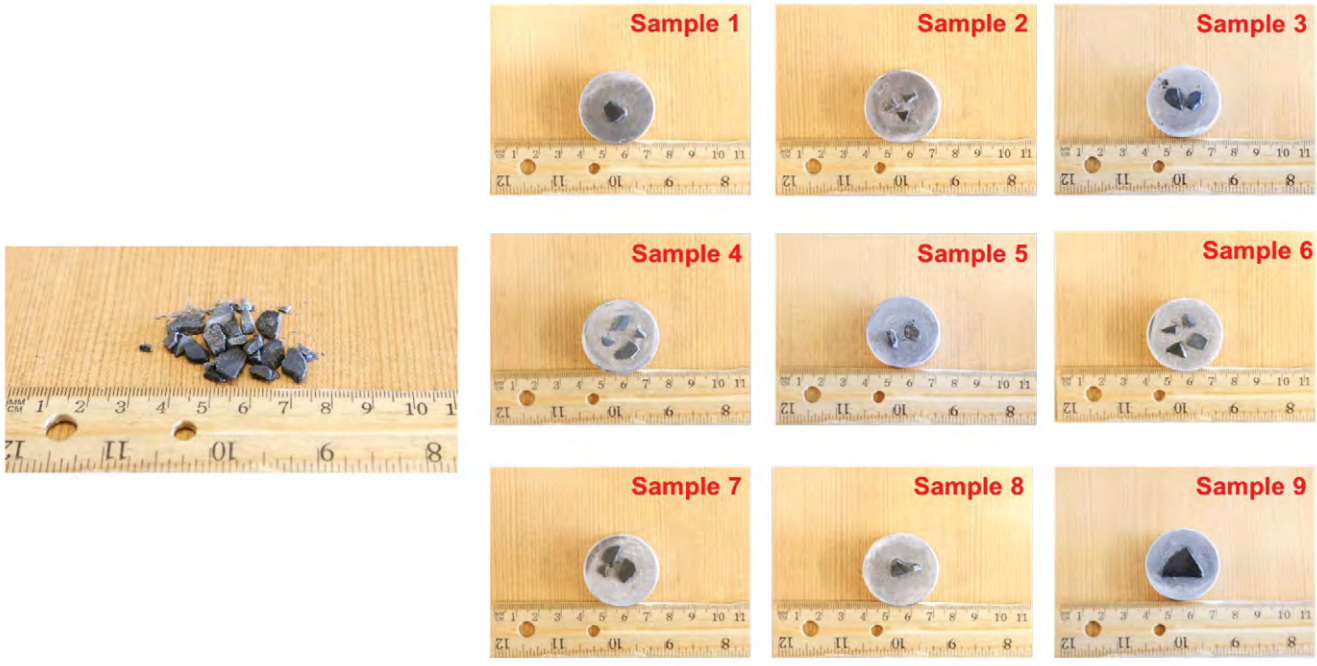

(a) (b)

Fig. 10—(a) Small pieces of the shales used to test the accuracy of the cutting scale. (b) Prepared samples are glued to an aluminum puck for nanoindentations.

The nanoindenter was first calibrated using fused silica, with known properties, glued to the aluminum puck. The fused silica is used to account for the effects of the device stiffness, including the aluminum substrate on the acquired data. We did not embed the small pieces in resin, as other researchers did (Deirieh et al., 2012; Shukla et al., 2013), because it can form a substrate softer than the specimen. A substrate with lower resistance against the load can impact the accuracy of the results. We also ensured that the polished small pieces are well positioned and attached to the puck with minimal glue. Loads are applied perpendicular to the sample such that the sample remains between the nanoindenter tip and the aluminum puck.

Independent core-scale measurements were conducted on the core plugs, and the average of the Young's moduli under different confining stresses (40.6, 50.6, and 30.5 MPa) is used to test the proposed method. We applied nanoindentations with regular 2.2-mm spacings to small pieces obtained from the core plugs. Figure 11 shows the results. The difference between the average modulus based on nanoindentations and the independent core-scale measurements remains smaller than 30% for all the samples. The difference becomes smaller when the finished surface reaches a higher level of smoothness.

It is difficult to reach a high level of smoothness for small pieces similar to that of a core plug shown in Fig. 5. The difference between the finished surface is caused by the high level of irregularity in the initial state of cuttings. Polishing small pieces using the preparation stages discussed in this study is even more difficult when the shale sample is more brittle.

The difference between the finished surfaces is apparent in Fig. 12 and can also be seen to some extent by comparing the outcomes of different stages in Fig. 5. Nanoindentation, in general, is a high-precision measurement and is influenced by local flaws, such as small fractures. The local flaws reduce the sample resistance against deformation and lower the Young's modulus obtained from nanoindentations.

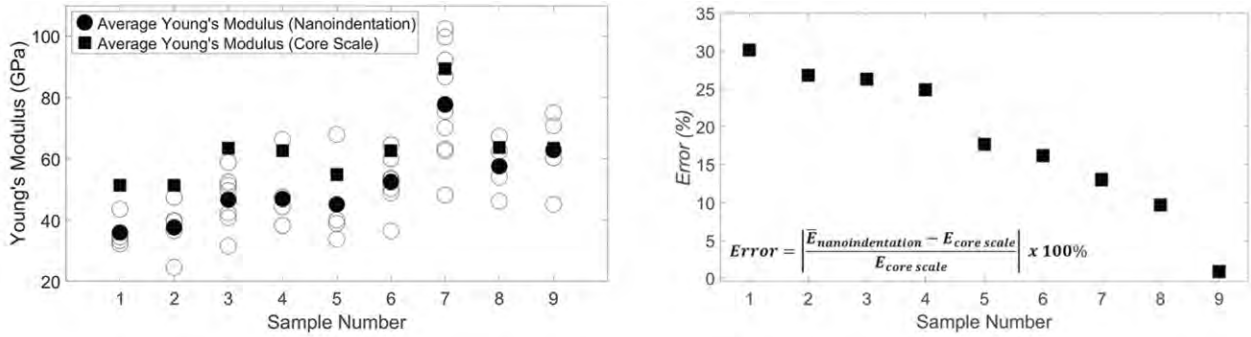

(a) (b)

Fig. 11—(a) Young's moduli of the shale samples obtained from independent triaxial tests using core plugs and from nanoindentations using small pieces. (b) Error decreases for samples whose surfaces reach a higher level of smoothness after preparation.

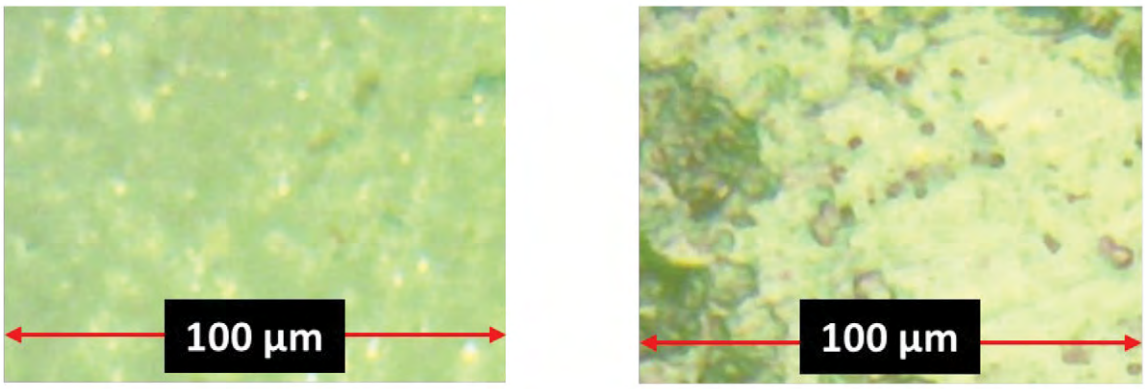

(a) (b)

Fig. 12—(a) The polished surface of the core plug, which corresponds to Stage 7 in Fig. 5, reaches a higher level of smoothness than that of (b) the cutting that corresponds to Fig. 9b. The interpreted results of the cuttings with the smoothest surface, which are less influenced by local flaws, are closer to the core-scale measurements.

DISCUSSION

The main objective of the conducted study was to propose a method applicable to shale cuttings. Predicting geomechanical properties at the core scale from nanoindentations will provide additional information that can be helpful in developing more realistic reservoir models. The shale surface was prepared using standard methods that are best designed for large samples. The presented results (Fig. 10) are based on using regular spacings, rather than finding the smoothest area to make the process more systematic. The results were improved when the smoothest area was picked for indentation, in that the error was smaller. Our observation is that improving the sample preparation will reduce errors. Using ion-milling techniques, which are better suited to smaller samples, is expected to improve the results.

Analyzing cuttings for formation characterization is appealing for a variety of reasons. Cuttings can help to better characterize the formation heterogeneity along the wellbore when only small pieces are available. Cuttings can also be obtained easily at minimal cost, in contrast to large samples, and can be used in close-to-real-time conditions.

There are limitations to the application of nanoindentations to cuttings and the sample preparation in our study. It is not always possible to determine the bedding orientation in the cuttings, and this becomes more complicated when the sample is smaller. Thus, one Young's modulus was reported for each sample at the core scale, which may be interpreted as an effective isotropic response. The Young's modulus based on nanoindentations was compared with independent core-scale measurements. Determining anisotropic properties based on nanoindentations entails loading in different directions. It also requires more advanced preparation techniques to reach a high level of smoothness (Stage 4 or in Fig. 5) on the rock surface in different directions.

The proposed method in this study is concerned with predicting geomechanical properties using cuttings at the core scale. One of the main advantages of the cuttings is that they are abundant and more easily recovered than the core plugs. Thus, the accurate interpretation of the properties is significant, especially if the collected cuttings on the surface can be related to the formation depth. The sample depth was not discussed in our study.

The geomechanical properties at the core scale were predicted from nanoindentations applied in a systematic pattern in this study. The assumption was that the average modulus obtained from nanoindentations represents the sample behavior at the core scale when the average property does not change with decreasing distance. Hence, no upscaling was performed to determine the core-scale properties.

CONCLUSIONS

The objective of the present study was to propose a new method that can be used for shale formation characterization using cuttings. The proposed method is required because large samples (~1 in.) are often unavailable. Cuttings are often the only source available and were used to determine geomechanical properties at the core scale.

The Young's moduli of the shale samples at the core scale were determined using nanoindentations on shale cuttings. The predicted results are promising, as the error in predicting core-scale measurements is smaller than 30% for all the samples analyzed. Our study shows that the rock surface smoothness has a major impact on the results obtained from nanoindentations. Surface grinding and then polishing were conducted. The two processes are important in order to remove local defects on the rock surface and to obtain properties more representative of bulk behavior. It was observed that surface grinding is more crucial, and polishing may be omitted when the applied load is close to 500 mN. The average moduli, which were obtained from nanoindentations, increased more than 50% after grinding but changed less than 10% after polishing.

Nanoindentation and its governing equations, as well as the necessary preparation for making nanoindentations, were discussed. As shown in the present study, nanoindentation is an appealing approach, as it can be applied to small samples. Nanoindentation is a high-precision measurement, and the outcome is sensitive to the sample preparation. Our study reveals that the predicted results from cuttings are closer to core-scale measurements when the sample is better prepared. Analyzing cuttings based on the conducted study has applications in the petroleum industry because it can enable us to better characterize the formation heterogeneity along the wellbore, especially in horizontal drilling, where large samples are usually not recovered.

ACKNOWLEDGMENTS

The authors would like to acknowledge the support of the Qatar National Research Fund (a member of the Qatar Foundation) through Grant #NPRP11S-0109-180241. The findings achieved herein are solely the responsibility of the authors.

NOMENCLATURE

Abbreviations

REV = representative elementary volume

Symbols

a = projected-area radius
A_c = projected area
c = plastic-zone radius
E = Young's modulus
E_i = indenter modulus
E_s = specimen modulus
H = specimen hardness
M = indentation modulus
p_{max} = maximum applied load
S = slope of load-displacement at the beginning of unloading
ν = Poisson's ratio
ν_i = indenter Poisson's ratio
ν_s = specimen Poisson's ratio
α = shape factor
ΔE_s = change in the interpreted Young's modulus due to the change in the Poisson's ratio
$\Delta \nu_s$ = change in the Poisson's ratio
σ_{yield} = yield strength
θ = geometrical parameter

REFERENCES

Abdolhosseini Qomi, M.J., Ebrahimi, D., Bauchy, M., Pellenq, R., and Ulm, F.J., 2017, Methodology for Estimation of Nanoscale Hardness via Atomistic Simulations, *Journal of Nanomechanics and Micromechanics*, **7**(4), 04017011. DOI: 10.1061/(ASCE)NM.2153-5477.0000127.

Abedi, S., Slim, M., and Ulm, F.J., 2016a, Nanomechanics of Organic-Rich Shales: The Role of Thermal Maturity and Organic Matter Content on Texture, *Acta Geotechnica*, **11**(4), 775–787. DOI: 10.1007/s11440-016-0476-2.

Abedi, S., Slim, M., Hofmann, R., Bryndzia, T., and Ulm, F.J., 2016b, Nanochemo-Mechanical Signature of Organic-Rich Shales: A Coupled Indentation–EDX Analysis, *Acta Geotechnica*, **11**(3), 559–572. DOI: 10.1007/s11440-015-0426-4.

Bhushan, B., and Gupta, B.K., 1991, *Handbook of Tribology: Materials, Coatings, and Surface Treatments*, Krieger Publishing Company, United States.

Bobji, M.S., and Biswas, S.K., 1998, Estimation of Hardness by Nanoindentation of Rough Surfaces, *Journal of Materials Research*, **13**(11), 3227–3233. DOI: 10.1557/JMR.1998.0438.

Bobko, C.P., Gathier, B., Ortega, J.A., Ulm, F.J., Borges, L., and Abousleiman, Y.N., 2011, The Nanogranular Origin of Friction and Cohesion in Shale—A Strength Homogenization Approach to Interpretation of Nanoindentation Results, *International Journal for Numerical and Analytical Methods in Geomechanics*, **35**(17), 1854–1876. DOI: 10.1002/nag.984.

Constantinides, G., Ulm, F.J., and Van Vliet, K., 2003, On the Use of Nanoindentation for Cementitious Materials, *Materials and Structures*, **36**(3), 191–196. DOI: 10.1007/BF02479557.

Constantinides, G., and Ulm, F.J., 2004, The Effect of Two Types of CSH on the Elasticity of Cement-Based Materials: Results From Nanoindentation and Micromechanical Modeling, *Cement and Concrete Research*, **34**(1), 67–80. DOI: 10.1016/S0008-8846(03)00230-8.

De Paula, O., Pervukhina, M., Gurevich, B., Lebedev, M., Martyniuk, M., and Delle Piane, C., 2010, Estimation of Carbonate Elastic Properties Using Nanoindentation and Digital Images, *Proceedings, 72nd EAGE Conference and Exhibition Incorporating SPE EUROPEC 2010*, Barcelona, Spain, 14–17 June. DOI: 10.3997/2214-4609.201400858.

Deirieh, A., Ortega, J.A., Ulm, F.J., and Abousleiman, Y., 2012, Nanochemomechanical Assessment of Shale: Coupled WDS-Indentation Analysis, *Acta Geotechnica*, **7**(4), 271–295. DOI: 10.1007/s11440-012-0185-4.

Gao, Q., Tao, J., Hu, J., and Yu, X.B., 2015, Laboratory Study on the Mechanical Behaviors of an Anisotropic Shale Rock, *Journal of Rock Mechanics and Geotechnical Engineering*, **7**(2), 213–219. DOI: 10.1016/j.jrmge.2015.03.003.

Hertz, H.,1896, Über die Berührung Fester Elastischer Körper (On the Contact of Elastic Solids, *Journal für die Reine und Angewandte Mathematik*, **92**(881), 156–171. Translated by D.E. Jones and G.A. Schott and reprinted in English in *Hertz' Miscellaneous Papers*, Macmillan & Co., London, 1896, Ch. 5. URL: https://openlibrary.org/books/OL24171839M/Miscellaneous_papers. Accessed July 22, 2020.

Hill, R., 1963, Elastic Properties of Reinforced Solids: Some Theoretical Principles, *Journal of the Mechanics and Physics of Solids*, **11**(5), 357–372. DOI: 10.1016/0022-5096(63)90036-X.

Huber, M.T., 1904, Zur Theorie der Berührung Fester Elastischer Körper, *Annalen der Physik*, **319**(6), 153–163. DOI: 10.1002/andp.19043190611.

ISO 4287, Geometrical Product Specifications (GPS)–Surface Texture: Profile Method–Terms, Definitions and Surface Texture Parameters, 1997, Geneva, Switzerland: International Organization of Standardization.

Jennings, H.M., Thomas, J.J., Gevrenov, J.S., Constantinides, G., and Ulm, F.J., 2005, Nanostructure of CSH Gel in Cement Paste as a Function of Curing Conditions and Relative Humidity, *Proceedings, International Conference on Creep, Shrinkage and Durability of Concrete and Concrete Structures, Concreep7*, Ecole Centrale de Nantes, France, September, 19–37. URL: https://www.researchgate.net/publication/283716499. Accessed July 22, 2020.

Johnson, K.L., 1970, The Correlation of Indentation Experiments, *Journal of the Mechanics and Physics of Solids*, **18**(2), 115–126. DOI: 10.1016/0022-5096(70)90029-3.

Laugier, M.T., 1987, New Formula for Indentation Toughness in Ceramics, *Journal of Materials Science Letters*, **6**(3), 355–356. DOI: 10.1007/BF01729352.

Lawn, B.R., Evans, A.G., and Marshall, D.B., 1980), Elastic/Plastic Indentation Damage in Ceramics: The Median/Radial Crack System, *Journal of the American Ceramic Society*, **63**(9–10), 574–581. DOI: 10.1111/j.1151-2916.1980.tb10768.x.

Li, W.H., Shin, K., Lee, C.G., Wei, B.C., Zhang, T.H., and He, Y.Z., 2008, The Characterization of Creep and Time-Dependent Properties of Bulk Metallic Glasses Using Nanoindentation, *Materials Science and Engineering: A*, **478**(1–2), 371–375. DOI: 10.1016/j.msea.2007.06.015.

Li, W., and Sakhaee-Pour, A., 2016, Macroscale Young's Moduli of Shale Based on Nanoindentations, *Petrophysics*, **57**(6), 597–603.

Mavko, G., Mukerji, T., and Dvorkin, J., 2009, *The Rock Physics Handbook: Tools for Seismic Analysis of Porous Media*, Cambridge University Press. DOI: 10.1017/CBO9780511626753.

Miller, M., Bobko, C., Vandamme, M., and Ulm, F.J., 2008, Surface Roughness Criteria for Cement Paste Nanoindentation, *Cement and Concrete Research*, **38**(4), 467–476. DOI: 10.1016/j.cemconres.2007.11.014.

Monfared, S., Laubie, H., Radjai, F., Hubler, M., Pellenq, R., and Ulm, F.J., 2018, A Methodology to Calibrate and to Validate Effective Solid Potentials of Heterogeneous Porous Media From Computed Tomography Scans and Laboratory-Measured Nanoindentation Data, *Acta Geotechnica*, 1–26. DOI: 10.1007/s11440-018-0687-9.

Ortega, J.A., Ulm, F.J., and Abousleiman, Y., 2007, The Effect of the Nanogranular Nature of Shale on Their Poroelastic Behavior, *Acta Geotechnica*, **2**(3), 155–182. DOI: 10.1007/s11440-007-0038-8.

Ortega, C., and Aguilera, R., 2014, A Complete Petrophysical-Evaluation Method for Tight Formations From Drill Cuttings Only in the Absence of Well Logs, Paper SPE-161875, *SPE Journal*, **19**(4), 636–647. DOI: 10.2118/161875-PA.

Pharr, G.M., Oliver, W.C., and Brotzen, F.R., 1992, On the Generality of the Relationship Among Contact Stiffness, Contact Area, and Elastic Modulus During Indentation, *Journal of Materials Research*, **7**(3), 613–617. DOI: 10.1557/JMR.1992.0613.

Riester, L., Blau, P.J., Lara-Curzio, E., and Breder, K., 2000, Nanoindentation With a Knoop Indenter, *Thin Solid Films*, **377–378**, 635–639. DOI: 10.1016/S0040-6090(00)01298-0.

Rybacki, E., Reinicke, A., Meier, T., Makasi, M., and Dresen, G., 2015, What Controls the Mechanical Properties of Shale Rocks? Part I: Strength and Young's Modulus, *Journal of Petroleum Science and Engineering*, **135**, 702–722. DOI: 10.1016/j.petrol.2015.10.028.

Sayers, C.M., 2013, The Effect of Kerogen on the Elastic Anisotropy of Organic-Rich Shales, *Geophysics*, **78**(2), 65–74. DOI: 10.1190/geo2012-0309.1.

Shukla, P., Kumar, V., Curtis, M., Sondergeld, C.H., and Rai, C.S., 2013, Nanoindentation Studies on Shales, Paper ARMA 13-578 presented at the 47th US Rock Mechanics/Geomechanics Symposium, San Francisco, California, USA, 23–26 June. URL: https://www.researchgate.net/publication/289466818_Nanoindentation_studies_on_shales. Accessed July 22, 2020.

Sneddon, I.N., 1965, The Relation Between Load and Penetration in the Axisymmetric Boussinesq Problem for a Punch of Arbitrary Profile, *International Journal of Engineering Science*, **3**(1), 47–57. DOI: 10.1016/0020-7225(65)90019-4.

Sone, H., and Zoback, M.D., 2013, Mechanical Properties of Shale-Gas Reservoir Rocks–Part 1: Static and Dynamic Elastic Properties and Anisotropy, *Geophysics*, **78**(5), D381–D392. DOI: 10.1190/geo2013-0050.1.

Tai, K., Ulm, F.J., and Ortiz, C., 2006, Nanogranular Origins of the Strength of Bone, *Nano Letters*, **6**(11), 2520–2525. DOI: 10.1021/nl061877k.

Tutuncu, A.N., Myers, M.T., and Arasteh, M.M., 2004, Use of Cutting Velocities for Real Time Pore Pressure and Fracture Gradient Prediction, US Patent No. 2004/0236513 A1.

Tutuncu, A.N., Myers, M.T., and Arasteh, M.M., 2005, Use of Cutting Velocities for Real Time Pore Pressure and Fracture Gradient Prediction, US Patent No. 6,968,274.

Ulm, F.J., and Abousleiman, Y., 2006, The Nanogranular Nature of Shale, *Acta Geotechnica*, **1**(2), 77–88. DOI: 10.1007/s11440-006-0009-5.

Ulm, F.J., Vandamme, M., Bobko, C., Alberto Ortega, J., Tai, K., and Ortiz, C, 2007, Statistical Indentation Techniques for Hydrated Nanocomposites: Concrete, Bone, and Shale, *Journal of the American Ceramic Society*, **90**(9), 2677–2692. DOI: 10.1111/j.1551-2916.2007.02012.x.

Uribe, D., Saenger, E.H., and Steeb, H., 2016, Digital Rock Physics: A Case Study of Carbonate Rocks, *PAMM*, **16**(1), 399–400. DOI: 10.1002/pamm.201610188.

Vialle, S., and Lebedev, M., 2015, Heterogeneities in the Elastic Properties of Microporous Carbonate Rocks at the Microscale From Nanoindentation Tests, *SEG International Exhibition and Annual Meeting Technical Program Expanded Abstracts*, 3279–3284. DOI: 10.1190/segam2015-5885016.1.

Volinsky, A.A., Vella, J.B., and Gerberich, W.W., 2003, Fracture Toughness, Adhesion and Mechanical Properties of Low-K Dielectric Thin Films Measured by Nanoindentation, *Thin Solid Films*, **429**(1–2), 201–210. DOI: 10.1016/S0040-6090(03)00406-1.

Wang, Z., Wang, H., and Cates, M.E., 2001, Effective Elastic Properties of Solid Clays, *Geophysics*, **66**(2), 428–440. DOI: 10.1190/1.1444934.

Zhu, W., Fonteyn, M.T.J., Hughes, J., and Pearce, C., 2009, Nanoindentation Study of Resin Impregnated Sandstone and Early-Age Cement Paste Specimens, *in* Bittnar, Z., Bartos, P.J.M., Němeček, J., Šmilauer, V., and Zeman, J., editors, *Nanotechnology in Construction 3*, 403–408, Springer, Berlin, Heidelberg, Germany. DOI: 10.1007/978-3-642-00980-8_55. ISBN: 978-3-642-00979-2.

ABOUT THE AUTHORS

Erica Esatyana is a PhD candidate in petroleum engineering at the University of Houston. Her educational background is both in petroleum engineering from Heriot-Watt University (MS degree) and Trisakti University Jakarta (BS degree). Currently, she is doing research projects related to nanomechanical and geomechanical properties of shale formations.

A. Sakhaee-Pour is an assistant professor of petroleum engineering at the University of Houston. Previously, he worked for two years as a post-doctoral fellow at the Institute for Computational Engineering and Sciences. His current research interests include relating nano- to microscale measurements to large-scale geomechanical properties and modeling multiphase flow in unconventional formations. He holds a PhD degree in petroleum engineering from the University of Texas at Austin and an MS degree in mechanical engineering from Sharif University of Technology.

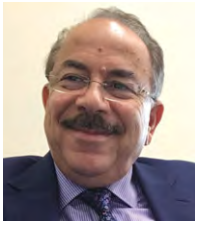

Fadhil Sadooni is currently a research professor with the Environmental Science Center, Qatar University and was an adviser of the vice president of Research and Graduate Studies in the university. Fadhil received a PhD degree in petroleum geoscience from the University of Bristol, UK. Prior to joining Qatar University, he worked for 17 years with the petroleum industry in the Middle East and SE Asia. He started his career as a rig geologist drilling the Cretaceous carbonate reservoirs of northern Iraq. Fadhil also worked with Yarmouk University in Jordan and was the chairman of the Geology Department at the United Arab Emirates University between 2002 to 2006. He has published more than 50 papers in peer-reviewed journals and coauthored more than 10 books in Arabic and English on the different aspects of geology, including the *Petroleum Geology of Iraq* published by the Scientific Press with more than 40 conference presentations. Fadhil has worked as a consultant for many oil companies on hydrocarbon exploration in the Middle East. His present research focuses on carbonate reservoirs characterization, shale deposits of Eastern Arabia, and microbial sediments.

Hamad Al-Saad Al-Kuwari is a professor of Geology and the director of the Environmental Studies Center, Qatar University. He has a PhD degree in micropaleontology and stratigraphy from the University of Cairo, Egypt. Dr. Al-Kuwari was the chairman of the Geology Department, Qatar University, and the director of the Center of Sustainable Development at the College of Science before being selected to manage the Environmental Science Center in 2017. Dr. Al-Kuwari was awarded around 10 grants from different funding agencies. He has published around 30 papers in the leading journals in his field and has given many presentations at international and regional specialized conferences. Dr. Al-Kuwari was awarded the Honor award, Arabian Pioneers in Geology (2007), and The State Encouragement Award (2017). His most recent research focused on the microbial mediated minerals, such as dolomite and clay minerals, supported twice by the National Priority Research Program of Qatar Foundation and reservoir characterization of the Arabian Basin.

PETROPHYSICS, VOL. 61, NO. 5 (OCTOBER 2020); PAGES 417–433; 18 FIGURES; 3 TABLES. DOI: PJV61N5-2020a2

Classification of Adsorption Isotherm Curves for Shale Based on Pore Structure

Yuanyuan Tian[1], Qing Chen[1], Changhui Yan[1,*], Hucheng Deng[1], and Yanqing He[1]

ABSTRACT

In the study of shale gas reservoirs, the characteristics of pore structure can be determined according to the shape of the adsorption isotherm curve. When applying conventional classifications known as the Brunauer-Deming-Deming-Teller (BDDT), de Boer, and International Union of Pure and Applied Chemistry (IUPAC) classification to categorize adsorption isotherm curves for shale, these classifications can't accurately demonstrate pore structure in different shale reservoirs. Based on the characteristics of pore structure in shale, we chose pore shape, pore size, and pore-throat sorting as parameters to study changes in adsorption isotherm curves due to different grades of these three parameters. We then generated 27 types of adsorption isotherm curves to match the corresponding characteristics of the pore structure in shale. This new classification method is applied to categorize 101 adsorption isotherm curves measured by shale samples and analyzes the characteristics of pore structure. In a comparison of analysis results from other methods, this new classification method is justified to be more practical.

INTRODUCTION

As energy structure has changed in the past decades, shale gas plays an important role in unconventional reservoir exploitation for many countries, such as China, the US, Canada, and Australia. (Ross and Bustin, 2008; Kalantari-Dahaghi, 2011; Torghabeh et al., 2014; Pang et al., 2017). With one of the largest technically recoverable shale gas storages in the world (US Energy Information Administration, 2015), China has been focused on shale gas exploration and development in recent years. The main exploitation projects have been carried out in the Sichuan Basin, Tarim Basin, and Yangtze Platform (Ross and Bustin, 2009; Yan et al., 2009).

Shale is very different from conventional reservoirs. It is composed of two distinct components: organic and inorganic materials (Tian et al., 2017). Kerogen is the main constituent of the organic matter. There are a considerable amount of micropores (pore size < 2 nm) and mesopores (pore size between 2 to 50 nm) in organic matter (Kang et al., 2011). Inorganic materials in shale mainly consist of clay minerals (including illite, montmorillonite, chlorite, and kaolinite), quartz, and feldspar. The total amount of kaolinite, montmorillonite, illite, and chlorite can reach 70% for some shale samples, and clay minerals also can have nanoporous structures (Yaalon, 1962; Jiao et al., 2014). In a shale gas reservoir, a large amount of micropores results in ultralow permeability, which is a crucial parameter for shale gas prospection (Schwartz et al., 2019). Meanwhile, the presence of micropores increases specific surface area, and surface adsorption on large specific surface area can significantly enhance gas in place in shale (Pang et al., 2018). As a result, pore structure analysis is significant for shale gas exploitation and gas in place in shale (Jin and Firoozabadi, 2016; Xu et al., 2020).

The pore structures of shale reservoirs have been studied by various experimental methods, such as scanning electron microscope (SEM), mercury intrusion, low-temperature nitrogen adsorption, and carbon dioxide adsorption (Dewers et al., 2012; Yang et al., 2013). Mercury intrusion is used to exploit macropores (pore size > 50 nm) (Bustin et al., 2008), and it offers more information about throat rather than pores. (Clarkson et al., 2013). Low-temperature nitrogen adsorption and CO_2 adsorption can be used to detect pore sizes of less than 50 nm (Clarkson et al., 2011). When applying gas adsorption to evaluate shale nanoporous structures, density functional theory (DFT), the Horvath-Kawazoe (HK) model, the Barrett-Joyner-Halenda (BJH)

Manuscript received by the Editor January 2, 2020; revised manuscript received June 11, 2020; accepted June 14, 2020.
[1]College of Energy, Chengdu University of Technology, Dongsanlu #1, Er'xian bridge road, Chenghua district, Chengdu, Sichuan province, P.R.China; yuanyuan-tian@outlook.com; chenqing@mail.cdut.edu.cn; ych@cdut.edu.cn; denghucheng@cdut.cn; heyanqingimpact@hotmail.com
*Corresponding author

method, and the multipoint Brunauer, Emmett, Teller (BET) method are frequently used to calculate specific surface area or pore-size distribution (Ravikovitch et al., 1998; Dombrowski and Lastoskie, 2002; Li et al., 2016). Based on adsorption-desorption isotherms plotted by experimental data of low-temperature nitrogen adsorption P/P_0 vs. V, where P is adsorption pressure in MPa, P_0 is saturated vapor pressure in MPa, and V is the volume of adsorbate in pores in cc/g, different classifications of gas adsorption isotherms are also applied to characterize shale-pore structures, such as the Brunauer-Deming-Deming-Teller (BDDT) classification, the de Boer classification, and the International Union of Pure and Applied Chemistry (IUPAC) classification (Anovitz and Cole, 2015; Zhang et al., 2016).

The BDDT classification is based on the shape of adsorption isotherms (Brunauer et al., 1940). It can be inferred from this classification that the adsorption mechanism is monolayer adsorption, multilayer adsorption, or capillary condensation. Furthermore, the pore-size distributions in adsorbents can be defined as micropore, mesopore, and macropore. The de Boer classification considers both the shape of the adsorption isotherm and hysteresis loop (Everett and Stone, 1958). It is one of the most widely used methods to characterize the pore shapes of porous materials. There are five types of adsorption isotherms according to the de Boer classification, and each type corresponds to a certain pore shape such as cylindrical, slit, conical, two nonparallel planes, and ink-bottle pores. The IUPAC classification focuses on the shape of the hysteresis loop and defines two extreme types as H1 and H4, which indicate pores forming uniform spheres in fairly regular arrays and narrow slit pores separately, and two intermediate types between these two types (Gregg and Sing, 1983).

It is worth mentioning that all previous adsorption isotherm classifications are based on the characteristics of homogeneous adsorbents, which are particularly different from shale. None of these classifications can investigate a shale's pore structure comprehensively because researchers usually focus on a single factor like pore shape or pore size. In addition, while using adsorption isotherm classifications, pore sorting is ignored. To the best of our knowledge, there is no work to combine a shale's pore structure and shape of the adsorption isotherm. Our research aims at proposing a fast and accurate method to study a shale's pore structure as pore shape, pore size, and pore-throat sorting based on establishing a new adsorption isotherm classification for shale.

TEST SAMPLES AND EXPERIMENTS

All 106 core samples (Samples D1 to D106) are black and dark gray shale rocks from the Wulalik Formation, Pingliang Formation (Ordovician), black shale from the Yanchang Formation (Triassic) in the Ordos Basin, and black gray and dark gray shale rocks from the Niutitang Formation in the Sichuan Basin.

The tests are conducted by the Quadrasorb SI surface area and pore-size analyzer. In our experiment, nitrogen is used as the adsorbate. The lower limitation of the specific surface area is 0.01 m^2/g for nitrogen. In the aspect of pore-size distribution analysis, the minimum pore volume is 0.0001 cm^3/g (at standard temperature and pressure), and the pore-size range is 0.35 to 400 nm.

All samples were crushed to 60 to 80 mesh (180 to 250 μm). The pulverized samples were dried and vacuumized at 353.15 K for 12 hours for degassing in order to prepare the samples for the gas adsoption method. In the gas expansion process, the crushed samples were added in low-temperature-resistant test tubes of the experimental instrument, and N_2 adsorption-desorption isotherms were obtained under the relative pressure ranging from 0.01 to 0.995 at 77 K. The adsorption isotherm is derived point by point by measuring the quantity of nitrogen adsorbed and the equilibrium pressure as pressure increasing. On the contrary, the desorption isotherm can be obtained by measuring the quantities of gas removed from the sample as the relative pressure decreasing. With the QuadraWin software, the adsorption-desorption isotherm curves are generated automatically.

CONVENTIONAL CLASSIFICATION IN APPLICATION TO SHALE

Many studies on the classification of adsorption isotherm curves have been done. Classifications based on the shape of adsorption curves include the BDDT classification and the modified BDDT classification done by Sing et al. (1985); classifications based on the adsorption curve coupled with the shape of the hysteresis loop include the de Boer classification and the IUPAC classification.

The BDDT classification focuses on the van der Waals adsorption of gases and divides adsorption isotherms into five types (Brunauer et al., 1940) (Fig. 1). Type I isotherms are given by microporous solids having relatively small external surfaces. Type II is the S-shaped or sigmoid isotherm and is

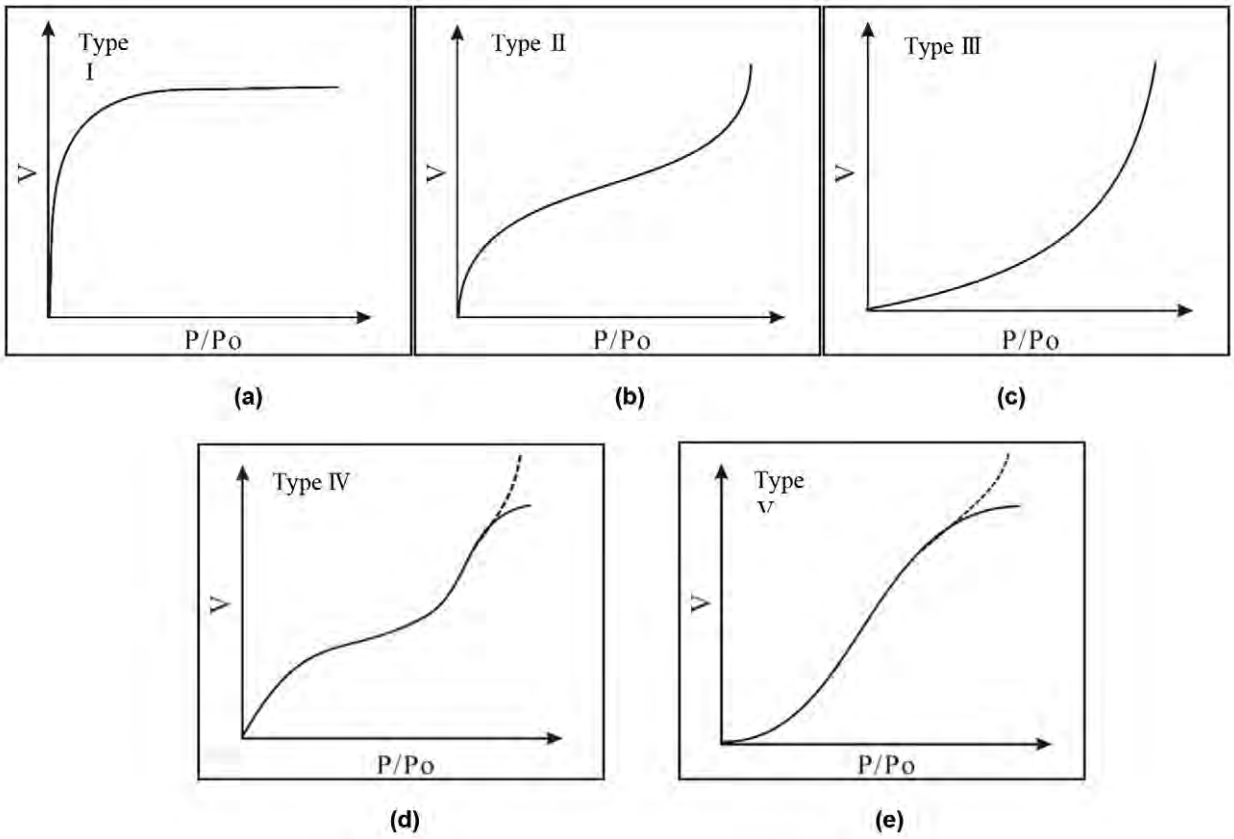

Fig. 1—Classification of the BDDT adsorption isotherm (Brunauer, 1940; Gregg and Sing, 1982). The dashed line in (d) Type IV and (e) Type V refers to an adsorption isotherm of porous media with a relatively small external surface, and the solid line refers to the adsorption isotherm of porous media with a relatively large external surface.

the normal form of isotherm obtained with a nonporous or macroporous adsorbent. A Type III isotherm is convex to the P/P_0 axis over its entire range, and this type is a well-known BET adsorption isotherm. Type IV and Type V are closely related to Types II and III. Characteristic features of Type IV and Type V isotherms are their hysteresis loop, which is associated with capillary condensation compared with Type II and Type III (Sing et al., 1985). Adsorption isotherms for shale belong to Type IV and Type V (Fig. 2).

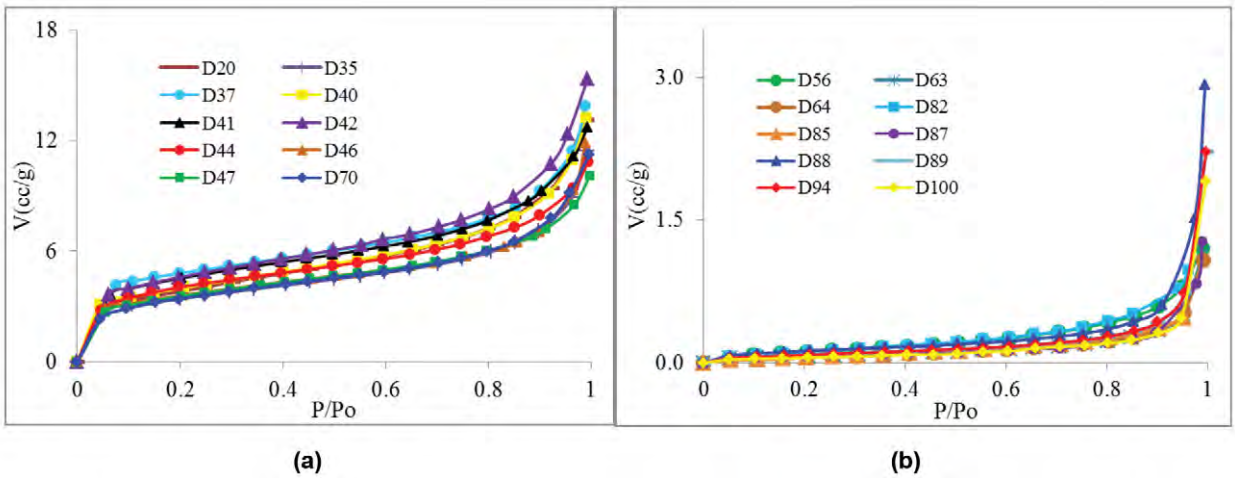

Fig. 2—Typical adsorption isotherms of Type IV and Type V according to the BDDT classification. (a) Type IV adsorption isotherms; (b) Type V adsorption isotherms.

de Boer and Lippens divided adsorption/desorption isotherms with hysteresis loops into five types (de Boer and Lippens, 1964; Tang et al., 2015) (Fig. 3). The shape of the hysteresis loop corresponds to the pore shape. Type A is specific for cylindrical pores with a similar radius. Type B is specific for pores formed between two planes. Type C adsorption/desorption isotherm is formed in conical pores. Type D hysteresis loop is corresponding to the shape of pores formed from two nonparallel planes. Type E has a spherical shape of pores, with numerous narrowings and open ends, along with different forms of "ink bottle" (Nagolska and Gawdzińska, 2011). All shale samples can be divided into three groups based on the de Boer classification as Type B, Type D, and Type E (Fig. 4).

The IUPAC classification was identified based on experimental isotherms observed in disordered solids (Gregg and Sing, 1982; Sing et al., 1985; Fan et al., 2013) (Fig. 5). Type H1 and Type H4 are two extreme types. In Type H1, the two branches are almost vertical and nearly parallel over an appreciable range of gas uptake. It indicates a limited pore-size distribution of the measured samples. Type H4 remains nearly horizontal and parallel over a wide range of P/P_0. Types H2 and H3 may be regarded as intermediate between these two extremes. Type H2 usually happens to slit-like pores. The samples have various distributions of pore types and pore size. Type H3 usually occurs with open-wedge pores (Zhang et al., 2016). According to the IUPAC classification, the adsorption/desorption isotherms of the shale samples show features of Type H2, Type H3, and Type H4 (Fig. 6).

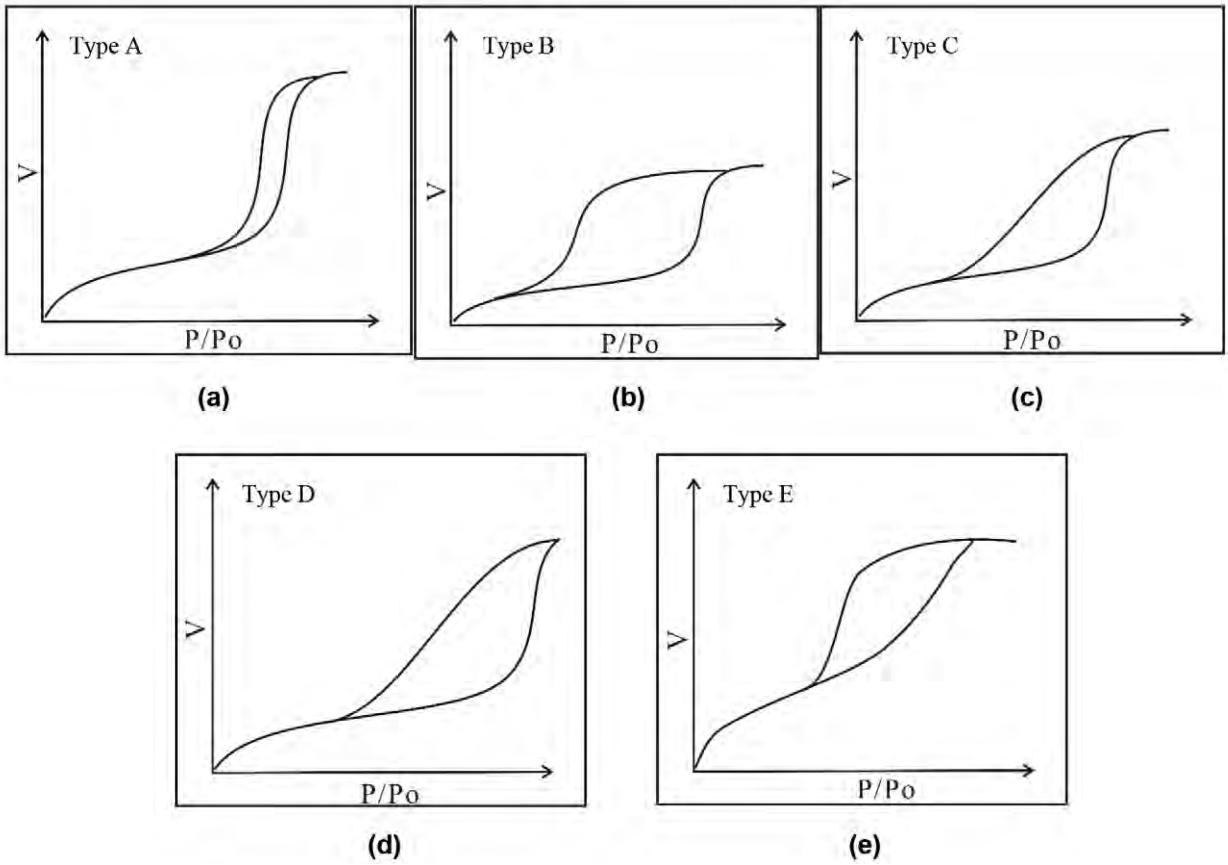

Fig. 3—Classification of de Boer adsorption/desorption isotherms (de Boer et al., 1964). (a) Type A; (b) Type B; (c) Type C; (d) Type D; and (e) Type E. The lower line is the adsorption curve, and the upper line is the desorption curve.

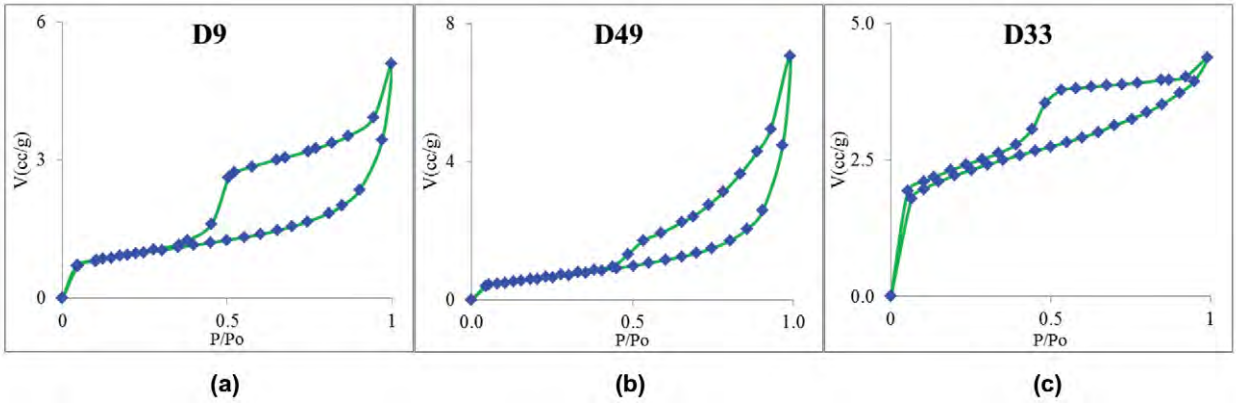

Fig. 4—Typical adsorption isotherms of Type B, Type D, and Type E according to the de Boer classification. (a) Type B adsorption isotherm; (b) Type D adsorption isotherm; and (c) Type E adsorption isotherm.

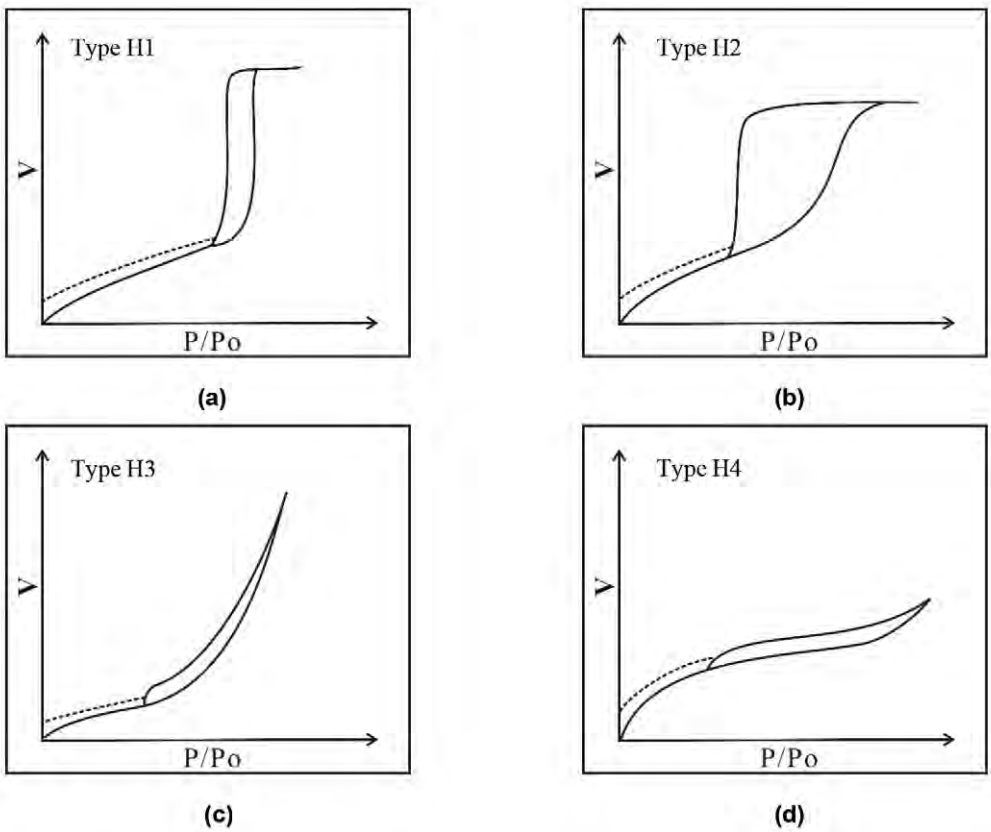

Fig. 5—Classification of the IUPAC adsorption/desorption isotherms (Sing et al., 1985). (a) Type H1; (b) Type H2; (c) Type H3; and (d) Type H4.

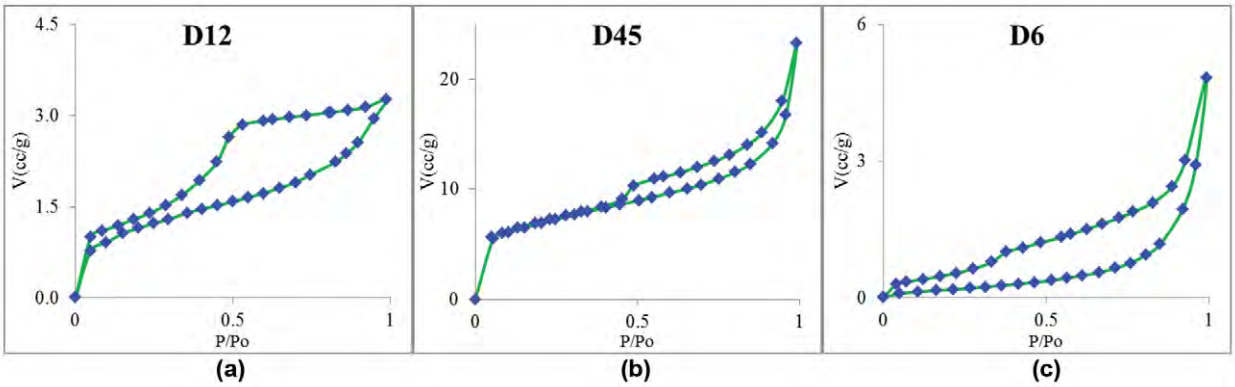

Fig. 6—Typical adsorption isotherms of Type B, Type D, and Type E according to the de Boer classification. (a) Type H2 adsorption isotherm; (b) Type H3 adsorption isotherm; and (c) Type H4 adsorption isotherm.

These three classifications reveal the characterizations of all shale samples we measured (Durán-Valle, 2012; Zhang et al., 2016). Of the samples, 60.38% have micropores and mesopores, and the rest are samples with mesopores and macropores based on the BDDT classification. The results based on the de Boer classification depict the pore shape of shale samples as slit pores formed by two parallel plates or nonparallel planes except for six spherical-pore samples. When the IUPAC classification is applied, it shows that most shale samples we measured are slit-pore shale or open-wedge pore shale, and only 8% of the samples are bottleneck pore (Table 1).

However, the BDDT classification does not take the hysteresis into consideration. Thus, some important information reflecting the pore structure of the shale is neglected when using the BDDT classification. In addition, the adsorption isotherm curves for all shale core samples only occupy two types in the BDDT classification, which can't demonstrate the diversity of shale samples. It illustrates that the main types of pores in shale are narrow-slit pores and tilt-plate crossbedding pores when applying the de Boer classification to analyze adsorption isotherm curves for 106 shale samples. Therefore, the result of the de Boer classification is monotonous. The IUPAC classification indicates that these shale samples contain a large amount of ink-bottle pores, narrow-slit pores, and a small amount of slit pores. From the quantity of types obtained by the IUPAC classification, it is better than the de Boer and BDDT classifications. However, due to the diversity of the shale's pore structure, none of these methods can evaluate the characteristics of the pore structure in shale completely.

Shale adsorption capacity is dependent on the type and quantity of minerals, type and amount of organic matter, and characteristics of the pore structure. This feature leads to the diversity and specialty of adsorption isotherm curves in shale. Therefore, a new classification method focusing on the classification of shale adsorption isotherm curves is necessary.

Table 1—Classification of Adsorption Isotherm for Shale Samples by Conventional Classifications

Classification	Type	Number of Samples	Percentage (%)	Properties
BDDT	Type IV	64	60.38	Micropore and mesopore
	Type V	42	39.62	Mesopore and macropore
de Boer	Type B	49	46.23	Slit pore
	Type D	55	51.89	Pore formed from two nonparallel planes
	Type E	2	1.89	Spherical pore
IUPAC	H2	49	46.23	Slit pore
	H3	54	50.94	Open-wedge pore
	H4	3	2.83	Bottleneck pore

GENERATING A NEW CLASSIFICATION FOR SHALE ADSORPTION ISOTHERM CURVES

A shale adsorption isotherm curve is a representation of a characteristic of the pore structure in a shale reservoir. As an unconventional reservoir, the shape and size of the pores and sorting of pore throat for shale have direct effects on reserves calculation, productivity analysis, and production performance. Therefore, the effects on adsorption isotherm and hysteresis by these three parameters should be taken into account to discuss the new classification for shale adsorption isotherm curves.

The Effect of Pore Shape on Adsorption Isotherm Curves

Shale contains a lot of clay, quartz, feldspar, and rock debris. The content and arrangement of these fragments are different, which result in a variety of pore shapes in shale. The pore shape of shale is not only a considerable factor in shale gas adsorption but also a probable reason for permeability variation in shale (Zheng et al., 2019a; Zheng et al., 2019b). According to SEM figures, slit-pore, wedge-shaped, and cylindrical pores are three common pore structures in shale (Fig. 7a). In the de Boer classification (de Boer et al., 1958), pore shape affects the adsorption isotherm curve and shape of the hysteresis loop. For slit-shaped pores, the hysteresis loop is wide, and its axis is parallel to the *x*-axis. The adsorption curve drastically increases nearly at saturated vapor pressure, but the desorption curve rapidly decreases at medium relative pressure, which results in a flat hysteresis loop with the smallest vertical spacing. For a wedge-shaped pore, the hysteresis loop is relatively planar with a spacing between the spacing of a cylindrical pore and the spacing of a slit pore. For a cylindrical-shaped pore, hysteresis appears in the medium relative pressure region. The vertical intervals of the adsorption curve and desorption curve are barely parallel, and the hysteresis has the largest vertical spacing (Fig. 7b). When the pore structure changes from cylindrical to wedge and then to slit, adsorption and desorption curves change from parallel to the vertical axis and then to the horizontal axis (Fig. 7c). The hysteresis loop is from steep with large vertical spacing to flat with large horizontal spacing.

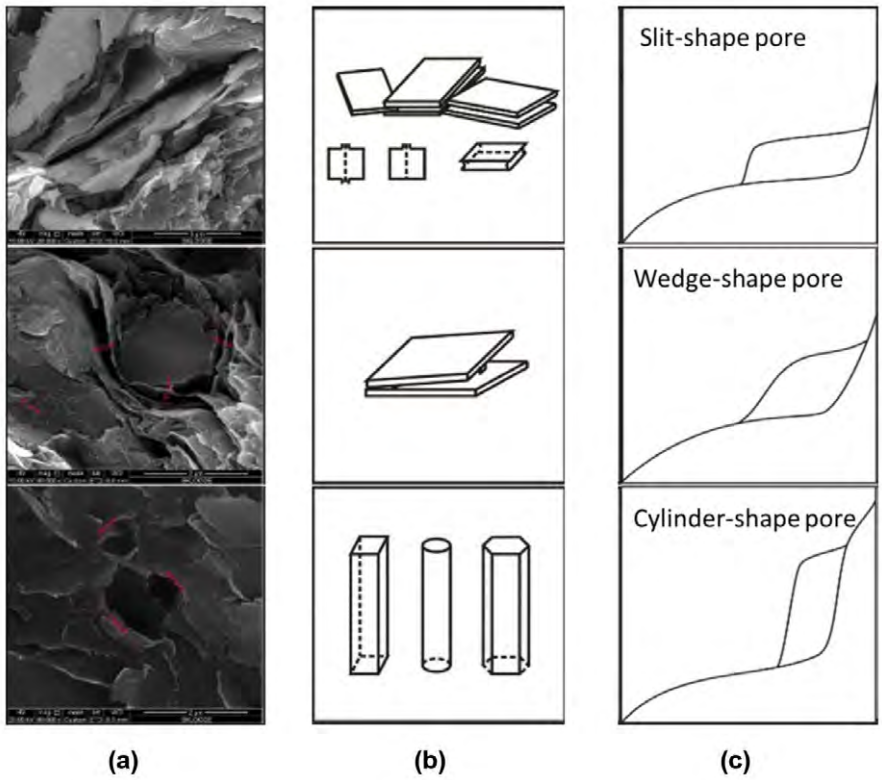

Fig. 7—Main pore types in shale and the effect of pore shape to adsorption isotherm curves. (a) SEM images; (b) pore shape; and (c) adsorption-desorption curves. Curves in (c) are adsorption-desorption curves of slit-shaped pore, wedge-shaped pore, and cylinder-shaped pore, respectively.

Effect of Pore Size on Adsorption Isotherm Curves

Shale contains micropores, mesopores, and macropores, and pore size is one of the most important factors in shale gas flow (Shen et al., 2018) (Alfi et al., 2019). The distribution of adsorption potential in pores with different pore sizes is not uniform, resulting in a discrepancy in the shape of the adsorption isotherm curve. Both simulation and experimental projects reveal that pore size affects the shape of the adsorption isotherm curve and hysteresis loop significantly (Neimark et al., 1998; Sayari et al., 1998; Kruk et al., 2000; Ravikovitch and Neimark, 2001) (Fig. 8). The hysteresis is dependent on the pore size; the starting point of hysteresis (SPH) will move forward to the low-pressure region, and the area of hysteresis will gradually decrease until it totally disappears. It is in accordance with the results derived from the experimental analysis of the shale samples. The comparison of Samples D2, D90, and D28 obviously shows that Sample D2 has the widest hysteresis loop, and the starting pressure of the hysteresis loop is lower than Samples D90 and D28. On the contrary, the hysteresis loop of Sample D28 is narrower and starts at higher pressure (Fig. 9). The rank of pore sizes of these three samples is d (D28) > d (D90) > d (D2) (Fig. 10). Therefore, for shale, the area and horizontal spacing of the hysteresis loop is small for shale with micropores. The relative pressure at the starting point of hysteresis is relatively low (about $P/P_0 < 0.4$); for shale with macropores, the area of the hysteresis loop is large, and the relative pressure at the starting point of hysteresis is high (about $P/P_0 > 0.6$); for shale with mesopores, the area of the hysteresis loop and relative pressure at the starting point of the hysteresis are medium (P/P_0 is around 0.5), which is located between the value of micropores and macropores (Fig. 11).

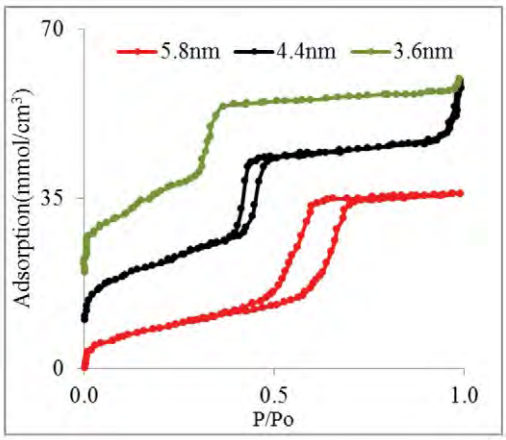

Fig. 8—Comparison of the adsorption isotherms on MCM-41 with different pore sizes (Ravikovitch et al., 2001).

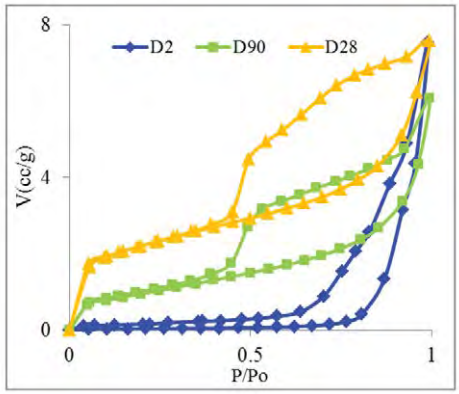

Fig. 9—Adsorption isotherms of shale samples.

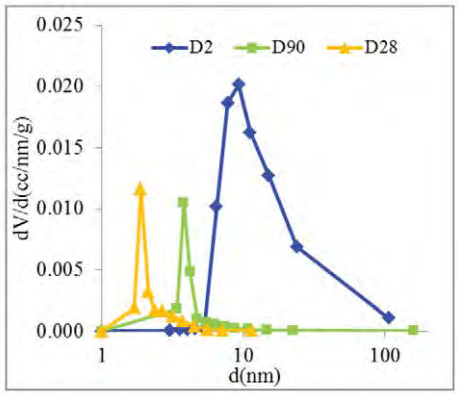

Fig. 10—Pore-size distribution of shale samples.

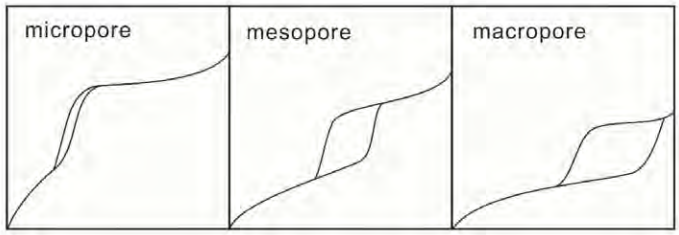

Fig. 11—Effect of pore size to adsorption isotherm curve in shale.

Effect of Pore-Throat Sorting on Adsorption Isotherm Curves

The sorting of pore throat is a crucial parameter for the evaluation of reservoir properties. The hysteresis is very complicated in ink-bottle pores due to pore blockage (Fig. 12a) (Thommes, 2010). When the bottleneck is smaller than the body, the blockage might happen during desorption. The bottle may be blocked because the neck is filled by absorbates. When pressure drops to capillary evaporation pressure at the neck of the bottle, the gas will rapidly desorb and flow out. Thus, the homogeneity of the ink bottleneck

affects the shape of the desorption curve in the hysteresis loop (Fig. 12b). When the size of the ink bottleneck is almost equivalent, the desorption curve decreases rapidly. However, the size of the ink bottleneck is different, and the desorption curve decreases slowly.

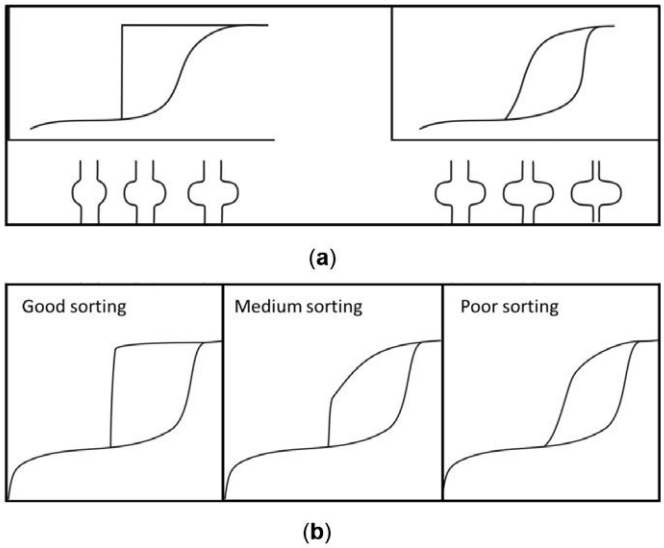

Fig. 12—Effect of pore-throat sorting to the adsorption isotherm curve in shale. (a) Adsorption-desorption curves of ink-bottle pore with various pore size or throat size. (b) Adsorption-desorption curves of pores with different pore sorting.

The pore shape in shale reservoirs is similar to the ink-bottle model. The body of the ink-bottle pore corresponds to the pore in shale, and the ink bottleneck is equivalent to the pore throat. Therefore, the sorting of pore throat affects the shape of the desorption curve in the hysteresis loop of the shale. For poor-sorting shale rocks, as shown in Fig. 12, the desorption curve gradually decreases. There is no sudden pressure change; for medium-sorting shale, the desorption curve has a sudden pressure drop, but the desorption curve falls in a certain range; for good-sorting shale rocks, the desorption curve has a sudden pressure drop and declines at a rapid speed.

New Classification of Adsorption Isotherm Curves

Figures 7, 11, and 12 show the effect of pore shape, size, and throat sorting to adsorption isotherm curves of shale, respectively. However, adsorption in shale is dependent on these three parameters simultaneously. Due to sedimentation, diagenesis, and catagenesis, shale samples reveal a variety of diversity. According to the three parameters mentioned above, 27 types of curves are concluded. Various types of curves reflect different pore shapes, size, and throat sorting, as shown in Fig. 13. The pore size of slit pore is measured by the distance between two parallel plates. Pore size for a wedge-shaped pore or cylindrical-shaped pore is defined as a pore radius of pore sections. In order to demonstrate the pore structure for different shapes of curves, 27 types of curves are categorized into three templates. Each template contains a certain pore shape corresponding to the adsorption isotherm curve for different pore sizes and throat sorting. In the template, the sorting of the pore throat is from poor to good along the *x*-axis from left to right, which illustrates that the desorption curve in the hysteresis loop changes from flat to steep. Pore size is from big to small along the *y*-axis from bottom to top, which reflects that pressure at the starting point of hysteresis gradually increases, and the area of hysteresis keeps increasing.

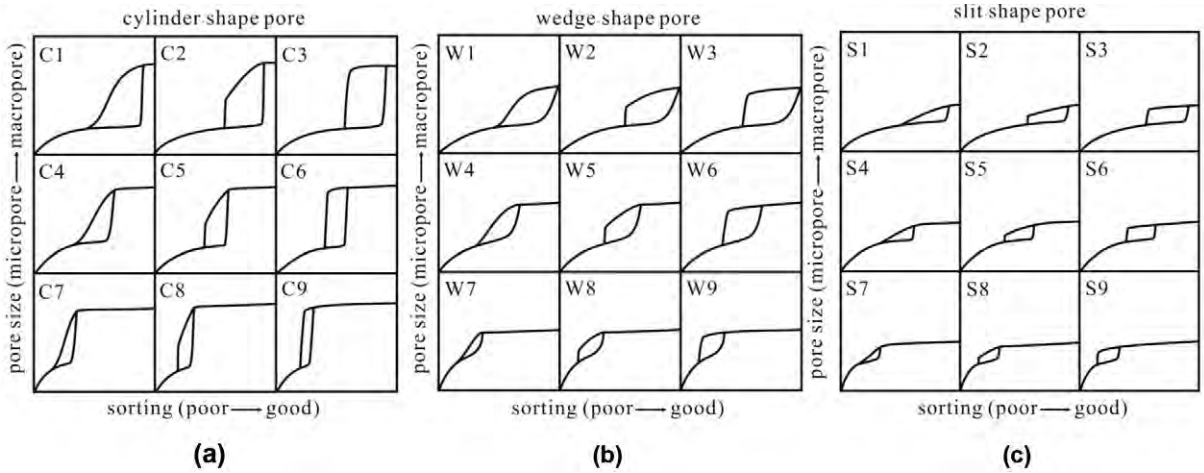

Fig. 13—A template of adsorption isotherm classification curves for (a) cylinder-shaped pores, (b) wedge-shaped pores, and (c) slit-shaped pores. (From left to right in the diagram) Adsorption curves indicate the pore structure changes from poor sorting to good sorting, and (from bottom to the top of the diagram) adsorption curves show pore size increases gradually.

As we plotted adsorption-desorption curves of shale, the profile of the hysteresis loop, the starting point of hysteresis, indicated capillary condensation in pores and a downtrend of the desorption curve are all explicit. In the workflow in Fig. 14, the shape of pores is determined by the relationship of the axis of the hysteresis loop and *x*-axis (or *y*-axis). The area of the hysteresis loop and the pressure of the SPH are evidence of pore-size estimation. For pore-throat sorting, it's directly confirmed by the form of the desorption curve.

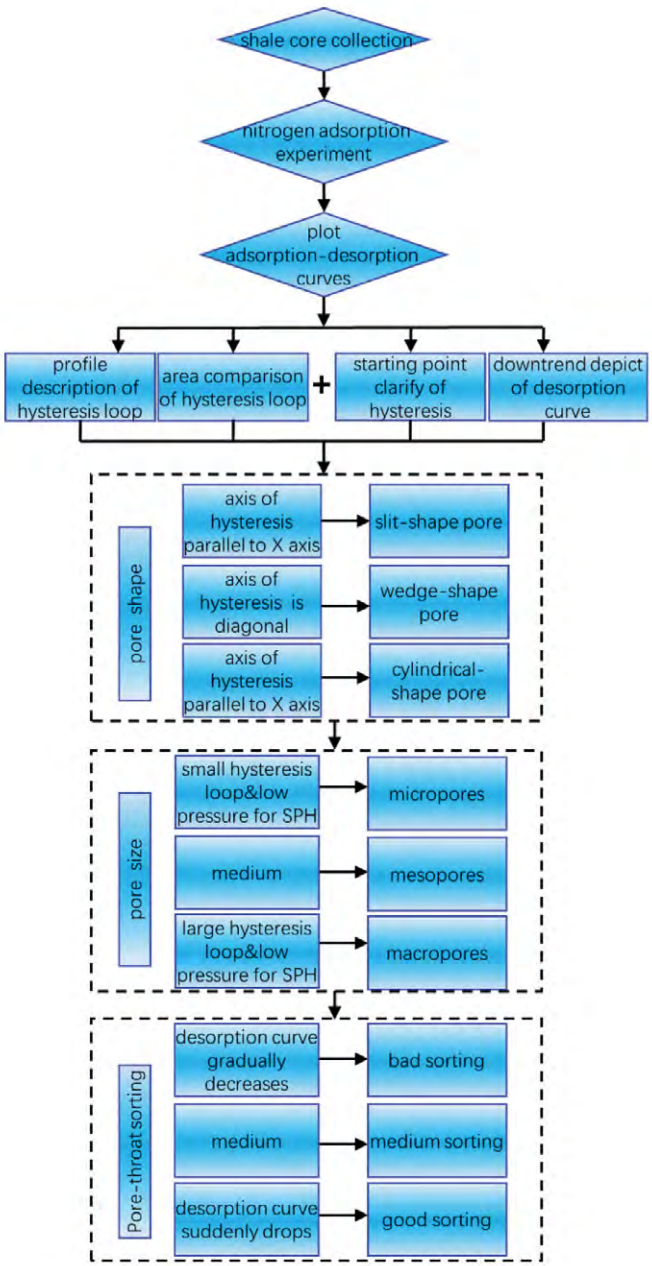

Fig. 14—Workflow of pore structure evaluation by classification of adsorption isotherm curves.

APPLICATION OF NEW CLASSIFICATION OF ADSORPTION ISOTHERM CURVES

We applied the new classification of adsorption isotherm curves to the adsorption isotherm curves of 106 shale samples. Eight curves belong to Type W4; the pore structures of these shale samples are poor sorting, medium-pore size, and wedge shaped. Twenty curves belong to Type W5; medium sorting, medium-pore size, and wedge shaped are the pore properties of these shale samples. Twenty-four curves belong to Type W6; these shale samples are medium sorting and are medium size with a wedge shape. Sixteen curves belong to Type W8; these shale samples have mainly wedge-shaped pores, micropores, and are poorly sorted. Eleven curves belong to Type W9; pores of these shale samples are mainly wedge-shaped micropores and poor sorting. The remaining samples are all slit-shaped pores. Among them, 15 samples are poor sorting and mesopore shale (Type S4); five samples are medium sorting and mesopore shale (Type S5); four samples are good sorting and mesopore shale (Type S6); three samples are medium sorting and micropore shale (Type S8) (Fig. 15). The adsorption isotherm curves for all samples are categorized, as shown in Table 2. The new classification characterizes the shapes of adsorption isotherm curves of all the shale samples and generates multiple categories of curve templates, which reflect the diversity of different adsorption isotherm curves, as shown in Fig. 13.

DISCUSSION

According to the results of the new classification of adsorption isotherm curves for 106 core samples, the pore shapes of Samples D7 and D78 are wedge shaped and slit shaped, respectively. To verify research results about pore shape, a scanning electron microscope experiment was performed. Figure 16a is an SEM image magnified 10,000 times for Sample D7. From the SEM image, the pores in Sample D7 are mainly wedge-shaped pores. The voids between fragments of minerals and matrix provide the main pore volume. Figure 16b is an SEM image magnified 20,000 times for Sample D78. Though wedge-shaped pores exist in this sample, the majority of pores are slit shaped. These pores are very regular pores with parallelly aligned clays on both sides. Based on the SEM images, the new classification of adsorption isotherm curves agrees well with the pore-shape categorization.

Table 2—Classification and Pore-Structure Characteristics of Shale Adsorption Isotherm Curves From Ordos Basin and Sichuan Basin

Isotherm Curve Type	Fraction of Total (%)	Pore Characteristics	Sample
W4	7.55	Poor-sorting wedge-shaped mesopore	D50, D73, D77, D84, D85, D86, D99, D106
W5	18.87	Medium sorting wedge-shaped mesopore	D45, D58, D59, D61, D66, D67, D68, D70, D72, D74, D75, D76, D81, D82, D83, D92, D96, D97, D101, D103
W6	22.64	Good-sorting wedge-shaped mesopore	D19, D23, D27, D41, D42, D43, D44, D47, D53, D54, D55, D56, D57, D60, D62, D65, D69, D71, D79, D90, D91, D93, D95, D98
W8	15.09	Medium-sorting wedge-shaped micropore	D6, D7, D8, D15, D18, D20, D22, D24, D28, D30, D34, D35, D36, D37, D38, D40
W9	10.38	Good-sorting wedge-shaped micropore	D1, D4, D17, D21, D25, D26, D29, D32, D33, D39, D51
S4	14.15	Poor-sorting slit mesopore	D2, D3, D5, D49, D63, D64, D80, D87, D88, D89, D94, D100, D102, D104, D105
S5	4.73	Medium-sorting slit mesopore	D11, D12, D31, D46, D78
S6	3.77	Good-sorting slit mesopore	D9, D10, D48, D52
S8	2.83	Medium-sorting slit micropore	D13, D14, D16

According to the results of the classification, Samples D15 and D39 are micropore samples, and Samples D46 and D81 are mesopore samples. Based on the adsorption isotherm data for the samples, we applied the BJH method to obtain the pore-size distribution for these four samples, as revealed in Fig. 17, and then the average diameter for each sample shown in Table 3. The peaks of the pore size of Samples D15 and D39 are less than 2 nm, and both average pore sizes are less than 2 nm. Thus, Samples D15 and D39 are microporous samples based on the pore-size classification. However, the peaks of the pore sizes and average pore sizes for Samples D46 and D81 are larger than 2 nm but less than 50 nm. Thereby, they belong to mesoporous samples. The pore-size distributions from the BJH method for these four samples agree well with the new classification.

From the classification results, Samples D89 and D5 are poor sorting, Samples D11 and D7 are medium sorting, and Samples D65 and D9 are good sorting. The histogram of the pore size of these six core samples can be obtained from the pore-size distribution, as shown in Fig. 18. For Sample D89, multiple peaks are observed. Therefore, Sample D89 is poor sorting. The peak in Sample D5 is not obvious, and most ratios of corresponding pore volume to total pore volume are around 10%. Therefore, Sample D5 is poor sorting. The peaks of Samples D11 and D7 are obvious. The ratio of corresponding pore volume to total pore volume for both samples is around 15 to 25%. The frequency on the right-hand side of the peak rapidly decreases. Thus, these two samples belong to medium sorting. The peaks of Samples D65 and D9 are outstanding. The ratio of corresponding pore volume to total pore volume for both samples is more than 50%. The frequency on the right-hand side of the peak drastically declines and approaches to zero, which shows that Samples D65 and D9 are good-sorting samples. The results of the new classification agree well with the results from the histogram of the pore size.

By applying the new classification method to categorize the adsorption isotherm curve, the characteristics of pore structure (shape, size, and throat sorting) for shale samples can be preliminarily determined. Estimating reservoir properties based on the characteristics of the pore structure makes a more effective reorganization to shale reservoirs. Meanwhile, a new theoretical basis can be provided when it is applied to calculate reserves of shale. Furthermore, a more reasonable development can be chosen to exploit shale gas, which can save the cost due to inappropriate treatment and stimulate the production of shale gas.

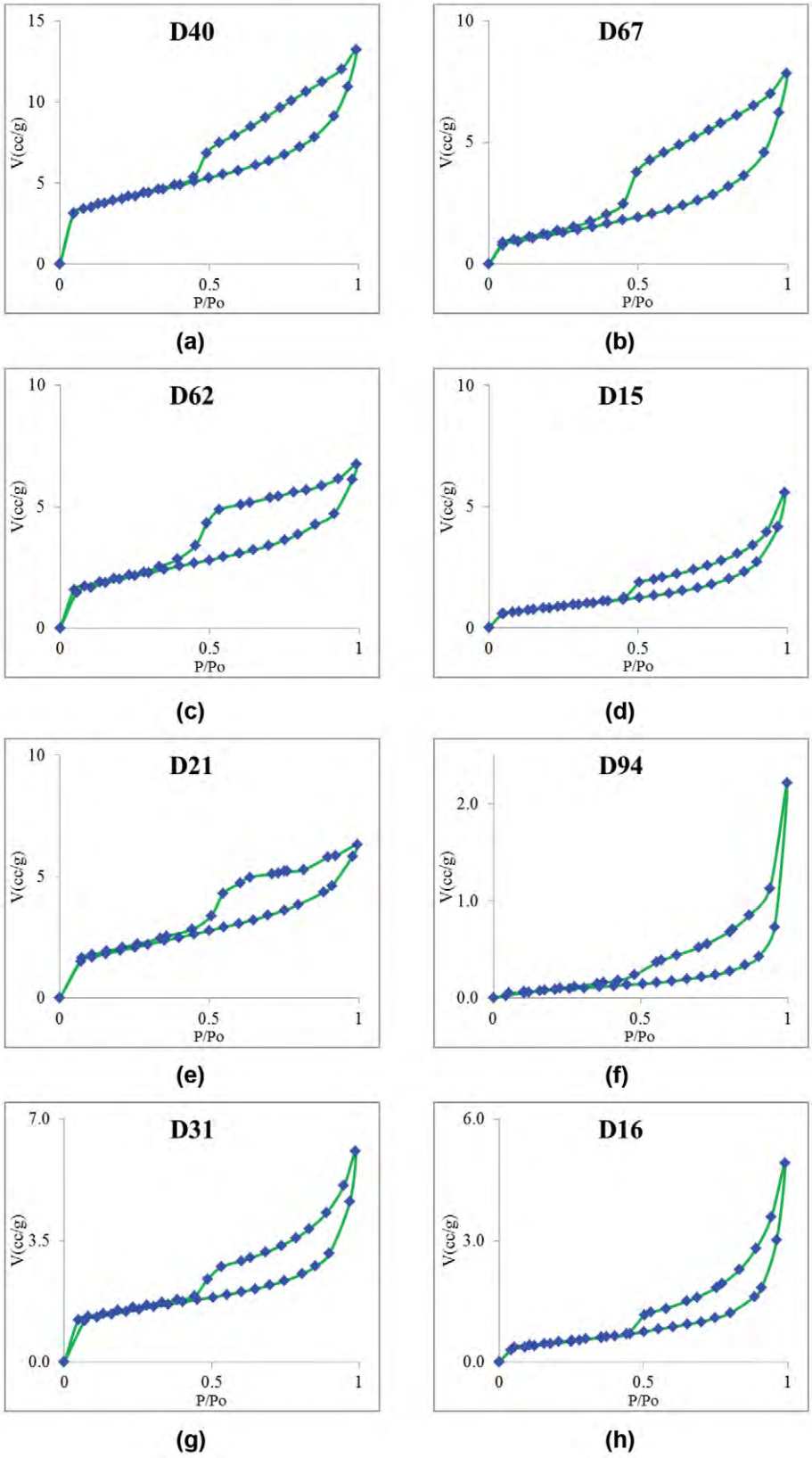

Fig. 15—Typical adsorption isotherms of shale samples according to the new classification: (a) Type W4; (b) Type W5; (c) Type W6; (d) Type W8; (e) Type W9; (f) Type S4; (g) Type S5; and (h) Type S8.

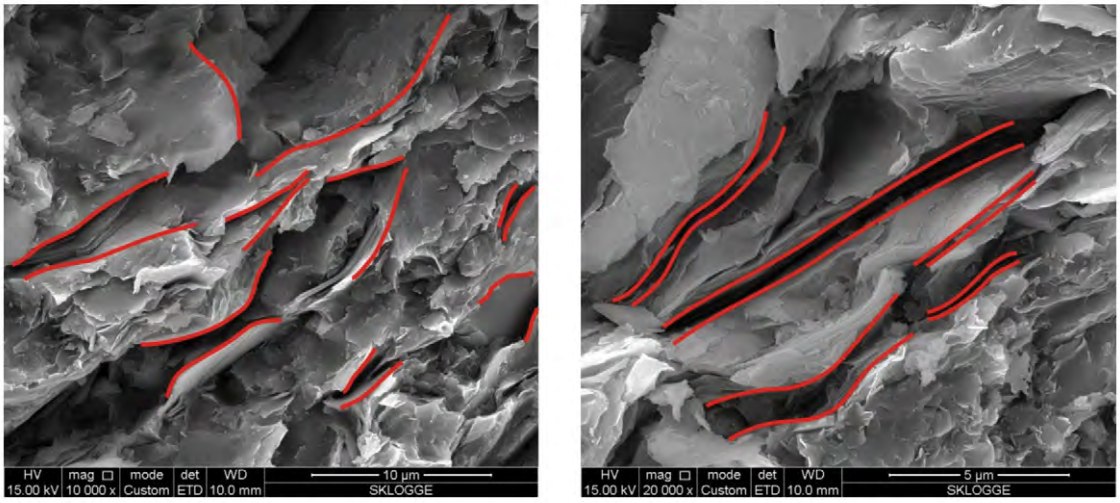

Fig. 16—SEM images of typical shale samples. (a) SEM image magnified 10,000 times for Sample D7. (b) SEM image magnified 20,000 times for Sample D78.

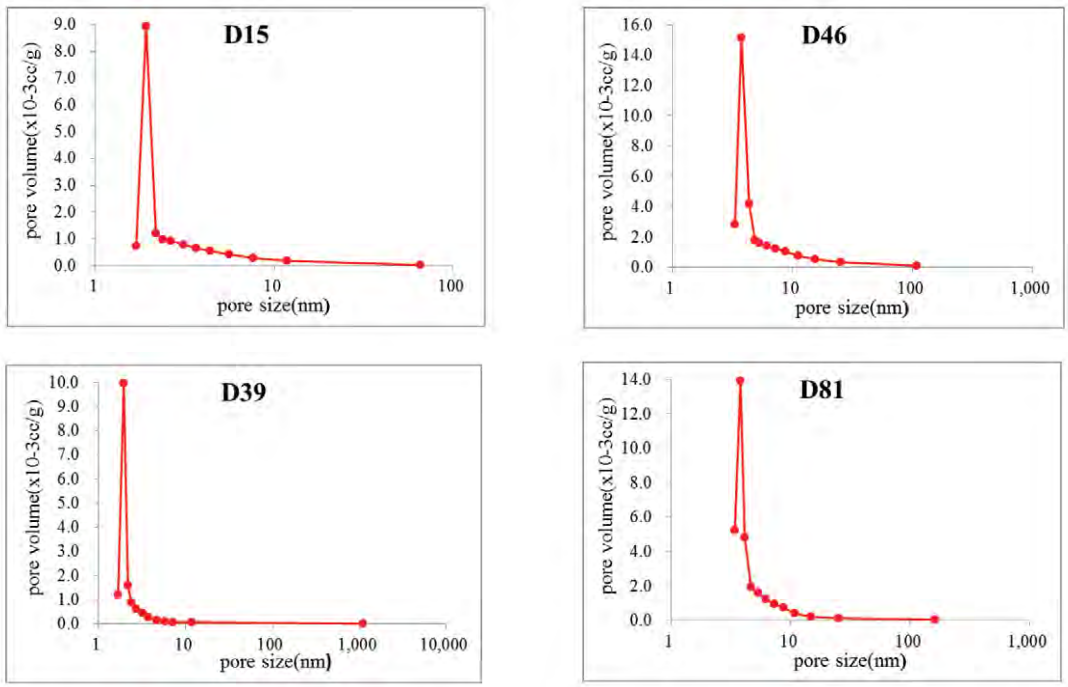

Fig. 17—Diagram of pore-diameter distribution of typical shale samples.

Table 3—Average Pore Size of Shale Samples

Sample	Average Size (nm)
D15	1.93
D39	1.92
D46	3.738
D81	3.789

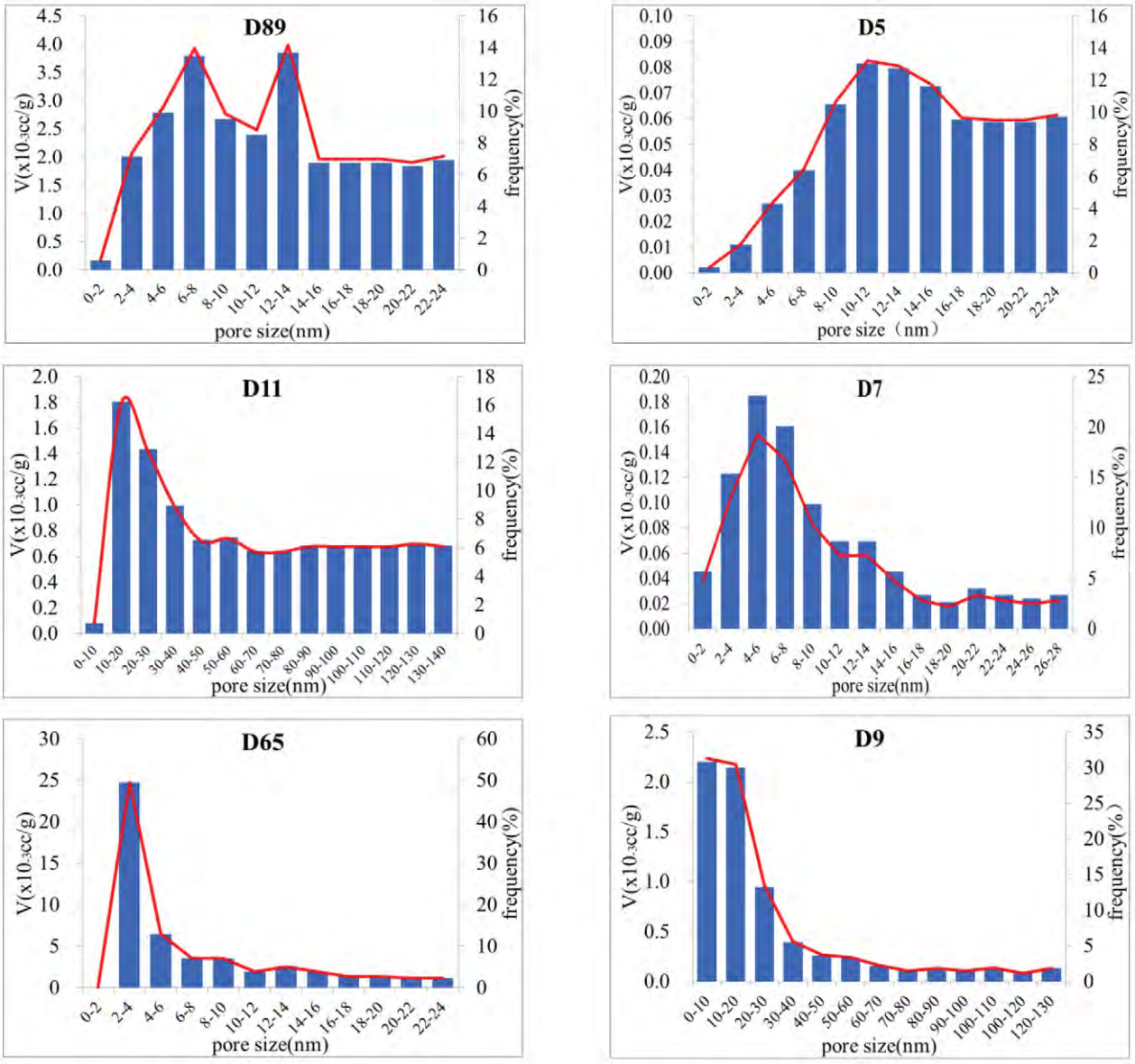

Fig. 18—Histogram of pore diameters of typical shale samples.

CONCLUSIONS

- By applying three conventional classifications of adsorption isotherm curves to categorize the shale adsorption isotherm curve, we found that the results of three classifications are monotonous, which cannot accurately conclude types of adsorption isotherm curves. Therefore, they can't properly evaluate characteristics of pore structure.
- Pore shape, size, and throat sorting have effects on the shale adsorption isotherm curve. Pore shape is relevant to the shape of adsorption and desorption curves. As for shape changes from slit to wedge shaped and then to cylindrical, the adsorption-desorption curve changes from flat to steep; pore size affects the horizontal location and area of the hysteresis loop. With size changing from small to large, the hysteresis loop would move forward to the right-hand side, and the area of hysteresis would increase; pore-throat sorting impacts the shape of desorption. From poor to good sorting, the desorption curve in hysteresis changes from flat to steep.
- According to the pore shape, size, and throat sorting in shale, adsorption isotherm curves are categorized into 27 types. The generated adsorption isotherm curve classification fully considers the characteristics of pore structure in shale. It has a detailed classification with obvious features for each

type of curve, which satisfies the requirement of classification of adsorption isotherm curves in shale.
- This new classification method is applied to categorize 106 adsorption isotherm curves measured by core samples from the Sichuan Basin and Ordos Basin, which reflects the diversity of pore structure for different core samples. Moreover, the accuracy of the results obtained by the new classification of adsorption isotherm curves is justified based on SEM images, pore-size distribution, and histogram.

ACKNOWLEDGMENTS

This research was enabled in part by support provided by The National Natural Science Foundation of China (Grant No. 51674046).

NOMENCLATURE

Abbreviations

BDDT = Brunauer-Deming-Deming-Teller method
BET = Brunauer, Emmett, Teller method
BJH = Barrett-Joyner-Halenda method
DFT = density functional theory
IUPAC = International Union of Pure and Applied Chemistry method
SEM = scanning electron microscope
SPH = starting point of hysteresis

REFERENCES

Alfi, M., Barrufet, M., and Killough, J., 2019, Effect of Pore Sizes on Composition Distribution and Enhance Recovery From Liquid Shale—Molecular Sieving in Low Permeability Reservoirs, *Fuel*, **235**, 1555–1564. DOI: 10.1016/j.fuel.2018.08.063.

Anovitz, L.M., and Cole, D.R., 2015, Characterization and Analysis of Porosity and Pore Structures, *Reviews in Mineralogy and Geochemistry*, **80**(1), 61–164. DOI: 10.2138/rmg.2015.80.04.

Brunauer, S., Deming, L.S., Deming, W.E., and Teller, E., 1940, On a Theory of the van der Waals Adsorption of Gases, *Journal of the American Chemical Society*, **62**, 1723–1732. DOI: 10.1021/ja01864a025.

Bustin, R.M., Bustin, A.M.M., Cui, A., Ross, D., and Pathi, V.M., 2008, Impact of Shale Properties on Pore Structure and Storage Characteristics, Paper SPE-119892 presented at the SPE Shale Gas Production Conference, Fort Worth, Texas, USA, 16–18 November. DOI: 10.2118/119892-MS.

Clarkson, C.R., Jensen, J.L., and Blasingame, T., 2011, Reservoir Engineering for Unconventional Gas Reservoirs: What Do We Have to Consider?, Paper SPE-145080 presented at the North American Unconventional Gas Conference and Exhibition, The Woodlands, Texas, USA, 14–16 June. DOI: 10.2118/145080-MS.

Clarkson, C.R., Solano, N., Bustin, R.M., Bustin, A.M.M., Chalmers, G.R.L., He, L., Melnichenko, Y.B., Radliński, A.P., and Blach, T.P., 2013, Pore Structure Characterization of North American Shale Gas Reservoirs Using USANS/SANS, Gas Adsorption, and Mercury Intrusion, *Fuel*, **103**, 606–616. DOI: 10.1016/j.fuel.2012.06.119.

de Boer, J.H., and Lippens, B.C., 1964, Studies on Pore Systems in Catalysts II. The Shapes of Pores in Aluminum Oxide Systems, *Journal of Catalysis*, **3**(1), 38–43. DOI: 10.1016/0021-9517(64)90090-9.

Dewers, T.A., Heath, J., Ewy, R., and Duranti, L., 2012, Three-Dimensional Pore Networks and Transport Properties of a Shale Gas Formation Determined From Focused Ion Beam Serial Imaging, *International Journal of Oil, Gas and Coal Technology*, **5**, 229–248. DOI: 10.1504/IJOGCT.2012.046322.

Dombrowski, R.J., and Lastoskie, C.M., 2002, A Two-Stage Horvath-Kawazoe Adsorption Model for Pore Size Distribution Analysis, *Studies in Surface Science and Catalysis*, **144**, 99–106. DOI: 10.1016/S0167-2991(02)80225-7.

Durán-Valle, C.J., 2012, Techniques Employed in the Physicochemical Characterization of Activated Carbons, Chapter 3, *in* Virginia Hernández Montoya and Adrian Bonilla-Petriciolet, editors, *Lignocellulosic Precursors Used in the Synthesis of Activated Carbon–Characterization Techniques and Applications in the Wastewater Treatment*, INTECH. DOI: 10.5772/39366. ISBN: 978-953-51-0197-0.

Everett, D.H., and Stone, F.S., 1958, *The Structure and Properties of Porous Materials*, **10**, Butterworths Scientific Publications, London, England. ISBN: 0408358602.

Fan, C., Do, D.D., and Nicholson, D., 2013, Condensation and Evaporation in Capillaries with Nonuniform Cross Sections, *Industrial & Engineering Chemistry Research*, **52**(39) 14304–14314. DOI: 10.1021/ie402549z.

Gregg, S.J., and Sing, K.S.W., 1982, *Adsorption, Surface Area, and Porosity*, Second Edition, Academic Press, London. ISBN: 978-0123009562.

Jiao, K., Yao, S., Liu, C., Gao, Y., Wu, H., Li, M., and Tang, Z., 2014, The Characterization and Quantitative Analysis of Nanopores in Unconventional Gas Reservoirs Utilizing FESEM–FIB and Image Processing: An Example From the Lower Silurian Longmaxi Shale, Upper Yangtze Region, China, *International Journal of Coal Geology*, **128–129**, 1–11. DOI: 10.1016/j.coal.2014.03.004.

Jin, Z., and Firoozabadi, A., 2016, Thermodynamic Modeling of Phase Behavior in Shale Media, Paper SPE-176015, *SPE Journal*, **21**, 190–207. DOI: 10.2118/176015-PA.

Kalantari-Dahaghi, A., 2011, Systematic Approach to Numerical Simulation and Modelling of Shale Gas Reservoirs, *International Journal of Oil, Gas and Coal Technology*, **4**(3), 209–243. DOI: 10.1504/IJOGCT.2011.040837.

Kang, S.M., Fathi, E., Ambrose, R.J., Akkutlu, I.Y., and Sigal, R.F., 2011, Carbon Dioxide Storage Capacity of Organic-Rich Shales, Paper SPE-134583, *SPE Journal*, **16**(4), 842–855.

DOI: 10.2118/134583-PA.

Kruk, M., Jaroniec, M., Ko, C.H., and Ryoo, R., 2000, Characterization of the Porous Structure of SBA-15, *Chemistry of Materials*, **12**(7), 1961–1968. DOI: 10.1021/cm000164e.

Li, T., Tian, H., Chen, J., and Cheng, L., 2016, Application of Low Pressure Gas Adsorption to the Characterization of Pore Size Distribution of Shales: An Example from Southeastern Chongqing Area, China, *Journal of Natural Gas Geoscience*, **1**(3), 221–230. DOI: 10.1016/j.jnggs.2016.07.001.

Nagolska, D., and Gawdzińska, K., 2011, Application of Capillary Hysteresis Phenomenon for Evaluation of Recycling Possibility of Selected MMC, *Archives of Foundry Engineering*, **11**, 145–150. ISSN:1897-3310.

Neimark, A.V., Ravikovitch, P.I., Grün, M., Schüth, F., and Unger, K.K., 1998, Pore Size Analysis of MCM-41 Type Adsorbents by Means of Nitrogen and Argon Adsorption, *Journal of Colloid and Interface Science*, **207**(1), 159–169. DOI: 10.1006/jcis.1998.5748.

Pang, Y., Soliman, M.Y., Deng, H., and Emadi, H., 2017, Analysis of Effective Porosity and Effective Permeability in Shale-Gas Reservoirs With Consideration of Gas Adsorption and Stress Effects, Paper SPE-180260, *SPE Journal*, **22**(6), 1,739–1759. DOI: 10.2118/180260-PA.

Pang, Y., Soliman, M.Y., and Sheng, J., 2018, Investigating Gas-Adsorption, Stress-Dependence, and Non-Darcy-Flow Effects on Gas Storage and Transfer in Nanopores by Use of Simplified Local Density Model, Paper SPE-187961, *SPE Reservoir Evaluation & Engineering*, **21**(1), 73–95. DOI: 10.2118/187961-PA.

Ravikovitch, P.I., Haller, G.L., and Neimark, A.V., 1998, Density Functional Theory Model for Calculating Pore Size Distributions: Pore Structure of Nanoporous Catalysts, *Advances in Colloid and Interface Science*, **76–77**, 203–226. DOI: 10.1016/S0001-8686(98)00047-5.

Ravikovitch, P.I., and Neimark, A.V., 2001, Characterization of Nanoporous Materials from Adsorption and Desorption Isotherms, *Colloids and Surfaces A: Physicochemical and Engineering Aspects*, **187–188**, 11–21. DOI: 10.1016/S0927-7757(01)00614-8.

Ross, D.J., and Bustin, R.M., 2008, Characterizing the Shale Gas Resource Potential of Devonian–Mississippian Strata in the Western Canada Sedimentary Basin: Application of an Integrated Formation Evaluation, *AAPG Bulletin*, **92**(1), 87–125. DOI: 10.1306/09040707048.

Ross, D.J., and Bustin, R.M., 2009, The Importance of Shale Composition and Pore Structure Upon Gas Storage Potential of Shale Gas Reservoirs, *Marine and Petroleum Geology*, **26**(6), 916–927. DOI: 10.1016/j.marpetgeo.2008.06.004.

Sayari, A., Kruk, M., Jaroniec, M., and Moudrakovski, I.L.,1998, New Approaches to Pore Size Engineering of Mesoporous Silicates, *Advanced Materials*, **10**(16), 1376–1379. DOI: 10.1002/(SICI)1521-4095(199811)10:16<1376::AID-ADMA1376>3.0.CO;2-B.

Schwartz, B., Huffman, K., Thornton, D., and Elsworth, D., 2019, A Strain Based Approach to Calculate Disparities in Pore Structure Between Shale Basins During Permeability Evolution, *Journal of Natural Gas Science and Engineering*, **68**, 102893. DOI: 10.1016/j.jngse.2019.05.006.

Shen, Y., Pang, Y., Shen, Z., Tian, Y., and Ge, H., 2018, Multiparameter Analysis of Gas Transport Phenomena in Shale Gas Reservoirs: Apparent Permeability Characterization, *Scientific Reports*, **8**, 1–14. DOI: 10.1038/s41598-018-20949-2.

Sing, K.S.W., Everett, D.H., Haul, R.A.W., Moscou, L., Pierotti, R.A., Rouquerol, J., and Siemieniewska, T., 1985, Reporting Physisorption Data for Gas/Solid Systems With Special Reference to the Determination of Surface Area and Porosity (Recommendations 1984), *Pure and Applied Chemistry*, **57**(4), 603–619. DOI: 10.1351/pac198557040603.

Tang, X., Jiang, Z. Li, Z., Gao, Z., Bai, Y., Zhao, S., and Feng, J., 2015, The Effect of the Variation in Material Composition on the Heterogeneous Pore Structure of High-Maturity Shale of the Silurian Longmaxi Formation in the Southeastern Sichuan Basin, China, *Journal of Natural Gas Science and Engineering*, **23**, 464–473. DOI: 10.1016/j.jngse.2015.02.031.

Thommes, M., 2010, Physical Adsorption Characterization of Nanoporous Materials, *Chemie Ingenieur Technik*, **82**(7), 1059–1073. DOI: 10.1002/cite.201000064.

Tian, Y., Yan, C., and Jin, Z., 2017, Characterization of Methane Excess and Absolute Adsorption in Various Clay Nanopores from Molecular Simulation, *Scientific Reports*, **7**(1), 12040. DOI: 10.1038/s41598-017-12123-x.

Torghabeh, A.K., Rezaee, R., Moussavi-Harami, R., and Pimentel, R., 2014, Unconventional Resource Evaluation: Kockatea Shale, Perth Basin, Western Australia, *International Journal of Oil, Gas and Coal Technology*, **8**(1), 16–30. DOI: 10.1504/IJOGCT.2014.064420.

US Energy Information Administration, 2015, Technically Recoverable Shale Oil and Shale Gas Resources: China, US DOE, Washington, DC (September 2015), https://www.eia.gov/analysis/studies/worldshalegas/pdf/China_2013.pdf (accessed July 4, 2020).

Xu, S., Hao, F., Shu, Z., Zhang, A., and Yang, F., 2020, Pore Structures of Different Types of Shales and Shale Gas Exploration of the Ordovician Wufeng and Silurian Longmaxi Successions in the Eastern Sichuan Basin, South China, *Journal of Asian Earth Sciences*, **193**, 104271. DOI: 10.1021/acs.energyfuels.0c00782.

Yaalon, D.H., 1962, Mineral Composition of Average Shale, *Clay Minerals*, **5**(27), 31–36. DOI: 10.1180/claymin.1962.5.27.05.

Yan, C.Z., Huang, Y.Z., Ge, C.M., Dong, D.Z., and Cheng, K.M., 2009, Shale Gas: Enormous Potential of Unconventional Natural Gas Resources, *Natural Gas Industry*, **29**(5), 1–6 (in Chinese with English abstract).

Yang, F., Ning, Z., Hu, C., Wang, B., Peng, K., and Liu, H., 2013, Characterization of Microscopic Pore Structures in Shale Reservoirs, *Acta Petrolei Sinica*, **34**(2), 301–311. DOI: 10.7623/syxb201302012.

Zhang, Y., Shao, D., Yan, J., Jia, X., Li, Y., Yu, P., and Zhang, T., 2016, The Pore Size Distribution and Its Relationship With Shale Gas Capacity in Organic-Rich Mudstone of Wufeng-

Longmaxi Formations, Sichuan Basin, China, *Journal of Natural Gas Geoscience*, **1**(3), 213–220. DOI: 10.1016/j.jnggs.2016.08.002.

Zheng, D., Wang, W., and Reza, Z., 2019a, Integrated Pore-Scale Characterization of Mercury Injection/Imbibition and Isothermal Adsorption/Desorption Experiments Using Dendroidal Model for Shales, *Journal of Petroleum Science and Engineering*, **178**, 751–765. DOI: 10.1016/j.petrol.2019.03.054.

Zheng, X., Zhang, B., Sanei, H., Bao, H., Meng, Z., Wang, C., and Li, K., 2019b, Pore Structure Characteristics and Its Effect on Shale Gas Adsorption and Desorption Behavior, *Marine and Petroleum Geology*, **100**, 165–178. DOI: 10.1016/j.marpetgeo.2018.10.045.

ABOUT THE AUTHORS

Yuanyuan Tian is a postdoctoral fellow in the College of Energy at Chengdu University of Technology, China. She holds a bachelor's degree in resource exploration engineering and master's and PhD degrees in petroleum engineering from Chengdu University of Technology. Her current research interests include the evaluation of shale gas reservoirs and shale gas flow in nanoporous media.

Qing Chen is an associate professor in the College of Energy at Chengdu University of Technology, China. She holds a bachelor's degree in nuclear technology and master's and PhD degrees in petroleum engineering from Chengdu University of Technology. Her research interests include the exploitation of natural gas and the evaluation of unconventional reservoirs.

Changhui Yan is a professor in the College of Energy at Chengdu University of Technology, China. He holds a bachelor's degree in geology and master's and PhD degrees in mineral resource exploration from Chengdu University of Technology. His research interests include the evaluation of unconventional reservoirs and development engineering of shale gas.

Hucheng Deng is the dean of the Industrial Technology College at Chengdu University of Technology, China. Deng holds a bachelor's degree in petroleum engineering from Chengdu University of Technology, China, and a master's degree in computer application technology from Southwest Jiaotong University, China. His research includes shale gas reservoir geology and the evaluation of natural fractures in oil and gas reservoirs.

Yanqing He is a PhD candidate in petroleum engineering at Chengdu University of Technology, China. He holds bachelor's and master's degrees in petroleum engineering from Chengdu University of Technology, China. His current research interests include shale gas development, gas adsorption, non-Darcy flow, and reservoir engineering.

PETROPHYSICS, VOL. 61, NO. 5 (OCTOBER 2020); PAGES 434–449; 16 FIGURES; 2 TABLES. DOI: PJV61N5-2020a3

Automatic Detection of Anomalous Density Measurements due to Wellbore Cave-in

Deepthi Sen[1]*, Cen Ong[2], Sribharath Kainkaryam[2], and Arvind Sharma[2]

ABSTRACT

We present a workflow for automatic detection and flagging of faulty formation density log measurements associated with wellbore cave-in ("bad holes"). We use an unsupervised time-series clustering algorithm to simultaneously cluster caliper and density logs, resulting in a labeled data set. Subsequently, we train a number of supervised learning algorithms on the labeled data set to detect bad holes when caliper measurements are unavailable. The workflow is shown to offer superior performance to conventional bad-hole detection methods, such as rugosity calculation, while requiring minimal user intervention. The workflow has been applied to a set of 3,762 Permian wells in order to tag and delete density values recorded at wellbore cave-ins. A density prediction model trained on the deleted data set is used to repredict the densities at the cave-in sections. This is shown to reduce erratic oscillations in density brought about by wellbore cave-in.

INTRODUCTION

High-quality well-log data are essential for reservoir characterization. Petrophysical evaluation of well-log measurements provides important properties, such as lithology, porosity, and permeability (Mukerji et al., 2001; Sarasty and Stewart, 2003), which are crucial components for the determination of production potential of a hydrocarbon reservoir. Petrophysical interpretation of well-log data also provides a framework for the interpretation of seismic properties, such as P- and S-wave velocities (Gupta et al., 2012; Gray et al., 2015).

Openhole measurement of formation bulk density (ρ_B) is one of the most commonly recorded well logs in any basin. Formation density tools record ρ_B by means of induced radiation wherein gamma rays are emitted into the formation through an open hole. The rays lose a fraction of its energy due to scattering by electrons (in the formation and mudcake) along its path, and the degree of attenuation is proportional to ρ_B. The detectors in the density tool measure the energy of the returning radiation, from which ρ_B may be estimated (Pickell and Heacock, 1960).

Even though formation density logs are most commonly used to compute the total porosity of the formation, they may also be used in tandem with other logs for lithology identification and to test for the presence of gas in the formation. However, ρ_B measurements are prone to error arising from a number of factors, such as the borehole quality and presence of barites in drilling mud (Glover, 2013). Ensuring borehole quality is particularly important since a density log is a short-range tool, and it is imperative that the sonde maintains contact with the wellbore at all times. These issues may be partly overcome by applying dual-density compensation using a compensated density log, which corrects the measurement using long-spaced and short-spaced readings (Glover, 2013). However, long-spaced and short-spaced measurements lose their meaning in a caved-in or uneven borehole (Gavriliu and Batchelor, 2019).

Therefore, the identification of bad-hole readings in formation bulk density logs is crucial to subsequent petrophysical analyses that rely on ρ_B readings (Ugborugbo and Rao, 2009; Wen et al., 2011). There are different methods for classifying bad recordings. Kumar et al. (2018) use ρ_B vs. neutron porosity (φ_N) and ρ_B vs. sonic traveltime (ΔT) crossplots to determine erroneous density data.

Formation density logs are primarily run alongside caliper (κ) logs in order to isolate bad recordings of ρ_B that arise due to wellbore cave-ins. This is because wellbore cave-ins are often accompanied by increased or highly oscillatory readings of the caliper log, and this signature may be used to detect bad holes (Bassiouni, 2012). Even though rugosity (γ) is a qualitative measure of wellbore smoothness, petrophysicists conventionally express it as a function of depth (z):**

$$\gamma(z) = \left|\frac{\partial \kappa(z)}{\partial z} + \frac{\partial^2 \kappa(z)}{\partial z^2}\right| \quad (1)$$

**Personal communication with D. Smith, 2019, Denver: International Reservoir Technologies, Inc.

Manuscript received by the Editor June 3, 2020; revised manuscript received August 15, 2020; manuscript accepted August 17, 2020.
[1]Texas A&M University, RICH 702, Richardson Petroleum Engineering Building, 3116 TAMU, 245 Spence St., College Station, TX 77843
[2]TGS Houston, 10451 Clay Rd., Houston, TX 77041
*Corresponding author: deept_tamu@tamu.edu

A cutoff is then applied on rugosity, and those sections of the density log corresponding to higher rugosity are deleted. A rugosity value of 0.075 is typically used as cutoff. A shortcoming of such an approach is apparent in Fig. 1, where the rugosity curve does not result in the removal of an entire section of bad readings without manual intervention. The rugosity curve, which is computed based on the first and second derivative of a noisy curve, is inherently noisy. The application of an amplitude cutoff on such a curve is insufficient in removing all the measurements recorded in a bad-hole interval, as seen in Fig. 1. de Macedo et al. (2020) made use of Doll's geometric factor (Doll, 1949) to account for density corrections due to wellbore cave-ins by expressing the measured density as a weighted sum of formation and mud densities. The authors assume a linear relationship between the minimum and maximum values of caliper readings and the geometric factor, which subsequently yields the slope and intercept used in formulating the density correction. Gavriliu and Batchelor (2019) describe yet another approach to account for the effects of rugosity in density measurements, which is to model the space

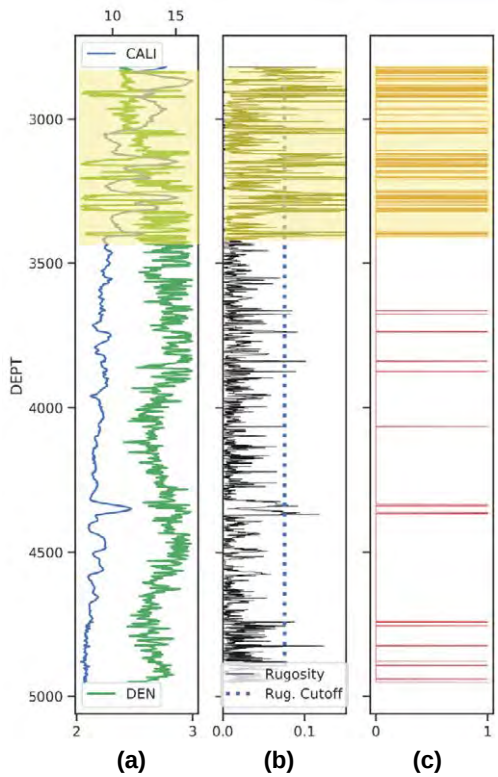

Fig. 1—Bad-hole classification with rugosity cutoff may lead to frequent oscillations in the predicted cluster sequence (highlighted). The measured caliper and density are given in (a). The rugosity calculated using Eq. 1 and the rugosity cutoff of 0.075 have been plotted in (b). The predicted cluster sequence based on the rugosity cutoff has been shown in (c), with Cluster 1 representing bad-hole conditions.

investigated by the tool and derive an appropriate density correction. Liu and Zhao (2015) apply a similar method based on geometric factors to coalbed methane reservoirs to deduce an appropriate density correction. However, the derived density corrections in all of the above works are highly empirical since the authors impose assumptions on aspects, such as the caliper-geometric factor relationship and borehole shape, which may not hold in all cases.

Johnston and Guichard (2015) analyzed scatterplots of drilling parameters, such as weight on bit (WOB) against torque and rate of penetration, to identify bad-hole sections in wellbores drilled in the UK continental shelf. Jain et al. (2019) used a cascaded scheme of machine-learning algorithms—cross-entropy clustering, Gaussian mixture model, and hidden Markov model—to simultaneously classify multiple well logs into a sequence of clusters. This scheme was subsequently used for automatic quality control of recorded logs.

Clustering of time-series data is an area of active research within the pattern recognition community. A popular approach to time-series clustering involves fitting a model (or a mixture of models) to raw time-series data considering that each time series is generated by this model (Liao, 2005). A significant portion of the literature on model-based time-series clustering relies on hidden Markov models (HMM), augmented by some form of initialization—*k*-means (Smyth, 1997) and dynamic time warping (Oates et al., 1999). These approaches fit an HMM to each cluster in the data set by iteratively estimating the transition and emission probabilities via an expectation-maximization algorithm (such as Baum-Welch or segmental *k*-means) and subsequently computing the most likely state sequence (via Viterbi algorithm) (Rabiner, 1989; Sen et al., 2014). One of the main disadvantages of these approaches is that the number of HMM states are left to the user to decide. Hallac et al. (2017) present a novel graph-based algorithm for time-series clustering, which yields highly interpretable cluster sequences and is less prone to overfitting than earlier methods. This approach, called Toeplitz Inverse Covariance-based Clustering (TICC), formulates the model-fitting procedure in a way such that closed-form solutions are available for the optimization problem. This makes the algorithm suitable for clustering very long time series since the computational expense scales only linearly with the length of the series (Hallac et al., 2017).

METHODOLOGY

Our workflow incorporates aspects of both unsupervised and supervised learning. We propose to use

the TICC algorithm to cluster well logs in a data set of a well containing both caliper and ρ_B measurements (Data Set 1). The algorithm generates labels that correspond to good/bad clusters. Once the labeled data set is generated, a supervised learning method may be used to map a number of features, such as density logs, location coordinates, and depth, to a particular label. This trained model can then be applied to a bigger data set that does not necessarily contain caliper measurements (Data Set 2) to cluster these as good/bad. The general workflow is illustrated in Fig. 2.

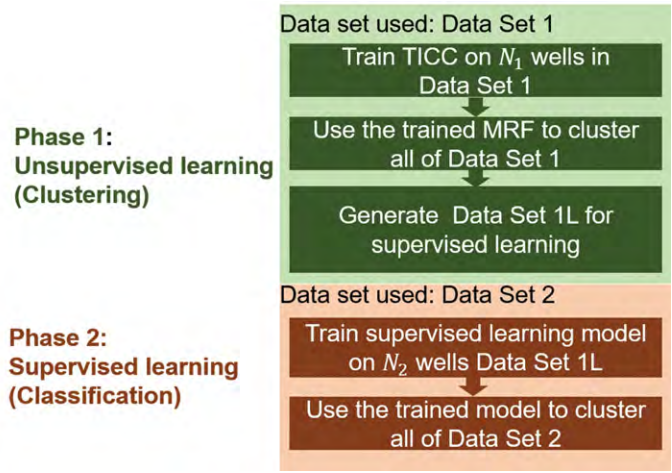

Fig. 2—Proposed workflow consists of unsupervised labeling of well logs using recorded ρ_B and κ in a data set where these readings are available (Data Set 1). The labeled data set (Data Set 1L) thus created may be used to train a supervised learning model that classifies bad holes in a data set where κ is not available (Data Set 2).

The first phase consists of automatically creating labels on well logs for which ρ_B and κ are available. To this end, we use an unsupervised learning technique called Toeplitz Inverse Covariance-based Clustering (TICC) (Hallac et al., 2017). TICC essentially clusters a multivariate time series by identifying distinct time signatures in the time series. The algorithm consists of building a graphical model of dependencies between variables, which are expressed in the form of a Markov Random Field (MRF). A detailed description of the TICC algorithm is provided in a subsequent section, "Phase 1: Unsupervised Learning."

The second phase of our workflow involves training a supervised machine-learning model using the labels generated by the TICC. This is a supervised binary classification problem, where the selected input features include ρ_B, z, latitude (θ_{LAT}), longitude (θ_{LON}), and gamma ray (*GR*) logs. Since our primary objective is to flag bad-density readings, ρ_B is an obvious choice for an input feature vector. The location-based features z, θ_{LAT}, and θ_{LON} are chosen to provide spatial context to the model. *GR* logs provide a mapping between the lithology (shale vs. nonshale) and the presence or absence of wellbore cave-ins. Additionally, *GR* is highly ubiquitous and is available in almost all wells in the Permian Basin, where we base our study. We test six models, namely, linear discriminant analysis (LDA), logistic regression, random forest, extreme gradient boost (XGBoost), gradient boosting classifier (GBC), and recurrent neural network (RNN). The classification probabilities provided by these models are used along with a Viterbi-like algorithm in order to compute the classification sequence with the maximum likelihood for any well log. Details on Phase 2 are provided in a subsequent section, "Phase 2: Supervised Learning."

Phase 1: Unsupervised Learning

Wellbore cave-ins usually manifest as erratic fluctuations in the caliper and ρ_B readings, with a slight positive shift in mean κ and a negative shift in ρ_B, as seen in Fig. 3. Cave-ins result in a sudden increase in wellbore radius, which causes the ρ_B sonde to lose contact with the formation (Bassiouni, 2012). Since accurate ρ_B measurement requires the sonde to maintain contact with the formation, the cave-in results in unrealistic ρ_B readings, which should be dropped in any subsequent analysis.

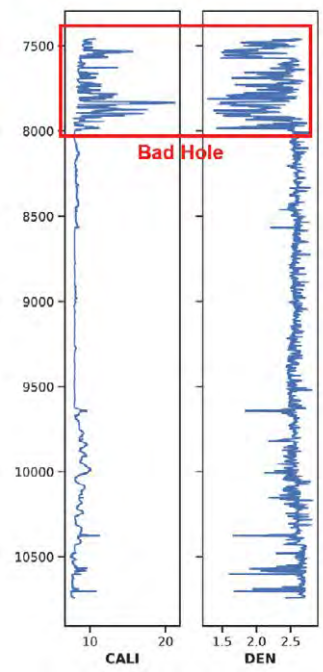

Fig. 3—Illustration of wellbore cave-in in the section between 7,500 and 8,000 ft is characterized by erratic oscillations in the caliper (κ) and density (ρ_B) measurements.

Toeplitz Inverse Covariance-Based Clustering (TICC). The primary objective of Phase 1 is to discover repetitions of simultaneous erratic measurements in ρ_B and κ measurements. TICC achieves this objective by segmenting the well log (expressed as a depth series) and learning the interdependencies within and between ρ_B and κ readings in short intervals. A brief discussion on TICC is given below. The reader is referred to Hallac et al. (2017) for a fuller treatment of the TICC algorithm.

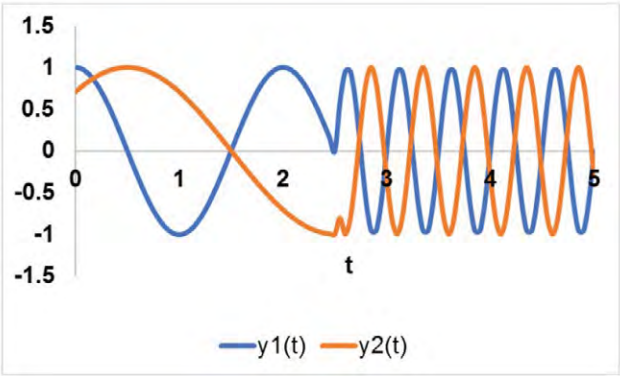

Fig. 4—A multivariate time series showing two different time signatures—input for the TICC algorithm.

Consider a simple multivariate time series $\bar{y}(t)$ given in Fig. 4. The dimensionality of $\bar{y}(t)$ is $n = 2$. The time series clearly contains two time signatures—a low-frequency signature from $t = 0$ to $t = 2.5$ and a high-frequency signature from $t = 2.5$ to $t = 5$. In order to cluster using TICC, $\bar{y}(t)$ is transformed into a series of n_w short windows of length w (Fig. 5a). The variables in each window are assumed to hold some dependency amongst each other. It is also expected that the dependency between variables will be significantly different in the two regions with different signatures. For instance, the variances of the caliper and density recordings and their interdependencies are expected to be different in a region with wellbore cave-in from those in a regular wellbore. TICC captures these variances and interdependencies (Fig. 5b), which are distinct for each of the two "clusters" in the form of Gaussian inverse covariance matrices $\Theta_i \in R^{nw \times nw}, i \in 1,2$, where $R^{nw \times nw}$ represents the set of real matrices of shape $nw \times nw$. These Θ_i represent the conditional independence structure between the variables describing a Markov Random Field (MRF) for each cluster, as in Fig. 5b. In an MRF, the w values of each variable form the vertices of a graph (the blue and orange circles). There exists an edge between any two of these vertices if the conditional dependency is nonzero. For example, given the values of $y_1(2),\ldots,y_1(w)$ and $y_2(2),\ldots,y_2(w)$, $y_1(1)$ and $y_2(1)$ are still not independent. This kind of correlation is called partial correlation and indicates a stronger relationship than a mere correlation between $y_1(1)$ and $y_2(1)$. On the contrary, given the values of $y_1(1),y_1(3),\ldots,y_1(w)$ and $y_2(1),y_2(3),\ldots,y_2(w)$, $y_1(2)$ and $y_2(2)$ are independent. It is to be noted that $y_1(2)$ and $y_2(2)$, when plotted, may still show a nonzero correlation. However, this correlation may be due to some other confounding variable (like $y_2(1)$), which affects both $y_1(2)$ and $y_2(2)$. Inverse covariance matrices Θ_i capture this partial correlation between the variables in each window for each cluster.

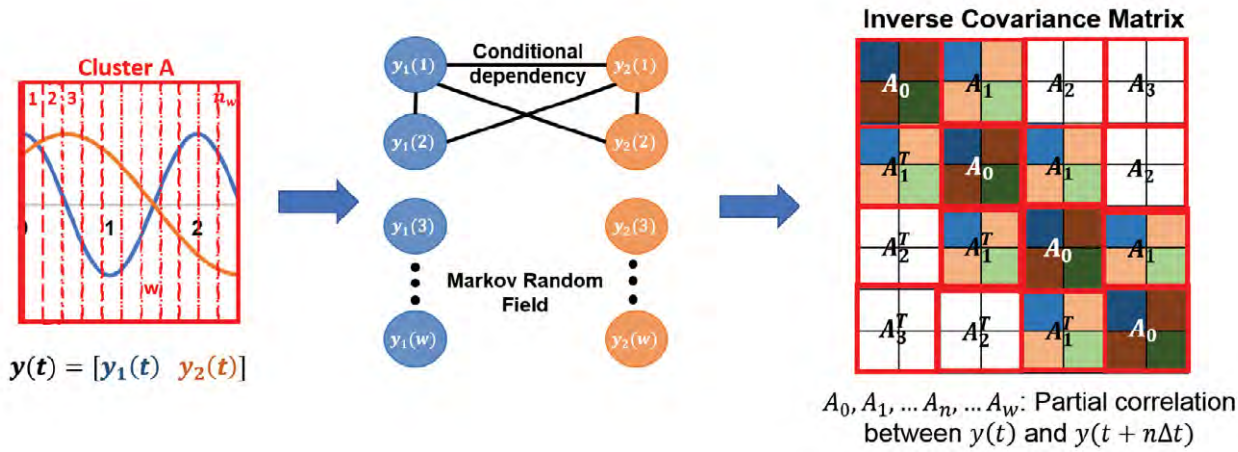

Fig. 5—A schematic illustration of (a) a windowed multivariate time series, (b) conditional dependencies learned by TICC, and (c) the corresponding inverse covariance matrix for a single cluster.

A Toeplitz matrix A of dimension $m \times m$ is a "constant diagonal matrix" of the form

$$A = \begin{pmatrix} a_0 & a_{-1} & a_{-2} & a_{-3} & \cdots & a_{-(m-1)} \\ a_1 & a_0 & a_{-1} & a_{-2} & \cdots & \vdots \\ a_2 & a_1 & a_0 & a_{-1} & \cdots & \vdots \\ \vdots & & & & & \vdots \\ \vdots & & & & & \vdots \\ a_{m-1} & \cdots & \cdots & a_2 & a_1 & a_0 \end{pmatrix}$$

where $A_{ij} = A_{i+1,j+1} = a_{i-j}$. In the case of TICC, the inverse covariance matrices Θ_i are structurally constrained to be a block Toeplitz, as shown in Fig. 5(c). This means that each element in A, such as $a_{-1}, a_{-2}, \ldots, a_{-(m-1)}$, is replaced by the partial correlation matrix between variables at different time shifts. For example, a_0 would be replaced by the partial correlation between coincident measurements—$y_1(1)$ and $y_2(1)$, $y_1(2)$ and $y_2(2)$, and so on. Similarly, a_{-1} will be replaced by A_1, the partial correlation between measurements that are one time step apart—$y_1(1)$ and $y_2(2)$, $y_1(2)$ and $y_2(3)$, and so on. Likewise, a_1 will be replaced by the transpose of A_1 since Θ_i is the inverse of the covariance matrix, which is necessarily symmetric. The main implication of a block Toeplitz structure is that, within each window, the dependencies are time invariant—the relationship between $y_1(1)$ and $y_2(2)$ also exists between $y_1(2)$ and $y_2(3)$. Having such a structure makes it possible for the algorithm to pick out cluster signatures irrespective of where in the time series it occurs.

TICC is solved using an expectation-maximization (EM)-like algorithm. The number of clusters N_{clust} is specified by the user. Since our objective is to classify the depth series of ρ_B and κ measurements into good and bad clusters, corresponding to normal wellbore and wellbore cave-in, we require binary classification labeling ($N_{clust} = 2$). Each cluster is associated with a certain signature in ρ_B and κ in a small measurement window of length w. Thus, each measurement is associated with a window of measurements around it, to which we assign a cluster.

Therefore, the time series is first transformed into windows, and the cluster sequence is initialized by assigning exactly one cluster to each window. The inverse covariance matrix (Θ) for each of the clusters is computed by minimizing the negative log-likelihood, given the cluster sequence **P**. The negative log-likelihood is given by

$$\sum_{\bar{y}(t) \in P_i} -ll(\bar{y}(t), \Theta_i) = -|P_i|\left(\log\det\{\Theta_i\} + tr(S_i\Theta_i)\right) + C \qquad (2)$$

where $|P_i|$ denotes the number of points in cluster i, S_i denotes the empirical covariance matrix of points in cluster i, and C is a constant. The log-likelihood captures the probabilities that a particular window of measurements belongs to either cluster; the variance in ρ_B and κ in the bad cluster is expected to be more severe than in the good cluster. Since ρ_B and κ measurements in each cluster are assumed to be distributed according to a multivariate Gaussian, the log-likelihood is a function of the cluster covariance matrices (and hence the inverse covariance matrices Θ_i). Hence, the computation of Θ_i is expressed as a minimization of the negative of log-likelihood as in Eq. 2, subject to a constraint on the structure of Θ_i to be a block Toeplitz.

$$\underset{\Theta_i \in \mathcal{T}}{minimize} \; -\log\det\{\Theta_i\} + tr(S_i\Theta_i) + \frac{1}{|P_i|}\|\lambda \circ \Theta_i\|_1 \qquad (3)$$

where $\mathcal{T}$ represents the set of block Toeplitz matrices. The minimization problem is solved using the alternating direction method of multipliers (ADMM), the details of which may be found in Hallac et al. (2017); Boyd and Vandenberghe (2004).

Once Θ_i is computed, we reassign clusters to each of the data points by solving a combinatorial optimization problem wherein the maximum likelihood path is computed, given the measurements and Θ_i. This is expressed as

$$minimize \quad \sum_{i=1}^{N_{clust}} \sum_{\bar{y}(t) \in P_i} -ll(\bar{y}(t), \Theta_i) + \beta \mathbf{1}\{\bar{y}(t-1) \notin P_i\} \qquad (4)$$

Hence, given a sequence of windowed measurements of ρ_B and κ, we compute the cluster sequence that maximizes the joint probability of the measurement sequence. Note that a switch in clusters carries a penalty of β. This regularization is imposed to suppress frequent oscillations in the cluster assignment.

Results From TICC

In Phase 1, we chose $N_1 = 700$ wells from Data Set 1 and formed a depth series from the ρ_B and κ readings. The areal locations of the wells in Data Set 1 and those used for training the TICC model are shown in Fig. 6. N_1 has been chosen such that wellbore cave-in signatures in different parts of the basin are adequately represented in the TICC calibration data set. Concatenation of measurements from several wells is justified by the use of small windows over which TICC computes its MRF. In such a case, the number of windows with overlapping measurements from two different wells will be negligibly small. An implementation of TICC based on Hallac et al. (2017) is available at Hallac (2017). This implementation is used to train a TICC model on the concatenated data set.

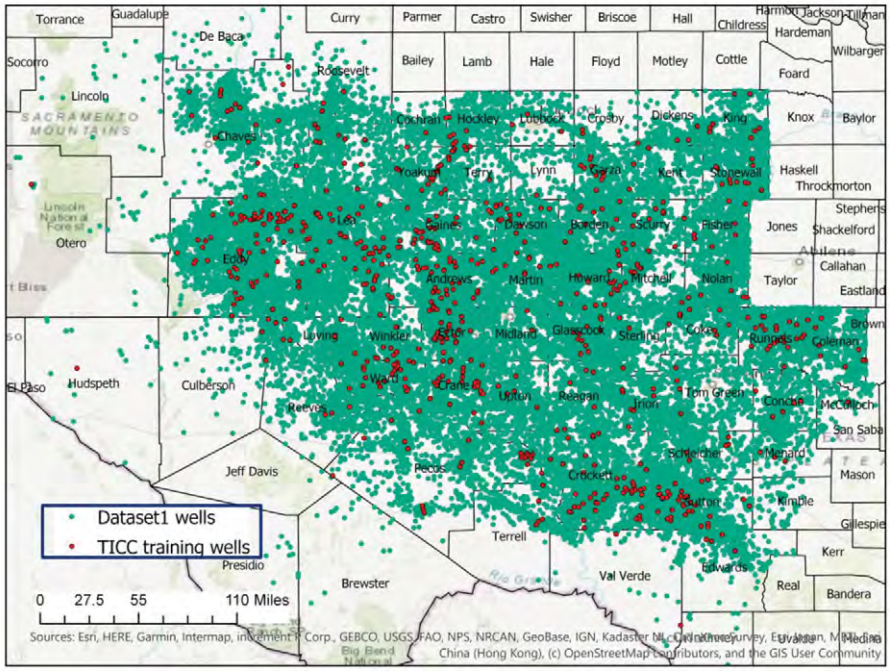

Fig. 6—Data Set 1 (green) contains 99,000 Permian wells for which density and caliper log recordings are available. TICC is trained on a subset of 700 wells (red).

The predictions from the trained TICC model on four wells are shown in Fig. 7. The effects of changing penalty parameter β and the MRF sparsity parameter λ are illustrated in Fig. 8. As β is increased, the smoothness of the predicted cluster sequence increases. However, this comes at the expense of reduced sensitivity to well cave-ins in thinner formations. The effect of changing β is apparent in the first and third panels of Fig. 8. With a lower value of $\beta = 600$, the clustering algorithm identifies three distinct erratic signatures in ρ_B and κ, whereas $\beta = 1{,}200$ generates an unfragmented interval of erratic signatures. It is also worth noting that $\beta = 1{,}200$ ignores the thin section of erraticity at the depth of 8,000 ft, where $\beta = 600$ identifies it.

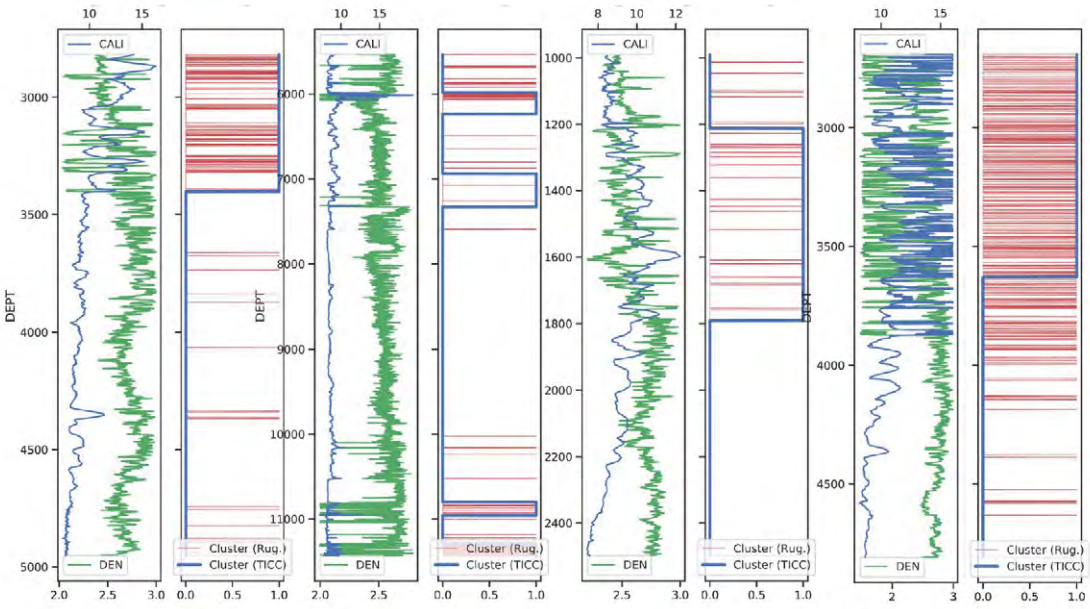

Fig. 7—Results of bad-hole detection via caliper-ρ_B clustering using TICC are compared with those obtained via the rugosity method for three wells. Cluster 0 represents normal wellbore (good cluster), and Cluster 1 represents bad hole (bad cluster/wellbore cave-in).

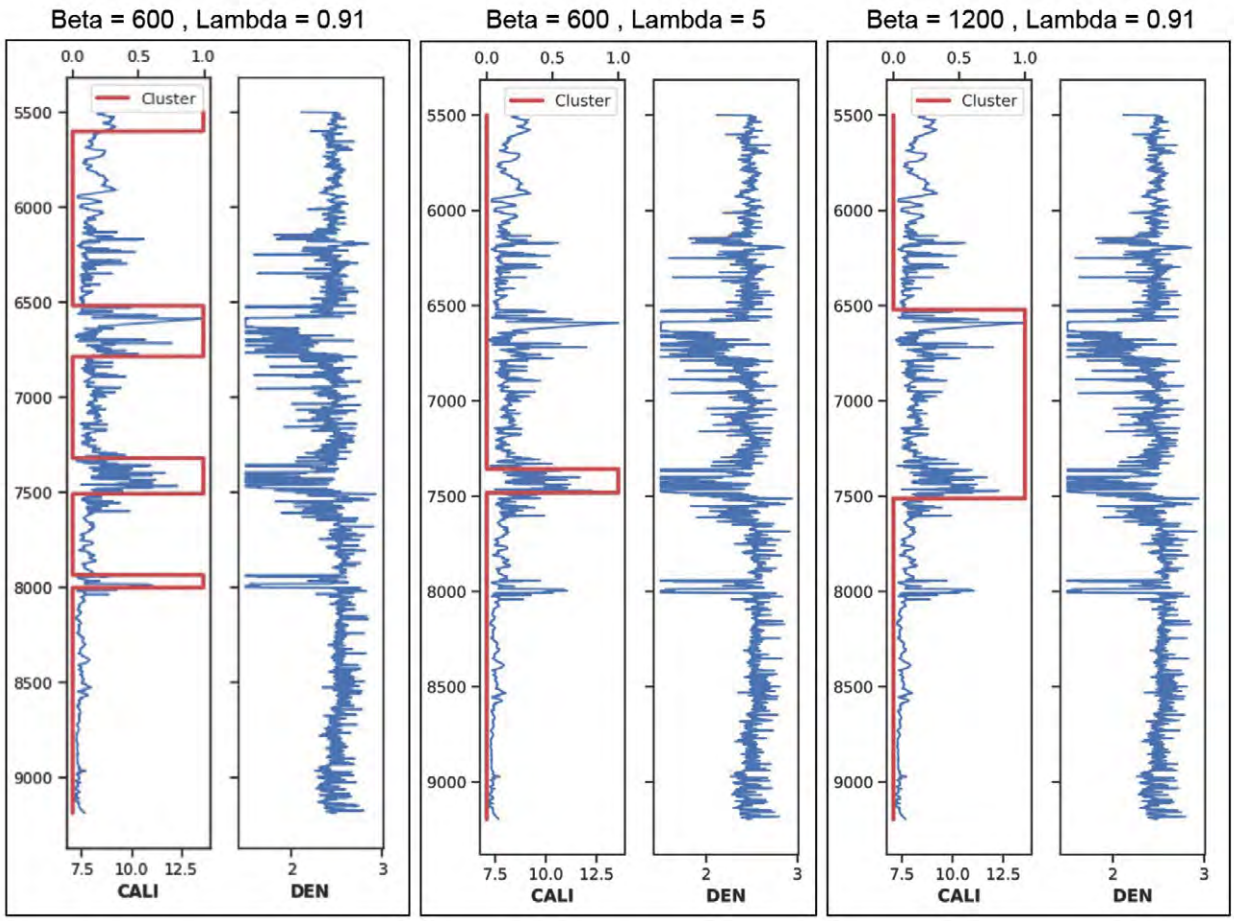

Fig. 8—Effect of changing TICC parameters: penalty (β) and MRF sparsity (λ).

Increasing λ leads to increased sparsity on the inverse covariances Θ_i. This means that more elements in Θ_i are set to zero, resulting in a higher degree of conditional independence between variables. This contributes to the sensitivity of the clustering algorithm in identifying subsequences where the change in signatures between κ and ρ_B is only mildly correlated. The effect of changing λ is apparent in the first and second panels of Fig. 8. Here, β is kept fixed at 600, and λ is changed. It can be seen that with a higher λ, the TICC only identifies the portion near 7,500 ft where both ρ_B and κ show extremely erratic oscillations. The sections near 6,500 and 8,000 ft are left out since the frequency of oscillations in κ is not as much as those in ρ_B.

Phase 2: Supervised Learning

Once the trained TICC model is used to cluster all wells in Data Set 1, we have a labeled data set of 99,000 wells—Data Set 1L. The primary feature vectors in Data Set 1L are the following:

- Depth z (ft)
- Latitude θ_{LAT} (degrees)
- Longitude θ_{LON} (degrees)
- Density ρ_B (g/cc)
- Gamma ray GR (API)

Additionally, a rolling coefficient of variation of ρ_B computed over a window of length $2w_r$ (denoted as $CV_{\rho B,2wr}$), around the depth of interest z (extending by length w_r on either side of z), is also added to the list of feature vectors. $CV_{\rho B,2wr}$ is computed as a function of depth as

$$CV_{\rho_{B,w_r}}(z) = \frac{\sigma_{\rho_{B_i}}(z)}{\mu_{rho_{B_i}}(z)} \quad (5)$$

where ρ_{Bi} = $\{\rho_{Bt-wr},\rho_{Bt-wr}+1,...,\rho_{Bt},...,\rho_{Bt+wr}\}$, σ represents standard deviation, and μ is the mean. A scatterplot of the input features segregated based on the labels are shown in Fig. 9. Depth ρ_B and $CV_{\rho B',2wr}$ offer a considerable degree of separability between the two clusters. In general, points belonging to the good cluster show a higher value of ρ_B and a lower value of $CV_{\rho B',2wr}$ than those in the bad cluster. Additionally, the variance in $CV_{\rho B',2wr}$ is very low, whereas the bad-cluster points are fairly spread out in terms of $CV_{\rho B',2wr}$. The separation in ρ_B and $CV_{\rho B',2wr}$ are evident in Fig. 10, where higher values of $CV_{\rho B',2wr}$ and lower values of ρ_B correspond to the bad-cluster sections in the wellbore.

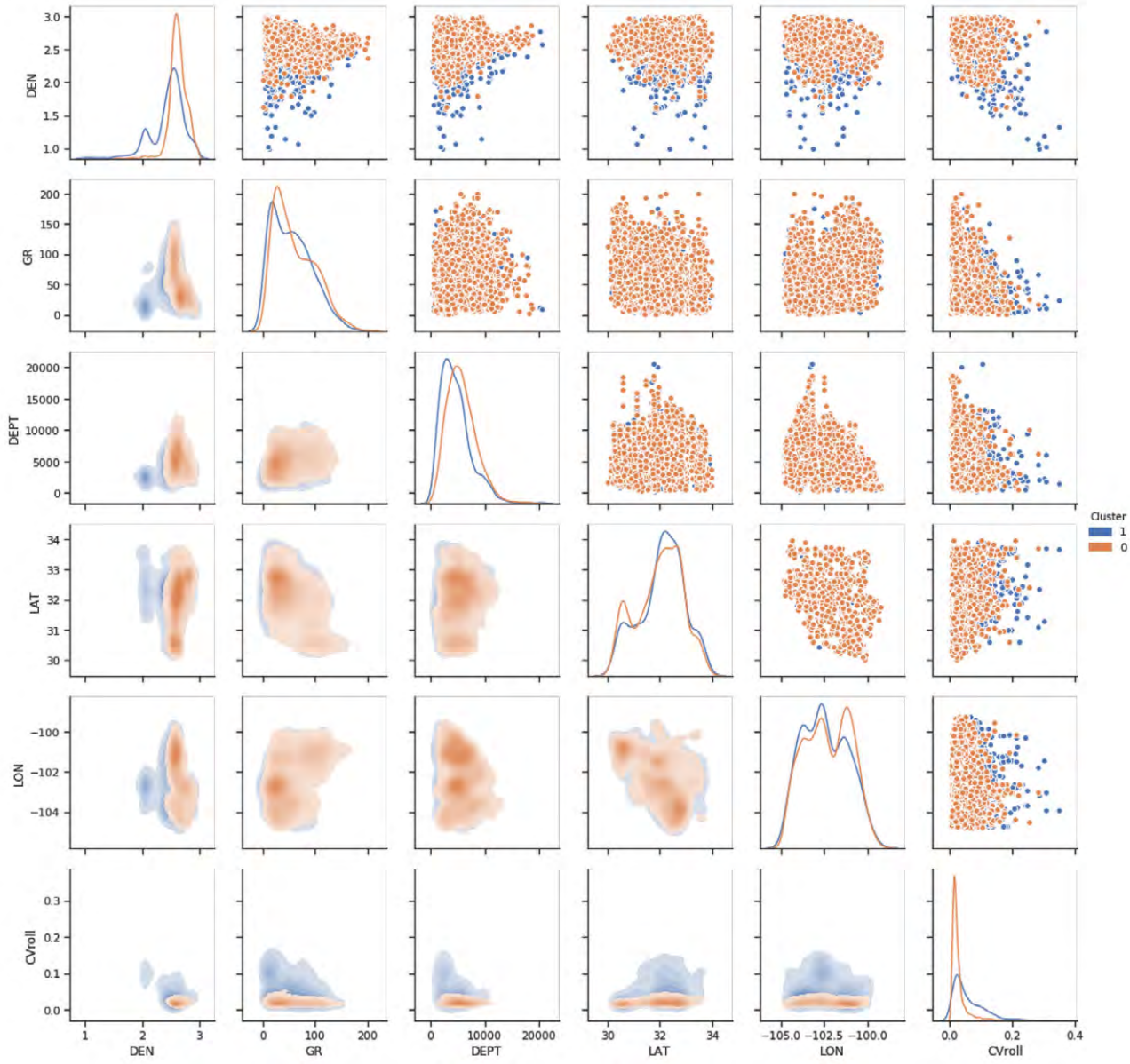

Fig. 9—Scatterplot of input features in the training set for supervised learning, segregated by cluster number. The points in orange correspond to good clusters, whereas those in blue correspond to bad clusters.

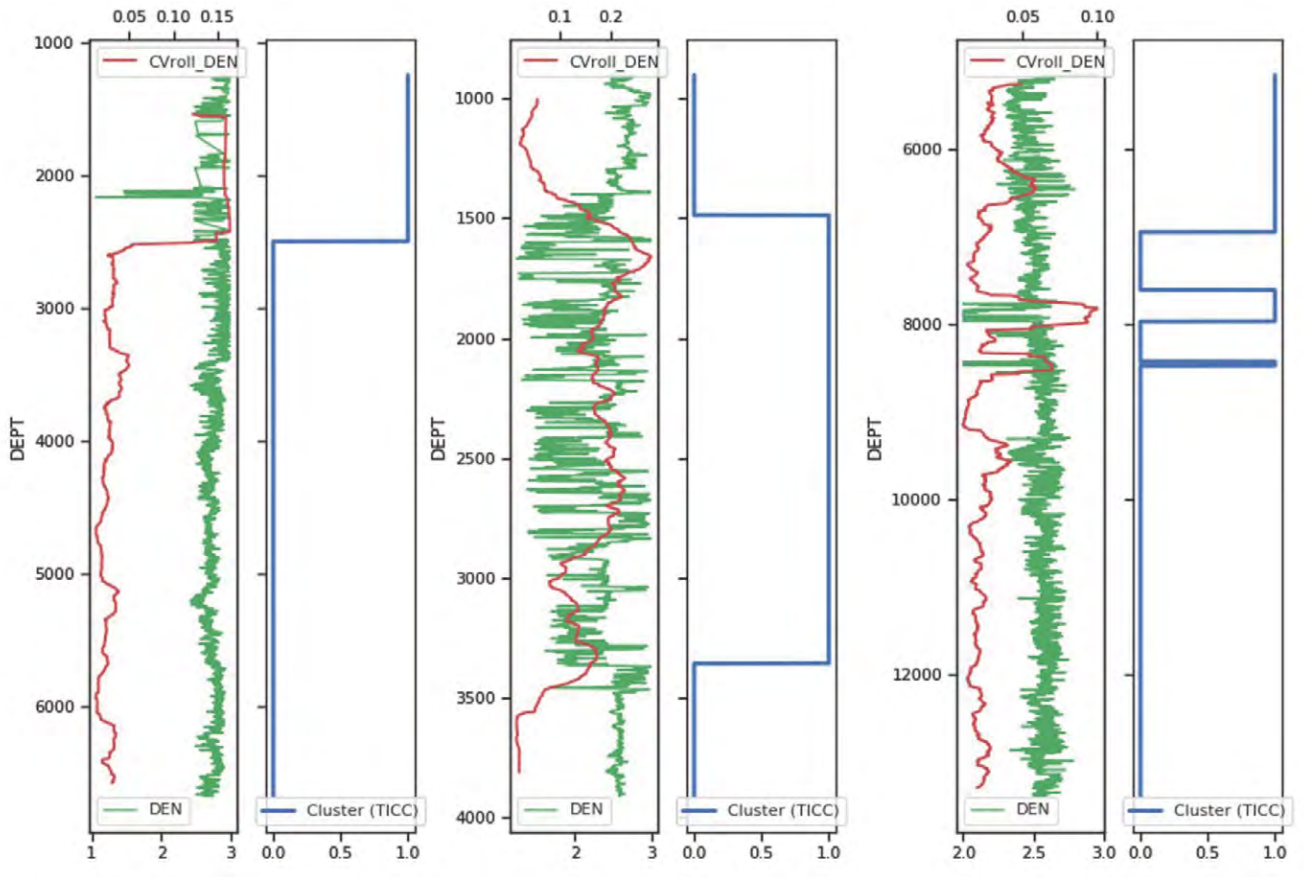

Fig. 10—Rolling coefficient of variance of ρ_B, $CV_{\rho B, 2wr}$ for a window size $2w_r$ = 400 data points, plotted alongside ρ_B and TICC-based clustering.

Since this is a binary classification problem, the target variables are either 0 or 1. As outlined in "Methodology," we train five commonly used supervised learning models—vis-a-vis, LDA, logistic regression, random forest, XGBoost, and GBC—to predict the cluster number for any well, given the input features. These models are trained on 1,400 randomly chosen wells from Data Set 1L and tested on another 600 wells from the same data set. These are shown in Fig. 11. Since the frequency of occurrence of bad clusters in the training data set was approximately one-third that of good clusters, we used Synthetic Minority Over-sampling Technique (SMOTE) (Chawla et al., 2002) to balance the data set before model training.

A major drawback of using a regression-based approach for depth-series data is that the predictions at any point (depth) z are assumed to be independent of predictions at nearby depths (say $z - 1$). In order to address this issue, we resort to a Viterbi-type approach to solving for the path with the maximum likelihood, subject to penalties for cluster switches. It is to be noted that this is essentially the same approach that is used to solve for the cluster assignments as part of TICC. The only difference is that, instead of computing the negative log-likelihood from the inverse covariance, we calculate the same directly from the classification probabilities outputted by the supervised learning model.

In addition to the five supervised classification models described above, we also trained a simple recurrent neural network (RNN)-based model wherein the output from the RNN at the previous depth $z - 1$ is fed back as the input for cluster prediction at z. The architecture of the model is shown in Fig. 12.

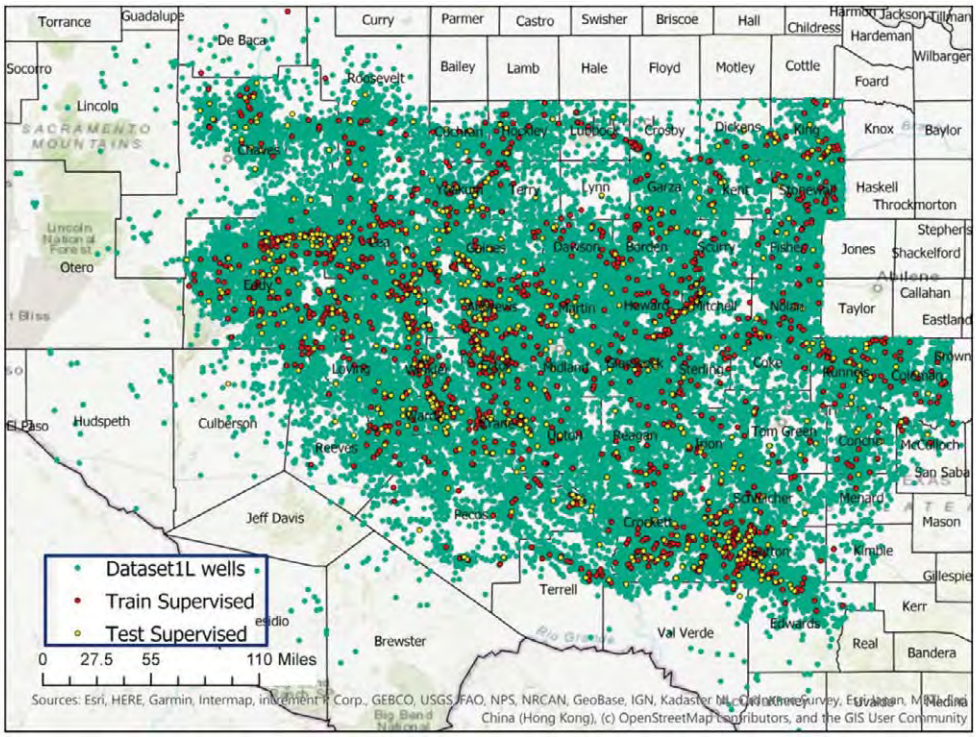

Fig. 11—Data Set 1L is the labeled version of Data Set 1 (green). A subset of 1,400 wells (red) is chosen to train the supervised classification models. The accuracy of these is tested for 600 wells (yellow).

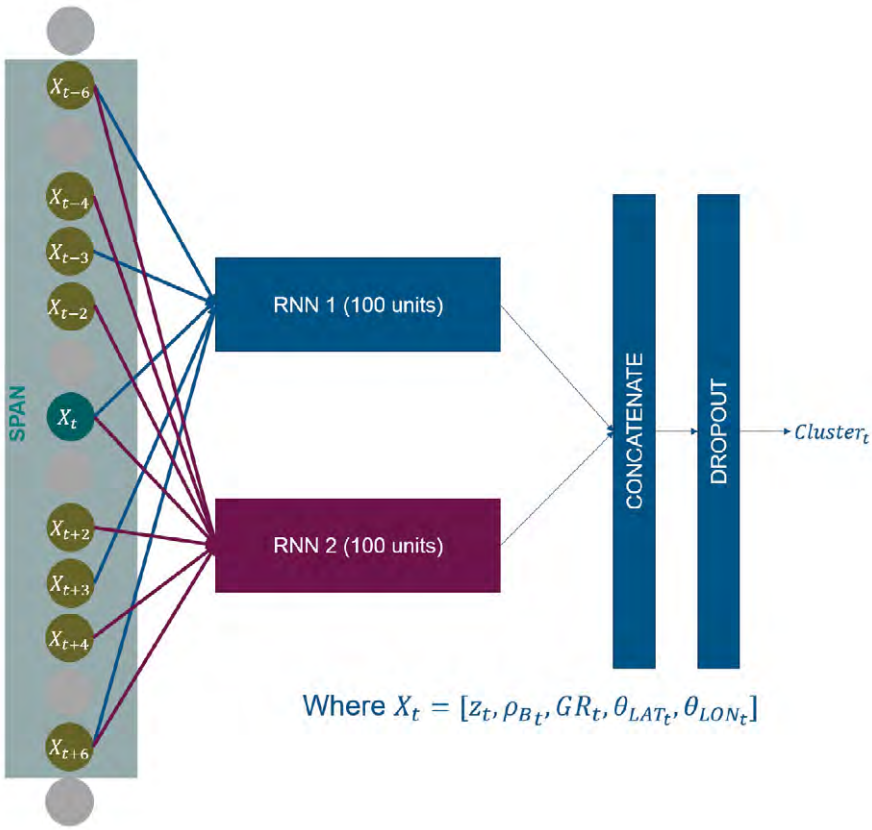

Fig. 12—RNN-based architecture for well-log classification.

We use two RNNs, whose outputs are concatenated and passed to a fully connected layer, activated by a sigmoid function. Each of the two RNNs takes as input a 2D array of input of size $D_{RNNi} \times N_{feat}$ where D_{RNNi} stands for the length of the input window passed to the i^{th} RNN, and N_{feat} is the number of features. As shown in Fig. 12, in order to make a prediction at $z = z_{pred}$, the input vectors at the depths $z = \{z - zspan, z - (zspan - zskipi), z - (zspan - 2zskipi),..., z + (zspan - zskipi), z + z_{span}\}$ are passed to the i^{th} RNN. Such an architecture is chosen so as to provide the RNN with sufficient contextual information at the i^{th} depth without drastically increasing the dimensionality of the input. Dropout layers are added in order to prevent overfitting while training. Binary cross entropy is used as a loss function. The results obtained before and after Viterbi smoothing for different RNN architectures (corresponding to various values of span and skips) are shown in Fig. 13. The confusion matrices for these architectures are given in Table 1. It is seen that the overall classification accuracy is not very sensitive to the architecture. However, higher spans with lower values skips are slower to train. Additionally, Fig. 13 shows that smaller spans result in increasingly noisy cluster sequences, for a given value of penalty in Viterbi smoothing.

It is worth noting that training an RNN requires more time and computation than the models we used in the previous section. Hence, the training and test data sets have been reduced in size—we use 84 wells to train the RNN and 36 wells to test the model. The locations of these wells are shown in Fig. 14.

Results From Supervised Learning

The clustering results for a single well using the six models are shown in Fig. 15. The cluster predictions obtained by merely using a threshold of 0.5 on the predicted probabilities and those computed using the Viterbi-based approach are plotted with thin and thick green lines, respectively. The Viterbi-based approach evidently results in smoother clustering sequences as compared to the former.

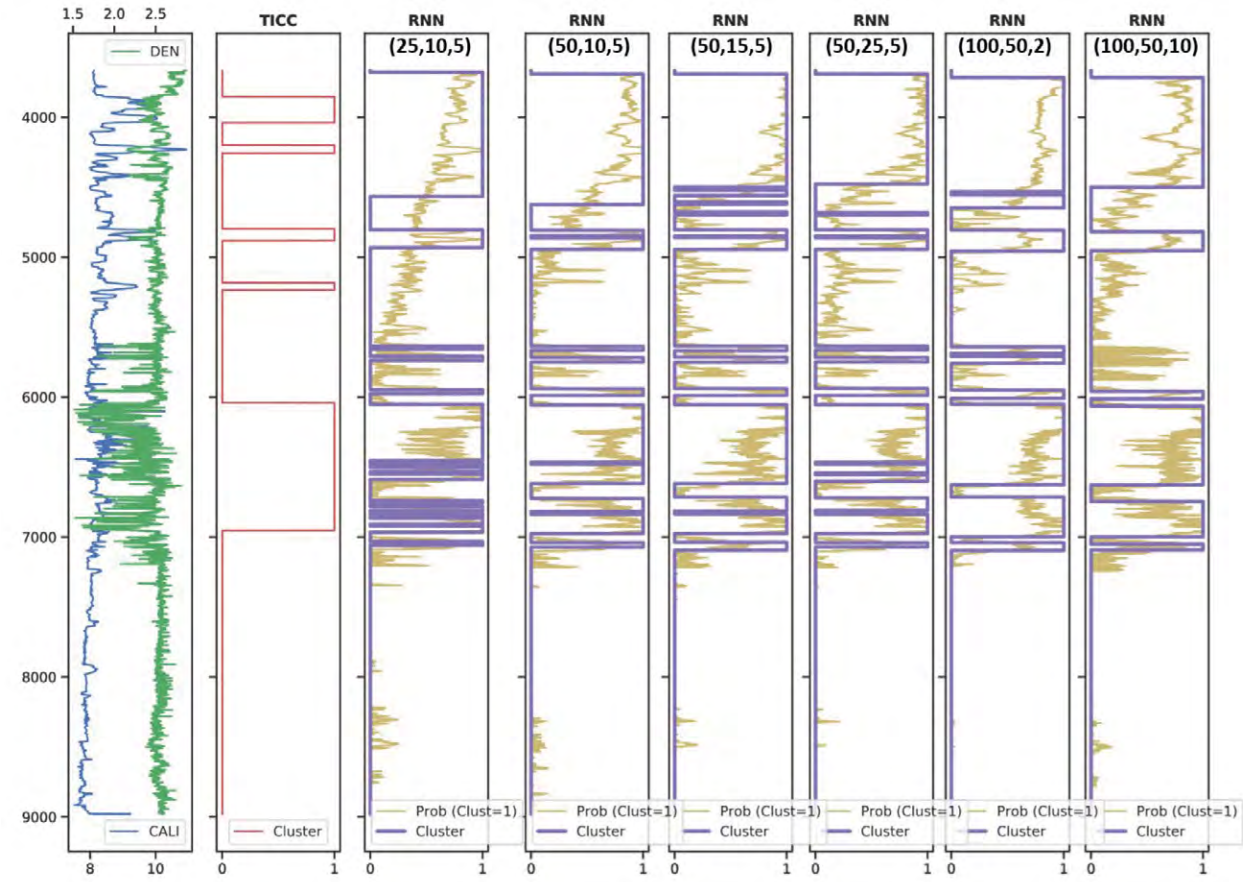

Fig. 13—Performance of various RNN architectures for predicting labels in a single well. The architecture used is described by the tuple (span, skip1, skip2) in the heading of each panel. The significance of span and skips are described in Fig. 12.

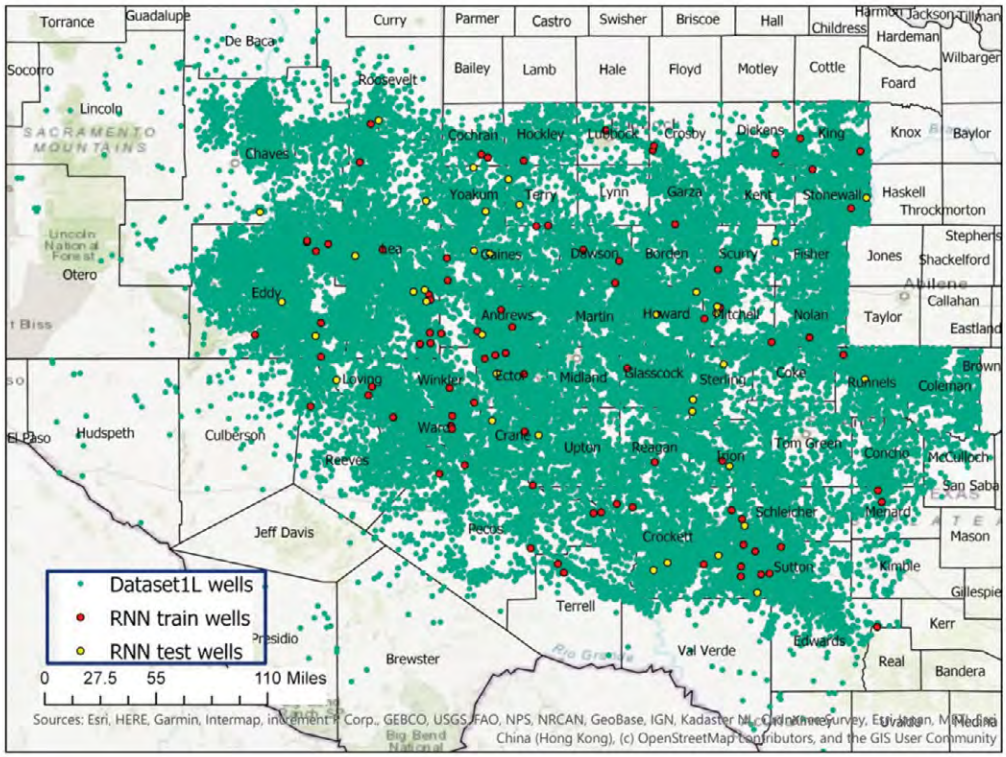

Fig. 14—Data Set 1L is the labeled version of Data Set 1 (green). A subset of 84 wells (red) is chosen to train the RNN. The accuracy of these is tested for 36 wells (yellow).

Table 1—Classification Performance of Various RNN Architectures

Span	Skip1	Skip2	TN	FP	FN	TP
50	10	5	**86**	14	28	**72**
25	10	5	**85**	15	25	**75**
100	50	2	**84**	16	29	**71**
100	50	10	**85**	15	25	**75**
50	15	5	**84**	16	25	**75**
50	25	5	**88**	12	32	**68**

Classification performance is based in terms of percent true negative (TN), false positive (FP), false negative (FN), and true positive (TP) based on 36 test wells.

The performance of the supervised training algorithms (post-Viterbi smoothing) is given in Table 2. These were computed based on predictions from 600 wells, which were held out during the training phase, as a validation data set. However, as explained earlier, the training and test data sets for the RNN model consists of 84 and 36 wells, respectively.

As seen in Table 2, even though the prediction accuracy for good clusters remains the same across all models considered, there is a marked improvement in bad-cluster prediction performance by using RNN.

APPLICATIONS

The primary application of the proposed bad-hole detection workflow is to improve the quality of training data sets for formation density prediction models. In order to demonstrate this functionality, an unsupervised technique was used to detect and flag bad-hole sections in 3,762 Permian wells. A gradient boost algorithm (LightGBM) that predicts formation density was trained on 2,538 of these wells (Model 1). The input features consisted of z, location (θ_{LAT} and θ_{LON}), gamma ray, sonic traveltime, and deep resistivity. All data points corresponding to good and bad clusters were used at this stage. Subsequently, these sections corresponding to bad clusters were deleted, and a second model (Model 2) was trained on the remaining data points (corresponding to good clusters) in the same 2,538 training wells.

The results for two test wells from this experiment are shown in Fig. 16. These indicate that, while the difference in predictions between the two models is negligible in good-hole conditions, a marked difference exists in the bad-hole regions. The variation in predicted density by

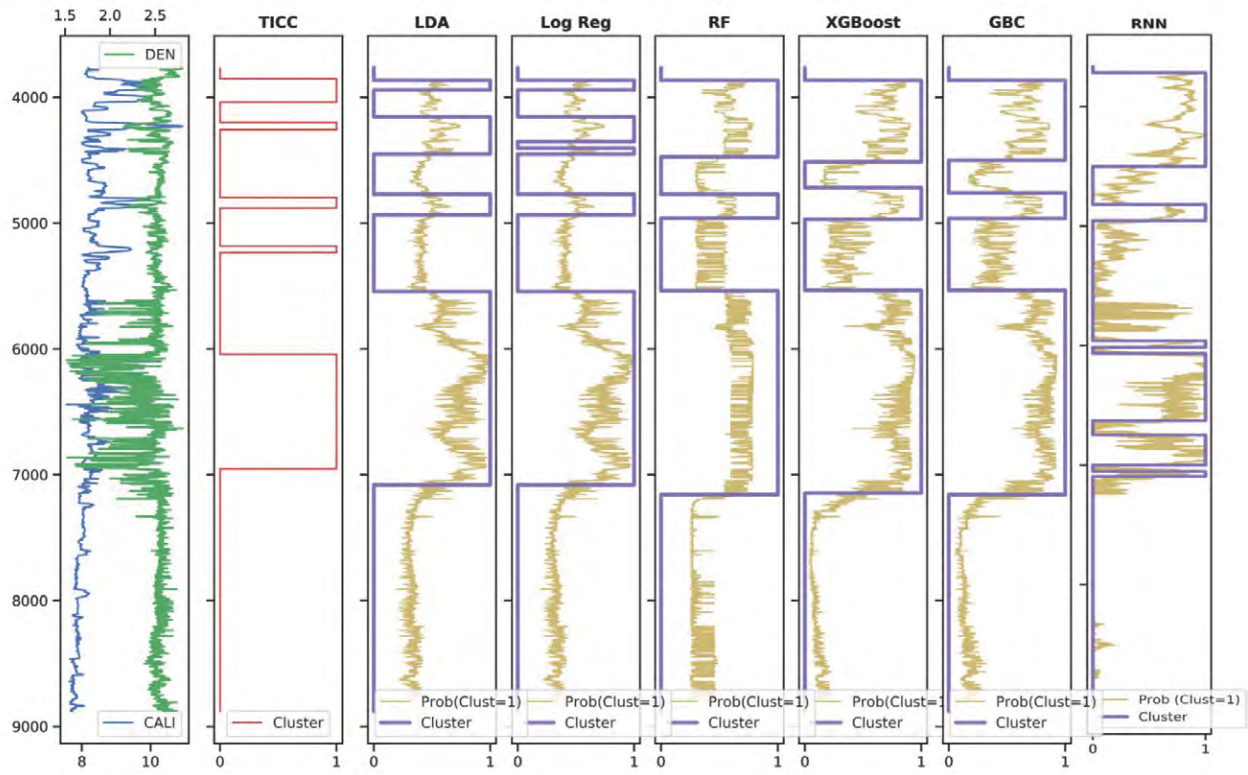

Fig. 15—Results of supervised binary classification on a single test well. The plot in yellow shows the predicted probability for a bad cluster. The thick purple line plots the Viterbi sequence of predicted clusters.

Table 2—Classification Performance of Various Supervised Learning Models

Model	TN	FP	FN	TP
LDA	**87**	13	46	**54**
LogReg	**80**	20	47	**53**
RF	**80**	20	39	**61**
XGBoost	**79**	21	35	**65**
GBC	**80**	20	38	**62**
RNN*	**80**	20	25	**75**

Models are quantified in terms of percent true negative (TN), false positive (FP), false negative (FN), and true positive (TP). Note that the testing accuracy of the RNN is based on 36 wells, whereas that of other models is based on 600 wells.

Model 1 tends to replicate the bad-hole oscillations at depths where wellbore cave-ins are frequent. However, on deleting the bad-hole densities, Model 2 predicts values that are interpolated from good measurements in surrounding regions and sections. This leads to reduced oscillations in density, while preserving the curve signature.

A closer look at the distribution of bad clusters in the data set, shown in Fig. 9 (first column), reveals that a significant portion of these (blue) are characterized by low-density measurements and occur at shallower depths (~2,500 ft) in an areal region bounded by 31.5°N to 34.0°N latitude and −104°W to −102°W longitude. This group of measurements is also characterized by higher $CV_{\rho B'2wr}$, which signifies the high degree of oscillations. The reduction in oscillations in Model 2 (trained without bad clusters) may be explained by the fact that density interpolation is performed based on data points from good clusters (orange in Fig. 9) corresponding to similar values of latitude, longitude, and depth. The $CV_{\rho B'2wr}$ for these data points are also much smaller, which leads to smoother measurements.

CONCLUSIONS AND FUTURE WORK

A novel workflow to simultaneously cluster formation density and caliper logs has been demonstrated in this work. Additionally, the results of clustering have been used as a labeled data set for supervised learning by which bad-hole densities may be detected and deleted, even when κ readings are not available. These methods have been tested on wells

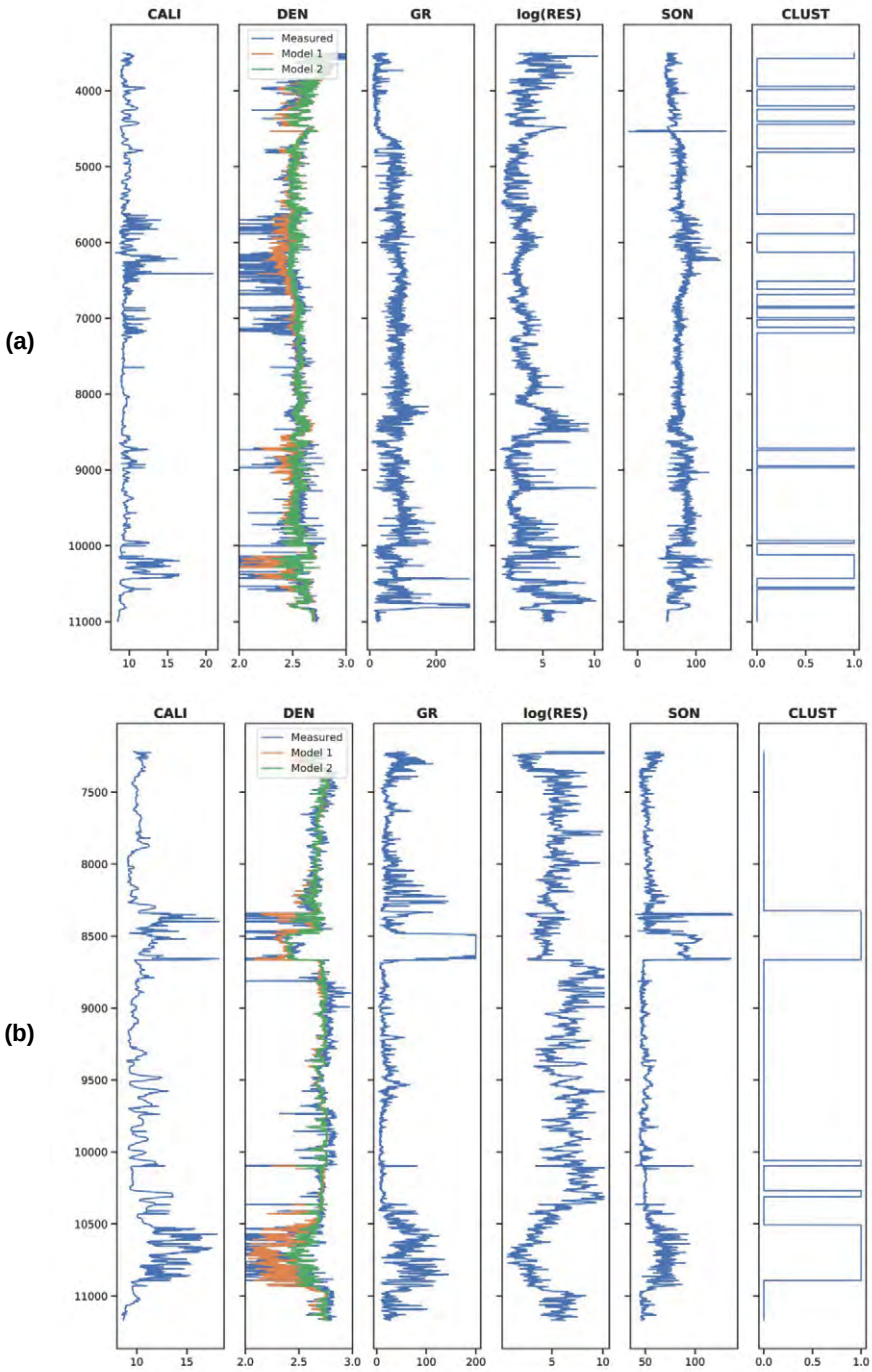

Fig. 16—Density prediction results for two test wells (a) and (b) using light GBM models trained on a data set of 2,538 Permian wells before (Model 1) and after (Model 2) removal of bad-hole sections, as predicted by TICC.

in the Permian Basin and are shown to offer promising results. The clustering workflow may greatly benefit from the use of derived curves, such as density correction logs, as input. A comparison study between the density prediction using the proposed workflow and those obtained using conventional density correction has been left for future work. Furthermore, we also plan to investigate ways to quantify depth-series clustering performance, with the aim of tuning TICC parameters for optimal results. A natural extension to this work would be to use the workflow for formation top detection by means of multiclass classification. This has been left for future work.

ACKNOWLEDGMENTS

We wish to thank Carl Neuhaus, Sathiya Namasivayam, David Smith, James Keay, Alex Fick, and Jason Kegel for their support. We also thank TGS management for permission to publish this work.

NOMENCLATURE

Symbols

ρB = formation density recording
φN = neutron porosity recording
ΔT = sonic log traveltime recording
κ = caliper recording
γ = rugosity of caliper recording
θLAT = latitude of wellbore
θLON = longitude of wellbore
$\bar{y}(t)$ = multivariate time series
$y1$,$y2$ = component univariate time series comprising $\bar{y}(t)$
nw = number of windows
w = length of time-series window
n = dimensionality of time series
Θ_i = inverse covariance matrix of the i^{th} cluster
$Nclust$ = number of clusters
$\mathbf{P}$ = cluster sequence
P_i = data points belonging to cluster i in $\mathbf{P}$
β = clustering switching penalty in TICC
λ = regularization parameter for inverse covariance matrix sparsity in TICC
σ = standard deviation
μ = mean
CV = coefficient of variation
$DRNN$ = length of input window passed to RNN
$Nfeat$ = number of input features passed to RNN

REFERENCES

Bassiouni, Z., 2012, Well Logs Quality Control Issues. URL: http://oilproduction.net/files/Well%20Logs%20Quality%20Control%20Issues.pdf. Accessed August 22, 2020.

Boyd, S., and Vandenberghe, L., 2004, *Convex Optimization*, Cambridge University Press. ISBN: 978-0521833783.

Chawla, N.V., Bowyer, K.W., Hall, L.O., and Kegelmeyer, W.P., 2002, SMOTE: Synthetic Minority Over-Sampling Technique, *Journal of Artificial Intelligence Research*, **16**, 321–357. DOI: 10.1613/jair.953.

de Macedo, I.A.S., de Figueiredo, J.J.S., and de Sousa, M.C., 2020, Density Log Correction for Borehole Effects and Its Impact on Well-to-Seismic Tie: Application on a North Sea Data Set, *Interpretation*, **8**(1), T43–T53. DOI: 10.1190/INT-2019-0004.1.

Doll, H.G., 1949, Introduction to Induction Logging and Application to Logging of Wells Drilled With Oil Base Mud, Paper SPE-949148, *Journal of Petroleum Technology*, **1**(6), 148–162. DOI: 10.2118/949148-G.

Gavriliu, D., and Batchelor, J., 2019, Drillhole Rugosity Correction for Gamma-Gamma Density Tools – A Space Modelling Approach, Presented at the Australasian Exploration Geoscience Conference, Perth, Australia, 2–5 September. URL: https://www.aig.org.au/wp-content/uploads/2020/01/21.pdf. Accessed August 22, 2020.

Glover, P., 2013, Petrophysics MSc. Course Notes, URL: http://homepages.see.leeds.ac.uk/~earpwjg/PG_EN/CD%20Contents/GGL-66565%20Petrophysics%20English/Chapter% 2013.PDF. Accessed August 22, 2020.

Gray, D., Day, S., and Schapper, S., 2015, Rock Physics Driven Seismic Data Processing for the Athabasca Oil Sands, Northeastern Alberta, *CSEG Recorder*, **40**(3), 32–40. URL: https://csegrecorder.com/articles/view/rock-physics-driven-seismic-data-processing-for-the-athabasca-oil-sands. Accessed August 22, 2020.

Gupta, S.D., Chatterjee, R., and Farooqui, M., 2012, Rock Physics Template (RPT) Analysis of Well Logs and Seismic Data for Lithology and Fluid Classification in Cambay Basin, *International Journal of Earth Sciences*, **101**(5), 1407–1426. DOI: 10.1007/s00531-011-0736-1.

Hallac, D., 2017, Toeplitz Inverse Covariance-Based Clustering of Multivariate Time Series Data. URL: http://github.com/davidhallac/TICC. Accessed August 22, 2020.

Hallac, D., Vare, S., Boyd, S.P., and Leskovec, J., 2017, Toeplitz Inverse Covariance-Based Clustering of Multivariate Time Series Data, *Proceedings*, *27th International Joint Conference on Artificial Intelligence*, Melbourne, Australia, 19–25 August, 5254–5258. URL: https://www.ijcai.org/Proceedings/2018/0732.pdf. Accessed August 22, 2020.

Jain, V., Wu, P.-Y., Akkurt, R., Hodenfield, B., Jiang, T., Maehara, Y., Sharma, V., and Abubakar, A., 2019, Class-Based Machine Learning for Next-Generation Wellbore Data Processing and Interpretation, Paper SS, *Transactions*, *SPWLA 60th Annual Logging Symposium*, The Woodlands, Texas, USA, 15–19 June.

Johnston, J., and Guichard, A., 2015, Using Big Data Analysis Tools to Understand Bad Hole Sections on the UK Continental Shelf, Paper SPE-1015-0060, *Journal of Petroleum Technology*, **67**(10), 60–63. DOI: 10.2118/1015-0060-JPT.

Kumar, M., Dasgupta, R., Singha, D.K., and Singh, N.P., 2018, Petrophysical Evaluation of Well Log Data and Rock Physics Modeling for Characterization of Eocene Reservoir in Chandmari Oil Field of Assam-Arakan Basin, India, *Journal of Petroleum Exploration and Production Technology*, **8**, 323–340. DOI: 10.1007/s13202-017-0373-8.

Liao, T.W., 2005, Clustering of Time Series Data a Survey, *Pattern Recognition*, **38**, 1857–1874. DOI: 10.1016/j.patcog.2005.01.025.

Liu, Z., and Zhao, J., 2015, Correcting Hole Enlargement Impacts on Density Logs for Coalbed Methane Reservoirs, *The Open Petroleum Engineering Journal*, **8**(1), 72–77. DOI: 10.2174/1874834101508010072.

Mukerji, T., Avseth, P., Mavko, G., Takahashi, I., and González, E.F., 2001, Statistical Rock Physics: Combining Rock Physics, Information Theory, and Geostatistics to Reduce Uncertainty in Seismic Reservoir Characterization, *The Leading Edge*, **20**(3), 313–319. DOI: 10.1190/1.1438938.

Oates, T., Firoiu, L., and Cohen, P.R., 1999, Clustering Time Series With Hidden Markov Models and Dynamic Time Warping, *Proceedings, IJCAI-99 Workshop on Neural, Symbolic and Reinforcement Learning Methods for Sequence Learning*, 17–21. URL: https://cs.fit.edu/~pkc/ml/related/oates-ijcaisl99.pdf. Accessed August 22, 2020.

Pickell, J.J., and Heacock, J.G., 1960, Density Logging, *GEOPHYSICS*, **25**(4), 891–904. DOI: 10.1190/1.1438769.

Rabiner, L.R., 1989, A Tutorial on Hidden Markov Models and Selected Applications in Speech Recognition, *Proceedings, IEEE*, **77**(2), 257–286. DOI: 10.1109/5.18626. URL: https://web.ece.ucsb.edu/Faculty/Rabiner/ece259/Reprints/tutorial%20on%20hmm%20and%20applications.pdf. Accessed August 22, 2020.

Sarasty, J.J., and Stewart, R.R., 2003, Analysis of Well-Log Data from the White Rose Oilfield, Offshore Newfoundland, *CREWES Research Reports*, **15**, 1–16. URL: https://crewes.org/ForOurSponsors/ResearchReports/2003/2003-02.pdf. Accessed August 22, 2020.

Sen, D., Raihan, D.A.V., and Chidambaram, M., 2014, Multiway Continuous Hidden Markov Model-Based Approach for Fault Detection and Diagnosis, *AIChE Journal*, **60**(6), 2035–2047. DOI: 10.1002/aic.14386.

Smyth, P., 1997, Clustering Sequences With Hidden Markov Models, *Advances in Neural Information Processing Systems*, 648–654. URL: https://papers.nips.cc/paper/1217-clustering-sequences-with-hidden-markov-models.pdf. Accessed August 22, 2020.

Ugborugbo, O., and Rao, T., 2009, Impact of Borehole Washout on Acoustic Logs and Well-to-Seismic Ties, Paper SPE-128346 presented at the Nigeria Annual International Conference and Exhibition, Abuja, Nigeria, 3–5 August. DOI: 10.2118/128346-MS.

Wen, T., Rui, X., Ling-ling, Z., and Xiao-gang, W., 2011, Comparison and Limitation Analysis of Approaches for Porosity Evaluation From NMR and Three Porosity Logs in Low Permeability Gas Sands With Bad Borehole, Paper SPE-141040 presented at the SPE Middle East Unconventional Gas Conference and Exhibition, Muscat, Oman, 31 January–2 February. DOI: 10.2118/141040-MS.

ABOUT THE AUTHORS

Deepthi Sen is a PhD student at Texas A&M University. Her research focuses on the application of machine-learning algorithms to reservoir modeling and simulation.

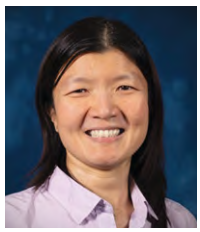

Cen Ong is a data scientist at TGS working on data-driven energy products. Her past experiences include software engineering and research roles at Repsol and Schlumberger. She is an active member of the Society of Exploration Geophysicists (SEG).

Sribharath Kainkaryam leads a team of data scientists and data engineers at TGS. Prior to joining TGS in 2018, he was a research scientist working on imaging and velocity model-building challenges at Schlumberger.

Arvind Sharma is vice president of Data and Analytics at TGS. In this role, he is responsible for machine-learning initiatives as well as broader digital transformation. He has over 10 years of experience in various E&P and software-related work.

PETROPHYSICS, VOL. 61, NO. 5 (OCTOBER 2020); PAGES 450–472; 13 FIGURES; 1 TABLE. DOI: PJV61N5-2020a4

Towards a Petrophysically Consistent Implementation of Archie's Equation for Heterogeneous Carbonate Rocks[1]

Raghu Ramamoorthy[2], T.S. Ramakrishnan[3], Suvodip Dasgupta[3], and Ishan Raina[3]

ABSTRACT

Archie's empirical resistivity-saturation relation of 1942 is widely applied in the petroleum industry. Despite its shortcomings, Archie's equation is the basis for inferring water saturation, even in carbonates with complex pore structure, albeit with empirical tuning of cementation and saturation exponents. Industry literature is replete with examples of why this approach leads to erroneous estimates of the water saturation, and methods have been proposed where the range of saturation present in the reservoir has been subdivided into segments, each having a different set of exponents. Here, based on a homogenization methodology, we propose an effective resistivity model of an inter- and intragranular vuggy carbonate, when the pore sizes in the subsystems are well separated. The model is applied both for water-wet and mixed-wet rocks with appropriate modifications. Methodologies for apportioning pore fractions and their sizes depend on the openhole logs and/or core data. Computed results show significant deviations from Archie correlations in microporous or vuggy intervals. Results are verified on several Middle East carbonate formations against core and evidence from nuclear logs.

INTRODUCTION

Archie (1942) proposed a relationship between the formation water saturation, S_w, and its true resistivity, R_t, porosity, ϕ, and the resistivity of the aqueous phase, R_w, given by

$$S_w = \sqrt[n]{\left(\frac{R_w}{\phi^m R_t}\right)} \tag{1a}$$

where m and n are the cementation and saturation exponents, respectively. Archie suggested that both m and n be set to two. Defining R_0 as the resistivity for aqueous saturation of unity with a fluid of resistivity R_w,

$$R_0 = \frac{R_w}{\phi^m} \tag{1b}$$

Archie further set the ratio,

$$\frac{R_t}{R_0} = I = \frac{1}{{S_w}^n} \tag{1c}$$

where the ratio came to be known as the Resistivity Index (RI), denoted by I.

In many carbonates, m and n take on values much different from two and are thought to be saturation dependent (Sweeney and Jennings, 1960; Lucia, 1983; Focke and Munn, 1987; Dixon and Marek, 1990). Keller (1953), Sweeney and Jennings (1960), Morgan and Pirson (1964), Mungan and Moore (1968), Donaldson and Siddiqui (1989), and Tsakiroglou and Fleury (1999) advocate relating saturation exponent to wettability state. Dixon and Marek (1990) and Ma et al. (2005) suggested that the saturation cycle in the reservoir be first identified, and a different set of Archie parameters be applied to each identified cycle. Although the exponent may differ with a quantifiable wettability, and more importantly, with the directionality of saturation change, particularly in oil-wet media, the apparent variability of the exponent due to microscopic structure remains to be quantified.

Complex geometries in carbonates may be conceptualized as a juxtaposition of different pore systems (Archie, 1952; Dunham, 1962). The resulting capillary pressure may be approximated as a homogenized curve of systems in capillary equilibrium. Water saturation is different within each microscopic heterogeneity (by which we mean

Manuscript received by the Editor August 27, 2019; revised manuscript received July 24, 2020; manuscript accepted July 29, 2020.
[1]Originally presented at the SPWLA 60th Annual Logging Symposium, The Woodlands, Texas, USA, June 17–19, 2019, Paper P.
[2]Raghu Advisory Services, P.O.Box 26537, Abu Dhabi, United Arab Emirates; rraghu59@gmail.com
[3]Schlumberger-Doll Research, One Hampshire St, Cambridge, MA 02139, United States; ramakrishnan@slb.com
Schlumberger Middle East S.A., P.O.Box 21, Abu Dhabi, United Arab Emirates; sdasgupta2@slb.com
Schlumberger, 895 Rue de la Vieille Poste, 34000 Montpellier, France; iraina@slb.com

that on the length scale of the larger feature, homogenization of small-scale features alone is feasible), and the composite behavior may deviate measurably from Archie-like behavior. By homogenizing a smaller-scale feature, we also bypass issues with regard to accessibility because it is assumed to be "locally infinite." This is an approximation, which, in the limit of the macroscopic length to the microscopic scale (a pore size) going to infinity, becomes exact. Thus, the medium is approximated by each system having its own capillary pressure curve, and our assumption of access to each system is based on local capillary pressure equilibrium. For example, in a water-wet inter/intragranular system, wherein the two characteristic pore sizes differ considerably, hydrocarbon migrates into the intergranular network before accumulating within grains. The displacement sequence is reversed during water-based mud-filtrate invasion in water-wet media. Accessibility to vugs of an invading phase may occur when the interspersed smaller-scale pore system may have a negligible invading phase. The invading phase may span the intergranular pores negligibly as long as the length of intergranular pore space between vugs is sufficiently large in length measured in pore units ($\boldsymbol{L}$). At the onset of percolation, the invading phase has a saturation that scales as $\boldsymbol{L}^{-\beta/\nu}$ where $\boldsymbol{\beta}$ and $\boldsymbol{\nu}$ are percolation exponents, whose ratio is approximately 0.5. (Chandler et al., 1982; Stauffer and Aharony, 2018). Thus, even when there is no size overlap between vugs and intergranular pores, this assumption is not impractical. Conversely, when the vugs have their own communicating pathway, accessibility to vugs independent of the intergranular pathway is assured.

For multipore systems, Petricola et al. (2002) proposed a sequential method of applying the Archie equation for a rock partitioned into three systems. Here, we propose a solution for a rock partitioning similar to that of Petricola et al., though the topology and the effective conductivity relationships rely on the homogenization methodology of Ramakrishnan et al. (2001). The intragranular (micro) pores are within the grains, the intergranular (macro) pores are between grains, and the vugs are dissolution features, also represented by the absence of grains. One input to pore partitioning is based on nuclear magnetic resonance (NMR) data; we suggest a multitude of inputs that enable a quantitative breakdown of porosity into its components.

Our present method is demonstrated for several cases of initial water-wet carbonate formation that have been subject to oil migration and, possibly, subsequent wettability alteration. We also consider the case when such a formation is subject to invasion by a water-based mud filtrate. With a view to keeping the method objective but practical, we provide detailed guidance for the selection of the parameters of the transform. The approach, while simple, honors the petrophysical principles governing the ingress and extraction of hydrocarbon in microscopically heterogeneous carbonate formations.

The necessity for saturation equations honoring the underlying pore-length scales and their topological placement is exemplified by examples in vuggy carbonates. For a given porosity, these exhibit high resistivity, even when water filled (Asquith, 1985), which can lead to futile production tests in water zones. Several researchers (Nugent et al., 1978; Brie et al., 1985) have developed methods to estimate m from a measure of the vug fraction from consideration of classical homogenization methods for spherical inclusions. The use of an elevated m value while holding the saturation exponent n at two results in an increase in the estimated S_w and is not self-consistent. Asakura et al. (2001) and Griffiths and Carnegie (2006) published examples of saturation computed from the thermal neutron-capture cross-section (Σ) log recorded by pulsed-neutron tools consistently showing higher oil saturation, especially near the oil-water contact, compared to that estimated from resistivity logs applying existing interpretation methods. They argued (as also Petricola and Watfa, 1995) that the brine-filled microporous grains around the oil-filled intergranular pores and vugs provide alternative conduction paths that, when not correctly accounted for, leads to pessimistic oil saturation estimates.

Thus, a self-consistent resistivity model that honors not only the distribution of the multiple phases, but also the effective conductivity due to their topological arrangement is needed for saturation estimation from openhole logs, particularly those with multiple depths of investigation. These models should account for accumulation and invasion pathways and wettability modification, if identifiable. Reserves estimates may be biased otherwise.

EFFECTIVE MEDIUM MODEL

Ramakrishnan et al. (1998, 2001) proposed a topological model of carbonate rock comprising microporous grains constituting intragranular porosity with intergranular or macroporosity between the grains. Vugs are depicted as dissolution events wherein one or more grains are missing. Figure 1 describes such an arrangement. V_v, V_m, and V_μ are the pore volume as a fraction of the whole rock contained in the vugs, intergranular pores, and intragranular pores, respectively. Their model applies to the topology regardless of the absolute pore sizes, as long as the characteristic pore

scales are well separated. It is noted that the sum of V_v, V_m, and V_μ is the total porosity, ϕ_t, of the rock.

To estimate the conductivity of such a rock under brine-saturated conditions, Ramakrishnan et al. (2001) accepted that the intergranular and intragranular pore systems obeyed the Archie correlation. The effective medium they chose was an extension of the differential Bruggeman approximation (Landauer, 1978) that in the limit satisfied the requisite correlation of Archie (1942). In their model, in the absence of scale invariance, the conductivity of the brine-filled grain (σ_{0g}) is given by

$$\sigma_{0g} = \sigma_w \phi_\mu^{\,m_\mu}, \tag{2}$$

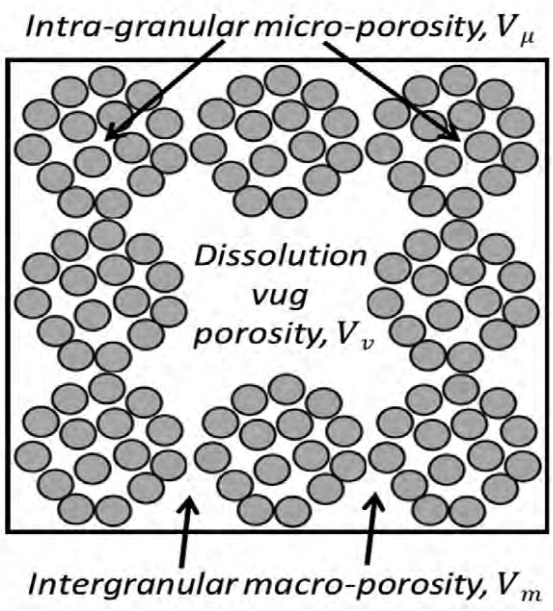

Fig. 1—Pictorial depiction of the Ramakrishnan et al. (1998) model for carbonate rocks.

where ϕ_μ is the intrinsic porosity of the grains given by

$$\phi_\mu = \frac{V_\mu}{1-V_v-V_m}. \tag{3}$$

The conductivity, $\sigma_{0\mu m}$, of the assemblage of such brine-filled microporous grains with brine in the intergranular pore space is computed from the modified differential Bruggeman effective medium conductivity result (Landauer, 1978; Ramakrishnan et al., 2001):

$$\frac{V_m}{1-V_v} = \left(\frac{\sigma_w}{\sigma_{0\mu m}}\right)^{\frac{m_m-1}{m_m}} \left(\frac{\sigma_{0g}-\sigma_{0\mu m}}{\sigma_{0g}-\sigma_w}\right) \tag{4}$$

We note that the term on the left of Eq. 4, $\frac{V_m}{1-V_v}$ is the intrinsic intergranular porosity, ϕ_m, while the intrinsic vug porosity, ϕ_v, is identical to the vug volume fraction, V_v.

The porosity exponent is different for the intra- or intergranular pore systems and is designated by the corresponding subscript μ or m. However, in practice, there is rarely sufficient data to support two different parameters. Hence, for the examples shown later, a single value of m is assumed for both pore systems.

In the above-mentioned work, the conductivity of the whole rock filled with brine when vugs are also present is given by symmetric Bruggeman solution

$$V_v\left(\frac{\sigma_w-\sigma_0}{\sigma_w+2\sigma_0}\right) + (1-V_v)\left(\frac{\sigma_{0\mu m}-\sigma_0}{\sigma_{0\mu m}+2\sigma_0}\right) = 0 \tag{5}$$

Knowing the conductivity of the brine-saturated rock, the effective Archie porosity exponent

$$m = \frac{\log\frac{\sigma_0}{\sigma_w}}{\log\phi}. \tag{6}$$

The length scale of resistivity measurement is a fraction of a meter to a few meters for downhole application and a few centimeters for laboratory cores. The differential effective medium theory or the symmetric Bruggeman approximation is applicable to such a resistivity measurement provided that at the length scale of the measurement, the microscopic features of the vugs, intergranular, or intragranular pores appear as a continuum. For us, this is satisfied quite adequately. This is not to say that the effective medium theories are exact in the asymptotic limit of feature size over the measurement limit approaching zero. The models are correct only under conditions of dilute inclusions, and any extensions of it to non-infinitesimal fractions of one component within the other is to be considered an approximation that can only be validated experimentally. Our earlier studies have supported the approach we have taken through experimental data obtained in fully saturated systems. For further reading, we refer the reader to Ramakrishnan et al. (2001) for data and Markel (2016) for the theoretical background.

The validity of the Ramakrishnan et al. model can be verified by core measurements of the Archie m exponent along with volume fraction estimates of the three components of porosity. These fractions may be approximated through optical and scanning electron microscope (SEM) petrography or from NMR and/or electrical images as proposed by Allen et al. (2001), Ramakrishnan et al. (2001), and others (Asakura et al., 2001; Gomaa et al., 2006). Mercury injection pore-size distributions may be used, though we recognize that this is a distribution of pore volume shielded by throats and is affected by the pore-space topology. When supported by petrographical evidence, mercury injection data is an inexpensive source of information on the pore partitions.

The identification of pore partitions is often difficult without an identifiable transition in slope.

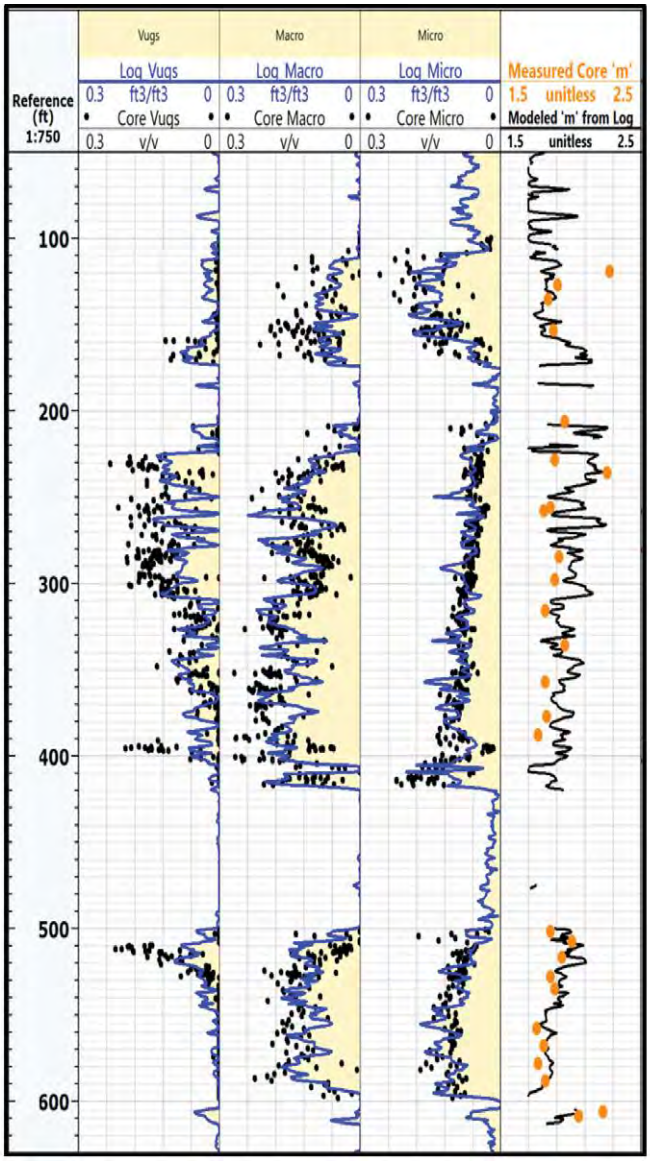

Fig. 2—Log-derived Archie *m* exponent from the current model compared to the measurement of the same parameter on core extracted from a Cretaceous carbonate formation. Note that we use the term micro to mean intragranular and macro to mean intergranular. No intrinsic absolute size is inferred.

We have extensively validated the Archie *m* computation from the Ramakrishnan-Bruggeman model based on pore partitions estimated from borehole logs with that measured on cores taken from the same well. Figure 2 is an example of a Cretaceous carbonate formation. Over 600 high-pressure mercury injection (MICP) end-trim samples were used to validate the pore partitions. The last track on the right compares our model *m* computed from the partitions derived from logs with the *m* measured on cores. Figure 3 shows a similar comparison of our model *m* estimated from log-derived pore partitions versus that measured on cores on a Jurassic carbonate reservoir in the Middle East. The pore partitions were confirmed by measurements on conventional core acquired over the same interval. Our model *m* is validated with core plug measurement every 6 feet. Similar validation was obtained on several Cretaceous and Jurassic reservoirs across the Middle East.

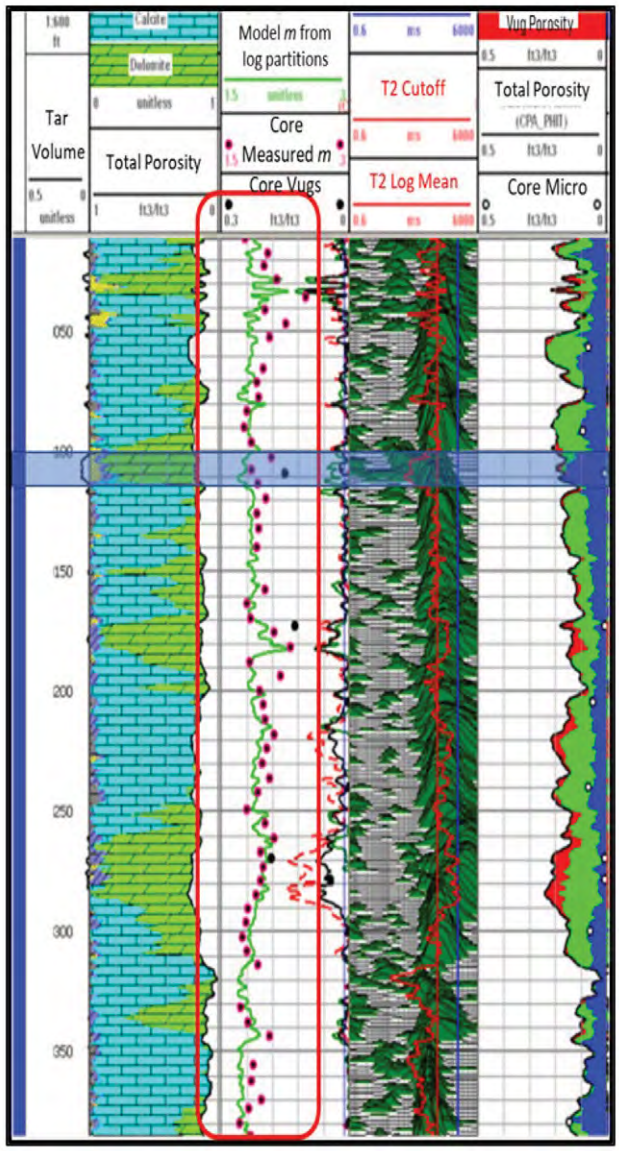

Fig. 3—Comparison of log derived Archie *m* exponent using the current model and that measured on core from a Jurassic carbonate reservoir. Zone of biodegraded heavy oil with associated bitumen just below X100 ft is highlighted. Both log- and core-derived pore partitions in this zone are not reliable.

EFFECTIVE MEDIUM WITH HYDROCARBON

To account for the effect of hydrocarbons, each of the three underlying equations of the Ramakrishnan-Bruggeman model must be modified. The new model is called the Raghu-Ramakrishnan model (referred to as the R-R model in the remainder of the paper). The conductivity of the grains with porosity ϕ_μ is

$$\sigma_g = \sigma_w S_{w\mu}^{n_\mu} \left(\phi_\mu\right)^{m_\mu} \tag{7}$$

where σ_g is the conductivity of the grains, and $S_{w\mu}$ is the water saturation within the grains. For completeness, the equations shown here allow for different n for each pore system designated by the corresponding subscript μ or m. In the examples discussed later, we have used a single value of n for both intragranular and intergranular pore systems, although this assumption may be removed by introducing an additional parameter.

For application to the assembly of grains, we first recognize that the effective conductivity of the intergranular fluid may be replaced by $\sigma_w S_{wm}^{n_m}$, where S_{wm} is the aqueous phase saturation in the intergranular pores for correct limiting behavior. This then allows us to modify Eq. 4 for the conductivity of an assemblage of microporous grains in a partially saturated intergranular porous network to

$$\frac{V_m}{1-V_v} = \left(\frac{\sigma_w S_{wm}^{n_m}}{\sigma_{\mu m}}\right)^{\frac{m_m-1}{m_m}} \left(\frac{\sigma_g-\sigma_{\mu m}}{\sigma_g-\sigma_w S_{wm}^{n_m}}\right) \tag{8}$$

We see that, in the limit of $\phi_\mu \rightarrow 0$ and the grains having zero conductivity, the correct Archie expression for intergranular unimodal pore system is retrieved.

The treatment of partial saturation in the vugs is more complicated. In any given vug, the fluid is either all brine or all hydrocarbon. During imbibition, in a water-wet medium, if we choose to retain all of the oil in vugs, the capillary pressure curve is vertically down, post-drainage. During the early part of the drainage, oil may be present only in a fraction of the vugs. Then, oil saturation would be less than unity in the vug system. If all vugs are filled with hydrocarbon, Eq. 5 changes to

$$-V_v\left(\frac{1}{2}\right) + (1-V_v)\left(\frac{\sigma_{\mu m}-\sigma}{\sigma_{\mu m}+2\sigma}\right) = 0 \tag{9}$$

where σ is the rock conductivity. Solving for σ, we get

$$\sigma = \sigma_{\mu m}\left(1-\frac{3}{2}V_v\right) \tag{10}$$

If, however, some vugs are filled with brine and the rest with hydrocarbon, we need to modify Eq. 5 for conductive and nonconductive inclusions. Recognizing that S_{wv} is the fraction of vug volume filled with brine and $(1 - S_{wv})$ is the fraction filled with hydrocarbon, we can use the symmetric Bruggeman relationship for the conductivity, σ, of the rock with the water-filled and oil-filled vugs as follows

$$S_{wv}V_v\left(\frac{\sigma_w-\sigma}{\sigma_w+2\sigma}\right) - \frac{(1-S_{wv})V_v}{2} + (1-V_v)\left(\frac{\sigma_{\mu m}-\sigma}{\sigma_{\mu m}+2\sigma}\right) = 0 \tag{11}$$

For a given saturation, these equations enable us to solve for conductivity for any saturation, provided proper accounting is carried out for apportioning aqueous phase fractions within each pore system. We do this by satisfying capillary pressure equilibrium, i.e., the sequence of occupancy due to well-separated capillary pressure curves is obeyed, without being concerned with access pathways to any of the systems, as stated in the introduction. This is tantamount to well-separated characteristic pore sizes for the three systems, each of them having a reasonably broad distribution that doesn't overlap measurably, and also having length scales such that each successively smaller-size systems' network appears to contain a sufficiently large number of pores that a system spanning path within it may be formed by an invading phase at nearly zero saturation of it. The reverse problem of estimating the saturation in each of the three pore systems and, consequently, the saturation in the whole rock given the conductivity cannot be solved uniquely unless some additional information is brought to bear.

PETROPHYSICAL CONSISTENCY

The preceding discussions provide a method to calculate the conductivity of a partially saturated rock. They do not stipulate how the saturation in the different pore systems may be quantitatively related, other than stating that capillary equilibrium must be taken into account. We propose to apply petrophysical insights in determining the order of desaturation and resaturation of the pore systems for estimating pore-component saturations, including when wettability changes may affect occupancy sequence. These insights relate to the individual pore-system saturations such that, at any point in the reservoir, only one pore system is undergoing a change in saturation, and the other two pore systems are automatically defined.

Formations laid down in marine environments are water-wet at least prior to hydrocarbon accumulation (Masalmeh and Oedai, 2011). Hence, the initial emplacement of hydrocarbons occurs under water-wet conditions, and the nonwetting fluid enters vugs, intergranular pores, and

intragranular pores, in that sequence (Robin, 2001). For practical purposes, it is reasonable to assume that the pore sizes are well separated in the three pore systems (any overlap is marginal), and therefore intrusion of one pore system occurs only after the displacement process completes in the larger pore system.

The separation of occupancy sequence into each class of pore system is justifiable if the pore sizes are well separated that the capillary pressure curves do not overlap. To see that this is reasonably founded, let us start with vugs having a size at least equal to that of a grain consisting of a large number of intragranular particles. Thus, the vug radius is much larger than that of intragranular particles, and therefore, intragranular pores. Now, the separation between grains is that of the intergranular pore, whose length scale is a fraction of a grain size for a reasonable packing without significant deformation of the grains. Now, even with 100 particles within a grain and a 0.2 porosity for the grain, the grain radius is about eight times larger than that of the particle. Thus, the characteristic intraparticle pore size is expected to be about eight times smaller than that of the characteristic intergranular pore. Size separation within the three-pore system, an assumption of our model and a common occurrence in several major Middle East carbonates, assures us that in drainage, invasion of hydrocarbon is mostly sequential.

The sequence of aqueous phase reentry may be complicated by wettability changes due to hydrocarbon presence, particularly those with acidic components whose chemical structures facilitate contact angle change following extraction into the aqueous phase (Fathi et al., 2011). In a transition zone, where hydrocarbon migration is incomplete, the medium could be mixed-wet, further complicating the occupancy sequence. Strict reversal of occupancy in pore systems with separated length scales is applicable when no wettability change is induced by the hydrocarbon components.

For practical applications, we can impose a threshold hydrocarbon saturation (set at 50% in the current implementation) within any given pore system before we consider that pore system being altered to oil-wet. For instance, if intergranular pores have been saturated with oil and the intragranular pores remain more than 50% water filled, then the former is changed to oil-wet while the latter remains water-wet, and the entire system is said to be mixed-wet. This is a specific case of mixed-wet. Pore-fluid replacement during water intrusion occurs by first displacing oil from the intragranular pores followed by oil displacement in the vugs and, finally, the intergranular pores. No phase replacement consideration is needed for intragranular pores if there has been no entry of hydrocarbon during drainage.

It must be emphasized that wettability alteration is also dependent on the nature of the rock and the hydrocarbon. For example, a dry gas reservoir may remain water-wet, even at high-gas saturations. Core studies performed on reservoir rock samples using hydrocarbons from the field should guide to confirm assumptions of wettability change. In our implementation, the user provides the wettability logical parameter for allowing wettability assessment at a user-defined threshold pore-component saturation.

The wettability assessment does not aim to determine the actual contact angle, only whether the rock is water-wet (contact angle < 90°) or oil-wet (contact angle > 90°). This is because our interest is only to determine the accessing sequence to each pore system.

PRIMARY DRAINAGE

For implementation, we propose a sequential application of the R-R model. Let us consider the primary drainage cycle first. For the deep-resistivity tool, measuring R_t, the reservoir is deemed to be under primary drainage, i.e., represents the uninvaded resistivity away from the borehole. The condition of primary drainage in the undisturbed region is not a limitation of the R-R model; it is just specific to the implementation discussed in this paper.

The method involves estimating the conductivity of the water-filled formation (R_0) followed by the conductivity at the end of fill of each pore system in order of vugs, then intergranular pores, and, finally, intragranular pores. Each pore system only fills to its residual water saturation (S_{wr}). Though not required, in our current implementation, S_{wr} in vugs is assumed zero (Petricola et al., 2001). Similarly, based on scale invariance, S_{wr} is the same for both the intergranular and intragranular systems, though this assumption may be removed. Benchmark conductivities are computed at the maximum hydrocarbon saturation of each pore system:

- R_{vHC}: vugs filled with hydrocarbon, rest brine
- R_{mHC}: intergranular porosity filled with hydrocarbon to S_{wr}; intragranular has brine
- $R_{\mu HC}$: intragranular porosity also filled with hydrocarbon to S_{wr}

These form the thresholds for determining the pore systems that have been drained by the hydrocarbon. The measured resistivity, R_t, is compared to each of the above to determine the smallest pore system containing hydrocarbon and its extent of drainage.

If $R_0 \le R_t < R_{vHC}$, the vugs are partly filled with hydrocarbon, while both intergranular porosity and intragranular porosity remain water filled ($S_{wm} = 1$; $S_{w\mu} = 1$). Eqs. 2 and 4 provide the intrinsic conductivity of the water-filled intra-interhost medium, $\sigma_{0\mu m}$. Then, Eq. 11 is used to compute the saturation in the vugs. The total water saturation, S_{wt}, is given by:

$$S_{wt} = \frac{S_{wv}V_v + S_{wm}V_m + S_{w\mu}V_\mu}{\phi} \quad (12)$$

If $R_{vHC} \le R_t < R_{mHC}$, then vugs are oil filled, intragranular pores are water filled, and intergranular pores are partly drained. $S_{wv} = 0$, $S_{w\mu} = 1$. The conductivity of the microporous grains is computed from Eq. 2. The intrinsic conductivity of the host (intra+intergranular) medium to vugs is computed from Eq. 10. The saturation in the intergranular pores is obtained from Eq. 8. The total water saturation, S_{wt}, is given by Eq. 12.

If $R_{mHC} \le R_t < R_{\mu HC}$, then vugs are oil filled, and intergranular pores are drained to S_{wr}. Intragranular pores are partly drained. $S_{wv} = 0$, $S_{wm} = S_{wr}$. The intrinsic conductivity of the host medium is computed from Eq. 10. The conductivity of the microporous grains can be computed from Eq. 8. The saturation in the intragranular pores can then be calculated from Eq. 7. S_{wt} is computed from Eq. 12 as before.

In summary, knowing the cutoff resistivities for complete drainage into each system and comparing the measured resistivity to R_t to the cutoffs enables us to obtain the system that is partially filled and sequentially solve for saturation in the partially filled system and the total saturation.

WATER INTRUSION

In the case of a hydrocarbon-bearing formation intersected by a borehole drilled with water-based mud, the invaded zone resembles a waterflood. The shallow R_{xo} log is expected to represent the flushed zone resistivity and is used to compute the flushed zone saturation, S_{xot}, and, therefore, the remaining oil saturation = $1 - S_{xot}$.

The waterflood cycle must account for the wettability state of the rock. Based on prior studies to determine whether the formations are altered to oil-wet after drainage, we facilitate accounting for changed wettability through the wettability logical parameter. This is used within each pore system provided a threshold hydrocarbon saturation is exceeded within that system. When the waterflood is complete in any given pore system, the saturation in that system reaches the residual oil saturation, S_{or}, for that system, which varies with the initial oil saturation and the maximum S_{or} (denoted S_{orM}) possible for that system. A form of such a relationship is due to Land (1968) and is applicable for water-wet media. For any wettability, the functional form may differ, but a dependency is expected. For the present, we apply this relationship, noting that it may be readily replaced by any other function, if empirically known.

The processing approach for the waterflood is very similar to that for drainage after the wettability state is defined—water-wet, mixed-wet, or oil-wet—which, in turn, defines the sequence in which each pore system gets flooded. For water-wet media, the sequence of waterflood is first intragranular, followed by intergranular, and finally vugs. In the case of oil-wet, the sequence is first vugs, followed by intergranular, and finally intragranular pores. The mixed-wet case is invoked specifically for intragranular pores remaining water-wet, while the intergranular pores and vugs become oil-wet. The sequence, in this case, is first intragranular pores, then vugs, and finally intergranular pores, in accordance with the progressive increase in water pressure in comparison to oil pressure. Capillary equilibrium, along with the direction of phase pressure difference, dictates the sequence.

An initial benchmark invaded zone rock resistivity, R_{inv0}, is computed for the rock at the identical saturation state as at the end of drainage, but with the replacement of the formation water salinity with that of mud filtrate. This represents the start of saturation change during the waterflood. As in drainage, benchmark total rock resistivities are determined at each limit of flood of the pore system—R_{inv1}, R_{inv2}, and R_{inv3}—with the subscripts 1, 2, or 3 representing the first, second, and last pore system to be flooded during the waterflood. The specific sequence is dependent on the wettability state at the end of drainage. The measured flushed zone resistivity is compared to the benchmarks to decide the stage of intrusion within the pore systems and identify the unflooded ones. Saturation at its flood completion is the S_{or} for that system. For the pore system not affected by the waterflood, only the formation water is replaced by the mud filtrate without any change in the saturation. The saturation, S_{xo}, for the system undergoing flood is calculated from the corresponding partial saturation equation for that pore system (Eq. 7, 8, or 11). After the individual pore-system saturation is defined, the total flushed zone water saturation, S_{xot}, is computed as

$$S_{xot} = \frac{S_{xov}V_v + S_{xom}V_m + S_{xo\mu}V_\mu}{\phi} \quad (13)$$

A detailed description of the implementation for both drainage and waterflood is provided in Appendix 1.

RESISTIVITY INDEX MODELING RESULTS

Our model was used to compute the resistivity index for various combinations of pore-component fractions in drainage and water intrusion cycles and changed wettability. For complete drainage, in each case, hydrocarbon intrusion proceeds until the rock is at residual water saturation progressively in each pore system from vugs to intragranular, in that order. Similarly, waterflood intrusion occurs until all pore systems are at their respective residual oil saturation. However, the sequence is dependent on any wettability alteration. When comparing these results to direct measurements on cores, it is important to remember that in the laboratory it is very difficult to achieve high enough capillary pressures to drain intragranular pores to residual water. However, several Middle East carbonate reservoirs have sufficient column height that a significant portion of the grain porosity is filled with hydrocarbon near the crest of the structure; therefore, the models heretofore are deemed to be representative of conditions in the reservoir.

Figures 4 through 7 present the results of the modeling. In each case, the following parameters are assumed:

- n for inter- and intragranular pores = 2
- S_{wr} in micropores and macropores = 0.05
- S_{orM} for all three pore systems = 0.3
- m for inter- and intragranular pores = 1.7

Points for primary drainage are shown in solid black triangles, and those for water intrusion are shown in open triangles (water-wet), open circles (mixed-wet), and open diamonds (oil-wet). The mixed-wet case assumes that the intragranular pores remain water-wet, while the intergranular pores and vugs are altered to oil-wet at the end of drainage. The drainage cycle is assumed to proceed under water-wet conditions in all cases. It is to be noted that the specific mixed-wet case wherein both the intragranular and intergranular pores remain water-wet and the vugs are altered to oil-wet is not separately modeled since the sequence of the waterflood, in this case, is the same as that for water-wet.

Inferences from the computations differ with the phase replacement cycle and are summarized accordingly. Note that we have left the residual oil saturation S_{orM} the same regardless of the wettability, in order to facilitate comparison just due to sequential occupancy difference.

Drainage Cycle Observations

In the presence of vugs, the initial change in resistivity index, RI, follows a trend where the saturation exponent n is close to unity and never exceeds 1.5. The conventional approach of assuming n = 2 will result in a significant increase in the estimated S_w. Since vugs are the first to be filled during hydrocarbon migration, we would expect the effective n close to the oil-water contact (OWC) will be less than 1.5. This has been observed and reported by Griffiths and Carnegie (2006) who compared saturation from resistivity with that from pulsed-neutron logs and concluded that very low values of n are required close to the OWC to match the two estimates (where these rocks were vuggy and/or had significant intergranular porosity).

During drainage of the intergranular pores, effective n ranges from 1.4 to 1.8. Finally, during the drainage of the intragranular pores, the effective n further increases, approaching a value of two. These results are consistent with the observations of Griffiths and Carnegie (2006), who remarked that high in the column and at low-water saturations, the estimates from resistivity and capture cross-section log can be reconciled with $n \approx 2$.

We emphasize that our model does not require the user to modify the intrinsic values of either m or n. The intergranular and intragranular m is set based on measurements on micritic homogenous core samples from the same formation (Ramakrishnan et al., 1998). Alternately, it can be set based on the minimum m measured on a large set of core samples from across the reservoir or formation. Another reliable input for this parameter is from a water zone with known formation water resistivity and porosity and reliable R_t log. The intergranular m can be calibrated, such that the modeled m matches that estimated from the resistivity log.

Waterflood Cycle Observations

The behavior during waterflood is very different for each of the three cases—water-wet, oil-wet, and mixed-wet. Negligible hysteresis is observed if rock remains water-wet after oil migration. Hysteresis is larger for mixed-wet and is pronounced for oil-wet rocks. This is in line with observations in the field. The magnitude of hysteresis increases with V_v. We observe that the effective n during waterflood can exceed a value of three for mixed-wet and oil-wet rocks.

Hysteresis has implications for the estimation of the flushed zone saturation. The difference between oil saturation in the undisturbed zone and that in the flushed zone is the moved hydrocarbon, and it is a measure of the recoverable reserves in the rock. Using an incorrect n of two will result in too high a hydrocarbon saturation in the flushed zone and, consequently, too low an estimate of moved hydrocarbon (Lalanne et al., 2010). Hence, by automatic adjustment of the effective n to lower values during drainage and higher values during waterflood, an increase in moved hydrocarbon is expected.

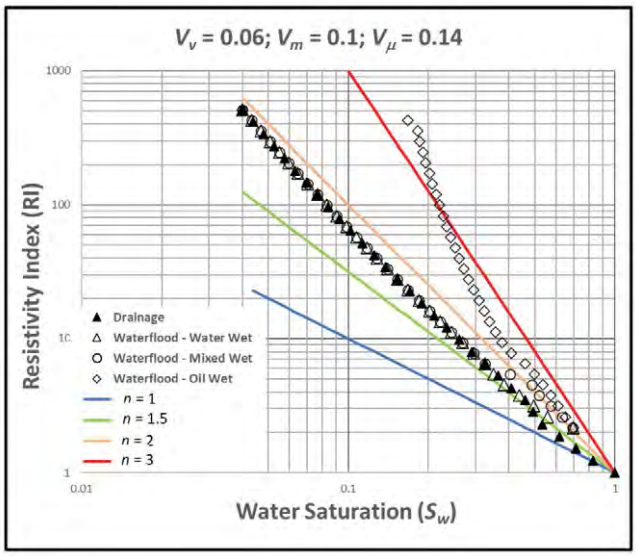

Fig. 4—RI modeling results for carbonate rock with 6-p.u. vugs, 10-p.u. macropores, and 14-p.u. micropores.

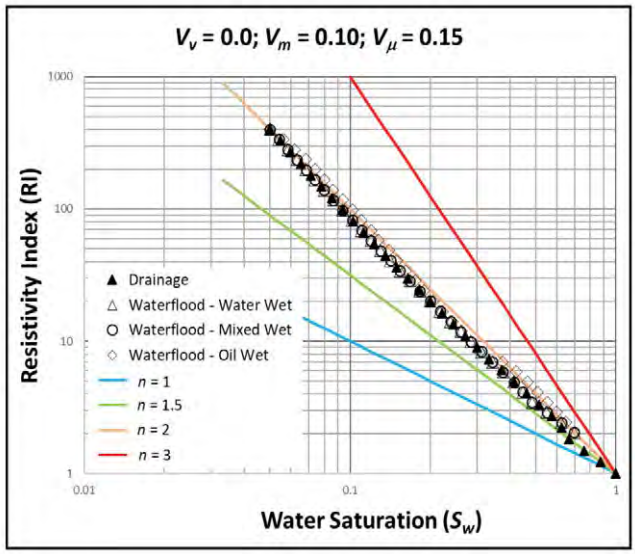

Fig. 6—RI modeling results for carbonate rock without vugs.

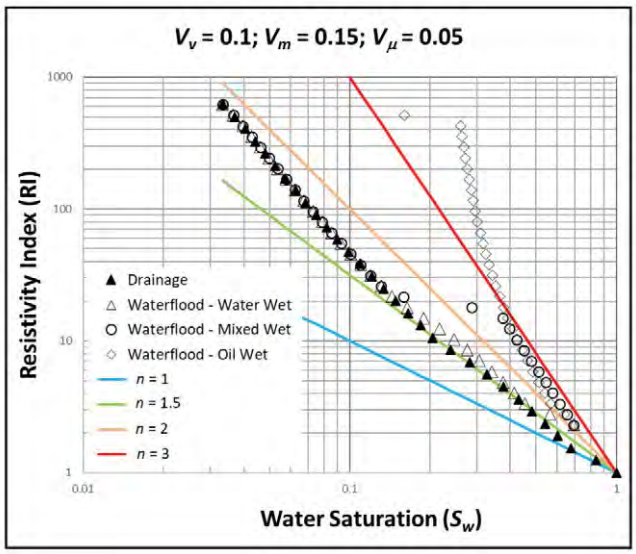

Fig. 5—RI modeling results for carbonate rock. Intergranular porosity and vug fractions increased at the expense of intragranular porosity compared to that in Fig. 4.

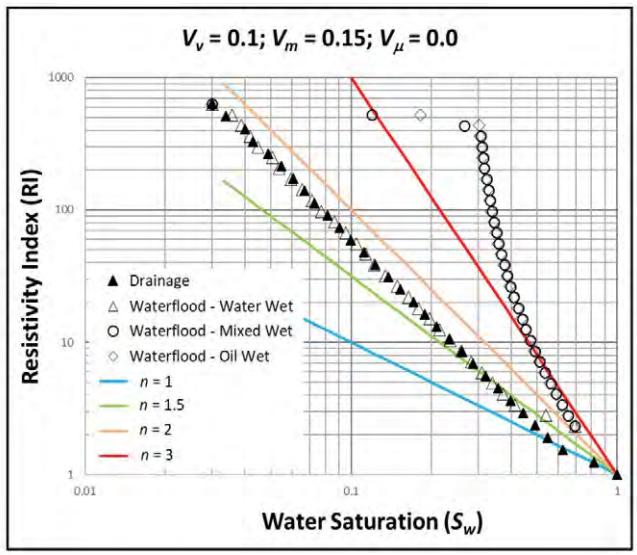

Fig. 7—RI modeling results for carbonate rock with negligible microporosity.

APPLICATION TO WELL-LOG DATA

The algorithm was tested on several wells from Middle East reservoirs. In each case, it is assumed that the formation and crude properties enable the wettability to change from water-wet to oil-wet in the pore systems accessed by oil by more than 50% in pore volume.

As can be seen, in addition to parameters that would be required for a typical Archie saturation computation, the algorithm requires just a few additional parameters:

- Pore-partition volume fractions
- Residual water saturation, S_{wr}
- Maximum residual oil saturation, S_{orM}
- Wettability logical parameter: Default is zero and implies no wettability alteration; one if adequate presence of crude alters wettability.

Table 1—Listing of User Inputs and Computation Outputs

Inputs for Calculating Water Resistivity	
Formation temperature	Provided as a log input
Formation water salinity	Parameter
Mud filtrate salinity	Parameter
Inputs for Model Calculations	
Vug porosity, V_v	Log Input
Intergranular porosity, V_m	Log Input
Intragranular porosity, V_μ	Log Input
R_t	Log Input
R_{xo}	Log Input
Intergranular *m*	Parameter (Default=1.7)
Intergranular *n*	Parameter (Default=2)
S_{wr}	Parameter (Default=0.1)
S_{orM}	Parameter (Default=0.3)
Wettability	0 or 1
Outputs	
Auxiliary outputs	R_w , R_{mf}, Bruggeman m
Drainage benchmarks	R_0, R_{vHC} , R_{mHC} , $R_{\mu HC}$
Water intrusion benchmarks	R_{inv0}, R_{inv1}, R_{inv2}, R_{inv3}
Pore system saturations	S_{wt}, S_{wv}, S_{wm}, $S_{w\mu}$ S_{xot}, S_{xov}, S_{xom}, $S_{xo\mu}$

Table 1 provides a listing of all user inputs and program outputs. Inputs may be either zoned parameters or log channels.

EXAMPLE 1: MIDDLE EAST WELL 1

Because a key input to the new model is the apportioning of porosity, we compare the processed results against available core data. Figure 8 displays results from log processing on a Middle East well 1 (MEW-1). The interval shown is an oil-bearing Cretaceous carbonate. Borehole NMR and electrical images were combined to generate the partitions from logs. The Ramakrishnan et al. (2001) model is used to generate the log-derived *m* from the partitions. There is only one user-defined input, the intergranular *m*, and this is usually determined based on measurements on homogenous micritic samples (Ramakrishnan et al., 1998). However, it may also be tuned based on the match to the entire set of samples. For the present example, m = 1.7 best matches the core measurements. This value is also reasonable from local knowledge. Core partitions were generated from high-pressure mercury injection measurements. Associated plugs at the same depth were measured for formation resistivity factor and Archie *m* exponent. Core measurements are performed on samples around 1 in. in diameter and no more than 1½ in. in length, whereas log measurements scan a volume of the formation of approximately 1 ft^3 in the region adjacent to the borehole; therefore, the correspondence between the two sets of measurements is acceptable.

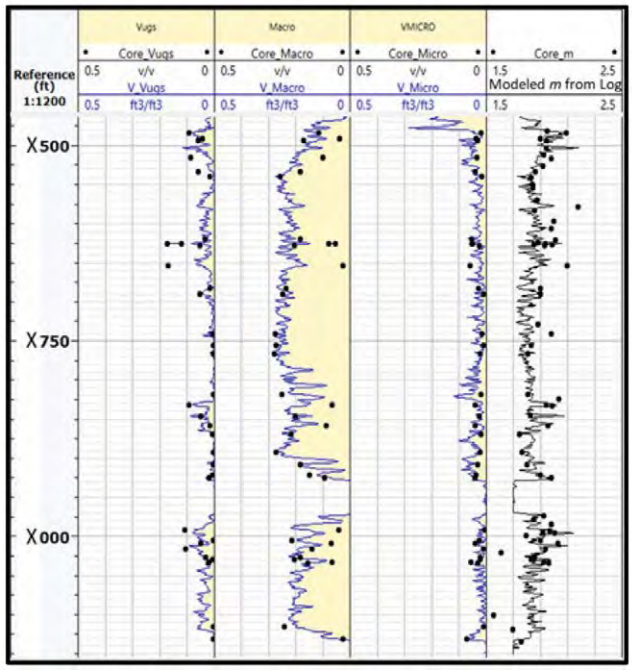

Fig. 8—Comparison of partitions and Archie porosity exponent against measurements on core on MEW-1. Micro and macro imply intragranular and intergranular, respectively.

For our initial attempt, we have set both S_{wr} and S_{orM} to 0.1. The results are displayed in Fig. 9. Track 2 displays the overlay of the R_t log with the drainage benchmarks. Track 3 displays the overlay of the R_{xo} log with the benchmarks from the water-intrusion cycle. There is a water zone at the base of the lower formation. The match between R_t and R_0 confirms the value of R_w used for processing. Likewise, the match between R_{xo} and R_{inv3} confirms the value of R_{mf} used in the processing.

In the zone highlighted by the orange rectangle, we observe that the R_t log reads higher than the benchmark $R_{\mu HC}$. Given that the latter represents the maximum expected resistivity of the formation, the mismatch implies an error in the input parameters. Most likely, the value of S_{wr} is too high and needs to be adjusted.

Likewise, the cyan rectangle highlights a systematic difference between the benchmark R_{inv3} and the R_{xo} log. Such a consistent separation points to a parameter error—most likely S_{orM}. The value will need to be increased to improve the match.

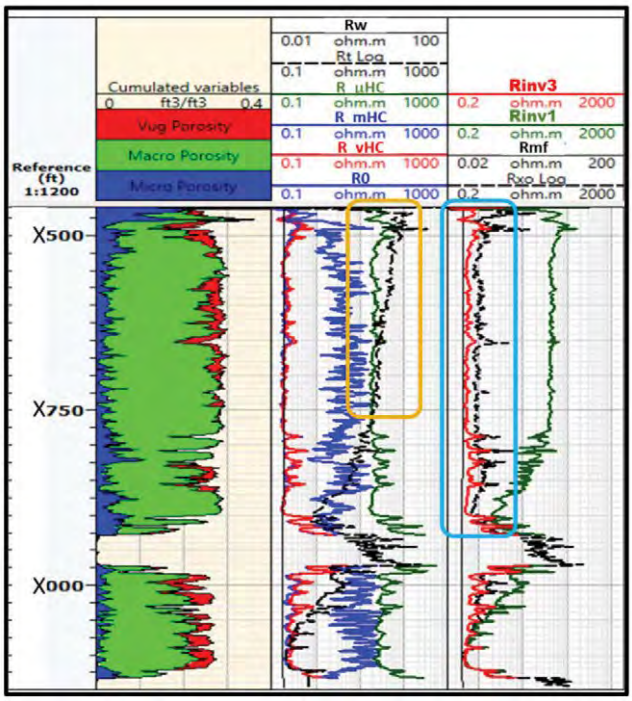

Fig. 9—Results for initial processing of data from MEW-1 using S_{wr} = S_{or}(max) = 0.1, n = 2, and R_w and R_{mf} set from local knowledge. Macro implies intergranular, and micro is synonymous with intragranular.

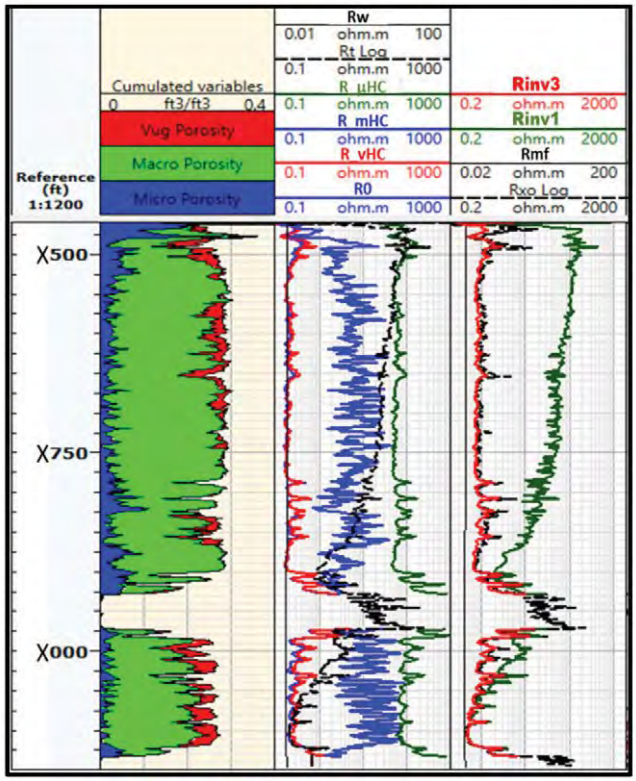

Fig. 10—Results on MEW-1 using refined parameters for S_{or_max} and S_{wr}.

Processing was repeated with S_{wr} = 0.06 and S_{orM} = 0.25. Figure 10 shows the results on the resistivity overlays. The R_t log overlaps with $R_{\mu HC}$ at the top of the logged interval. There is also a better match between the R_{xo} log and the R_{inv3} over the entire interval. Both of the adjusted S_{wr} and S_{orM} parameters are important for reservoir simulation. This is a very valuable output from our model.

Figure 11 displays the computed saturation results from our model and compares that to the saturation computed using Archie's equation with n = 2 and Bruggeman m.

Tracks 2 and 3 present the comparison. To the left of Track 2, we present the difference between the two S_w estimates—Archie S_w and the present model S_w. A positive difference is when our model predicts a higher oil saturation. While both estimates are nearly identical towards the top of the column, lower down in the transition zone, our model predicts 5 to 10 saturation units' higher oil saturation. This is consistent with the RI behavior observed in the previous section. Track 3 displays the comparison of S_{xo}. The difference log this time is $S_{xo\text{—model}} - S_{xo\text{—Archie}}$. A positive difference indicates lower oil saturation in our model results. We observe there is 2 to 5 saturation units' difference over most of the reservoir interval. The moved oil is shown by the shaded region in Track 4 (Archie) and Track 5 (present model). More moved oil is seen in the results of our model.

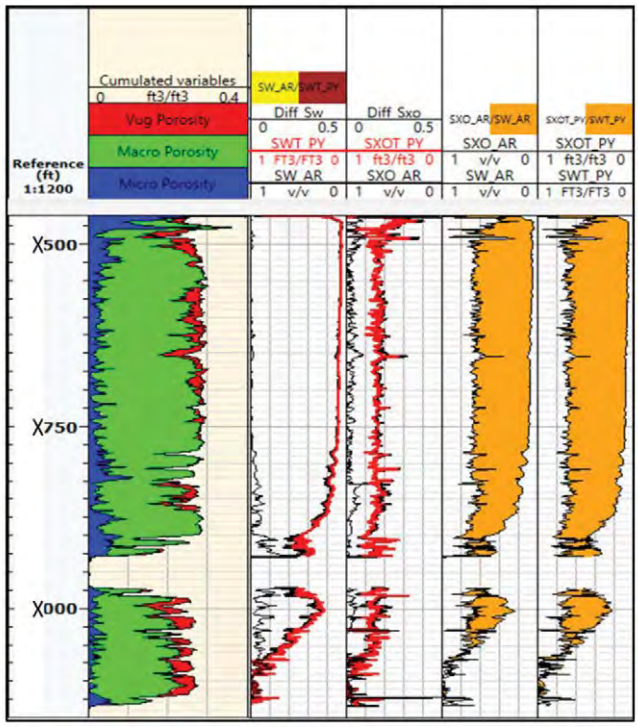

Fig. 11—Final results on MEW-1 comparing saturation from our model with that using Archie's equation with n = 2 and Bruggeman m.

EXAMPLE 2: MIDDLE EAST WELL 2

Our second case study is of a well drilled with oil-based mud (OBM). Several logs were recorded on wireline, such as array induction, epithermal neutron, triple-detector density, and NMR. Due to the presence of the OBM filtrate and formation hydrocarbon within the volume investigated by the NMR tool, we were unable to use the NMR data directly for pore partitioning. Fortunately, just 70 m away, a parallel well was drilled using water-based mud, and excellent NMR data were recorded on this well. Using the porosity log as guidance, we mapped the relative proportions of vugs and intergranular and intragranular porosity onto this well. Although this is not a substitute for direct measurement, it is an acceptable approach given the expected lateral variation of properties in the reservoir and the proximity of the two wells. Substantial vug porosity is present over the reservoir interval. The epithermal neutron tool also makes a shallow measurement of the thermal neutron-capture cross section (Σ) and is therefore affected by changes induced by invasion from the borehole fluid.

Figure 12 presents the data and results on well MEW-2. The array induction data are shown in Track 3 where the resistivity measurement at five depths of investigation (DOI) are shown. The shallowest and deepest have a nominal DOI of 10 in. (0.25 m) and 90 in. (2.29 m), respectively. Two intervals are highlighted. In the orange-shaded interval, the 90-in. log (red) reads less than the 10-in. log (green), indicating that the oil from the OBM is displacing water and increasing the resistivity in the vicinity of the borehole.

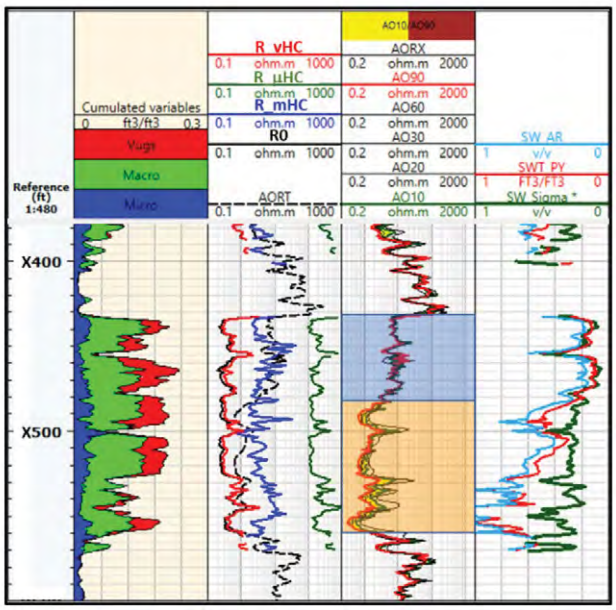

Fig. 12—Data and results on well MEW-2.

In the blue-shaded interval, all five resistivity curves stack on top of each other. This implies there is no change in resistivity, and consequently, saturation, from shallow to deep. Hence, the saturation estimated from the Σ log is an accurate measure of formation water saturation.

Track 2 displays the R_t log along with the four benchmark resistivities of the drainage cycle. Over the orange-shaded interval, $R_t < R_{mHC}$ implying that there is still mobile water between grains. This explains the presence of invasion over this interval. On the blue-shaded interval, $R_t > R_{mHC}$ implying intergranular pores to be at S_{wr} and oil drainage now occurring in intragranular pores, possibly with minimal invasion consequence. This is consistent with the five overlapping resistivity curves over this interval.

Track 4 displays S_w computed using our model (red curve). We have also presented the S_w using the Archie equation, applying the Bruggeman m and a constant n equal to two (cyan curve). The S_w computed from the Σ log is presented in green. Over the orange-shaded interval, the S_w from Σ reads substantially less than that from resistivity. This is due to the presence of the invading oil from the OBM in the vicinity of the borehole. Over the blue-shaded interval, the S_w from Σ precisely overlays that computed from resistivity using our model, whereas that using conventional Archie is reading nearly 10 saturation units higher. The match between the saturation from Σ and our model supports our method.

EXAMPLE 3: MIDDLE EAST WELL 3

The third well is interesting for several reasons. The only resistivity log acquired on the displayed interval is an LWD measurement. Hence, we do not have any inference of S_{xo}. Furthermore, there is very little vug porosity observed on the wireline NMR log, unlike the first two examples. The short reservoir interval includes a water leg over the bottom third of the interval logged.

Although there is no laboratory validation on the same well for the estimated porosity partitions, we have used parameters calibrated from NMR logs and core from nearby wells over the same formation.

Figure 13 presents the results of the use of our model on the data of this well. The resistivity overlay in Track 2 indicates that the section is in the transition zone, even at the top of the reservoir. The water zone is located below X750 ft. Intergranular porosity is filled to S_{wr} above X710 ft where the deep resistivity crosses the benchmark R_{mHC}. From this depth to the top of the layer, the grains remain mostly water filled, whereas the intergranular porosity is hydrocarbon filled to S_{wr}. Given that there is typically a factor of 10 to a 100 difference between the permeability of the intergranular

network and that of the grain, the well should produce with low to negligible water cut in the interval above X710 ft. This is an important insight that is available from our model that influences completion design. The water saturation estimate from our model is less than that from conventional Archie by 5 to 10 saturation units affecting resources and reserves. Such a difference in saturation is possible, even without vugs.

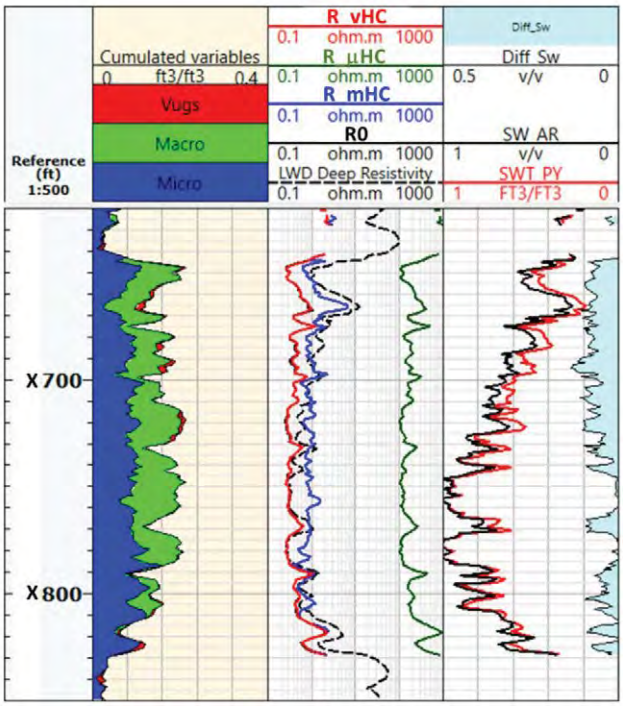

Fig. 13—Results from LWD deep resistivity processing on well MEW-3. Macro and micro designations for intergranular and intragranular pore systems.

MODEL CONSIDERATIONS AND LIMITATIONS

For this, we look at two aspects—the model itself and the implementation discussed here in this paper. The R-R model is expected to have wide applicability across a majority of the Middle East carbonate reservoirs. However, the model does not account for fractures, but may still be applied to characterize the matrix block between the fractures provided the vertical interval exceeds tool resolution. In low-porosity carbonates, fractures tend to be more prevalent, and therefore, any resistivity interpretation should be judiciously applied in conjunction with borehole image analysis. Also, the current model does not account for the effect of clays. In most Middle East carbonates, this is not a limitation.

Our examples assume that the R_t log is an accurate measure of the resistivity of the rock under primary drainage after migration of the hydrocarbon into the reservoir. This is not the case when the rock has been subject to production and is subjected to water encroachment or when the invasion is deep.

The current treatment of the R_{xo} log as a measurement of the rock after waterflood due to the invading mud filtrate is not applicable in wells drilled with OBM. In such wells, the rock is being further drained in the invaded region, and the drainage logic should be applied for the computation of S_{xo}. This also assumes that the invading fluid does not alter the wettability over the time scale of the invasion to measurement interval.

GUIDANCE FOR MODEL-SPECIFIC INPUTS

Our model requires some additional inputs to those required for the application of Archie's equation in saturation evaluation. These are:

- Porosity partitions: V_v, V_m, V_μ
- Intergranular porosity exponent, m
- Residual water saturation, S_{wr}
- Maximum residual oil saturation, S_{orM}
- Wettability logical parameter

The following discussions provide guidance for parameter assignment.

Pore Partitions

NMR logs recorded in water-based mud are recommended for providing this input. Since the partitions represent a specific topological arrangement, they should be verified through optical and SEM petrography on core samples acquired on the same borehole as the NMR log. Such an arrangement should be confirmed on at least one well in the same formation, after which the approach may be applied on other wells. More appropriately, a facies-dependent NMR interpretation is recommended (Ramakrishnan et al., 1999 and Fordham et al., 1999). Recent advances in image logs for OBM wells and in understanding NMR data in the presence of hydrocarbons (Machado et al., 2011; Cao Minh et al., 2016) indicate that it is possible to determine the pore partitions, even in such environments.

In the absence of borehole NMR data on the target well or other log-derived input to pore partitions, an estimate may be obtained from surrounding correlatable wells. While several assumptions underly such an approach and is not as reliable as data directly measured on the well, the industry has for several decades made the same assumptions when applying layer-based Archie parameters in their evaluation of well-log data.

Intergranular *m*

The model requires the user to specify the Archie porosity exponent for unimodal intergranular porosity. Ideally, this should be measured on a homogenous micritic sample. Typically, this will also be the minimum *m* observed on a diverse set of samples taken from the same formation under the same overburden stress (Ramakrishnan et al., 1998). The assumption here is that at least a few of the samples are uniform (unimodal pore-size distribution). It is also very easy to tune this parameter so that the log-derived Bruggeman *m* best matches that measured on core across the formation interval.

Residual Water Saturation, S_{wr}

This parameter is typically determined from high-capillary pressure oil-brine porous plate measurement on the core. Given that it is very challenging to achieve sufficient capillary pressure in the laboratory with existing porous plates to desaturate the microporous grains to S_{wr}, it is best to determine this parameter from sample inlet images during drainage experiments at high enough injection pressure, without violating the low-capillary number limit, best achieved having sufficiently long core samples.

Where there is sufficient column height in the reservoir to fully desaturate the micropores, as in Example 1, it is possible to tune this parameter through the match between the measured R_t and the drainage benchmark $R_{\mu HC}$.

Maximum Residual Oil Saturation, S_{orM}

This parameter is again best determined from coreflood experiments in the laboratory on homogenous unimodal intergranular rock. As seen in Example 1, it is also possible to tune this parameter through the match between the R_{xo} log and the waterflood benchmark R_{inv3} in a hydrocarbon zone. In some instances, for water-wet rocks, this parameter for vugs may need to be set to unity.

Wettability

The current implementation of the model requires the user to stipulate whether the formation is expected to alter wettability to oil-wet. The parameter takes one of two logical values: for example, zero implies that the rock remains water-wet, and one implies that the pore system changes to oil-wet when hydrocarbon saturation exceeds a threshold (in our examples set to 50%).

CONCLUSIONS AND RECOMMENDATIONS

The new model addresses the challenges to resistivity-based saturation evaluation in carbonates for reserves estimation. Our homogenization model for microporous carbonates explains the perceived enhanced conductivity; this model has been validated by core data and is consistent with downhole pulsed-neutron logs. Additional inputs, when compared to a conventional Archie interpretation, are volume fractions of pore-system components and are obtained from logs such as NMR, acoustics, and borehole images. Our approach also honors phase replacement physics for drainage and invasion and accounts for wettability. Saturation within the pore system is provided as a result and is expected to aid completion decisions on the well.

ACKNOWLEDGMENTS

The authors would like to thank Schlumberger for encouraging the work and providing the Techlog software platform to test the algorithms on log data. We also thank D.A. Boyd for his encouragement and comments.

NOMENCLATURE

Abbreviations

NMR = nuclear magnetic resonance
R-R model = Raghu-Ramakrishnan model
RI = resistivity index
SEM = scanning electron microscope

Symbols

I = resistivity index; unitless
L = characteristic length in pore units
m = Archie porosity exponent; unitless
n = Archie saturation exponent; unitless
β = percolation probability exponent
υ = percolation correlation length exponent
ϕ = porosity; fraction
R = resistivity; ohm.m
σ = conductivity; mS/m
S = saturation; fraction
Σ = thermal neutron-capture cross section; barn
V = volume fraction

Subscripts

c = connate
g = grain
inv = invaded or flushed zone
HC = hydrocarbon (used in benchmarks)
mf = mud filtrate
m = intergranular (colloquially macro)
M = maximum
μ = intragranular (colloquially micro)
μm = comprising intragranular and intergranular pores
r = residual
t = true or total
v = vugs
w = water or formation water
xo = flushed or invaded
0 = water-filled condition or benchmark 0 state
1 = first pore system
2 = second pore system
3 = third pore system

REFERENCES

Allen, D.F., Boyd, A., Massey, J., Fordham, E.J., Amabeoku, M.O., Kenyon, W.E., and Ward, W.B., 2001, The Practical Application of NMR Logging in Carbonates: 3 Case Studies, Paper K, *Transactions*, *SPWLA 42nd Annual Logging Symposium*, Houston, Texas, USA, 17–20 June.

Archie, G.E., 1942. The Electrical Resistivity Log as an Aid in Determining Some Reservoir Characteristics, Paper SPE-942054, *Petroleum Transactions of AIME*, **146**, 54–62. DOI:10.2118/942054-g.

Archie, G.E., 1952, Classification of Carbonate Reservoir Rocks and Petrophysical Considerations, *AAPG Bulletin*, **36**(2), 218–298. DOI: 10.1306/3D9343F7-16B1-11D7-8645000102C1865D.

Asakura, S., Hitoshi, T., Miwa, M., Kobayashi, O., Suzuki, M., and Nishi, M., 2001, A New Interpretation Model Using Nuclear Magnetic Resonance Log for Micritic Reservoirs, Paper SPE-68084 presented at the SPE Middle East Oil Show, Manama, Bahrain, 17–20 March. DOI: 10.2118/68084-MS.

Asquith, G.B., 1985, *Handbook of Log Evaluation Techniques for Carbonate Reservoirs, Methods in Exploration Series No. 5*, AAPG, Tulsa, Oklahoma, USA. ISBN-13: 978-0891816553.

Brie, A., Johnson, D.L., and Nurmi, R.D., 1985, Effect of Spherical Pores on Sonic and Resistivity Measurements, Paper W, *Transactions*, *SPWLA 26th Annual Logging Symposium*, Dallas, Texas, USA, 17–20 June.

Cao Minh, C., Jain, V., Griffiths, R., and Maggs, D., 2016, NMR T2 Fluid Substitution, Paper X, *Transactions*, *SPWLA 57th Annual Logging Symposium*, Reykjavik, Iceland, 25–29 June.

Chandler, R., Koplik, J., Lerman, K., and Willemsen, J.F., 1982, Capillary Displacement and Percolation in Porous Media, *Journal of Fluid Mechanics*, **119**, 249–267. DOI: 10.1017/S0022112082001335.

Dixon, J.R., and Marek, B.F., 1990, The Effect of Bimodal Pore Size Distribution on Electrical Properties of Some Middle Eastern Limestones, Paper SPE-20601 presented at the SPE 65th Annual Technical Conference and Exhibition, New Orleans, Louisiana, USA, 23–26 September. DOI: 10.2118/20601-MS.

Donaldson, E.C., and Siddiqui, T.K., 1989, Relationship Between the Archie Saturation Exponent and Wettability, Paper SPE-16790, *SPE Formation Evaluation*, **4**(3), 359–362. DOI: 10.2118/16790-PA.

Dunham, R.J., 1962, Classification of Carbonate Rocks According to Depositional Texture, *in* Ham, W.E., editor, *Classification of Carbonate Rocks*, *American Association of Petroleum Geologists Memoir*, 1, 108–121.

Fathi, S.J., Austad, T., and Strand, S., 2011, Water-Based Enhanced Oil Recovery (EOR) by "Smart Water": Optimal Ionic Composition for EOR in Carbonates, *Energy Fuels*, **25**, 5173–5179. DOI:10.1021/ef201019k.

Focke, J.W., and Munn, D., 1987, Cementation Exponents in Middle East Carbonate Reservoirs, SPE-13735, *SPE Formation Evaluations*, **2**(2), 155–167. DOI: 10.2118/13735-PA.

Fordham, E.J., Schwartz, L., Venkataramanan, L., Flaum, M., and Ramakrishnan, T.S., 1999, New Interpretation Methodology Based on Forward Models for NMR in Carbonates, Paper MMM, *Transactions*, *SPWLA Annual Symposium*, Oslo, Norway, 30 May–3 June.

Gomaa, N.M., Azer, S.R., Ouzzane, D.E., Saif, O., Okuyiga, M.O., Allen, D.F., Rose, D., Ramamoorthy, R., and Bize, E., 2006, Case Study of Permeability, Vug Quantification, and Rock Typing in a Complex Carbonate, Paper SPE-102888 presented at the SPE Annual Technical Conference and Exhibition, San Antonio, Texas, USA, 24–27 September. DOI: 10.2118/102888-MS.

Griffiths, R., and Carnegie, A., 2006, Evaluation of Low Resistivity Pay in Carbonates—A Breakthrough, Paper E, *Transactions*, *SPWLA 47th Annual Logging Symposium*, Veracruz, Mexico, 4–7 June.

Keller, G.V., 1953, Effect of Wettability on the Electrical Resistivity of Sand, *Oil & Gas Journal*, **31**(4), 62–65.

Land, C.S., 1968, Calculation of Imbibition Relative Permeability for Two- and Three-Phase Flow From Rock Properties, Paper SPE-1942, *SPE Journal*, **8**(2), 149–156. DOI: 10.2118/1942-PA.

Lalanne, B., Hamon, B., Peltier, S., and Saint-Pierre, A., 2010, A Case of Large Hysteresis on Resistivity Index Values Between Drainage and Imbibition Phases, Paper SCA2010-03 presented at the SCA Annual Symposium, Halifax, Nova Scotia, Canada, 4–7 October.

Landauer, R., 1978, Electrical Conductivity in Inhomogeneous

Media, *in* Electrical Transport and Optical Properties of Inhomogeneous Media, *AIP Conference Proceedings*, **40**, 2–45. URL: https://doi.org/10.1063/1.31150. Accessed August 12, 2020.

Lucia, F.J., 1983, Petrophysical Parameters Estimated From Visual Descriptions of Carbonate Rocks: A Field Classification of Carbonate Pore Space, Paper SPE-10073, *Journal of Petroleum Technology*, **35**(3), 629–637. DOI:10.2118/10073-PA.

Ma, S.M., Ramamoorthy, R., Al-Hajari, A., Kelder, O., and Srivastava, A., 2005, Dynamic Petrophysics – Applications of Time-Lapse Reservoir Monitoring in Saudi Arabia, Paper SPE-95882 presented at the 2005 SPE Annual Technical Conference and Exhibition, Dallas, Texas, USA, 9–12 October. DOI:10.2118/95882-MS.

Machado, V., Frederico, P., Bagueira, R., Boyd, A., Souza, A., Zielinski, L., and Junk, E., 2011, Carbonate Petrophysics in Wells Drilled With Oil-Base Mud, Paper B, *Transactions, SPWLA 52nd Annual Logging Symposium*, Colorado Springs, Colorado, USA, 14–18 May.

Markel, V.A., 2016, Introduction to the Maxwell Garnett Approximation: Tutorial, *Journal of the Optical Society of America A*, **33**(7), 1244–1256. DOI: 10.1364/JOSAA.33.001244.

Masalmeh, S., and Oedai, S., 2011, Oil Mobility in Transition Zones, Paper SCA2000-02 presented at the SCA Annual Symposium, Abu Dhabi, UAE.

Morgan, W.B., and Pirson, S.J., 1964, The Effect of Fractional Wettability on the Archie Saturation Exponent, Paper B, *Transactions, SPWLA 5th Annual Logging Symposium*, Midland, Texas, USA, 13–15 May.

Mungan, N., and Moore, E.J., 1968, Certain Wettability Effects on Electrical Resistivity in Porous Media, Paper PETSOC 68-01-04, *Journal of Canadian Petroleum Technology*, **7**(1), 20–25. DOI:10.2118/68-01-04.

Nugent, W.H., Coates, G.R., and Peebler, R.P., 1978, A New Approach to Carbonate Analysis, Paper O, *Transactions, SPWLA 19th Annual Logging Symposium*, El Paso, Texas, USA, 13–16 June.

Petricola, M.J.C., and Watfa, M., 1995, Effect of Microporosity in Carbonates: Introduction of a Versatile Saturation Equation, Paper SPE-29841 presented at the Middle East Oil Show, Manama, Bahrain, 11–14 March. DOI: 10.2118/29841-MS.

Petricola, M.J.C., Takezaki, H., and Asakura, S., 2002, Saturation Evaluation in Micritic Reservoirs: Raising to the Challenge, Paper 78533-MS presented at the Abu Dhabi International Petroleum Exhibition and Conference, Abu Dhabi, UAE, 13–16 October. DOI:10.2118/78533-MS.

Ramakrishnan, T.S., Rabaute, A., Fordham, E.J., Ramamoorthy, R., Herron, M., Matteson, A., Raghuraman, B., Mahdi, A., Akbar, M., and Kuchuk, F., 1998, A Petrophysical and Petrographic Study of Carbonate Cores From the Thamama Formation, Paper SPE-49502 presented at the 8th Abu Dhabi International Petroleum Exhibition and Conference, Abu Dhabi, UAE. DOI: 10.2118/49502-MS.

Ramakrishnan, T.S., Ramamoorthy, R., Fordham, E., Schwartz, L., Herron, M., Saito, N., and Rabaute, A., 2001, A Model-Based Interpretation Methodology for Evaluating Carbonate Reservoirs, Paper SPE-71704 presented at the SPE Annual Technical Conference and Exhibition, New Orleans, Louisiana, USA, 30 September–3 October. DOI: 10.2118/71704-MS.

Ramakrishnan, T.S., Schwartz, L., Fordham, E., Kenyon, W., and Wilkinson, D.J., 1999, Forward Models for Nuclear Magnetic Resonance in Carbonate Rocks, *The Log Analyst*, **40**(4), 260–270. ISSN: 0024-581X.

Robin, M., 2001, Interfacial Phenomena: Reservoir Wettability in Oil Recovery. Gas Science and Technology, *Revue d'IFP Energies Nouvelles, Institut Francais du Petrole*, **56(**1), 55–62. URL: https://hal-ifp.archives-ouvertes.fr/hal-02053878/document. Accessed August 12, 2020.

Stauffer, D., and Aharony, A., 2018, *Introduction to Percolation Theory*, second edition, CRC Press, London, England. DOI: 10.1201/9781315274386.

Sweeney, S.A., and Jennings, H.Y., Jr., 1960, Effect of Wettability on the Electrical Resistivity of Carbonate Rock From a Petroleum Reservoir, *The Journal of Physical Chemistry*, **64**(5), 551. DOI: 10.1021/j100834a009.

Tsakiroglou, C.D., and Fleury, M., 1999, Resistivity Index of Fractional Wettability Porous Media, *Journal of Petroleum Science and Engineering*, **22**(4), 253–274. DOI: 10.1016/S0920-4105(98)00085-0.

APPENDIX 1: ALGORITHM

Preamble

This appendix provides the detailed workflow and algorithms for the implementation of the Raghu-Ramakrishnan model for partially saturated carbonate rocks.

Relevant Equations

For the convenience of the reader, the relevant equations from the paper are reproduced here for easy reference.

Conductivity of brine-filled grain, σ_{0g}

$$\sigma_{0g} = \sigma_w \phi_\mu^{\,m_\mu}\,, \tag{A1}$$

Computation of Intrinsic intragranular-porosity, ϕ_μ

$$\phi_\mu = \frac{V_\mu}{1-V_v-V_m}\,. \tag{A2}$$

Effective conductivity of intragranular-intergranular host medium, $\sigma_{0\mu m}$

$$\frac{V_m}{1-V_v} = \left(\frac{\sigma_w}{\sigma_{0\mu m}}\right)^{\frac{m_m-1}{m_m}} \left(\frac{\sigma_{0g}-\sigma_{0\mu m}}{\sigma_{0g}-\sigma_w}\right) \tag{A3}$$

Effective conductivity of rock including vugs, σ_0

$$V_v\left(\frac{\sigma_w-\sigma_0}{\sigma_w+2\cdot\sigma_0}\right)+(1-V_v)\left(\frac{\sigma_{0\mu m}-\sigma_0}{\sigma_{0\mu m}+2\cdot\sigma_0}\right)= \quad \text{(A4)}$$

Effective Archie porosity exponent, m

$$m=\frac{\log\frac{\sigma_0}{\sigma_w}}{\log\phi}. \quad \text{(A5)}$$

Conductivity of partially saturated grains, σ_g

$$\sigma_g=\sigma_w S_{w\mu}^{n_\mu}\left(\phi_\mu\right)^{m_\mu} \quad \text{(A6)}$$

Conductivity of partially saturated intragranular-intergranular host medium, $\sigma_{\mu m}$

$$\frac{V_m}{1-V_v}=\left(\frac{\sigma_w S_{wm}^{n_m}}{\sigma_{\mu m}}\right)^{\frac{m_m-1}{m_m}}\left(\frac{\sigma_g-\sigma_{\mu m}}{\sigma_g-\sigma_w S_{wm}^{n_m}}\right) \quad \text{(A7)}$$

Total rock conductivity with oil-filled vugs, σ

$$\sigma=\sigma_{\mu m}\left(1-\frac{3}{2}V_v\right) \quad \text{(A8)}$$

Total rock conductivity with partially filled vugs, σ

$$S_{wv}V_v\left(\frac{\sigma_w-\sigma}{\sigma_w+2\sigma}\right)-\frac{(1-S_{wv})V_v}{2}+(1-V_v)\left(\frac{\sigma_{\mu m}-\sigma}{\sigma_{\mu m}+2\sigma}\right)=0 \quad \text{(A9)}$$

Total undisturbed zone water saturation, S_{wt}

$$S_{wt}=\frac{S_{wv}V_v+S_{wm}V_m+S_{w\mu}V_\mu}{\phi} \quad \text{(A10)}$$

Total flushed zone water saturation, S_{xot}

$$S_{xot}=\frac{S_{xov}V_v+S_{xom}V_m+S_{xo\mu}V_\mu}{\phi} \quad \text{(A11)}$$

Step 1: Computation of Bruggeman *m*

- **a)** From volume fractions, compute ϕ_μ, Eq. A2.
- **b)** Evaluate, σ_{0g}, using Eq. A1.
- **c)** Eq. A3 is used for $\sigma_{0\mu m}$.
- **d)** Water-filled rock, conductivity σ_0, from Eq. A4. Both Eqs. A3 and A4 are implicit for the parameter of interest, and suitable solvers must be used to determine the desired unknown.
- **e)** Bruggeman *m* from Eq. A5.

Step 2: Computation of Drainage Benchmarks

- **a) Benchmark 1:** Water-filled rock resistivity, R_0

$$R_0=\frac{1}{\sigma_0}$$

- **b) Benchmark 2:** Rock resistivity, R_{vHC}, vugs hydrocarbon filled, rest water filled is given by Eq. A8 substituting $\sigma_{0\mu m}$ for $\sigma_{\mu m}$:

$$\sigma_{vHC}=\left(1-\frac{3}{2}V_v\right)\sigma_{0\mu m}$$

$$R_{vHC}=\frac{1}{\sigma_{vHC}}$$

- **c) Benchmark 3:** Rock resistivity, R_{mHC}, vugs hydrocarbon filled, and intergranular pores at S_{wr} and intragranular pores water filled.

Compute σ_{0g} as in step 1b.

Use Eq. A7 substituting σ_{0g} for σ_g and S_{wr} for S_{wm}. Equation is implicit. Solve for $\sigma_{\mu m}$ from

$$\left(\frac{\sigma_{0\mu}-\sigma_{\mu m}}{\sigma_{0\mu}-\sigma_w S_{wr}^n}\right)\left(\frac{\sigma_w S_{wr}^n}{\sigma_{\mu m}}\right)^{\frac{(m-1)}{m}}=\frac{V_m}{(1-V_v)}$$

Compute effective rock conductivity, σ_{mHC}, with the hydrocarbon-filled vugs using Eq. A8.

$$\sigma_{mHC}=\left(1-\frac{3}{2}V_v\right)\sigma_{\mu m}$$

$$R_{mHC}=\frac{1}{\sigma_{mHC}}$$

- **d) Benchmark 4:** Rock resistivity, $R_{\mu HC}$, vugs hydrocarbon filled, and intragranular and intergranular pores are at S_{wr} is computed as follows.

Compute intrinsic conductivity of the microporous grains using Eq. A6 substituting S_{wr} for $S_{w\mu}$.

$$\sigma_g=\sigma_w {S_{wr}}^n {\phi_\mu}^m$$

Use equation A7 substituting S_{wr} for S_{wm}. Equation is implicit. Solve for $\sigma_{\mu m}$.

$$\left(\frac{\sigma_g-\sigma_{\mu m}}{\sigma_g-\sigma_w S_{wr}^n}\right)\left(\frac{\sigma_w S_{wr}^n}{\sigma_{\mu m}}\right)^{\frac{(m-1)}{m}}=\frac{V_m}{(1-V_v)}$$

Compute effective rock conductivity, $\sigma_{\mu HC}$, with the hydrocarbon-filled vugs using Eq. A8 from

$$\sigma_{\mu HC}=\left(1-\frac{3}{2}V_v\right)\sigma_{\mu m}$$

$$R_{\mu HC}=\frac{1}{\sigma_{\mu HC}}$$

Step 3: Compare Benchmark Resistivities and R_t

Case 0: $R_t < R_0$: Error in R_w or Bruggeman m (check pore partitions) or R_t (check the log).

Case 1: $R_0 \le R_t < R_{vHC}$: Hydrocarbon in vugs. Rest remain water filled.

Case 2: $R_{vHC} \le R_t < R_{mHC}$: Hydrocarbon to 100% in vugs. Intergranular has hydrocarbon. Intragranular pores remain water filled.

Case 3: $R_{mHC} \le R_t < R_{\mu HC}$: Hydrocarbon now fills all vugs and intergranular pores now desaturated to S_{wr} and hydrocarbon entering micropores.

Case 4: $R_{\mu HC} < R_t$: Error: S_{wr} may need to be reduced.

Step 4: Compute S_w

a) Case 1:

Intrinsic conductivity of the water-filled host (inter+intragranular) medium, $\sigma_{0\mu m}$, is already computed in step 1c.

Use Eq. A9 to compute S_{wv} substituting $\sigma_{0\mu m}$ for $\sigma_{\mu m}$ and recognizing that $\sigma = \frac{1}{R_t}$.

$$S_{wv}V_v\left(\frac{\sigma_w - \sigma}{\sigma_w + 2\sigma}\right) - \frac{(1 - S_{wv})V_v}{2} + (1 - V_v)\left(\frac{\sigma_{0\mu m} - \sigma}{\sigma_{0\mu m} + 2\sigma}\right) = 0$$

Compute connate oil (denoted by subscript c) and water saturation in each pore system.

$$S_{ocv} = 1 - S_{wv}$$
$$S_{wm} = 1;\ S_{ocm} = 0$$
$$S_{w\mu} = 1;\ S_{oc\mu} = 0$$

S_{wt} is computed using Eq. A10.

b) Case 2:

Intrinsic conductivity of the water-filled intragranular porous grains is already computed in step 1b.

Use Eq. A8 to compute intrinsic conductivity of the host medium, $\sigma_{\mu m}$, given the measured resistivity, R_t, and the vug volume fraction, V_v.

$$\sigma_{\mu m} = \frac{1}{R_t\left(1 - \frac{3}{2}V_v\right)}$$

Use Eq. A7 substituting $\sigma_{0\mu}$ for σ_{μ}. Equation is implicit. Solve for S_{wm}.

$$\left(\frac{\sigma_{0\mu} - \sigma_{\mu m}}{\sigma_{0\mu} - \sigma_w S_{wm}^n}\right)\left(\frac{\sigma_w S_{wm}^n}{\sigma_{\mu m}}\right)^{\frac{(m-1)}{m}} = \frac{V_m}{(1 - V_v)}$$

Compute connate oil and water saturation in each pore system from

$$S_{ocm} = 1 - S_{wm}$$
$$S_{wv} = 0;\ S_{ocv} = 1$$
$$S_{w\mu} = 1;\ S_{oc\mu} = 0$$

S_{wt} is computed using Eq. A10.

c) Case 3:

Intrinsic conductivity of the host medium, $\sigma_{\mu m}$, is computed as in step 4b.

Use Eq. A7 substituting S_{wr} for S_{wm}. Equation is implicit. Solve for σ_{μ}.

$$\left(\frac{\sigma_{\mu} - \sigma_{\mu m}}{\sigma_{\mu} - \sigma_w S_{wr}^n}\right)\left(\frac{\sigma_w S_{wr}^n}{\sigma_{\mu m}}\right)^{\frac{(m-1)}{m}} = \frac{V_m}{(1 - V_v)}$$

Compute intrinsic saturation within the micropores using Eq. A6.

$$S_{w\mu} = \left(\frac{\sigma_{\mu}}{\sigma_w \phi_{\mu}{}^m}\right)^{\frac{1}{n}}$$

Compute connate oil and water saturation in each pore system.

$$S_{oc\mu} = 1 - S_{w\mu}$$
$$S_{wv} = 0;\ S_{ocv} = 1$$
$$S_{wm} = S_{wr};\ S_{ocm} = 1 - S_{wr}$$

S_{wt} is computed using Eq. A10.

Step 5: Precomputations for Waterflood

a) Compute S_{or} for each pore system: For convenience, we have assumed maximum residual oil saturation to be the same in all of the pore systems.

$$C = \frac{(1 - S_{wr})}{S_{orM}} - 1$$
$$S_{oc\mu}^* = \frac{S_{oc\mu}}{1 - S_{wr}}$$
$$S_{ocm}^* = \frac{S_{ocm}}{1 - S_{wr}}$$
$$S_{ocv}^* = S_{ocv}$$
$$S_{or\mu} = \frac{S_{oc\mu}}{1 + CS_{oc\mu}^*}$$
$$S_{orm} = \frac{S_{ocm}}{1 + CS_{ocm}^*}$$
$$S_{orv} = \frac{S_{ocv}}{1 + CS_{ocv}^*}$$

b) Benchmark 0: Rock resistivity, R_{inv0}, after replacing formation water with mud filtrate. No change in saturation from drainage.

Conductivity of microporous grains is given by Eq. A6

$$\sigma_{xo\mu} = \sigma_{mf}\phi_{\mu}{}^{m}S_{w\mu}{}^{n}$$

Conductivity of the composite intragranular-intergranular system, $\sigma_{xo\mu m}$, is from Eq. A7:

$$\left(\frac{\sigma_{xo\mu}-\sigma_{xo\mu m}}{\sigma_{xo\mu}-\sigma_{mf}S_{wm}^{n}}\right)\left(\frac{\sigma_{mf}S_{wm}^{n}}{\sigma_{xo\mu m}}\right)^{\frac{(m-1)}{m}}=\frac{V_m}{(1-V_v)}$$

Rock conductivity, σ_{inv0}, including the vugs, is given by Eq. A9

$$S_{wv}V_v\left(\frac{\sigma_{mf}-\sigma_{inv0}}{\sigma_{mf}+2\sigma_{inv0}}\right)-\frac{(1-S_{wv})V_v}{2}+(1-V_v)\left(\frac{\sigma_{xo\mu m}-\sigma_{inv0}}{\sigma_{xo\mu m}+2\sigma_{inv0}}\right)=0$$

$$R_{inv0}=\frac{1}{\sigma_{inv0}}$$

c) Define wettability state

If wettability = 1, then
If $S_{w\mu}$ < 0.5, then oil-wet,
Else if S_{wm} < 0.5, then mixed-wet,
Else water-wet

Step 6a: Waterflood Computations in Oil-Wet Case
Computation of waterflood benchmarks:

Benchmark 1, R_{inv1}**:** Filtrate imbibition complete into vugs, which are now at S_{or}. Rest unchanged from drainage.

$\sigma_{xo\mu m}$ already computed in Step 5b.

Rock conductivity, σ_{inv1}, including the vugs, is given by Eq. A9

$$(1-S_{orv})V_v\left(\frac{\sigma_{mf}-\sigma_{inv1}}{\sigma_{mf}+2\sigma_{inv1}}\right)-\frac{(S_{orv})V_v}{2}+(1-V_v)\left(\frac{\sigma_{xo\mu m}-\sigma_{inv1}}{\sigma_{xo\mu m}+2\sigma_{inv1}}\right)=0$$

$$R_{inv1}=\frac{1}{\sigma_{inv1}}$$

Benchmark 2, R_{inv2}**:** Filtrate imbibition complete into vugs and intergranular pores, which are now at respective S_{or}, intragranular pores unchanged from drainage.

$\sigma_{xo\mu}$ already computed in Step 5b.

Conductivity of the composite intragranular-intergranular system, $\sigma_{xo\mu m}$, is (Eq. A7)

$$\left(\frac{\sigma_{xo\mu}-\sigma_{xo\mu m}}{\sigma_{xo\mu}-\sigma_{mf}(1-S_{orm})^{n}}\right)\left(\frac{\sigma_{mf}\cdot(1-S_{orm})^{n}}{\sigma_{xo\mu m}}\right)^{\frac{(m-1)}{m}}=\frac{V_m}{(1-V_v)}$$

Rock conductivity, σ_{inv2}, including the vugs, is given by Eq. A9

$$(1-S_{orv})V_v\left(\frac{\sigma_{mf}-\sigma_{inv2}}{\sigma_{mf}+2\sigma_{inv2}}\right)-\frac{(S_{orv})V_v}{2}+(1-V_v)\left(\frac{\sigma_{xo\mu m}-\sigma_{inv2}}{\sigma_{xo\mu m}+2\sigma_{inv2}}\right)=0$$

$$R_{inv2}=\frac{1}{\sigma_{inv2}}$$

Benchmark 3, R_{inv3}**:** Rock conductivity when filtrate imbibition is complete, and rock is at S_{or}.

Conductivity of microporous grains is given by Eq. A6:

$$\sigma_{xo\mu}=\sigma_{mf}\phi_{\mu}{}^{m}\left(1-S_{or\mu}\right)^{n}$$

Conductivity of the composite intragranular-intergranular system, $\sigma_{xo\mu m}$, is given by Eq. A7.

$$\left(\frac{\sigma_{xo\mu}-\sigma_{xo\mu m}}{\sigma_{xo\mu}-\sigma_{mf}(1-S_{orm})^{n}}\right)\left(\frac{\sigma_{mf}(1-S_{orm})^{n}}{\sigma_{xo\mu m}}\right)^{\frac{(m-1)}{m}}=\frac{V_m}{(1-V_v)}$$

Rock conductivity, σ_{inv3}, including the vugs, is derived from Eq. A9.

$$(1-S_{orv})V_v\left(\frac{\sigma_{mf}-\sigma_{inv3}}{\sigma_{mf}+2\sigma_{inv3}}\right)-\frac{(S_{orv})V_v}{2}+(1-V_v)\left(\frac{\sigma_{xo\mu m}-\sigma_{inv3}}{\sigma_{xo\mu m}+2\sigma_{inv3}}\right)=0$$

$$R_{inv3}=\frac{1}{\sigma_{inv3}}$$

Computation of Flushed Zone Saturation:

Case 1: $R_{inv1} < R_{xo}$**:** Water enters vugs. Intragranular pores and intergranular pores remain unchanged from drainage.

Conductivity of microporous grains, $\sigma_{xo\mu}$, is obtained from Eq. A6:

$$\sigma_{xo\mu}=\sigma_{mf}\phi_{\mu}{}^{m}S_{w\mu}{}^{n}$$

Conductivity of the composite intragranular-intergranular system, $\sigma_{xo\mu m}$, is based on Eq. A7 so that

$$\left(\frac{\sigma_{xo\mu}-\sigma_{xo\mu m}}{\sigma_{xo\mu}-\sigma_{mf}S_{wm}^{n}}\right)\left(\frac{\sigma_{mf}S_{wm}^{n}}{\sigma_{xo\mu m}}\right)^{\frac{(m-1)}{m}}=\frac{V_m}{(1-V_v)}$$

The above equation has been provided in its general form, though for the condition of oil-wet, we note that $S_{wm} = S_{wr}$.

Compute saturation in the vugs with Eq. A9 recognizing that $\sigma_{xo}=\frac{1}{R_{xo}}$.

$$S_{xov}V_v\left(\frac{\sigma_{mf}-\sigma_{xo}}{\sigma_{mf}+2\sigma_{xo}}\right)-\frac{(1-S_{xov})V_v}{2}+(1-V_v)\left(\frac{\sigma_{xo\mu m}-\sigma_{xo}}{\sigma_{xo\mu m}+2\sigma_{xo}}\right)=0$$

$$S_{xo\mu}=S_{w\mu}$$

$$S_{xom}=S_{wr}$$

Compute S_{xot} with Eq. A11.

Case 2: $R_{inv2} < R_{xo} < R_{inv1}$**:** Water enters intergranular pores. Intragranular pores are unchanged from drainage. Vugs are at S_{or}.

Conductivity of microporous grains, $\sigma_{xo\mu}$, is given by Eq. A6.

$$\sigma_{xo\mu} = \sigma_{mf}{\phi_\mu}^m {S_{w\mu}}^n$$

Conductivity of the composite intragranular-intergranular system, $\sigma_{xo\mu m}$, is given by Eq. A9 and recognizing that $\sigma_{xo} = \frac{1}{R_{xo}}$.

$$(1 - S_{orv})V_v\left(\frac{\sigma_{mf} - \sigma_{xo}}{\sigma_{mf} + 2\sigma_{xo}}\right) - \frac{(S_{orv})V_v}{2} + (1 - V_v)\left(\frac{\sigma_{xo\mu m} - \sigma_{xo}}{\sigma_{xo\mu m} + 2\sigma_{xo}}\right) = 0$$

Compute saturation in the intergranular pores, S_{xom}, with Eq. A7.

$$\left(\frac{\sigma_{xo\mu} - \sigma_{xo\mu m}}{\sigma_{xo\mu} - \sigma_{mf}S_{xom}^n}\right)\left(\frac{\sigma_{mf}S_{xom}^n}{\sigma_{xo\mu m}}\right)^{\frac{(m-1)}{m}} = \frac{V_m}{(1 - V_v)}$$

$$S_{xo\mu} = S_{w\mu}$$

$$S_{xov} = 1 - S_{orv}$$

Compute S_{xot} with Eq. A11.

Case 3: $R_{inv3} < R_{xo} < R_{inv2}$**:** Water enters intragranular pores. Intergranular pores and vugs at respective S_{or}.

Conductivity of the composite intragranular-intergranular system, $\sigma_{xo\mu m}$, is based on Eq. A9 and recognizing that $\sigma_{xo} = \frac{1}{R_{xo}}$, we have

$$(1 - S_{orv})V_v\left(\frac{\sigma_{mf} - \sigma_{xo}}{\sigma_{mf} + 2\sigma_{xo}}\right) - \frac{(S_{orv})V_v}{2} + (1 - V_v)\left(\frac{\sigma_{xo\mu m} - \sigma_{xo}}{\sigma_{xo\mu m} + 2\sigma_{xo}}\right) = 0$$

Conductivity of microporous grains, $\sigma_{xo\mu}$, is based on Eq. A7:

$$\left(\frac{\sigma_{xo\mu} - \sigma_{xo\mu m}}{\sigma_{xo\mu} - \sigma_{mf}(1 - S_{orm})^n}\right)\left(\frac{\sigma_{mf}(1 - S_{orm})^n}{\sigma_{xo\mu m}}\right)^{\frac{(m-1)}{m}} = \frac{V_m}{(1 - V_v)}$$

Compute saturation in the intragranular pores, $S_{xo\mu}$, with Eq. A6.

$$S_{xo\mu} = \left(\frac{\sigma_{xo\mu}}{\sigma_w{\phi_\mu}^m}\right)^{\frac{1}{n}}$$

$$S_{xom} = 1 - S_{orm}$$

$$S_{xov} = 1 - S_{orv}$$

Compute S_{xot} with Eq. A11.

Step 6b: Waterflood Computations in Mixed-Wet Case

Computation of Waterflood Benchmarks:

Benchmark 1, R_{inv1}**:** Filtrate invasion is complete into intragranular pores down to S_{or}. Rest are unchanged from drainage. Conductivity of microporous grains is given by Eq. A6:

$$\sigma_{xo\mu} = \sigma_{mf}{\phi_\mu}^m\left(1 - S_{or\mu}\right)^n$$

Conductivity of the composite intragranular-intergranular system, $\sigma_{xo\mu m}$, is given by Eq. A7:

$$\left(\frac{\sigma_{xo\mu} - \sigma_{xo\mu m}}{\sigma_{xo\mu} - \sigma_{mf}S_{wm}^n}\right)\left(\frac{\sigma_{mf}S_{wm}^n}{\sigma_{xo\mu m}}\right)^{\frac{(m-1)}{m}} = \frac{V_m}{(1 - V_v)}$$

Rock conductivity, σ_{inv1}, including the vugs, is given by Eq. A9

$$S_{wv}V_v\left(\frac{\sigma_{mf} - \sigma_{inv1}}{\sigma_{mf} + 2\sigma_{inv1}}\right) - \frac{(1 - S_{wv})V_v}{2} + (1 - V_v)\left(\frac{\sigma_{xo\mu m} - \sigma_{inv1}}{\sigma_{xo\mu m} + 2\sigma_{inv1}}\right) = 0$$

The above equation has been provided in its general form, though for the condition of mixed-wet, we note that $S_{wv} = 0$. Hence, Eq. A8 may be used for σ_{inv1}.

$$\sigma_{inv1} = \left(1 - \frac{3}{2}V_v\right)\sigma_{xo\mu m}$$

$$R_{inv1} = \frac{1}{\sigma_{inv1}}$$

Benchmark 2, R_{inv2}**:** Filtrate invasion is complete into intragranular and vugs, which are now at respective S_{or}; intergranular pores unchanged from drainage.

$\sigma_{xo\mu}$ and $\sigma_{xo\mu m}$ are computed as illustrated in the earlier step.

Rock conductivity, σ_{inv2}, including the vugs, is given by Eq. A9

$$(1 - S_{orv})V_v\left(\frac{\sigma_{mf} - \sigma_{inv2}}{\sigma_{mf} + 2\sigma_{inv2}}\right) - \frac{(S_{orv})V_v}{2} + (1 - V_v)\left(\frac{\sigma_{xo\mu m} - \sigma_{inv2}}{\sigma_{xo\mu m} + 2\sigma_{inv2}}\right) = 0$$

$$R_{inv2} = \frac{1}{\sigma_{inv2}}$$

Benchmark 3, R_{inv3}**:** Rock conductivity when filtrate invasion is complete, and rock is at S_{or}. Conductivity of microporous grains, $\sigma_{xo\mu}$, already computed in earlier step. Conductivity of the composite intragranular-intergranular system, $\sigma_{xo\mu m}$, is computed using Eq. A7.

$$\left(\frac{\sigma_{xo\mu} - \sigma_{xo\mu m}}{\sigma_{xo\mu} - \sigma_{mf}(1 - S_{orm})^n}\right)\left(\frac{\sigma_{mf}(1 - S_{orm})^n}{\sigma_{xo\mu m}}\right)^{\frac{(m-1)}{m}} = \frac{V_m}{(1 - V_v)}$$

Rock conductivity, σ_{inv3}, including the vugs, is given by Eq. A9.

$$(1-S_{orv})V_v\left(\frac{\sigma_{mf}-\sigma_{inv3}}{\sigma_{mf}+2\sigma_{inv3}}\right)-\frac{(S_{orv})V_v}{2}+(1-V_v)\left(\frac{\sigma_{xo\mu m}-\sigma_{inv3}}{\sigma_{xo\mu m}+2\sigma_{inv3}}\right)=0$$

$$R_{inv3}=\frac{1}{\sigma_{inv3}}$$

Computation of Flushed Zone Saturation:

Case 1: $R_{inv1} < R_{xo}$**:** Water enters intragranular pores. Vugs and intergranular pores unchanged from drainage.

Conductivity of the composite intragranular-intergranular system, $\sigma_{xo\mu m}$, is from Eq. A8.

$$\sigma_{xo\mu m}=\frac{1}{R_{xo}\left(1-\frac{3}{2}V_v\right)}$$

Conductivity of the grains, $\sigma_{xo\mu}$, is from Eq. A7. Then

$$\left(\frac{\sigma_{xo\mu}-\sigma_{xo\mu m}}{\sigma_{xo\mu}-\sigma_{mf}S_{wm}^n}\right)\left(\frac{\sigma_{mf}S_{wm}^n}{\sigma_{xo\mu m}}\right)^{\frac{(m-1)}{m}}=\frac{V_m}{(1-V_v)}$$

Compute saturation from

$$S_{xo\mu}=\left(\frac{\sigma_{xo\mu}}{\sigma_w{\phi_\mu}^m}\right)^{\frac{1}{n}}$$

$$S_{xov}=0$$

$$S_{xom}=S_{wm}$$

Compute S_{xot} (Eq. A11).

Case 2: $R_{inv2} < R_{xo} < R_{inv1}$**:** Water entering in vugs. Intragranular pores at S_{or}. Intergranular pores unchanged from drainage.

Conductivity of microporous grains, $\sigma_{xo\mu}$, is given by Eq. A6.

$$\sigma_{xo\mu}=\sigma_{mf}{\phi_\mu}^m\left(1-S_{or\mu}\right)^n$$

Conductivity of the composite intragranular-intergranular system, $\sigma_{xo\mu m}$, is given by Eq. A7

$$\left(\frac{\sigma_{xo\mu}-\sigma_{xo\mu m}}{\sigma_{xo\mu}-\sigma_{mf}S_{wm}^n}\right)\left(\frac{\sigma_{mf}S_{wm}^n}{\sigma_{xo\mu m}}\right)^{\frac{(m-1)}{m}}=\frac{V_m}{(1-V_v)}$$

Compute saturation in the vugs, S_{xov}, with Eq. A9 recognizing that $\sigma_{xo}=\frac{1}{R_{xo}}$.

$$S_{xov}V_v\left(\frac{\sigma_{mf}-\sigma_{xo}}{\sigma_{mf}+2\sigma_{xo}}\right)-\frac{(1-S_{xov})V_v}{2}+(1-V_v)\left(\frac{\sigma_{xo\mu m}-\sigma_{xo}}{\sigma_{xo\mu m}+2\sigma_{xo}}\right)=0$$

$$S_{xo\mu}=1-S_{or\mu}$$

$$S_{xom}=S_{wm}$$

Compute S_{xot} (Eq. A11).

Case 3: $R_{inv3} < R_{xo} < R_{inv2}$**:** Water entering in intergranular pores. Intragranular pores and vugs at respective S_{or}.

Conductivity of the composite intragranular-intergranular system, $\sigma_{xo\mu m}$, is given by Eq. A9 recognizing that $\sigma_{xo}=\frac{1}{R_{xo}}$.

$$(1-S_{orv})V_v\left(\frac{\sigma_{mf}-\sigma_{xo}}{\sigma_{mf}+2\sigma_{xo}}\right)-\frac{(S_{orv})V_v}{2}+(1-V_v)\left(\frac{\sigma_{xo\mu m}-\sigma_{xo}}{\sigma_{xo\mu m}+2\sigma_{xo}}\right)=0$$

Conductivity of microporous grains, $\sigma_{xo\mu}$, is given by Eq. A6.

$$\sigma_{xo\mu}=\sigma_{mf}{\phi_\mu}^m\left(1-S_{or\mu}\right)^n$$

Compute saturation in the intergranular pores, S_{xom}, with Eq. A7.

$$\left(\frac{\sigma_{xo\mu}-\sigma_{xo\mu m}}{\sigma_{xo\mu}-\sigma_{mf}S_{xom}^n}\right)\left(\frac{\sigma_{mf}\cdot S_{xom}^n}{\sigma_{xo\mu m}}\right)^{\frac{(m-1)}{m}}=\frac{V_m}{(1-V_v)}$$

$$S_{xo\mu}=1-S_{or\mu}$$

$$S_{xov}=1-S_{orv}$$

Compute S_{xot} with Eq. A11.

Step 6c: Waterflood Computations in Water-Wet Case

Computation of Waterflood Benchmarks:

Benchmark 1, R_{inv1}**:** Filtrate imbibition complete into intragranular pores which are now at residual oil. Rest are unchanged from drainage

Conductivity of microporous grains is given by Eq. A6

$$\sigma_{xo\mu}=\sigma_{mf}{\phi_\mu}^m\left(1-S_{or\mu}\right)^n$$

Conductivity of the composite intragranular-intergranular system, $\sigma_{xo\mu m}$, is from Eq. A7:

$$\left(\frac{\sigma_{xo\mu}-\sigma_{xo\mu m}}{\sigma_{xo\mu}-\sigma_{mf}S_{wm}^n}\right)\left(\frac{\sigma_{mf}\cdot S_{wm}^n}{\sigma_{xo\mu m}}\right)^{\frac{(m-1)}{m}}=\frac{V_m}{(1-V_v)}$$

Rock conductivity, σ_{inv1}, including the vugs, is solved from Eq. A9, i.e.,

$$S_{wv}V_v\left(\frac{\sigma_{mf}-\sigma_{inv1}}{\sigma_{mf}+2\sigma_{inv1}}\right)-\frac{(1-S_{wv})V_v}{2}+(1-V_v)\left(\frac{\sigma_{xo\mu m}-\sigma_{inv1}}{\sigma_{xo\mu m}+2\sigma_{inv1}}\right)=0$$

$$R_{inv1}=\frac{1}{\sigma_{inv1}}$$

Benchmark 2, R_{inv2}: Filtrate imbibition complete into intragranular and intergranular pores, which are now at respective S_{or}; vugs unchanged from drainage.

$\sigma_{xo\mu}$ already computed in earlier step.

Conductivity of the composite intragranular-intergranular system, $\sigma_{xo\mu m}$, is given by Eq. A7 so that

$$\left(\frac{\sigma_{xo\mu}-\sigma_{xo\mu m}}{\sigma_{xo\mu}-\sigma_{mf}(1-S_{orm})^n}\right)\left(\frac{\sigma_{mf}(1-S_{orm})^n}{\sigma_{xo\mu m}}\right)^{\frac{(m-1)}{m}}=\frac{V_m}{(1-V_v)}$$

Rock conductivity, σ_{inv2}, including the vugs, is (Eq. A9)

$$S_{wv}V_v\left(\frac{\sigma_{mf}-\sigma_{inv2}}{\sigma_{mf}+2\sigma_{inv2}}\right)-\frac{(1-S_{wv})V_v}{2}+(1-V_v)\left(\frac{\sigma_{xo\mu m}-\sigma_{inv2}}{\sigma_{xo\mu m}+2\sigma_{inv2}}\right)=0$$

$$R_{inv2}=\frac{1}{\sigma_{inv2}}$$

Benchmark 3, R_{inv3}: Rock conductivity when filtrate imbibition is complete, and rock is at S_{or}.

Conductivity of microporous grains and the host, i.e., $\sigma_{xo\mu}$ and $\sigma_{xo\mu m}$, are obtained as in the previous step.

Rock conductivity, σ_{inv3}, including the vugs, is solved from (Eq. A9)

$$(1-S_{orv})V_v\left(\frac{\sigma_{mf}-\sigma_{inv3}}{\sigma_{mf}+2\sigma_{inv3}}\right)-\frac{(S_{orv})V_v}{2}+(1-V_v)\left(\frac{\sigma_{xo\mu m}-\sigma_{inv3}}{\sigma_{xo\mu m}+2\sigma_{inv3}}\right)=0$$

$$R_{inv3}=\frac{1}{\sigma_{inv3}}$$

Computation of Flushed Zone Saturation:

Case 1: $R_{inv1} < R_{xo}$: Water enters intragranular pores. Vugs and intergranular pores are unchanged from drainage. Conductivity of the composite intragranular-intergranular system, $\sigma_{xo\mu m}$, is given by Eq. A9 recognizing that $\sigma_{xo}=\frac{1}{R_{xo}}$. Therefore,

$$S_{wv}V_v\left(\frac{\sigma_{mf}-\sigma_{xo}}{\sigma_{mf}+2\sigma_{xo}}\right)-\frac{(1-S_{wv})V_v}{2}+(1-V_v)\left(\frac{\sigma_{xo\mu m}-\sigma_{xo}}{\sigma_{xo\mu m}+2\sigma_{xo}}\right)=0$$

Conductivity of the grains, $\sigma_{xo\mu}$, is (Eq. A7):

$$\left(\frac{\sigma_{xo\mu}-\sigma_{xo\mu m}}{\sigma_{xo\mu}-\sigma_{mf}S_{wm}^n}\right)\left(\frac{\sigma_{mf}\cdot S_{wm}^n}{\sigma_{xo\mu m}}\right)^{\frac{(m-1)}{m}}=\frac{V_m}{(1-V_v)}$$

Compute saturation in the intragranular pores from Eq. A6:

$$S_{xo\mu}=\left(\frac{\sigma_{xo\mu}}{\sigma_w{\phi_\mu}^m}\right)^{\frac{1}{n}}$$

$$S_{xov}=S_{wv}$$

$$S_{xom}=S_{wm}$$

Compute S_{xot} using Eq. A11.

Case 2: $R_{inv2} < R_{xo} < R_{inv1}$: Water enters in intergranular pores. Intragranular pores are at S_{or}. Vugs unchanged from drainage. Conductivity of microporous grains, $\sigma_{xo\mu}$, is given by Eq. A6 so that

$$\sigma_{xo\mu}=\sigma_{mf}{\phi_\mu}^m\left(1-S_{or\mu}\right)^n$$

Conductivity of the composite intragranular-intergranular system, $\sigma_{xo\mu m}$, is given by Eq. A9. Recognizing that $\sigma_{xo}=\frac{1}{R_{xo}}$.

$$S_{wv}V_v\left(\frac{\sigma_{mf}-\sigma_{xo}}{\sigma_{mf}+2\sigma_{xo}}\right)-\frac{(1-S_{wv})V_v}{2}+(1-V_v)\left(\frac{\sigma_{xo\mu m}-\sigma_{xo}}{\sigma_{xo\mu m}+2\sigma_{xo}}\right)=0$$

Compute saturation in the intergranular pores, S_{xom}, with Eq. A7.

$$\left(\frac{\sigma_{xo\mu}-\sigma_{xo\mu m}}{\sigma_{xo\mu}-\sigma_{mf}S_{xom}^n}\right)\left(\frac{\sigma_{mf}\cdot S_{xom}^n}{\sigma_{xo\mu m}}\right)^{\frac{(m-1)}{m}}=\frac{V_m}{(1-V_v)}$$

$$S_{xo\mu}=1-S_{or\mu}$$

$$S_{xom}=S_{wm}$$

Compute S_{xot} with Eq. A11.

Case 3: $R_{inv3} < R_{xo} < R_{inv2}$: Water enters vugs. Intragranular pores and intergranular pores are at respective S_{or}. Conductivity of grains, $\sigma_{xo\mu}$, is computed as in earlier step. Conductivity of the composite intragranular-intergranular system, $\sigma_{xo\mu m}$, is given by Eq. A7 so that

$$\left(\frac{\sigma_{xo\mu}-\sigma_{xo\mu m}}{\sigma_{xo\mu}-\sigma_{mf}(1-S_{orm})^n}\right)\left(\frac{\sigma_{mf}(1-S_{orm})^n}{\sigma_{xo\mu m}}\right)^{\frac{(m-1)}{m}}=\frac{V_m}{(1-V_v)}$$

Compute saturation in the vugs, S_{xov}, using Eq. A9. Recognizing that , we have

$$S_{xov}V_v\left(\frac{\sigma_{mf}-\sigma_{xo}}{\sigma_{mf}+2\sigma_{xo}}\right)-\frac{(1-S_{xov})V_v}{2}+(1-V_v)\left(\frac{\sigma_{xo\mu m}-\sigma_{xo}}{\sigma_{xo\mu m}+2\sigma_{xo}}\right)=0$$

$$S_{xo\mu}=1-S_{or\mu}$$

$$S_{xom}=1-S_{orm}$$

Compute using Eq. A11.

ABOUT THE AUTHORS

Raghu Ramamoorthy is a consultant petrophysicist based in Abu Dhabi, UAE. Earlier until 2017, he was a petrophysics advisor to Schlumberger in the Middle East. He has over 38 years in the oil industry, mostly served with Schlumberger in various capacities. He has several patents on interpretation techniques and logging technology and is widely published in the SPWLA, SPE, and AAPG. He has served on the Board of the SPWLA and is a recipient of the SPE Regional Award in Formation Evaluation. His current interests are in carbonate petrophysics, EOR, and the evaluation of tight gas reservoirs.

T.S. Ramakrishnan is a senior science advisor at the Schlumberger-Doll Research Center. His publications are on flow in porous media, petrophysics, enhanced oil recovery, carbon storage, reservoir completions and control, applied physics, and mathematics.

Suvodip Dasgupta is a senior petrophysicist with Schlumberger in the United Arab Emirates. He joined Schlumberger in 2007 as an LWD field engineer before moving into a petrophysics role. He is the petrophysics team leader in Abu Dhabi, focusing on formation evaluation with LWD and wireline data. He is a member of SPE and SPWLA with multiple publications, focusing on carbonates, acoustics, and unconventionals.

Ishan Raina is a senior petrophysicist with Schlumberger, with 10 years of experience in the industry during which he has worked in a variety of roles, including operations petrophysicist, studies petrophysicist, and core analyst, working in carbonate and source rock play environments. Ishan is currently based in France and is working on the development of next-generation wellbore interpretation workflows on cloud.

PETROPHYSICS, VOL. 61, NO. 5 (OCTOBER 2020); PAGES 473–481; 10 FIGURES; 2 TABLES. DOI: PJV61N5-2020a5

Revisiting the Concept of Wettability for Organic-Rich Tight Rocks: Application in Formation Damage–Water Blockage

Sanchay Mukherjee[1*], Son Thai Dang[1], Chandra Rai[1], and Carl Sondergeld[1]

ABSTRACT

Wettability is an important petrophysical property, which governs irreducible fluid saturations, relative permeability, and fluid invasion. Unlike conventional reservoirs, which have relatively uniform pore-surface properties, the concept of wettability is questionable in organic-rich tight reservoirs. These rocks do not only have a nanoporous system, but also possess multiple pore types with different interfacial affinities. Previous studies have shown that the unconventional reservoirs consist of three major pore types: inorganic pores (assumed to be water-wet), organic pores (assumed to be oil-wet, controlled by organic matter and thermal maturity), and mixed-wet pores (controlled by organic-inorganic distribution) (Curtis et al., 2012).

The current study revisits the concept of pore-type partitioning in tight rocks. We propose and demonstrate a new workflow to evaluate pore partitioning using four companion samples from Wolfcamp B Shale. First, all the specimens were vacuum dried at 100°C for 6 days to remove the free fluids until the weight stabilized. Total porosity was estimated as the sum of irreducible liquid volume (using nuclear magnetic resonance (NMR)) and gas-filled volume (using a high-pressure helium pycnometer). Two of the specimens were saturated with a single fluid (either dodecane or 2.5 wt% KCl brine)—first, via imbibition for 5 days, followed by step pressurization (up to 7,000 psi) to achieve 100% saturation. The imbibition step was done hydrostatically with fluid injected into the samples from all directions. The other companion specimens were subjected to multiple injection cycles—starting with imbibition, then counter imbibition, and finally, step pressurization with the replacing phase. During this process, we used brine-then-dodecane and dodecane-then-brine as the injection fluid sequences. The counter-imbibition process refers to the imbibition of the samples by one liquid followed by another liquid. All four samples were continuously monitored by both gravimetric and NMR measurements until equilibration. Relative fractions of both replaced and replacing phases were calculated from sample weights and pore-fluid volumes.

The new approach classifies the connected pore network into three categories—oil-wet, water-wet, and mixed-wet, respectively, occupying 50, 15, and 35% of total movable pore volume in the Wolfcamp B. Mixed-wet pore is defined as the pore fraction, in which both oil and water can replace air under capillary suction. Using a conventional NMR wettability index, based on the difference between brine and oil intakes (Looyestijn and Hofman, 2006), this sample would appear to be oil-wet. However, this is a misleading interpretation. It is important to emphasize that mixed-wet pores are not equivalent to neutral-wet systems. We observe that the mixed-wet pores prefer brine over oil. During the counter-imbibition step, the samples initially imbibed with dodecane tend to intake brine while replacing dodecane, whereas the samples initially imbibed with brine and then counter imbibed with dodecane do not show a significant change in fluid concentrations. Instead, it required 1,500 psi of injection pressure for dodecane to reenter the pore system.

During well completion, water blockage will likely happen in this formation due to the capillary preference of mixed-wet pores. This formation damage can be reduced by the addition of surfactants into fracturing fluids. Moreover, the effect of water blockage is expected to reduce with more than 1,500 psi of drawdown. Thus, the workflow is promising to fully describe the pore network in tight formations in which pore-type partitioning is a more reasonable concept than wettability.

INTRODUCTION

Wettability determines the preferential contact between the reservoir rock and fluids filling the pores. Wettability controls some of the petrophysical characteristics of the reservoir like relative permeability, residual fluid saturation, and capillary pressure, thus affecting the primary and secondary production from a well (Abdallah et al., 2007).

The Amott Harvey imbibition test, Bureau of Mines (USBM) test (Donaldson et al., 1969), and contact angle

Manuscript received by the Editor April 3, 2020; revised manuscript received May 22, 2020; manuscript accepted June 25, 2020
[1]Mewbourne School of Petroleum and Geological Engineering, The University of Oklahoma, 100 Boyd Street, Norman, OK-73069; sanchay.mukherjee@ou.edu; dangthaison@ou.edu; crai@ou.edu; csondergeld@ou.edu
*Corresponding author

measurements are some common techniques to measure wettability in conventional reservoirs. The Amott Harvey method combines spontaneous imbibition and forced displacement, and a sample's wettability is determined based on the difference between brine and oil saturation for a zero-capillary pressure.

The USBM method uses a centrifuge (representing capillary pressure) to spin the rock core sample and results in forced imbibition and drainage. Using contact angle measurements, the wetting characteristics of the pores are determined using the contact angle between the fluid and solid surface; the surface can be water-wet if the angle is less than 90°, oil-wet if greater than 90°, and neutral-wet if equal to 90° (Fanchi, 2002). However, in tight rocks, due to low permeabilities and small pore sizes, these conventional techniques of measuring wettability fail. Desaturation techniques, such as centrifuge and fluid displacement, are unable to yield higher differential pressure and achieve uniform fluid distribution due to the small pores and fractional wettability in them, thus failing their purpose in tight rocks.

Some recent techniques to evaluate wettability in tight rocks are spontaneous imbibition method (Lan et al., 2015; Akbarabadi et al., 2014), pore-space imaging method (Akbarabadi et al., 2017), and NMR-based methods (Sharma et al., 2007; Odusina et al., 2011; Tinni et al., 2017). Most of these studies confirm the presence of three types of pores: water-wet pores (inorganic pores), oil-wet pores (organic pores), and mixed-wet pores (see Fig. 1) (Odusina et al., 2011; Deglint et al., 2017). However, the concept of wettability is questionable in organic-rich tight reservoirs since the surface properties throughout the whole pore system are not uniform. The NMR-based method calculates the wettability index based on the interconnectivity between these three kinds of pores (Odusina et al., 2011). Along with wettability, porosity, permeability, and water saturation can also be measured from relaxation times from NMR measurements. These relaxation times of fluids in rocks vary with the interaction between pore fluid and matrix grains and yield the separation of effects of wetting and nonwetting fluids. The wettability index calculated based on the difference of spontaneous intakes of brine vs. oil can be masked by the volumetric difference between oil-wet and water-wet pores, whereas mixed-wet pores govern partial flows.

This study proposes a three-step workflow to characterize the pore types in tight rocks into three categories—oil-wet, water-wet, and mixed-wet pores—and quantify their relative proportions. The three steps in this workflow include spontaneous imbibition, then counter imbibition, and finally, step pressurization of replacing fluids.

METHODOLOGY

Four companion specimens (namely A, B, C, and D) from a single depth (within a 2-in. interval) of the Wolfcamp B Formation were used for this study. Petrophysical properties of the sample include Fourier transform infrared spectroscopy (FTIR)-mineralogy (Sondergeld and Rai, 1993; Ballard, 2007), LECO total organic carbon (TOC), porosity, and thermal maturity (Hawk) and are reported in Table 1. Total porosity was measured using the combination of helium high-pressure pycnometer (HPP) and NMR on plug specimens. HHP measures gas-filled porosity, while NMR captures liquid-filled porosity. These specimens were evaluated under handheld X-ray fluorescence (XRF) measurements and confirm minimal compositional heterogeneity (Appendix 1, Table A1.1).

All four specimens were dried at 100°C under vacuum for 6 days until the weight stabilized. After drying, the total porosity was remeasured as the sum of irreducible liquid volume (using NMR) and gas-filled volume (using HPP). First, Specimen A imbibed 2.5 wt% KCl brine, and Specimen B imbibed dodecane for 5 days, followed by step pressurization up to 7,000 psi, with the respective injection fluids to achieve 100% saturation (Fig. 2). The imbibition step was done hydrostatically with fluid injecting into the samples from all directions. Specimens C and D were

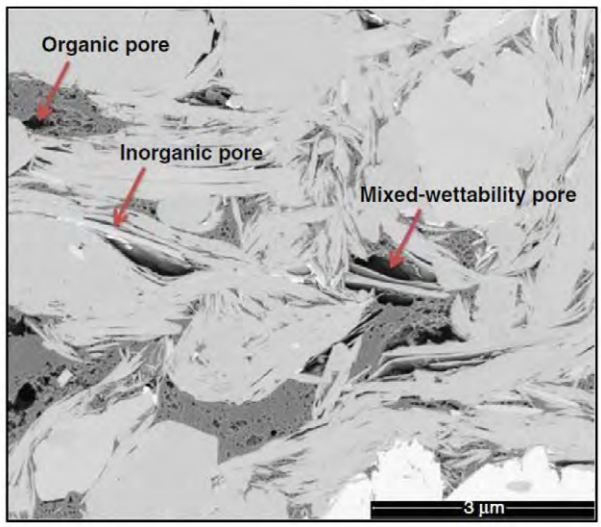

Fig. 1—SEM image of a shale sample (Marcellus Shale) showing the three kinds of pores: organic, inorganic, and mixed-wet pores. (Curtis et al., 2011)

Table 1—Petrophysical Properties of Wolfcamp B Samples

	Mineralogy (wt%)				TOC (wt%)	Porosity (%)		T_{max} (°C)
	Quartz	Clays	Carbonates	Others		Irreducible	Free	
Wolfcamp B	47	27	18	8	2.5	3	7.5	447

introduced to imbibition and counter imbibition, followed by step pressurization with the replacing phase (Fig. 3). For Specimen C, the sequence followed for imbibition and counter imbibition was brine-dodecane-dodecane pressurization (Sequence I), and for Specimen D, the sequence carried out for imbibition and counter imbibition was dodecane-brine-brine pressurization (Sequence II). The counter-imbibition process refers to the imbibition of the samples by one liquid followed by another liquid, without the implication of injection direction. All samples were continuously monitored by both gravimetric and NMR measurements until equilibrium. These measurements allowed us to calculate the relative fractions of both the replaced and replacing phases.

NMR data, including T2 relaxation distributions, were acquired at the frequency of 12 MHz, using Oxford GeoSpec+ spectrometers and Green Imaging acquisition and processing software (Fig. 4). The magnet temperature was set at 35°C throughout the experiments. The echo spacing, of 114 μs, was chosen to capture fast relaxation components in the shale samples (including fluids in small pores and heavy hydrocarbon components) (Dang et al., 2019). All NMR responses in this work were collected with a signal-to-noise ratio (SNR), between 100 to 150.

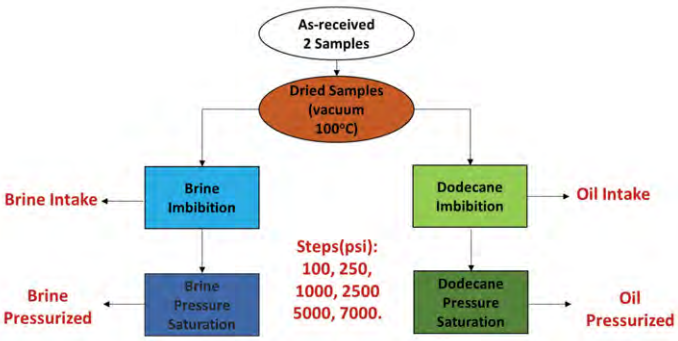

Fig. 2—Workflow for single-phase injection, either with 2.5 wt% KCl brine or dodecane. Two companion specimens were imbibed, counter imbibed, then followed by step pressurization with the same fluid.

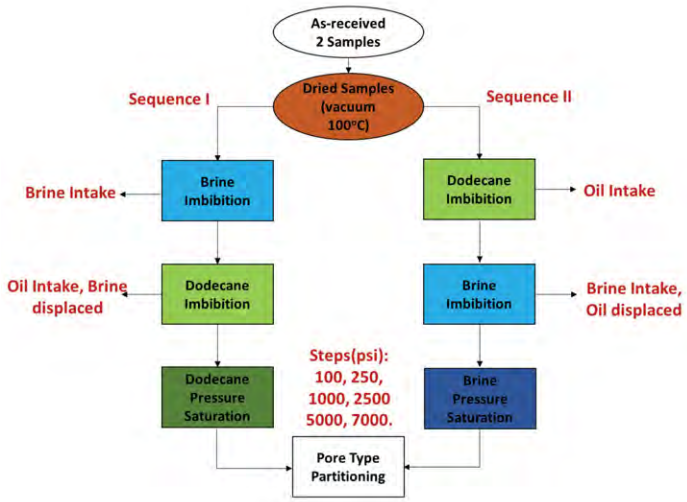

Fig. 3—Workflow for multiphase imbibition. The samples were imbibed and counter imbibed with different fluids (brine-then-dodecane and dodecane-then-brine), followed by step pressurization by the same fluid used in the counter-imbibition stage.

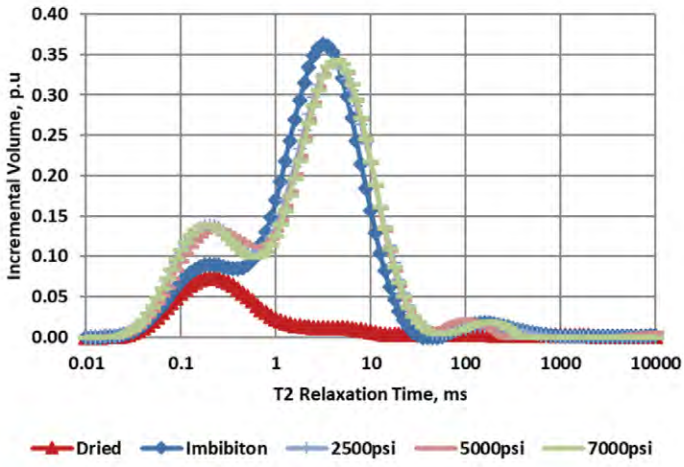

Fig. 4—An example of an acquired T2 NMR distribution showing the incremental volume (p.u.) as a function of fluid relaxation time (ms). In the context of tight source rock, the peak at a faster relaxation time represents fluid in small pores (generally, brine associating with clay pores), and the peak at higher relaxation times refers to oil (dodecane) signals.

RESULTS AND DISCUSSIONS

Fluid flow in a rock is impacted by different pore types and their distribution within the rock matrix. When there exists more than one fluid in the rock, the flow of one fluid is dependent on the other; the fluids might flow from one type of pore to another based on the capillary pressure barriers of the system (Tinni et al., 2017).

Figures 5a and 5b show the T2 NMR response for the Samples A and B when only single-phase fluid is injected into the rock. In both cases, we observe that even after vacuum drying the samples at 100°C until weight stabilization, a fraction of irreducible fluid remains in the rock. At the end of the pressurization step, the sample achieves a 100% saturation of 10.5 p.u. (confirmed by total porosity measured by HPP and NMR). In Fig. 5a, the NMR responses for the dry state, brine imbibition, and brine step pressurization (up to 7,000 psi) are also shown. The behavior signifies that brine enters easily into water-wet pores (in the fast relaxation area, 0.1 to 3 ms), which generally is associated with small clay pores; later, brine was forced into oil-wet pores (in the slow relaxation area), which either have large pore size or small surface relaxivity with respect to brine. Figure 5b shows the NMR responses for the following: the dry state, dodecane imbibition, and dodecane step pressurization (up to 7,000 psi). Interpreting the curves tells us that dodecane tends to get in the slow relaxation region of the distribution, which represents the large or organic oil-wet pores (1 to 10 ms). Only after applying a higher pressure (exceeding the capillary barrier) does dodecane enter the small water-wet pores (relaxation time of 0.1 to 1 ms).

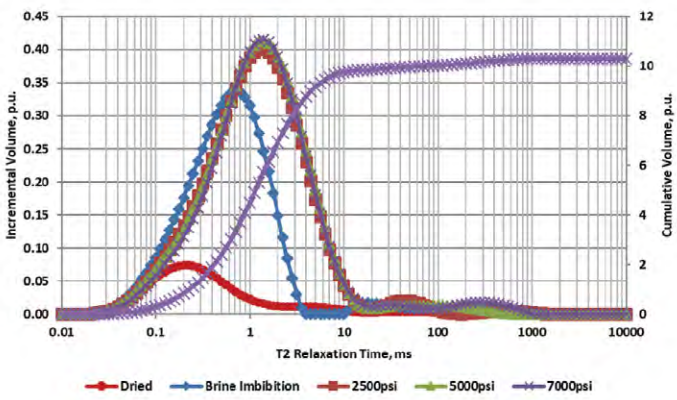

Fig. 5a—The NMR responses for the dry state, brine-imbibed state, and brine-forced state at different pressures. Brine enters easily into water-wet and mixed-wet pores (fast relaxation time). With increasing pressure, brine enters oil-wet pores (slow relaxation time). After fluid pressurization, cumulative NMR porosity matches with total porosity measured by HPP and NMR on the dried specimen.

For the multiphase injection step, the samples were vacuum dried until the weights stabilized. Figures 6a and 6b show the T2 NMR responses for Samples C and D when multiple fluids were injected. In Fig. 6a, the NMR responses for the dry state, brine imbibition after 5 days, followed by dodecane imbibition for 5 days are shown. The brine imbibition curve shows the brine intake of the rock, followed by brine displacement during dodecane imbibition. We observe that after brine imbibition, little dodecane entered the pore and had no brine production. However, in another case, Fig. 6b, where dodecane was imbibed first and then brine, the curves show a different behavior of brine displacing the dodecane over 5 days. This behavior is indicated by the increase in peak amplitudes in the fast relaxation region (brine signal) and a decrease in the slow relaxation region (dodecane signal). This preference of the pores for brine over oil can thus cause water blockage during field operations.

After the imbibition step, we pressure saturated the samples in both the sequences with the counter-imbibition fluid (dodecane for Sequence I and brine for Sequence II). Figures 7a and 7b show the T2 NMR responses for the Samples C and D for the pressurization steps. In Fig. 7a, the NMR responses for the dry state, brine imbibition after 5 days, dodecane imbibition after 5 days, and pressure saturation steps with dodecane (up to 7,000 psi) are shown. The curves indicate that after dodecane imbibition, higher pressure is

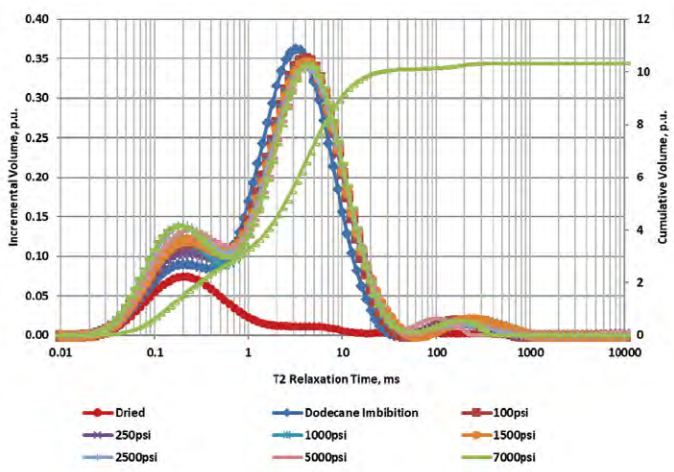

Fig. 5b—The NMR responses for the dry state, dodecane imbibition, and dodecane step pressurization (up to 7,000 psi) indicate that dodecane tends to get in the slow relaxation region of the distribution, which represents the large or organic oil-wet pores and that only on the application of higher pressures is the dodecane able to enter the small pores or water-wet pores of the rock. After fluid pressurization, the cumulative NMR porosity matches with total porosity measured by HPP and NMR on the dried specimen.

required to push the oil into the pores. This is represented by an increase in peaks in the slow relaxation region of the distribution and a decrease in the fast relaxation regions. Thus, this shows that with an increase in pressure, not only does oil enter into the pore system, but it also forces brine out of the pores. In Fig. 7b, NMR responses for the dry state, dodecane imbibition after 5 days, brine imbibition after 5 days, and pressure saturation steps with brine (up to 7,000 psi) are shown. The same peaks in the slow relaxation region and increasing peaks in the fast relaxation region show that on pressurizing the sample with brine, dodecane is not being pushed out; however, brine is entering the sample through small pores or water-wet pores.

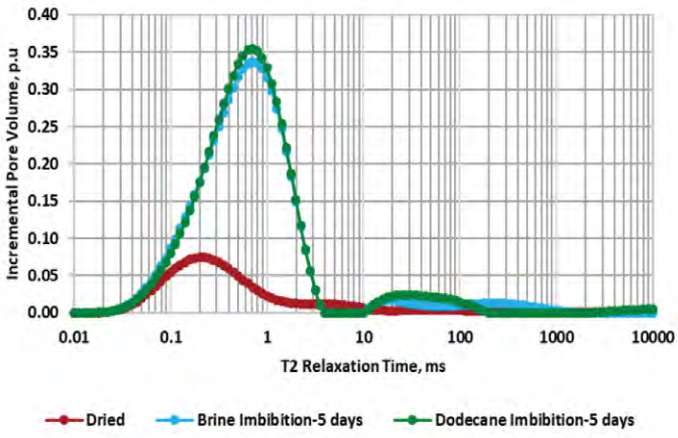

Fig. 6a—(Sequence I) The NMR responses for the dry state, brine imbibition after 5 days, and dodecane imbibition after 5 days show the brine intake of the rock, followed by brine displacement during dodecane imbibition. We observe that after brine imbibition not much dodecane can spontaneously enter the pore system. The blue color represents brine intake, and the green color represents dodecane intake.

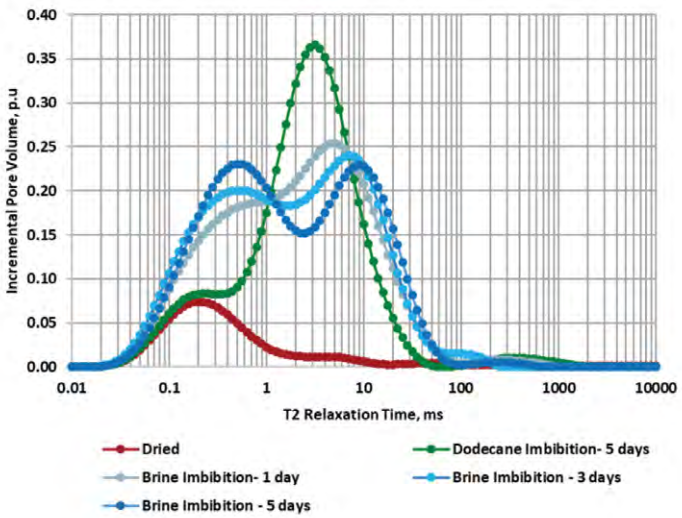

Fig. 6b—(Sequence II) The NMR responses for the dry state, dodecane imbibition, and counter imbibition by brine. The increase in peak amplitudes in the fast relaxation regions (brine signal) and the decrease in the slow relaxation region (dodecane signal) indicate the preference of the pores for brine over oil. This behavior in counter imbibition is opposite to Sequence I. The blue color represents brine intake, and the green color represents dodecane intake.

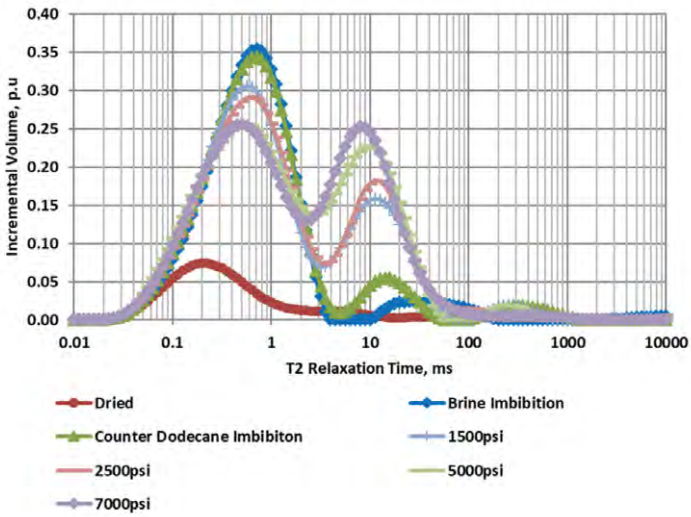

Fig. 7a—(Sequence I–continued) The NMR responses are shown for the dry state, brine imbibition after 5 days, dodecane imbibition after 5 days, and finally pressure saturation steps with dodecane (up to 7,000 psi). The increasing peaks in the slow relaxation region of the distribution and decreasing peaks in the fast relaxation regions show that by increasing the pressure, we are not only able to enter oil into the system, but also push out brine from the pores.

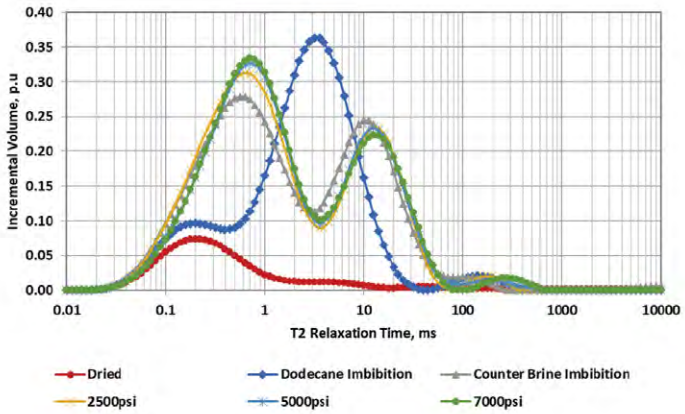

Fig. 7b—(Sequence II–continued) The NMR responses for the dry state, dodecane imbibition after 5 days, brine imbibition after 5 days, and pressure saturation steps with brine (up to 7,000 psi) are shown. The same peaks in the slow relaxation region and increasing peaks in the fast relaxation region indicate that although dodecane is not being pushed out, brine is entering the sample through small pores or water-wet pores.

All these experimental steps—drying, imbibition, counter imbibition, and pressurization along with both gravimetric (weight) and volumetric (NMR) measurements—were used to precisely calculate the concentration of replaced and replacing fluids.

Figure 8 shows the porosity variation as a function of time and steps followed for Sequence II (dodecane imbibition-brine, followed by brine pressurization). The pressure profile is also included in the same plot. As received, sample porosity was 5 p.u. After the drying stage, the porosity reduces to 3 p.u., but does not completely disappear due to the presence of irreducible fluid saturation and some fluids in the unconnected pores. The curves represent the initial imbibition of dodecane, followed by counter imbibition of brine and pressurization by brine. During counter imbibition, initially, brine pushes dodecane out from the pores, but after pressurization, it does not displace a significant quantity of dodecane.

Figure 9 shows the porosity variation as a function of time and steps followed for Sequence I (brine imbibition-dodecane; imbibition-dodecane; pressurization). Even after vacuum drying the samples, irreducible fluid is still observed. The sample is then brine imbibed and counter imbibed with dodecane. During counter imbibition and at lower pressures of saturation by dodecane, a small increase of dodecane volume entering the rock is observed, as well as a small volume of the brine expelled from the matrix. At or above a pressure of 1,500 psi, dodecane continues to flow through the pores without displacing any more brine, implying the oil phase regains continuity. This threshold pressure can be seen as the capillary pressure required to make the oil phase continuous and thus can help in determining the drawdown during production on a field scale. We can also quantify the type of pores present in the rock system using Eqs. 1, 2, and 3:

$$\emptyset_D = \emptyset_{oil\_wet} + \emptyset_{mixed\_wet} + \emptyset_{unconnected} \quad (1)$$

$$\emptyset_W = \emptyset_{water\_wet} + \emptyset_{mixed\_wet} + \emptyset_{unconnected} \quad (2)$$

$$\emptyset_{Total} = \emptyset_{oil_{wet}} + \emptyset_{water_{wet}} + \emptyset_{mixed_{wet}} + \emptyset_{unconnected} \quad (3)$$

We propose the following model for the Wolfcamp B rock type system (Fig. 10a). The rock consists of four types of pores: oil-wet (black), water-wet (gray), mixed-wet (fractional-wet), and unconnected pores (as shown by the yellow color). Sequence 1 is shown in Fig. 10b, and it indicates that dodecane enters the oil-wet pores, and at the same time, it enters the mixed-wet pores during the first step of dodecane imbibition. On counter imbibition by brine, brine replaces the oil in mixed-wet pores and also accesses the water-wet pores. At the end of this step, the fluid saturation approaches closely to 100%.

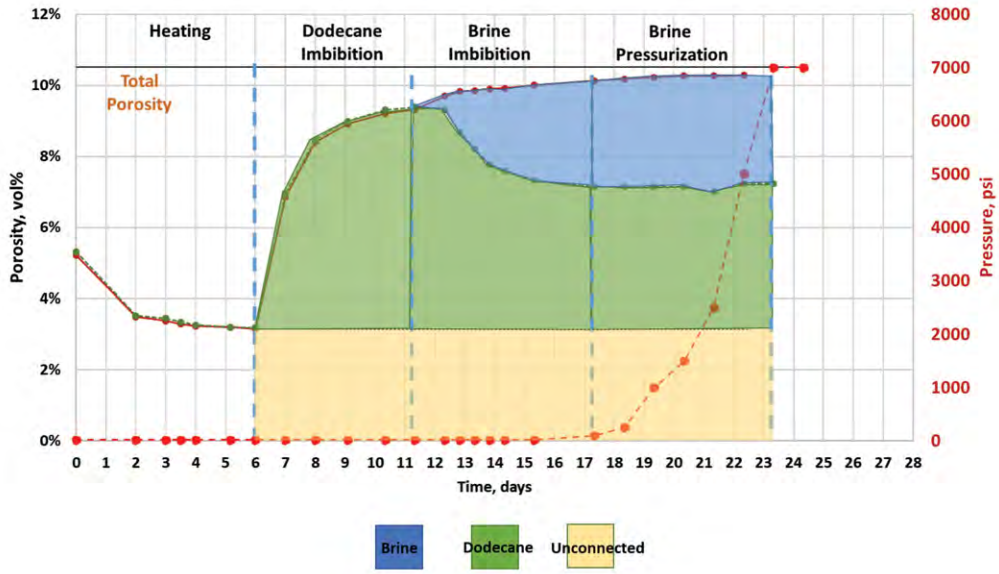

Fig. 8—Pore space occupied by brine and dodecane as a function of time during dodecane imbibition, followed by brine imbibition and pressurization. During the imbibition of brine after dodecane imbibition, a significant quantity of dodecane is pushed out from the pores by brine, which reduces over time, and on pressurization, not much dodecane is pushed out.

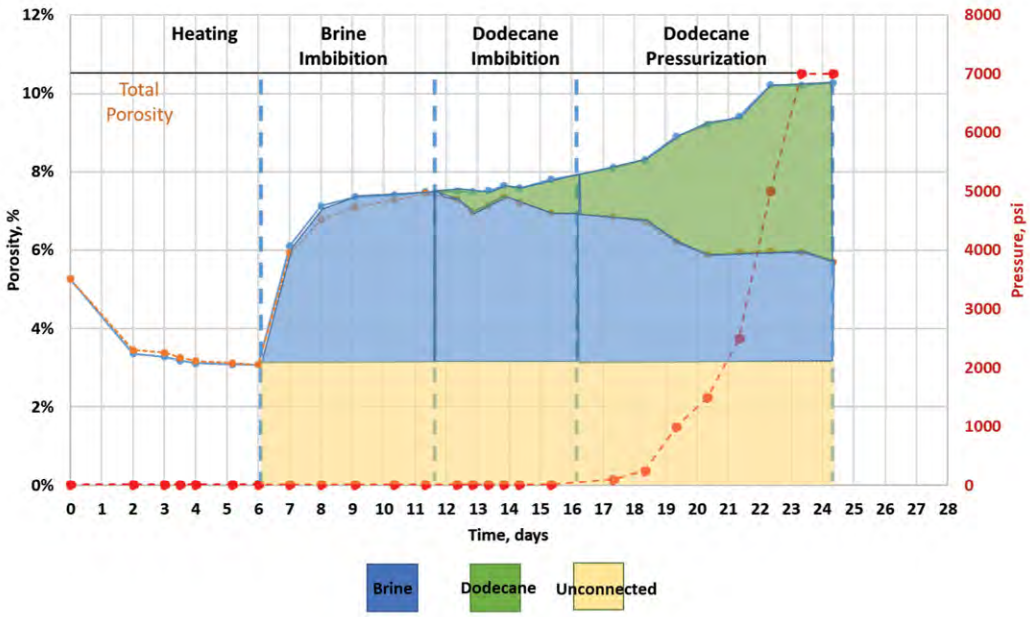

Fig. 9—Pore space occupied by brine and dodecane as a function of time during brine imbibition, followed by dodecane imbibition and pressurization. During counter imbibition and at lower pressures of saturation by dodecane, a small increase of dodecane volume entering the rock is recorded, as well as a small volume of the brine displaced from the matrix. At or above a pressure of 1,500 psi, dodecane continues to flow through the pores without displacing any more brine, implying the oil phase regains continuity.

In Sequence II (Fig. 10c), brine only occupies the water-wet and mixed-wet pores during the initial imbibition of brine in the rock. During the next step of counter imbibition by dodecane, the mixed-wet pores still prefer brine over oil as it blocks the access of dodecane in the oil-wet pores. Only after pressure saturating the sample at a pressure higher than 1,500 psi, more dodecane enters the oil-wet pores. This model helps to quantify the oil-wet, water-wet, and mixed-wet pores in the rock using Eqs. 1, 2, and 3, and the calculated values are shown in Table 2:

Table 2— Percentage of Oil-Wet, Water-Wet, and Mixed-Wet Pores in Wolfcamp B Samples

Wettability	Percentage of pores (%)
Oil-wet	50
Water-wet	15
Mixed-wet/unconnected	35

FIELD IMPLICATIONS

Hydraulic fracturing is a necessary stimulation process for tight reservoirs, in which the usage of fracturing fluid can affect formation performance. For the Wolfcamp B samples used in this study, during well completion, the water blockage is likely to happen due to water displacing oil residing in oil-wet pores. Initially, this might be favorable for the operator to boost the initial production rate; however, the water blockage in the later stage might hinder long-term production. The following solutions might help solve the problem of water blockage:

- Limiting the water invasion below the threshold before losing oil-phase continuity. This can be done by limiting soaking time or using available surfactants to reduce the interfacial tension during the fracturing fluid injection process (Hirasaki et al., 2008). The drawback of this process is that with the use of surfactants in fracturing fluid, the initial production rate might be reduced.
- Another solution can be to create a huge drawdown of 1,500 psi (for this formation) to regain the continuity of the oil phase.

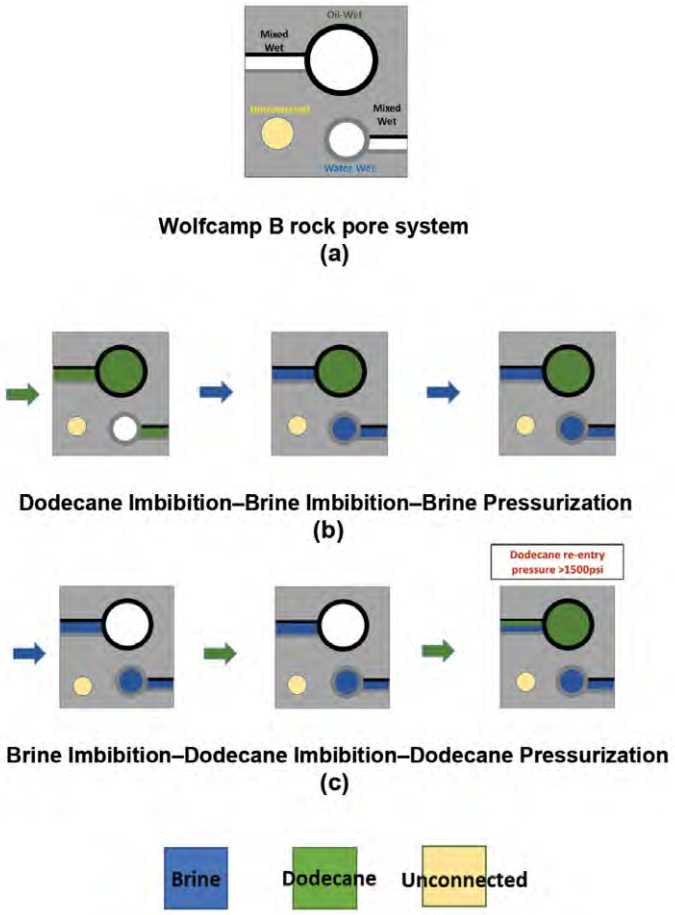

Fig. 10—Proposed model for the Wolfcamp B rock pore system. (a) The rock consists of four types of pores: oil-wet (black), water-wet (gray), mixed-wet (fractional-wet), and unconnected pores (yellow); (b) Sequence I shows dodecane entrance into the oil-wet pores and the mixed-wet pores during the first step of dodecane imbibition. On counter imbibition, brine replaces the oil in mixed-wet pores and also accesses the water-wet pores; (c) In Sequence II, brine only occupies the water-wet and mixed-wet pores during the initial imbibition of brine. During counter imbibition by dodecane, the mixed-wet pores prefer brine over oil, thus blocking dodecane from entering oil-wet pores. At a pressure higher than 1,500 psi, we are able to force more dodecane into the oil-wet pores.

CONCLUSIONS

The approach followed in this paper classifies the connected pore network in Wolfcamp B Formation into three categories: oil-wet, water-wet, and mixed-wet, respectively, occupying 50, 15, and 35% of the total movable pore volume. Mixed-wet pores represent a type of fractional-wet pores in which the smaller pores are water-wet and larger pores are oil-wet and that both oil and water can replace air under capillary suction forces. Using a conventional NMR wettability index, the sample might appear to be oil-wet based on the difference between the brine and oil intakes. However, this is a misleading interpretation. We observe that the mixed-wet pores prefer brine over oil. During the counter-imbibition step, the samples initially imbibed with dodecane tend to intake brine while displacing dodecane, whereas the samples initially imbibed with brine and then counter imbibed with dodecane do not show a significant change in fluid concentrations. Instead, it required 1,500 psi of injection pressure to reinject dodecane back into the pore system. Thus, only observing the contrast between oil and brine intake in tight rocks might not be sufficient to interpret the pore-system partitioning.

ACKNOWLEDGMENTS

We would like to thank the Unconventional Shale Gas Consortium for supporting this work. The support of Micaela Langevin and Jeremy Jernigen was critical to the laboratory studies. Integrated Core Characterization Center Contribution #164.

REFERENCES

Abdallah, W., Buckley, J.S., Carnegie, A., Edwards, J., Herold, B., Fordham, E., Graue, A., Habashy, T., Seleznev, N., Signer, C., Hussain, H., Montaron, B., and Ziauddin, M., 2007, Fundamentals of Wettability, *Schlumberger Oil Field Review*, **19**(2), 44–61. URL: https://www.slb.com/-/media/files/oilfield-review/p44-61-english. Accessed August 5, 2020.

Akbarabadi, M., and Piri, M., 2014, Nanotomography of the Spontaneous Imbibition in Shale, Paper URTEC-1922555 presented at the Unconventional Resources Technology Conference, Denver, Colorado, USA, 25–27 October. DOI: 10.15530/URTEC-2014-1922555.

Akbarabadi, M., Saraji, S, Piri, M., Georgi, D., and Delshad, D., 2007, Nanoscale Experimental Investigation of In-Situ Wettability and Spontaneous Imbibition in Ultra-Tight Reservoir Rocks, *Advances in Water Resources*, **107**, 160–179. DOI: 10.1016/j.advwatres.2017.06.004.

Ballard, B.D., 2007, Quantitative Mineralogy of Reservoir Rocks Using Fourier Transform Infrared Spectroscopy, Paper SPE-113023 presented at the SPE Annual Technical Conference and Exhibition, Anaheim, CA, USA, 11–14 November. DOI: 10.2118/113023-STU.

Curtis, M.E., Sondergeld, C.H., and Rai, C.S., 2011, Investigating the Microstructure of Gas Shales by FIB/SEM Tomography & STEM Imaging, Presented at the Oklahoma Geological Survey Workshop, Norman, Oklahoma, USA, 21 July. URL: http://www.ogs.ou.edu/MEETINGS/Presentations/ShalesMoving2011/CurtisMicro.pdf. Accessed on August 23, 2020.

Curtis, M.E., Sondergeld, C.H., Ambrose, R.J., and Rai, C.S., 2012, Microstructural Investigation of Gas Shales in Two- and Three-Dimensions Using Nanometer-Scale Resolution Imaging, *AAPG Bulletin*, **96**(4), 665–677. DOI: 10.1306/0815 1110188.

Dang, S.T., Sondergeld, C.H., and Rai, C.S., 2019, Interpretation of Nuclear-Magnetic-Resonance Response to Hydrocarbons: Application to Miscible Enhanced-Oil-Recovery Experiments in Shales, Paper SPE-191144, *SPE Reservoir Evaluation & Engineering*, **22**(1), 302–309. DOI: 10.2118/191144-PA.

Deglint, H., Ghanizadeh, A., DeBuhr, C., Clarkson, C., and Wood, J.W., 2017, Comparison of Micro- and Macro-Wettability Measurements for Unconventional Reservoirs: The Devil is in the Detail, Paper URTEC-2690338 presented at the Unconventional Resources Technology Conference, Austin, Texas, USA, 24–26 July. DOI: 10.15530/ URTEC-2017-2690338.

Donaldson, E.C., Thomas, R.D., and Lorenz, P.B., 1969, Wettability Determination and its Effect on Recovery Efficiency, Paper SPE-2338, *Society of Petroleum Engineers Journal*, **9**(1), 13–20. DOI: 10.2118/2338-PA.

Fanchi, J., 2002, Measures of Rock-Fluid Interactions, Chapter 7, *in Shared Earth Modeling*, 108–132, Gulf Professional Publishing. DOI: 10.1016/B978-0-7506-7522-2.X5000-9. ISBN: 9780750675222.

Hirasaki, G.J., Miller, C.A., and Puerto, M., 2008, Recent Advances in Surfactant EOR, Paper SPE-115386 presented at the SPE Annual Technical Conference and Exhibition, Denver, Colorado, USA, 21–24 September. DOI:10.2118/115386-MS.

Lan, Q., Dehghanpour, H., Wood, J., and Sanei, H., 2015, Wettability of the Montney Tight Gas Formation, Paper SPE-171620, *SPE Reservoir Evaluation & Engineering*, **18**(03), 417–431. DOI: 10.2118/171620-PA.

Looyestijn, W.J., and Hofman, J., 2006, Wettability-Index Determination by Nuclear Magnetic Resonance, Paper SPE-93624, *SPE Reservoir Evaluation & Engineering*, **9**(2), 146–153. DOI:10.2118/93624-PA.

Odusina, E., Sondergeld, C., and Rai, C., 2011, An NMR Study of Shale Wettability, Paper SPE-147371 presented at the Canadian Unconventional Resources Conference, Calgary, Alberta, Canada, 15–17 November. DOI: 10.2118/147371-MS.

Sharma, M., Bryant, S., Verdin, C.T., and Hirasaki, G., 2007, Integrated, Multi-Scale Characterization of Imbibition and Wettability Phenomena Using Magnetic Resonance and Wide-Band Dielectric Measurements, Final Report, US Department of Energy, National Petroleum Technology Office. URL: https://digital.library.unt.edu/ark:/67531/metadc901577/ m1/1/. Accessed August 5, 2020.

Sondergeld, C.H., and Rai, C.S., 1993, A New Concept of Quantitative Core Characterization, *The Leading Edge*, **12**(7), 774–779. DOI: 10.1190/1.1436968.

Tinni, A., Sondergeld, C., and Rai, C., 2017, Pore Connectivity Between Different Wettability Systems in Organic Rich Shales, Paper SPE-185948, *SPE Reservoir Evaluation and Engineering*, **20**(4), 1020–1027. DOI: 10.2118/185948-PA.

APPENDIX 1

Table A1.1—Properties of the Four Samples Showing Minimal Heterogeneity

Sample Number	Weight (g)	Bulk Density (g/cc)	Bulk Volume (cc)	T2 (cc)	T2 (p.u.)
1	34.28	2.482	13.81	0.73	5.2%
2	39.71	2.479	16.02	0.83	5.2%
3	33.19	2.478	13.39	0.70	5.3%
4	38.88	2.482	15.66	0.82	5.3%

ABOUT THE AUTHORS

Sanchay Mukherjee earned a BS degree in petroleum engineering from the University of Petroleum and Energy Studies (UPES), Dehradun, India, in 2016. He worked as a senior drilling engineer for Mineral Exploration Corporation Limited, India, from 2016 to 2018. Sanchay is currently an MS candidate at the University of Oklahoma. His research interests are reservoir characterization, EOR, and unconventional petrophysics.

Son Dang earned BS, MS, and PhD degrees in petroleum engineering from the University of Oklahoma (OU). His dissertation focuses on understanding drive mechanisms of gas injection EOR in tight formations. His research interests include geochemistry, petrophysics systematics, and spectroscopy analyses on unconventional reservoir rocks. He is now working as an NMR specialist and geoscientist at Stratum Reservoir, Houston, Texas.

Chandra Rai completed an MS degree in geophysics from the Indian School of Mines in 1971. He also completed a PhD in geology and geophysics from the University of Hawaii in 1977. Chandra worked as a technology director at Amoco for 18 years. He is currently a professor and the Martin G. Miller Chair at the University of Oklahoma. He teaches petrophysics, petrophysics lab, seismic reservoir modeling, unconventional reservoirs, and well logging. His research interests include reservoir characterization, petrophysics, and rock physics in unconventional reservoirs.

Carl Sondergeld completed an MA degree in geology at Queens College in 1972. He received a PhD in geophysics from Cornell University in 1977. Carl is currently a professor and the Curtis Mewbourne Chair at the University of Oklahoma. He teaches petrophysics, petrophysics lab, technical communications, seismic reservoir modeling, unconventional reservoirs, introduction to petroleum engineering, and well logging. He carries out research in the areas of rock physics, petrophysics, and geomechanics with an emphasis on unconventional shale gas and oil reservoirs.

PETROPHYSICS, VOL. 61, NO. 5 (OCTOBER 2020); PAGES 482–494; 14 FIGURES; 2 TABLES. DOI: PJV61N5-2020a6

Prediction of Sonic Wave Transit Times From Drilling Parameters While Horizontal Drilling in Carbonate Rocks Using Neural Networks

Ahmad Gowida[1] and Salaheldin Elkatatny[1*]

ABSTRACT

Sonic logging data are usually used to determine formation type, porosity, saturating fluids, and dynamic elastic parameters. Sonic logging data—compressional (P-wave) and shear (S-wave) transit times—can be obtained using acoustic logging tools. Sonic data are not always available for all the drilled wells aside from the sonic logging tools that are usually run into the well after the formation has been drilled.

The main objective of this paper is to develop a synthetic well-log generator tool to predict the P-wave and S-wave transit times (Δt_{comp} and Δt_{shear}, respectively) while drilling using a neural networks technique. To build the artificial neural network models, field data (1,421 points) have been collected from a horizontal well representing a carbonate formation within a field in the Middle East region that included mechanical drilling parameters and the corresponding well-log data (Δt_{comp} and Δt_{shear}). Another set of data (417 unseen data from the same field) was used to assess the robustness of these models for prediction purposes.

The results showed a significant agreement between the predicted and measured values of Δt_{comp} and Δt_{shear} indicated by correlation coefficient (R) of 0.94 and 0.93 with an average absolute percentage error (AAPE) of 1.18 and 0.87% for Δt_{comp} and Δt_{shear} predictions, respectively. Besides, the validation process manifested the capability of the developed models to predict Δt_{comp} and Δt_{shear} with an AAPE of 1.87 and 1.30% for the Δt_{comp} and Δt_{shear} models, respectively.

INTRODUCTION

Identifying the geomechanical properties of the formations is considered a key factor for formation evaluation and rock characterization processes (Darling, 2005). Estimating these parameters with high accuracy can help effectively save time, money, and risks. Rock strength parameters are considered essential for optimizing drilling operation efficiency and minimizing the associated risks due to a better understanding of the nature of the drilled formations (Nes et al., 2005). These geomechanical properties mainly include Poisson's ratio and Young's modulus. These parameters are usually used for developing geomechanical models, which are considered important tools for representing the in-situ stress state and the elastic behavior of the subterranean formations (Gatens et al., 1990). Thereafter, many problems during the drilling process can be avoided, like pipe sticking and kicks.

Static elastic parameters can be estimated accurately from laboratory measurements on retrieved core samples representing the in-situ stress-state condition of the formations under study (Tutuncu and Sharma, 1992). However, this approach is considered very costly and an ineffective use of time. Therefore, the dynamic elastic parameters are usually estimated instead using petrophysical well-log data, such as gamma ray, neutron porosity, and formation bulk density (Najibi et al., 2015). The core data can then be used to calibrate the dynamic geomechanical data (Ahmed and Meehan, 2016). Dynamic Young's modulus and Poisson's ratio can be calculated using the well-log data, namely compressional (P-wave), shear (S-wave) transit times, and formation bulk density (Δt_{comp}, Δt_{shear}, and bulk density (RHOB), respectively) (Fjar et al., 2008) using Eqs. 1 and 2:

$$\upsilon_{\text{dynamic}} = \frac{V_p^2 - 2V_s^2}{2(V_p^2 - V_s^2)} \quad (1)$$

$$E_{\text{dynamic}} = \frac{\rho \times V_s^2 \left(3V_p^2 - 4V_s^2\right)}{V_p^2 - V_s^2} \quad (2)$$

Manuscript received by the Editor March 28, 2020; revised manuscript received June 16, 2020; manuscript accepted July 6, 2020.
[1]Department of Petroleum Engineering, King Fahd University of Petroleum & Minerals, Dhahran 31261, Saudi Arabia, 5049;
g201708730@kfupm.edu.sa; elkatatny@kfupm.edu.sa
*Corresponding author: elkatatny@kfupm.edu.sa

where $\upsilon_{dynamic}$ is the dynamic Poisson's ratio, V_s is the shear-wave velocity in km/s, V_p is the compressional-wave velocity in km/s, $E_{dynamic}$ is the dynamic Young's modulus in GPa, and ρ is the formation bulk density in g/cm^3.

P-wave and S-wave velocities are usually measured in the field using a sonic logging tool. This tool provides the interval transit time of the formation denoted by Δt_{comp} for the compressional-wave velocity and Δt_{shear} for the shear-wave velocity. These velocities are greatly dependent on the formation type and the saturating fluid; thereafter, these data can be used for determining the formation type, porosity, and the fluid filling the pores (Bassiouni, 1994). Sonic data can be obtained using logging-while-drilling (LWD) tools; however, sonic tools are not usually integrated into such technique while drilling, especially in development wells. This is because of several economic and operational limitations due to the harsh drilling environment. Sonic data can also be obtained using wireline-logging tools, which are usually run after the formations have been drilled (Wraight et al., 1989; Bassiouni, 1994). Therefore, these data are not always available during the drilling operation, which increases the potential for several problems due to the lack of such data required for identifying the drilled formations.

Several trials have been reported in the literature for determining the velocities of the P-wave and S-wave. Carroll (1969) developed a correlation to estimate S-wave velocity from P-wave velocity for rocks with Poisson's ratio ranging from 0.15 to 0.35 and porosities between 0.1 to 0.3. Castagna et al. (1985) presented a correlation for estimating S-wave velocity as a function of the velocity of a P-wave via different correlations depending on the type of formations. Furthermore, Brocher (2005) also introduced a correlation to calculate S-wave velocity from P-wave velocity within the range of 1.5 to 8.5 km/s. Moreover, it was found that S-wave velocity can be predicted from logging data (RHOB, neutron porosity, and P-wave velocity) using artificial intelligence and regression-based correlations (Eskandari et al., 2004). Besides, P-wave can be predicted from logging data, including resistivity, porosity, and gamma ray, using regression approaches (de Augusto and Martins, 2009). Recently, several studies introduced the implementation of different artificial intelligence techniques for estimating sonic transit times from well-log data and seismic data (Maleki et al., 2014; Hadi and Nygaard, 2018; Elkatatny et al., 2018; Muqtadir et al., 2019).

Based on the literature, most of the trials for determining the sonic waves' velocities depended on the availability of other logging data; however, these logging data are not always available during the drilling operation due to the harsh drilling environment (Jackson and Heysse, 1994). Therefore, synthetic well-log generation using artificial intelligence methods has been presented as an effective tool for providing a complete well-log data profile when these data are not available or even for those sites where the well-log data are partially nonexistent (Zhang et al., 2018).

The nature of the subterranean formations significantly affects the drilling performance and, in turn, the parameters controlling the drilling operation (Bourgoyne et al., 1986). These parameters, including torque (T), weight on bit (WOB), mud pumping rate in gallon per minute (GPM), rotating speed in revolution per minute (RPM), drilling fluid pumping pressure (SPP), and rate of penetration (ROP), are usually adjusted based on the nature of the drilled formations (Mensa-Wilmot et al., 1999). Gowida et al. (2019) showed that these drilling parameters could be used for predicting the formation bulk density while drilling using artificial intelligence methods. Therefore, the objective of this study is to develop new models using neural networks (ANN) for predicting P-wave and S-wave velocities while drilling using the drilling parameters as inputs for feeding the models. Thereafter, the dynamic elastic parameters can be estimated using the predicted synthetic well-log data via Eqs. 1 and 2.

Artificial Neural Network (ANN)

Recently, the ANN technique has been implemented in many applications in the oil and gas industry (Ashena and Thonhauser, 2015). Its structure is inspired by the biological neural systems of human brains and imitates the way of processing the signals to produce the output (Angelini and Ludovici, 2009). The outstanding performance of ANN in different applications showed its great ability to outperform the conventional regression method and simulate nonlinear systems and complex problems (Razi and Naderi, 2013). The primary units for the neural network system are called "neurons," which are used for processing and training the network. The neural network is composed of a group of connections to link between the inputs, neurons, and the output. These connections are weighted based on the nature of the problem (Rao and Ramamurti, 1993). The backpropagation algorithm is considered one of the recommended algorithms for training the networks (Yagiz et al., 2012). There are three main types of layers forming the network: input, hidden, and output layers. Feeding the input layer with the input data, the data passes through the processing neurons in the hidden layer(s), thereafter passing through the output layer, which eventually produces

the predicted output (Lippman, 1987). Different transfer functions are assigned to the hidden and output layers to link between the layers. Optimizing the number of neurons is essential to avoid over/underfitting and the memorization issue (Rao and Ramamurti, 1993). A simplified schematic diagram typically mimics the developed neural network, which is depicted in the following section.

METHODOLOGY

Data Description

A field data set of 1,421 points is used for developing the proposed models, representing a horizontal well in the Middle East region. It includes drilling parameter measurements (T, ROP, RPM, SPP, WOB, and GPM) and the corresponding well-log data, namely compressional (P-wave) and shear (S-wave) transit times (Δt_{comp} and Δt_{shear}). These drilling parameters are usually adjusted based on the type of the drilled formation and are always available during the drilling operation. The drilling parameters used in this model are surface drilling information, and their measurements respond to the nature of the downhole formations at the bit. These data have been measured using highly precise sensors to provide actual measurements with high accuracy. The obtained data have passed through a step of corrections in order to remove noise and unreasonable readings from the data to be more reliable and representative. For building the proposed models, these drilling parameters are used as inputs for the network to predict Δt_{comp} and Δt_{shear} as outputs.

Data Processing

The obtained data were filtered from any noise and unreasonable values like negative and 999 values, especially found in the log data. The data were then cleaned from outliers that showed an obvious deviation from the normal trends of the data. These outliers were removed using a specially developed MATLAB program based on a box-and-whisker-plot technique, in which the top whisker represents the upper limit of the data, and the bottom whisker represents the lower limit of the data. Any value beyond these limits was considered an outlier and removed (Dawson, 2011). These limits were determined based on the statistical analysis of the data listed in Table 1. Statistical analysis was also performed on the filtered data, which showed good distribution of the data and coverage of wide ranges of the different input and output parameters, as listed in Table 1. Figure 1 shows a graphical presentation of the input data used for developing the proposed models along the selected depth.

Relative Importance Between Δt_{comp} and Δt_{shear} With the Drilling Parameters

The correlation coefficient (R) is selected to study the relative importance between the inputs (RPM, ROP, WOB, T, GPM, and SPP) and the outputs (Δt_{comp} and Δt_{shear}). For the P-wave model, it is found that Δt_{comp} has a correlation coefficient of –0.10, 0.23, 0.12, 0.07, 0.08, and 0.21 with GPM, RPM, SPP, T, WOB, and ROP, respectively. WOB and T have the lowest R-value with Δt_{comp}, as shown in Fig. 2. However, plotting Δt_{comp} vs. T and WOB showed that both T and WOB vary greatly with Δt_{comp}, as shown in Figs. 3a and 3b, respectively. Accordingly, these variations would have effects on the predicted Δt_{comp} values. The more information available on the problem attribute, the more accuracy is expected from the developed network. Therefore, these two inputs were not excluded despite their low-linear correlation coefficient with the output.

Table 1—Statistical Analysis for the Selected Data Set

Parameter	GPM	RPM	SPP (psi)	T (klb-ft)	WOB (klb)	ROP (ft/hr)	Δt_{comp} (µs/ft)	Δt_{shear} (µs/ft)
Minimum	193.66	60.63	2741.43	3.22	6.98	6.70	45.39	87.98
Maximum	273.77	134.12	3585.49	7.69	24.23	52.19	70.12	131.44
Mean	261.62	105.57	3348.12	5.93	17.71	28.87	52.48	98.94
Mode	263.10	120.61	3399.12	5.67	17.53	25.90	51.47	100.42
Range	80.11	73.49	962.83	4.87	17.24	45.49	24.73	43.47
Skewness	–2.11	–0.30	–0.85	–0.38	–0.84	–0.84	1.17	1.08

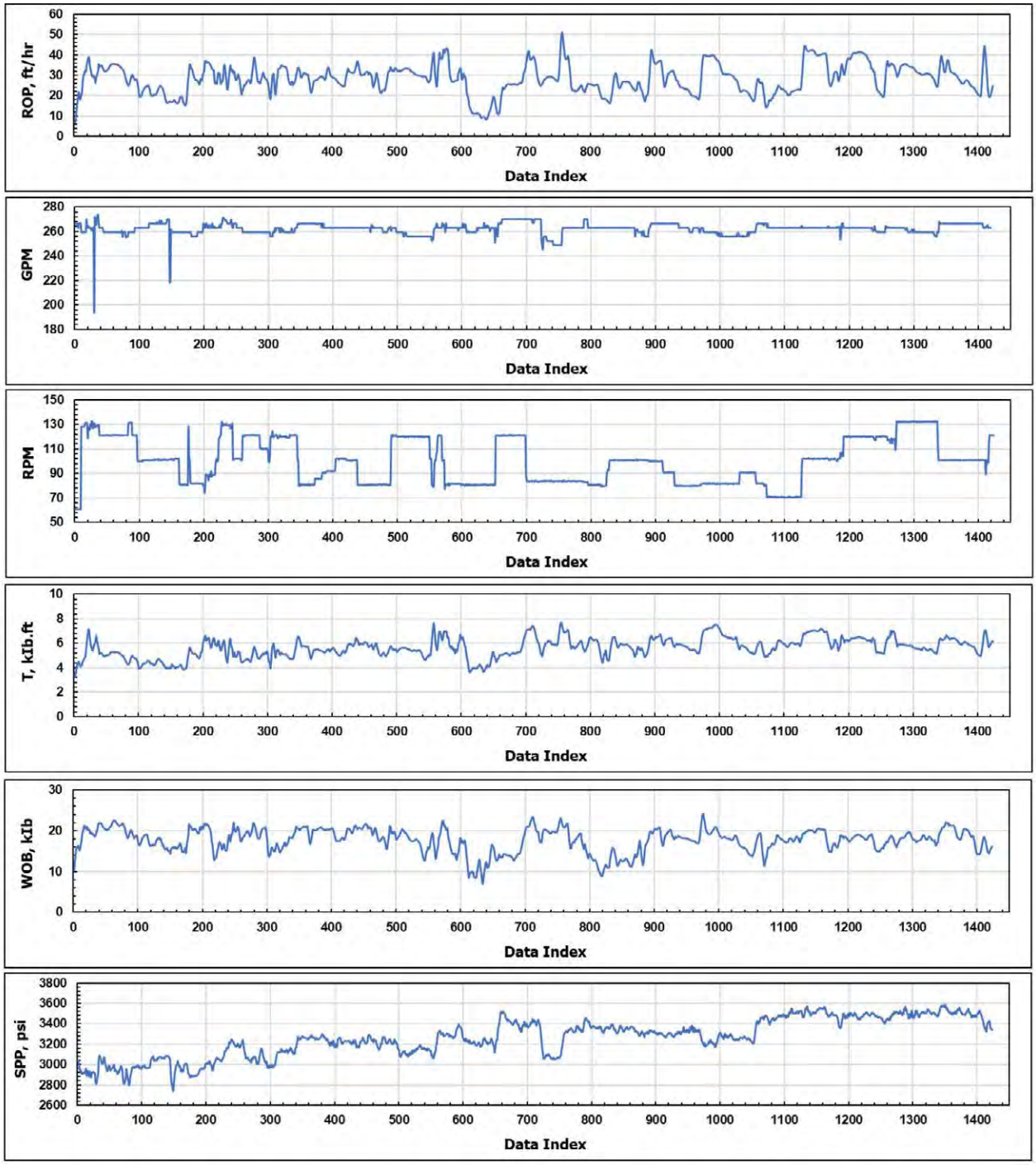

Fig. 1—Graphical presentation of the input data used for developing the proposed models.

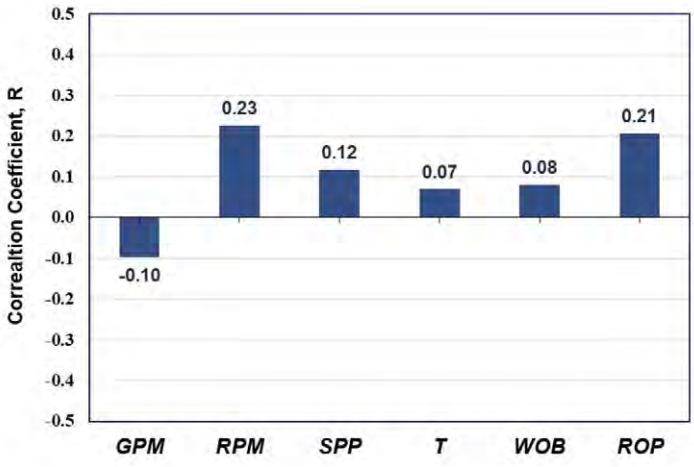

Fig. 2—Relative importance between the input(s) and compressional-wave transit time, Δt_{comp}.

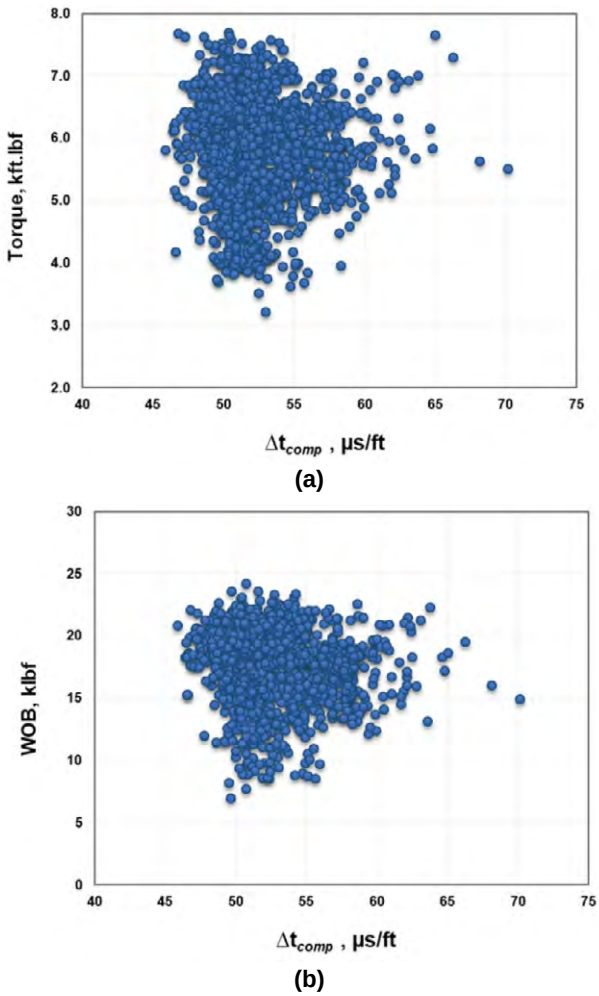

Fig. 3—The distribution of the two input parameters T and WOB with compressional-wave transit time (a) Δt_{comp} vs. T and (b) Δt_{comp} vs. WOB. This shows obvious variations in Δt_{comp} along with the T and WOB data ranges.

For the S-wave model, Δt_{shear} is found to have R of –0.12, 0.22, 0.17, –0.07, –0.17, and –0.08 with GPM, RPM, SPP, T, WOB, and ROP, respectively, as shown in Fig. 4. The low value of R only indicates that there is no significant linear relationship between the two variables under study; however, any other nonlinear relation between them may exist. ROP and T are found to have low R values with Δt_{shear}. So, to check the variation of these parameters with Δt_{shear}, Figs. 5a and 5b are plotted to show that ROP and T vary significantly with different Δt_{shear} values. These variations would probably help the neural networks to learn more about the nature of the problem so that it would be able to figure out any nonlinear relation between the inputs and the desired output.

P-WAVE AND S-WAVE TRANSIT-TIME MODEL DEVELOPMENT

The selected input parameters (GPM, RPM, SPP, T, WOB, and ROP) are then used for training the networks to optimize the neural network parameters. The ANN parameters to be optimized include:

- The splitting ratio of the data set for the training and testing processes
- Training algorithm
- Transfer functions
- Number of neurons in each hidden layer
- Number of hidden layer(s)
- Learning rate

The developed neural network was trained using the stochastic gradient descent optimization algorithm, and weights are updated using the backpropagation of error

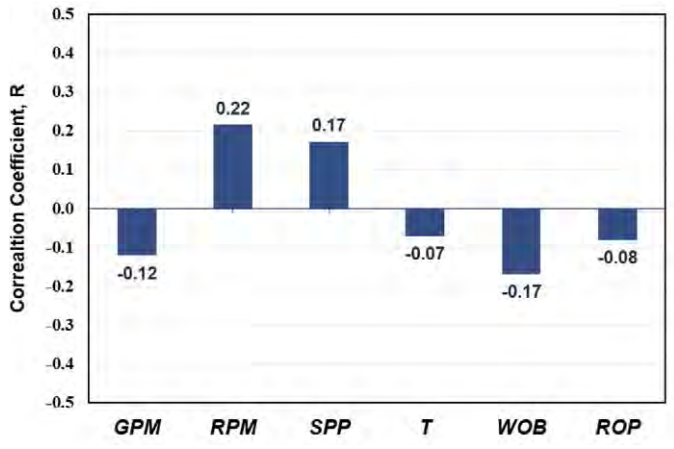

Fig. 4—Relative importance between the input(s) and shear-wave transit time, Δt_{shear}.

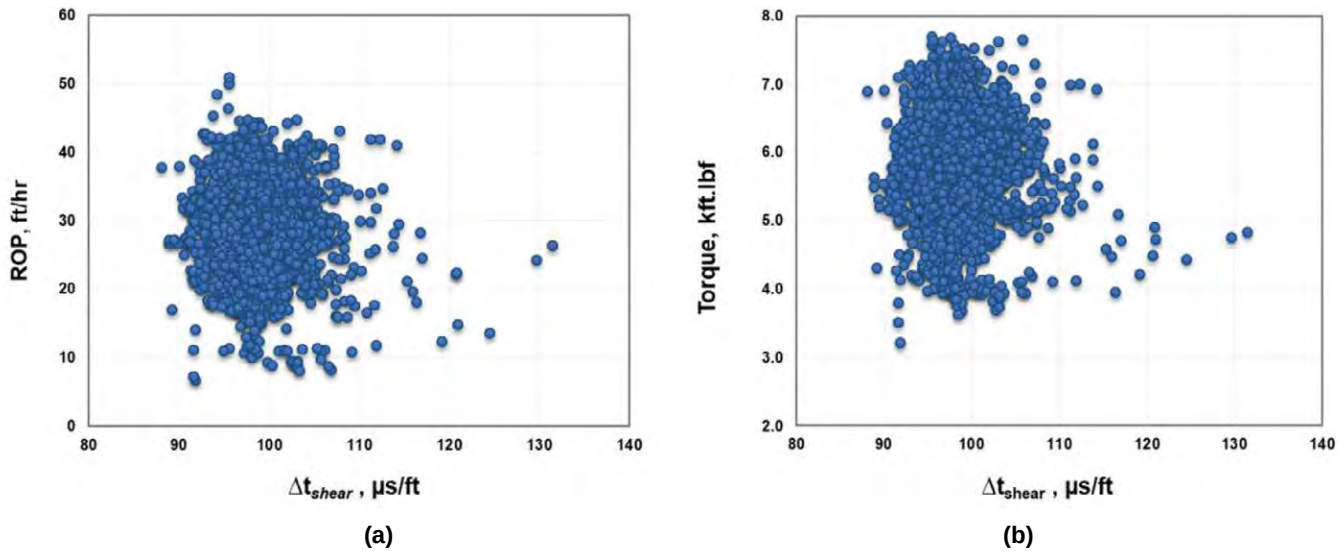

Fig. 5—The distribution of the two input parameters ROP and T with shear-wave transit time (a) Δt_{shear} vs. ROP and (b) Δt_{shear} vs. T. This shows an obvious variation in Δt_{shear} along with the whole data ranges of ROP and T.

algorithm. The gradient descent algorithm seeks to change the weights so that the next evaluation reduces the error, meaning the optimization algorithm is navigating down the gradient (or slope) of error. The mean squared error (MSE) was used as a function to loss to estimate the error and update the network weights to reduce that error to the minimum possible value.

The optimization process was implemented using different combinations of the available options of the aforementioned ANN parameters. The optimized parameters, which resulted in the highest correlation coefficient (R) and the lowest average absolute percentage error (AAPE) between the predicted and the measured values of Δt_{comp} and Δt_{shear}, were selected. The selected optimized parameters are listed in Table 2. Figure 6 shows the architecture of the developed Δt_{comp} and Δt_{shear} models.

The obtained results showed a high match between the predicted and measured Δt_{comp} values with R of 0.96 and 0.94 and an AAPE of 0.99 and 1.18% for the training and testing processes, respectively. In Fig. 7, the significant match between the actual and predicated Δt_{comp} values is also inferred from the crossplots, which show that the predicted values were so close to the actual values. Figure 8 shows a graphical distribution of the actual vs. predicted Δt_{comp} values for training and testing processes. Moreover, the absolute percentage error distribution between the actual and predicted Δt_{comp} values over the total used data points did not exceed 3.8% of the actual value, as shown in Fig. 9.

Table 2—Optimized ANN Parameters

Parameter	Optimized Parameter	
	P-Wave Model	S-Wave Model
Splitting Ratio (Training/Testing)	0.75 / 0.25	0.90 / 0.10
No. of Hidden Layers	1	
Neurons Number in Each Layer	20	23
Training Algorithms	Levenberg-Marquardt backpropagation (trainlm)	
Transfer Function	(Tans-Sigmoidal)	
Learning Rate	0.12	

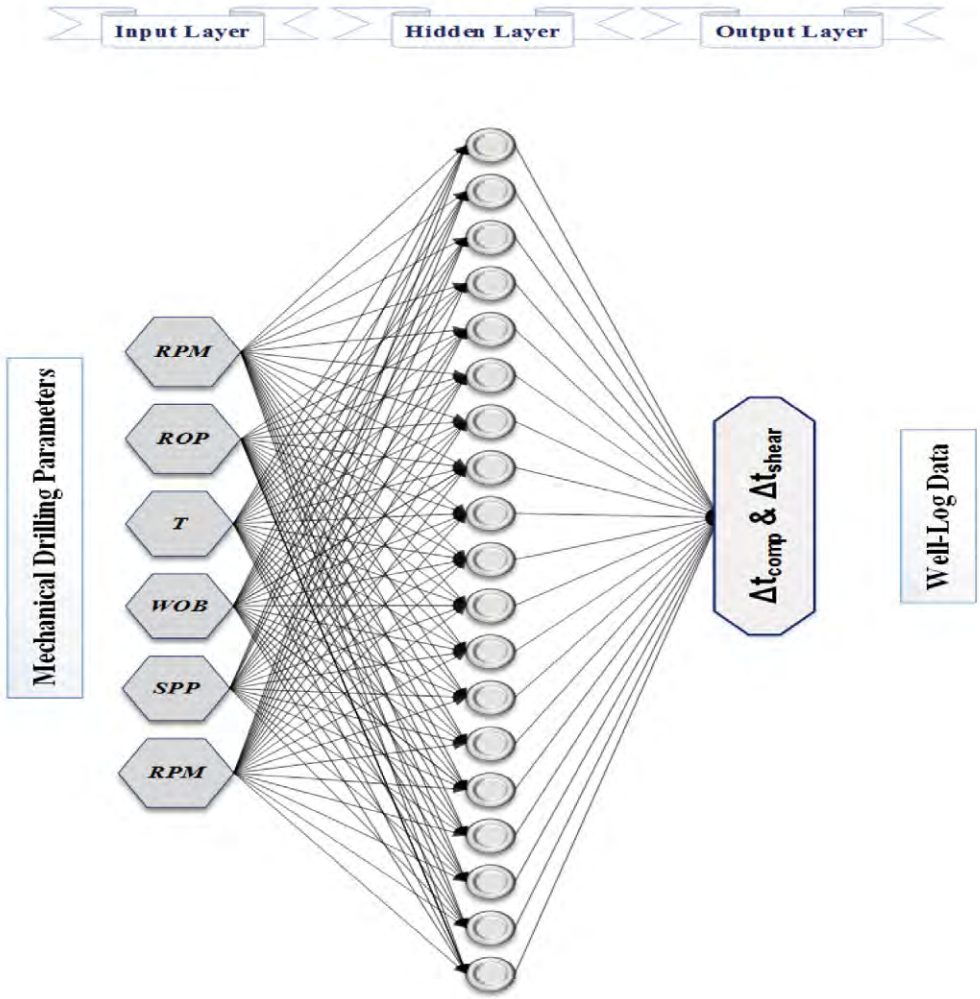

Fig. 6—Typical architecture of the developed ANN models.

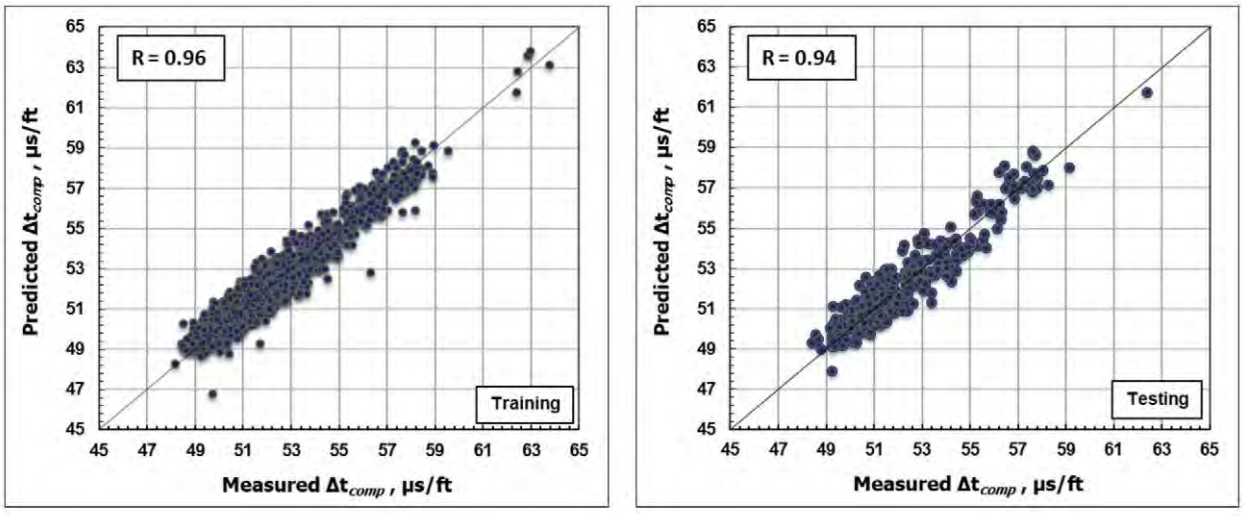

Fig. 7—Crossplots between the actual and predicted Δt_{comp} values for (a) training and (b) testing processes.

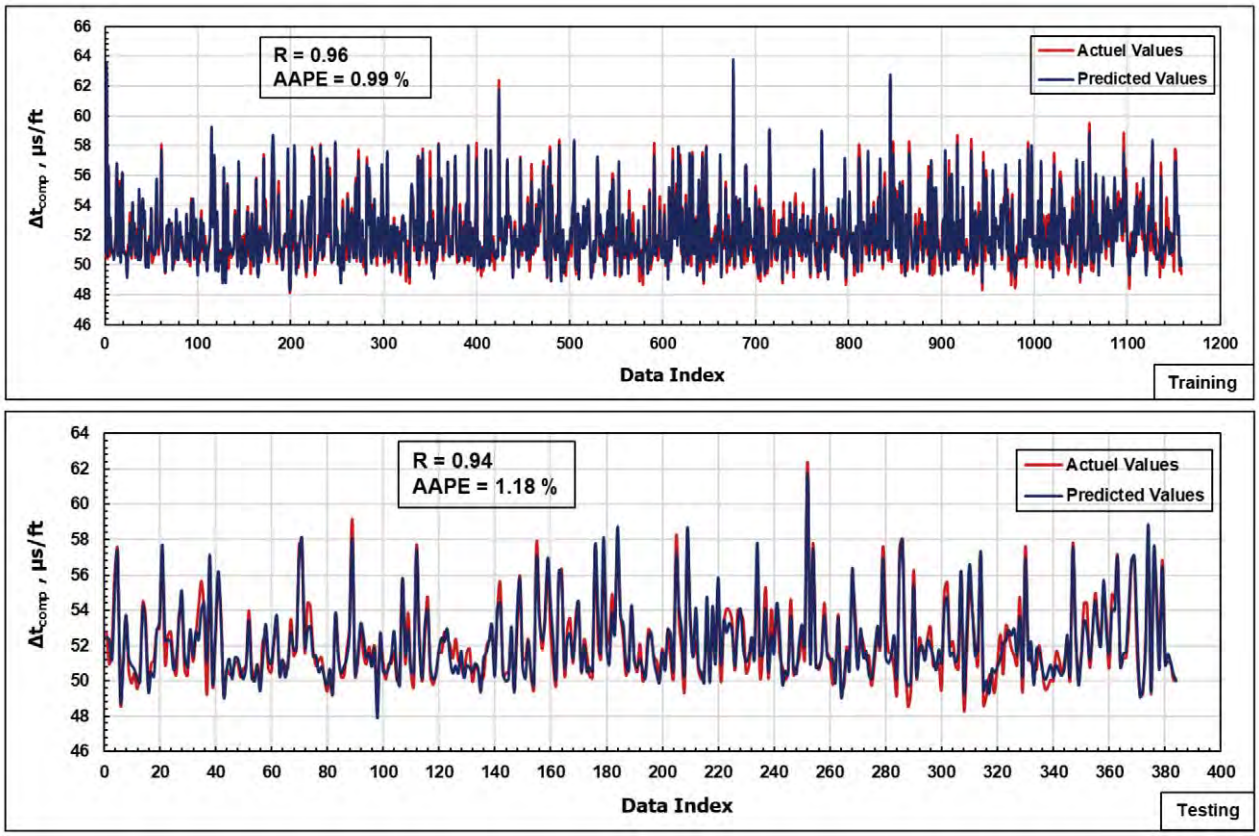

Fig. 8—Graphical distribution of the actual vs. predicted Δt_{comp} values for (a) training and (b) testing processes.

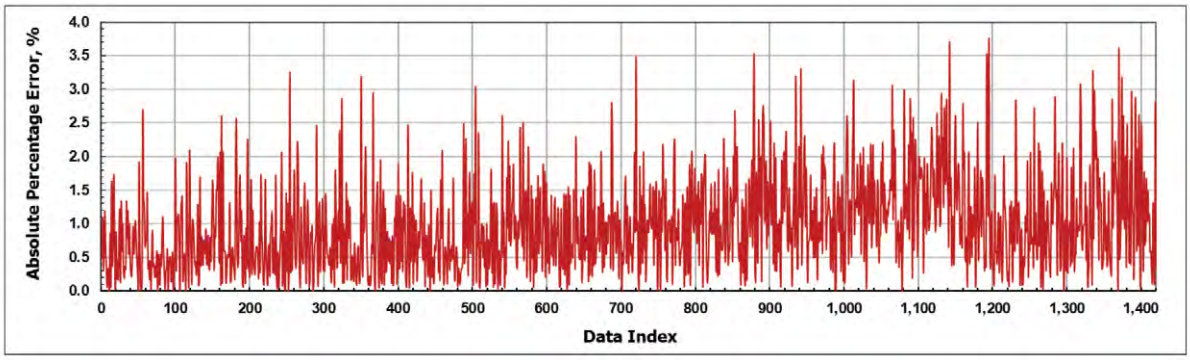

Fig. 9—Absolute percentage error distribution over the total used data points between actual and predicted Δt_{comp} values.

In Fig. 10, the crossplot of the actual and predicted Δt_{shear} showed the high accuracy of the developed model where R was 0.95 and 0.93 for the training and testing processes, respectively. In Fig. 11, the absolute error distribution confirmed the robustness of the developed model as the highest error did not exceed 3.6% of the measured Δt_{shear} values. Besides, as seen in Fig. 12, plotting the measured and predicted Δt_{shear} values on a graphical distribution infers the high accuracy of the prediction process as most of the predicted values are so close to the corresponding measured values and have an AAPE of 0.80 and 0.87% for the training and testing processes, respectively.

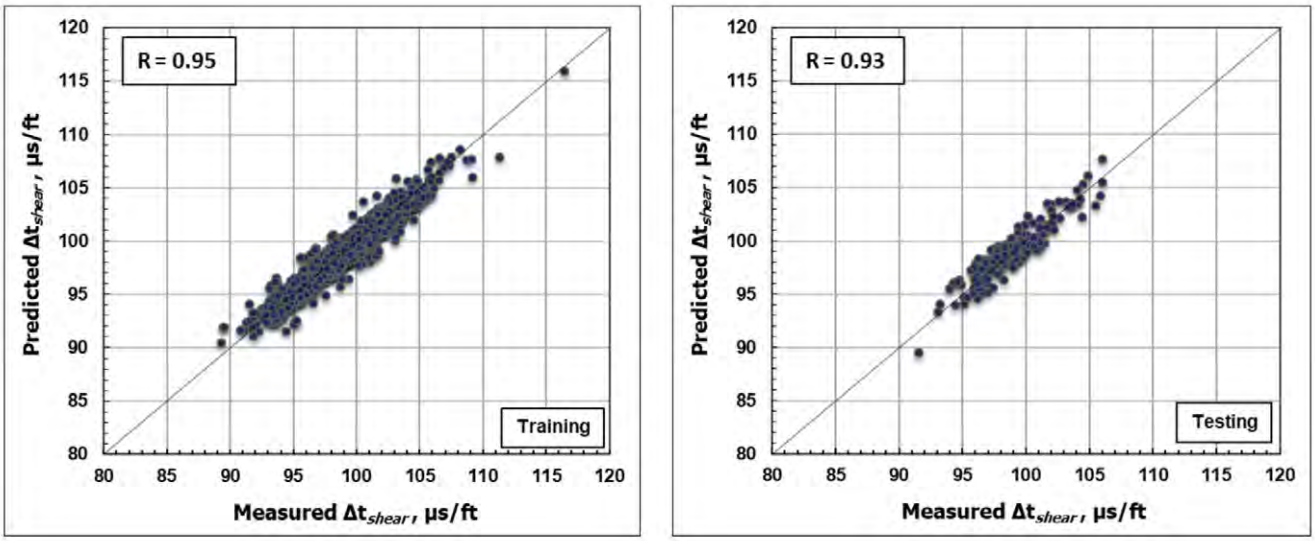

(a) (b)

Fig. 10—Crossplots between the actual and predicted Δt_{shear} values for (a) training and (b) testing processes.

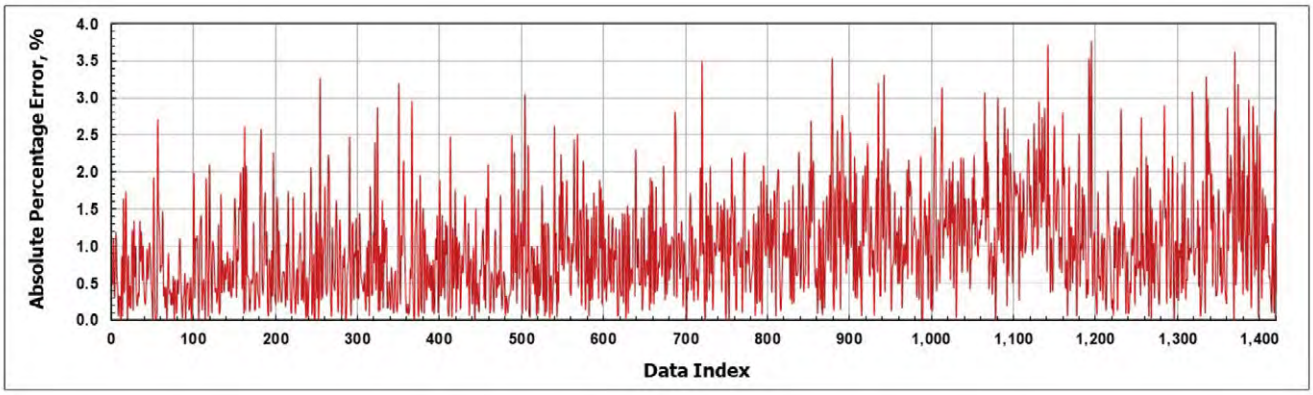

Fig. 11—Absolute percentage error distribution over the total used data points between actual and predicted Δt_{shear} values.

MODELS VALIDATION

To validate the developed P-wave and S-wave models, a data set collected from another well in the same field under study is used to feed the developed networks to predict Δt_{comp} and Δt_{shear}. The selected data set for the validation process included 417 data points for a continuous depth range comprising GPM, RPM, T, SPP, ROP, and WOB and the corresponding Δt_{shear} and Δt_{shear} well-log data. After feeding the developed models with the input data, the predicted results are then compared with the actual measured values. The results showed that the predicted Δt_{comp} and Δt_{shear} values considerably match the measured values (see Fig. 13) indicated by the AAPE of 1.87 and 1.30% for Δt_{comp} and Δt_{shear} models, respectively. Figure 14 also shows a crossplot between the actual and predicted values of sonic wave transit times during the validation process.

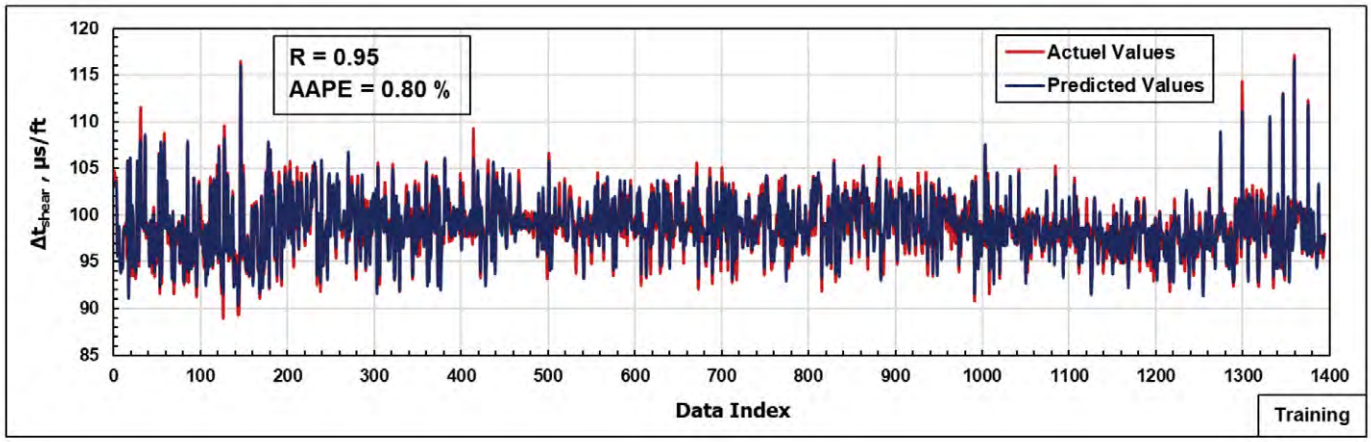

(a)

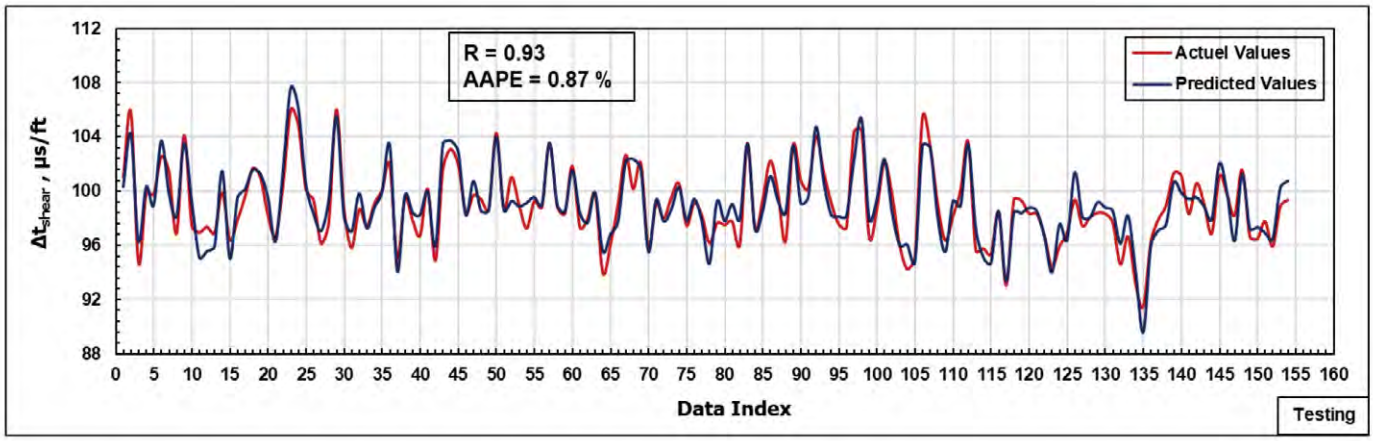

(b)

Fig. 12—Graphical distribution of the actual vs. predicted Δt_{shear} values for (a) training and (b) testing processes.

According to the discussed results, the developed models present a viable tool for predicting Δt_{comp} and Δt_{shear} while drilling directly for the permanently available mechanical drilling parameters. This technique can be used as an alternative to a conventional logging tool in development wells, especially since wireline-logging tools are usually run into the hole after the drilling operation, which can hinder the availability of such information. Sonic wave transit times are very beneficial for identifying the downhole formations during drilling to avoid many problems, such as sticking, kicks, and blowouts. Besides, it can provide more valuable information like formation porosity and the type of fluid saturating the pores. Such information is very important, especially while drilling reservoir sections for better planning decisions. Moreover, the integration between sonic wave data and the formation bulk density could be used to estimate the elastic parameters of the drilled formations so that their mechanical behavior can be calculated in real time during the drilling process, and adequate real-time actions can be taken.

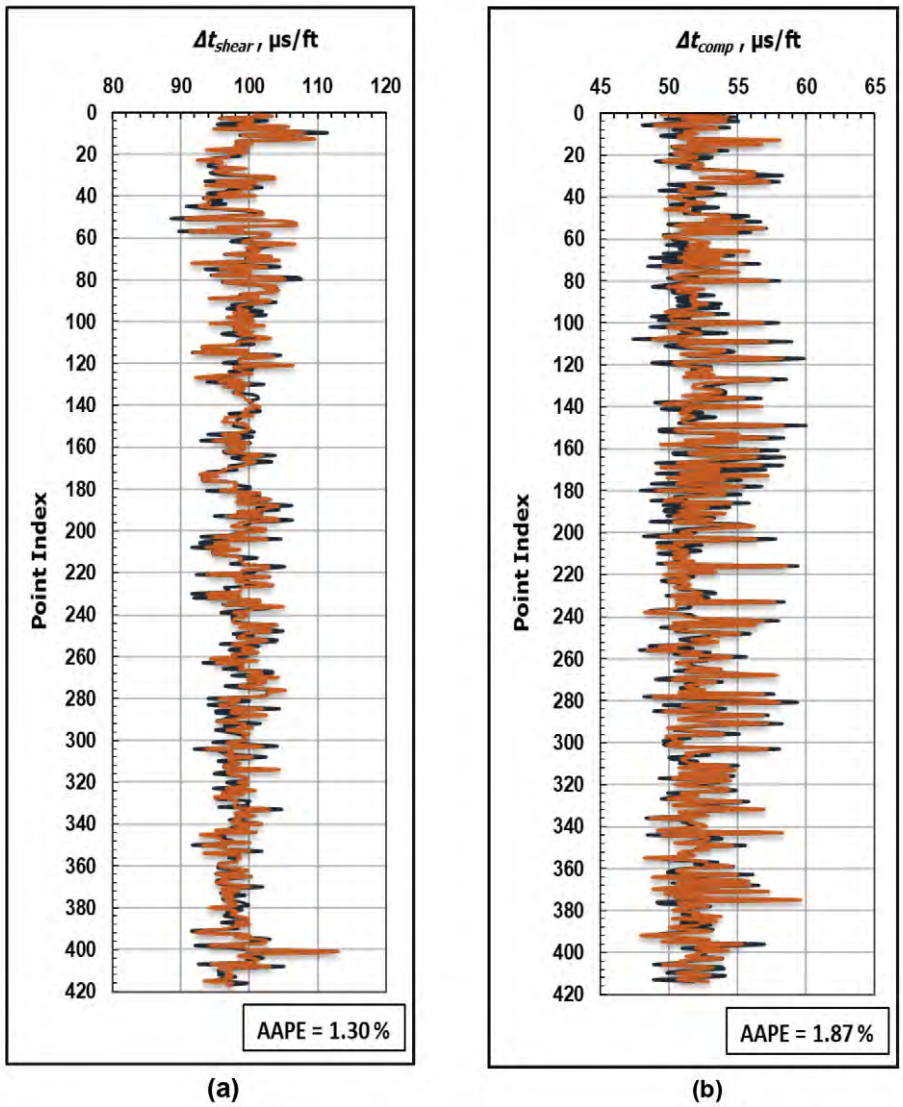

Fig. 13—Comparison between the measured and predicted values from (a) P-wave models and (b) S-wave models during the validation process.

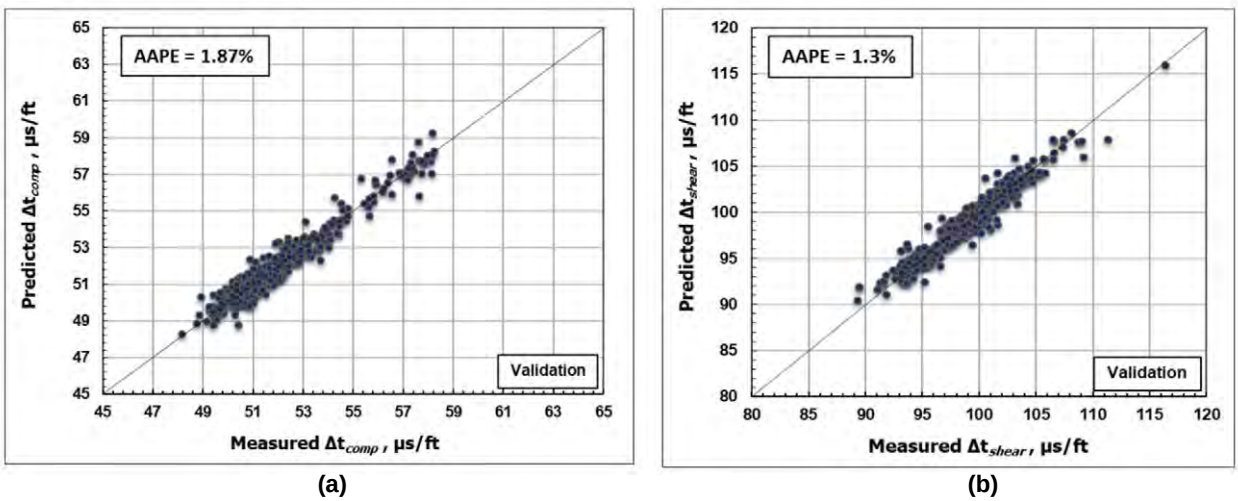

Fig. 14—Crossplots between the measured and predicted values from (a) P-wave models and (b) S-wave models during the validation process.

CONCLUSIONS

In this work, a neural network technique has been implemented to develop two models for predicting the compressional P-wave (Δt_{comp}) and the shear S-wave (Δt_{shear}) transit times based on mechanical drilling parameters (GPM, RPM, WOB, T, ROP, and SPP). The optimized ANN parameters for the developed models can be summarized as both Δt_{comp} and Δt_{shear} comprised of only one hidden layer containing 20 neurons for the Δt_{comp} model and 23 neurons for the Δt_{shear} model. Both models were trained using the Levenberg-Marquardt backpropagation algorithm with a learning rate of 0.12 using transfer functions of the Tans-Sigmoidal type. The results showed a significant agreement between the predicted and measured values with a correlation coefficient (R) of 0.94 and 0.93, in addition to an AAPE of 1.18 and 0.87% for Δt_{comp} and Δt_{shear} predictions, respectively. The developed models are then validated using 417 new (unseen) data points from the same field to test the robustness of these models. The validation process demonstrates the high accuracy of the developed models indicated by an AAPE of 1.87 and 1.30% for Δt_{comp} and Δt_{shear}, respectively. The prediction of Δt_{comp} and Δt_{shear} while drilling using the developed models will help to identify the nature of the drilled formations once the bit touches the rock, in addition to the ability to estimate the dynamic geomechanical elastic parameters (Poisson's ratio and Young's modulus) of the rock, which will help to avoid several interrupting problems.

NOMENCLATURE

Abbreviations

ANN =	artificial neural network
AAPE =	average absolute percentage error
GPM =	gallon per minute
RHOB =	bulk density, gm/cm^3
ROP =	rate of penetration, ft/hr
RPM =	revolution per minute
SPP =	standpipe pressure, psi
T =	torque, klb-ft
WOB =	weight on bit, klb
Tansig =	tangent sigmoid transfer function
Pure-linear =	linear transfer function

Symbols

Δt_{comp} =	P-wave transit time
Δt_{shear} =	S-wave transit time
ρ =	formation bulk density

REFERENCES

Angelini, E., and Ludovici, A., 2009, CDS Evaluation Model With Neural Networks, *Journal of Service Science and Management*, **2**(1), 15–28. DOI: 10.4236/jssm.2009.21003.

Ahmed, U., and Meehan, D.N., eds., 2016, *Unconventional Oil and Gas Resources: Exploitation and Development*, CRC Press. ISBN: 9781498759403.

Ashena, R., and Thonhauser, G., 2015, Application of Artificial Neural Networks *in* Geoscience and Petroleum Industry, Chapter 4, in Cranganu, C., Luchian, H., and Breaban, M.E., editors, *Artificial Intelligent Approaches in Petroleum Geosciences*,127–166, Springer International Publishing. DOI: 10.1007/978-3-319-16531-8.

Bassiouni, Z., 1994, *Theory, Measurement, and Interpretation of Well Logs (Vol. 4)*, Henry L. Doherty Memorial Fund of AIME, Society of Petroleum Engineers. ISBN: 978-1555630560.

Bourgoyne, A.T., Jr., Millheim, K.K., Chenevert, M.E., and Young, F.S., Jr., 1986, *Applied Drilling Engineering*, SPE Textbook Series, Volume 2. ISBN: 978-1555630010.

Brocher, T.M., 2005, Empirical Relations Between Elastic Wavespeeds and Density in the Earth's Crust, *Bulletin of the Seismological Society of America*, **95**(6), 2081–2092. DOI: 10.1785/0120050077.

Carroll, R.D., 1969, The Determination of the Acoustic Parameters of Volcanic Rocks From Compressional Velocity Measurements, *International Journal of Rock Mechanics and Mining Science & Geomechanics Abstracts*, **6**(6), 557–579. DOI: 10.1016/0148-9062(69)90022-9.

Castagna, J.P., Batzle, M.L., and Eastwood, R.L., 1985, Relationships Between Compressional-Wave and Shear-Wave Velocities in Clastic Silicate Rocks, *Geophysics*, **50**(4), 571–581. DOI: 10.1190/1.1441933.

Darling, T., 2005, *Well Logging and Formation Evaluation*, 1st edition, Gulf Professional Publishing. DOI: 10.1016/B978-0-7506-7883-4.X5000-1.

Dawson, R., 2011, How Significant Is A Boxplot Outlier?, *Journal of Statistics Education*, 2011, **19**(2). DOI:10.1080/10691898.2011.11889610.

de Augusto, F.O.A., and Martins, J.L., 2009, A Well-Log Regression Analysis for P-wave Velocity Prediction in the Namorado Oil Field, Campos Basin, *Revista Brasileira de Geofísica*, **27**(4), 595–608. DOI: 10.1590/S0102-261X2009000400005.

Elkatatny, S., Tariq, Z., Mahmoud, M.,Abdulraheem, A., and Mohamed, I., 2018, An Integrated Approach for Estimating Static Young's Modulus Using Artificial Intelligence Tools, *Neural Computing and. Applications*, **8**, 4123–4135. DOI: 10.1007/s00521-018-3344-1.

Eskandari, H., Rezaee, M.R., and Mohammadnia, M., 2004, Application of Multiple Regression and Artificial Neural Network Techniques to Predict Shear Wave Velocity From Wireline Log Data for a Carbonate Reservoir, South-West Iran, *CSEG Recorder*, **29**(7), 42–48.

Fjar, E., Holt, R.M., Raaen, A.M., and Horsrud, P., 2008, *Petroleum*

Related Rock Mechanics, Volume 53, second edition, Elsevier Science. ISBN: 9780444502605.

Gatens, J.M., III, Harrison, C.W., III, Lancaster, D.E., and Guidry, F.K., 1990, In-Situ Stress Tests and Acoustic Logs Determine Mechanical Properties and Stress Profiles in the Devonian Shales, Paper SPE-18523, *SPE Formation Evaluation*, **5**(03), 248–254. DOI: 10.2118/18523-PA.

Gowida, A., Elkatatny, S., and Abdulraheem, A., 2019, Application of Artificial Neural Network To Predict Formation Bulk Density While Drilling, *Petrophysics*, **60**(05), 660–674. DOI: 10.30632/PJV60N5-2019a9.

Hadi, F.A., and Nygaard, R., 2018, Shear Wave Prediction in Carbonate Reservoirs: Can Artificial Neural Network Outperform Regression Analysis?, Paper ARMA-2018-905 presented at the 52nd US Rock Mechanics/Geomechanics Symposium, Seattle, Washington, USA, 17–20 June.

Jackson, C.E., and Heysse, D.R., 1994, Improving Formation Evaluation by Resolving Differences Between LWD and Wireline Log Data, Paper SPE-28428 presented at the SPE Annual Technical Conference and Exhibition, New Orleans, Louisiana, USA, 25–28 September. DOI: 10.2118/28428-MS.

Lippman, R.P., 1987, An Introduction to Computing With Neural Nets, *IEEE ASSP Magazine*, **4**(2), 4–22. DOI: 10.1109/massp.1987.1165576.

Maleki, S., Moradzadeh, A., Riabi, R.G., Gholami, R., and Sadeghzadeh, F., 2014, Prediction of Shear Wave Velocity Using Empirical Correlations and Artificial Intelligence Methods, *NRIAG Journal of Astronomy and Geophysics*, **3**(1), 70–81. DOI: 10.1016/j.nrjag.2014.05.001.

Mensa-Wilmot, G., Calhoun, B., and Perrin, V.P., 1999, Formation Drillability-Definition, Quantification and Contributions to Bit Performance Evaluation, Paper SPE-57558 presented at the SPE/IADC Middle East Drilling Technology Conference, Abu Dhabi, UAE, 8–10 November. DOI: 10.2118/57558-MS.

Muqtadir A., Elkatatny, S.M., Tariq., Z., Mahmoud, M., and Abdulraheem, A., 2019, Application of Artificial Intelligence to Predict Sonic Wave Transit Time in Unconventional Tight Sandstones, Paper ARMA 19–1636 presented at the 53rd US Rock Mechanics/Geomechanics Symposium, New York, New York, USA, 23–26 June.

Najibi, A.R., Ghafoori, M., Lashkaripour, G.R., and Asef, M.R., 2015, Empirical Relations Between Strength and Static and Dynamic Elastic Properties of Asmari and Sarvak Limestones, Two Main Oil Reservoirs in Iran, *Journal of Petroleum Science and Engineering*, **126**, 78–82. DOI: 10.1016/j.petrol.2014.12.010.

Nes, O.M., Fjær, E., Tronvoll, J., Kristiansen, T.G., and Horsrud, P., 2005, Drilling Time Reduction Through an Integrated Rock Mechanics Analysis, Paper SPE-92531 presented at the SPE/IADC Drilling Conference, Amsterdam, Netherlands, 23–25 February. DOI: 10.2118/92531-MS.

Rao, S., and Ramamurti, V., 1993, A Hybrid Technique to Enhance the Performance of Recurrent Neural Networks for Time Series Prediction, *IEEE International Conference on Neural Networks*, **1**, 52–57. DOI: 10.1109/ICNN.1993.298532.

Razi, M., Arz, A., and Naderi, A., 2013, Annular Pressure Loss While Drilling Prediction With Artificial Neural Network Modeling, *European Journal of Scientific Research*, **95**(2), 272–288.

Tutuncu, A.N., and Sharma, M.M., 1992, Relating Static and Ultrasonic Laboratory Measurements to Acoustic Log Measurements in Tight Gas Sands, Paper SPE-24689 presented at the SPE Annual Technical Conference and Exhibition, Washington, DC, USA, 4–7 October. DOI: 10.2118/24689-MS.

Wraight, P.D., Evans, M., Marienbach, E., Rhein-Knudsen, E., and Best, D., 1989, Combination Formation Density and Neutron Porosity Measurements While Drilling, Paper B, *Transactions, SPWLA 30th Annual Logging Symposium*, Denver, Colorado, USA, 11–14 June.

Yagiz, S., Sezer, E.A., and Gokceoglu, C., 2012, Artificial Neural Networks and Nonlinear Regression Techniques to Assess the Influence of Slake Durability Cycles on the Prediction of Uniaxial Compressive Strength and Modulus of Elasticity for Carbonate Rocks, *International Journal for Numerical and Analytical Methods in Geomechanics*, **36**(14), 1636–1650. URL: https://doi.org/10.1002/nag.1066. Accessed August 24, 2020.

Zhang, D., Chen, Y., and Meng, J., 2018, Synthetic Well Logs Generation via Recurrent Neural Networks, *Petroleum Exploration and Development*, **45**(4), 629–639. DOI: 10.1016/S1876-3804(18)30068-5.

ABOUT THE AUTHORS

Ahmed Gowida is a PhD student in the Department of Petroleum Engineering at King Fahd University of Petroleum & Minerals (KFUPM), Dhahran, KSA. He holds an MSc degree from KFUPM and a BS degree from Suez University, Egypt. His areas of interest are artificial intelligence, geomechanics, drilling optimization, production enhancement, and reservoir characterization.

Salaheldin Elkatatny is an associate professor at King Fahd University of Petroleum & Minerals. He is an associate professor at Cairo University, on leave. He worked as a senior geomechanical engineer at Advantek International Company for 5 years. He received his PhD in petroleum engineering at Texas A&M University, College Station, Texas. He received his BSc and MSc degrees in petroleum engineering from Cairo University, Egypt. He also worked with SUCO Oil Company as a drilling engineer for a year. His areas of research include drilling fluid optimization, filter-cake removal, oil-well cementing, artificial intelligence, and geomechanics.

PETROPHYSICS, VOL. 61, NO. 5 (OCTOBER 2020); PAGES 495–518; 22 FIGURES; 1 TABLE. DOI: PJV61N5-2020a7

Integrated Multiphysics Workflow for Automatic Rock Classification and Formation Evaluation Using Multiscale Image Analysis and Conventional Well Logs

Andres Gonzalez[1], Lawrence Kanyan[1], Zoya Heidari[1*], and Olivier Lopez[2]

ABSTRACT

Conventional well-log-based rock classification often overlooks rock-fabric features (spatial distribution of solid and fluid-rock components), which makes it not comparable against geologic facies, especially in formations with complex rock fabric. This challenge is usually addressed by the identification of geological facies from the core description and their integration with measured petrophysical properties. However, manual identification of geological facies using core data is a tedious and time-consuming process. In this paper, we propose an automatic workflow for joint interpretation of conventional well logs, computed tomography (CT) scan/core images, and routine core analysis (RCA) data for simultaneously optimizing rock classification and formation evaluation. First, we perform conventional well-log interpretation to obtain petrophysical properties of the evaluated depth intervals. Subsequently, we automatically extract rock-fabric-related features derived from core photos and core CT scan images. Then, we use a clustering algorithm to obtain rock classes from the extracted rock-fabric features. We optimize the number of rock classes by iteratively increasing the number of rock classes from an initially assumed number until a permeability-based cost function converges below a predefined threshold. The proposed workflow will provide (i) quantitative wellbore/core image-based rock-fabric-related features, (ii) automatic integration of rock-fabric-related features with conventional well logs and RCA data, and (iii) automatic and simultaneous assessment of rock classes and petrophysical properties, honoring rock fabric. Additionally, the outcomes of the proposed workflow can help to expedite the process of geological facies classification by providing an overview of different lithologies and an overall stacking pattern.

We successfully applied the proposed workflow to a sedimentary sequence with vertically variable rock fabric and lithology. Dual-energy-acquired core CT scan images were available along with core photos, RCA data, and conventional well logs. Image-based integrated rock classes were in agreement with the lithologies encountered in the evaluated depth interval. Class-by-class permeability models improved permeability estimates by 89% (decrease in mean relative error) in comparison to formation-by-formation permeability estimates. Furthermore, the detected rock classes were consistently propagated to another well where core and CT scan images were not employed for rock classification. The detected rock classes were in agreement with lithofacies obtained from the core description. Permeability estimates were also in good agreement with available RCA data.

INTRODUCTION

The integration of geological facies and petrophysical properties is a crucial step in rock classification. Rock classification based solely on conventional logs often overlooks rock-fabric features and may not yield rock classes with well-defined dynamic behavior. Additionally, petrophysical rock classes may not always be related to reservoir geobodies, which makes the interwell extrapolation of petrophysical rock classes challenging. On the other hand, rock typing based solely on geological facies overlooks the rock dynamic properties, such as permeability, wettability, capillary pressures, and relative permeability. Rocks belonging to the same geological facies may have contrasting dynamic properties (Bae et al., 2006; Gomes et al., 2008). The contrast is further accentuated by early and late diagenetic changes that the rock may experience as well as by rock-fluid interactions.

To overcome these challenges, a synergistic integration of geological facies with associated dynamic properties is

Manuscript received by the Editor December 27, 2019; revised manuscript received June 24, 2020; manuscript accepted June 29, 2020
[1]Department of Petroleum and Geosystems Engineering at The University of Texas at Austin, 200 E Dean Keeton St., Austin, TX 78712; andresgonzalez@utexas.edu; lawrence.kanyan@utexas.edu; zoya@austin.utexas.edu
[2]Equinor, Arkitekt Ebbells veg 10, 7053 Ranheim, Norway; ollop@equinor.com

carried out to characterize the flow behavior of different rock types. The dynamic properties are usually available only from core measurements and indirectly from the interpretation of well-log measurements. The geological facies, on the other hand, are obtained by a physical description of core data, which is a tedious, time-consuming, and expert-dependent process. In order to reduce the time spent and the subjectivity introduced in the process of facies derivation from core description and wellbore image interpretation, several methodologies have been proposed to expedite and standardize intermediate steps of this process. Facies identification using well logs was first introduced by Serra and Abbott (1982). In this work, they used well logs capturing geological parameters (e.g., composition, texture, and sedimentary structure) and fluids along with clustering techniques to define "electrofacies." They used a dipmeter log as a proxy for rock texture (grain size, grain shape, sorting, distribution, matrix, and cement) and sedimentary structure (thickness and degree of lamination). Further development of dipmeter tools resulted in microresistivity imaging devices giving rise to resistivity image logs. Resistivity image logs contain essentially the same information as dipmeter logs but at a higher resolution and with a higher coverage of the wellbore circumference. The advent of this technology motivated the work of Torres et al. (1990), Delhomme (1992), Luthi (1994), Hall et al. (1996), Ye et al. (1997), Ye and Rabiller (1998), Kraaijveld and Epping (2000), Linek et al. (2007), Jungmann et al. (2011), and Kherroubi et al. (2016), among others. The main objective of the aforementioned authors was to quantify and characterize both rock texture and sedimentary structure using a combination of image analysis techniques and learning algorithms. The use of other types of wellbore/core image data (e.g., core photos, micro-CT, and CT scan images) for quantification and characterization of rock texture and sedimentary structure has been reported by Georgi et al. (1992), Chacko et al. (2012), Fitzsimons et al. (2016), and Govert et al. (2016), among others. The gross of the aforementioned references did not integrate the quantitative outcomes of rock texture and sedimentary structure with other well-log information to obtain "electrofacies" in the sense described by Serra and Abbott (1982). The use of wellbore/core image data, acquired honoring different physical principles and at different resolutions, reveals different characteristics of the evaluated rock interval. For instance, micro-CT scan images can reveal the pore structure of the rock, while resistivity image logs reveal structures of the rock in the millimeter scale.

Recent publications by Basu et al. (2002), Suarez-Rivera et al. (2012), and Al-Obaidi et al. (2018) integrated quantitative features derived from wellbore/core image data and well-log data for facies detection. Purba et al. (2018) developed a workflow for rock classification using well-log-based rock-fabric quantification. They used pore-scale images to carry out numerical simulations of electrical current and fluid flow, which quantified the relationship between electrical resistivity, conducting porosity, and permeability. Optimization of the number of rock classes in the aforementioned approach was accomplished by minimizing relative errors between permeability estimates in two subsequent iterative steps, following a similar method as the one proposed by Tibshirani et al. (2001) and Salvador and Chan (2004) using a cost function for the different number of classes and finding the "knee of error." Al-Obaidi et al. (2018) proposed an automatic workflow for rock classification by the integration of conventional well logs and image logs. The number of rock classes in the aforementioned workflow was obtained by means of a data clustering technique that seeks to automatically optimize the Bayesian Information Criterion (BIC).

Automatic detection of petrophysical rock classes and estimation of petrophysical properties through integration of wellbore/core image data with conventional well logs and RCA data is a nontrivial task. In this paper, we introduce a workflow for optimizing the number and location of rock classes through the integration of multiscale image data, conventional well logs, and RCA data. The proposed workflow employs image analysis and machine-learning techniques. Image-based rock-fabric features are derived from available multiscale image data using image analysis techniques. We identify rock classes in an iterative process by optimizing a permeability-based cost function. Finally, we use the image-derived rock classes to train a supervised learning algorithm in order to predict rock classes from well logs in an offset well without using core photos or CT scan images. In this paper, we use the term rock-fabric features as any quantitative feature extracted from wellbore/core image data that can be used for the detection of rock classes. On the other hand, the term texture is employed strictly in reference to image texture rather than rock texture. Texture in the image analysis domain is commonly defined as a region of an image where a local statistic is constant or varies slowly (Sklansky, 1978). On the other hand, rock texture is often defined as the size, shape, and arrangement of the grains that make up the rock (Serra and Abbott 1982).

METHOD

We introduced a workflow for automatic rock classification and integrated formation evaluation using conventional well logs, core CT scan images, core photos, and RCA data. Figure 1 shows the proposed workflow employed for automatic image-based rock class detection and formation evaluation. The proposed workflow includes conventional formation evaluation of the evaluated depth interval, rock-fabric features quantification from available multiscale image data, image-based rock classification, optimization of rock classes by the integration of image data with conventional well logs and RCA data, and propagation of rock classes to noncored wells. The following subsections describe the steps of the proposed workflow in more detail. The main steps of the proposed workflow can be summarized as follows:

1. Preprocessing of available image data
2. Extraction of image-based rock-fabric-related features
3. Conventional formation evaluation
4. Simultaneous detection of integrated rock classes (data clustering) and class-based assessment of petrophysical properties
5. Training of a supervised learning algorithm using the integrated rock classes as well as conventional well logs
6. Estimation of rock classes in noncored wells using the trained, supervised learning algorithm and conventional well logs from the noncored well
7. Class-based assessment of petrophysical properties in noncored wells

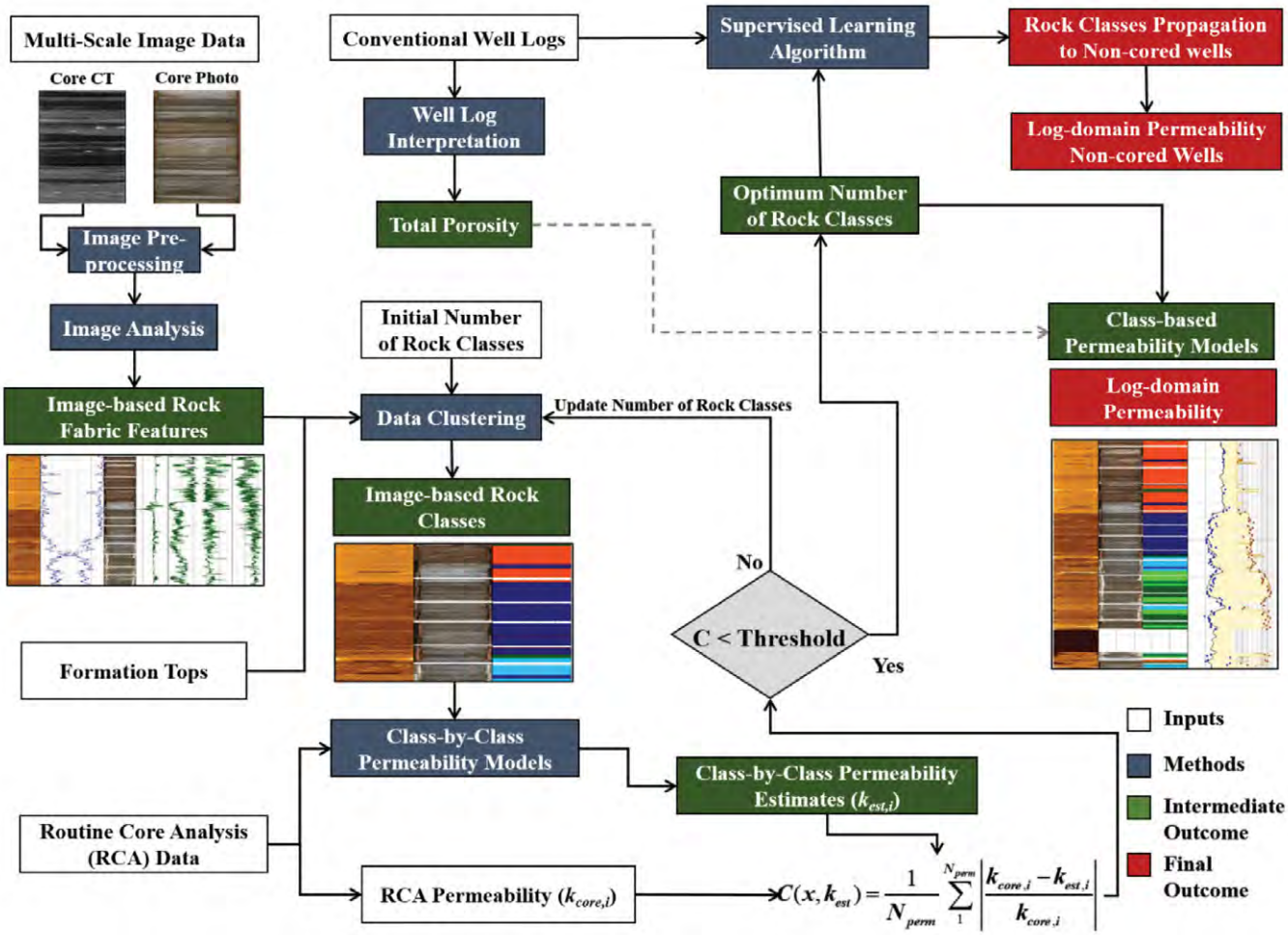

Fig. 1—Workflow for optimization of number and location of rock classes through the integration of multiscale image data, conventional well logs, and RCA data.

Conventional Formation Evaluation

The first step includes formation evaluation in the interval of interest using conventional well logs. At the initial stage, properties, such as porosity, water/hydrocarbon saturation, and permeability, are estimated assuming the same model parameters to the rock physics models in the entire depth interval for a given formation. After identification of the optimum number of classes, formation evaluation is carried out on a class-by-class basis. Input parameters for the rock physics models will be updated in each identified rock class.

Preprocessing of Image Data

Core CT scan images often include depth intervals with missing data due to poor core recovery, induced fractures, or rush plugs taken after core retrieval. These missing core intervals can introduce undesired responses in image-derived features, which ultimately will affect the detected rock classes. The same challenge appears when deriving features from core photos. Moreover, core photos could further be affected by the creation of induced fractures during the core slabbing process. Coring barrel is also visible in the photos on the edges. In order to minimize the effect of these artifacts, we employed two separate approaches to flag or to remove these image artifacts for each type of image data (i.e., CT scan images and core photos). Figure 2 shows depth intervals with missing core material for both core CT scan images and core photos. In the case of whole-core CT scan images, both the core barrel and the annulus between the core and the core barrel have been previously removed.

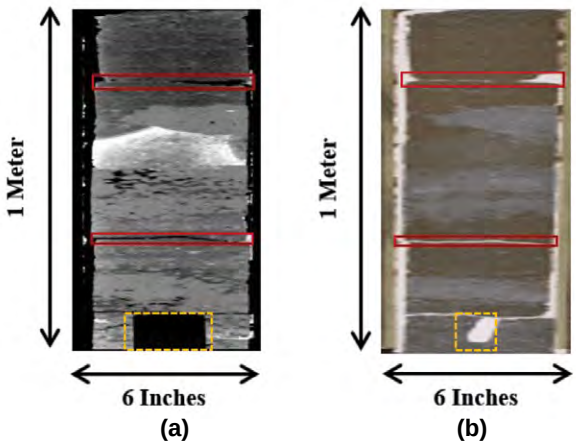

Fig. 2—Samples of image data with missing core material: (a) CT scan image YZ cut and (b) slabbed core photo. The red boxes indicate regions with missing core material. The yellow dashed lines indicate the location of a plug taken for RCA. The changes in the spatial distribution of grayscale intensity values in the CT scan image (a) represent changes in the fabric of the evaluated interval. Similarly, the change in colors from brown to gray displayed in the slabbed core photos (b) indicates the presence of cement.

CT Scan Images. The missing core intervals have a zero CT reading. Therefore, to flag these intervals, we first computed the mode of the gray-level values at each depth. Then, we defined a two-conditional criterion as follows: if the mode at a particular depth was zero and frequency of the mode at that depth was more than 30% of the total number of pixels, the depth interval was automatically flagged. As an alternate approach, we trained a multilayer perceptron for detecting the missing core-depth intervals. Nevertheless, the results obtained with the two conditional criteria approach provided more consistent results. Thus, we used this technique for the preprocessing of all the available CT scan image data. Figure 3a shows the histogram and cumulative frequency of the region of the CT scan image enclosed in the red box. The histogram shows a mode of zero with a cumulative frequency higher than 30%.

Core Photos. Figure 3b shows the histograms for each individual channel from a slabbed core photo in an 8-bit RGB format. We removed the core barrel visible on the edges of the photos by clipping the image on the sides. Unlike CT scan images, in which the regions of missing core intervals have zero values, the missing intervals in core cover a wide range on the grayscale spectrum when the color image is loaded as a grayscale image. On the gray-level histogram from 0 to 255 scale, the fractures are darker compared to the intact rock and hence form the left-end tail of the histogram (i.e., gray-level values of less than 50). The areas of seal peel are white and form the right-end tail of the gray-level histogram (i.e., gray-level values of greater than 210). In areas where the core barrel is visible in the middle of the core photo due to poor core recovery, we recognized a distinctive response on the textural entropy. These areas have smoother texture compared to the rocks and hence low-entropy values (less than 0.3 on normalized entropy histogram). After identification, the parts of images with fractures, seal peel, and barrel were captured in a mask image. We applied a dilation morphological operation on the mask image to fill in the holes that were not detected by histogram cutoffs. The locations on the image identified with the mask were then replaced with null values and hence not taken into account in subsequent analyses.

Image-Based Rock-Fabric Features

The numerical description of an image often includes gray-level and textural descriptors in the case of grayscale images and color and textural features in the case of color images. The word “texture” in this paper is strictly related to texture content in the image analysis context and should not be confused with the texture in the geology domain. In this

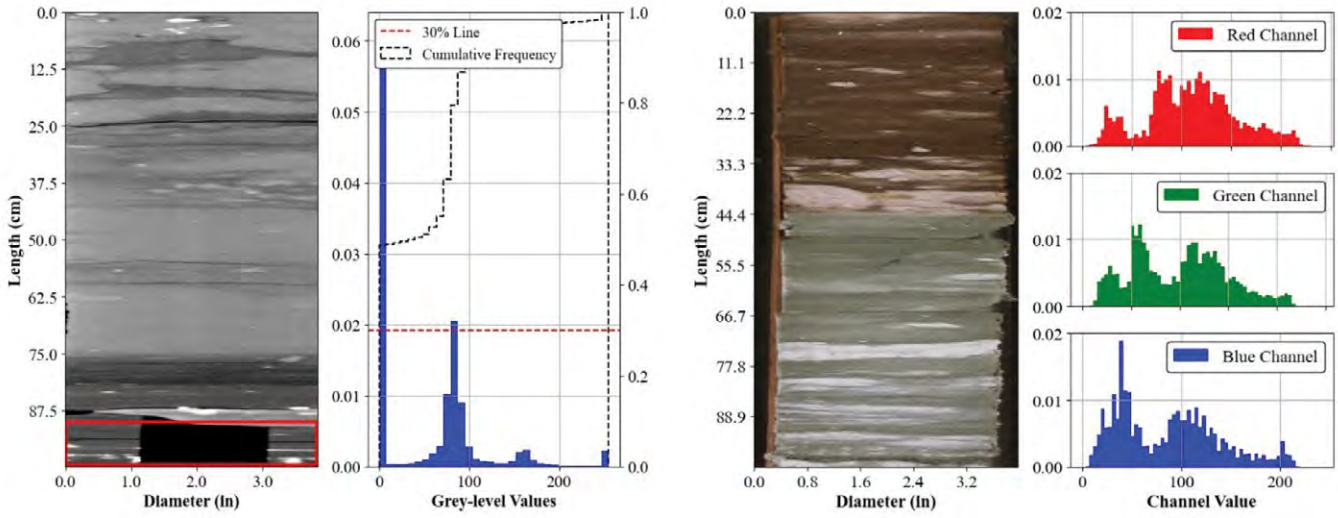

Fig. 3—Histogram of (a) CT scan image YZ cut and (b) slabbed core photo. The histogram and cumulative frequency curve correspond to the region enclosed by the red box in the (a) CT scan image. The red dashed line represents the 30% threshold for the cumulative frequency curve.

paper, we computed features for color/grayscale and texture for each type of image data in order to capture and quantify rock-fabric features. Computation of the extracted features is independent of the direction of the well (i.e., deviated wells or vertical wells) and the presence of dipping beds. However, both the angle of dipping beds and the directional profile of the well should be taken into account in the rock classes detection step.

Gray-Level Features of Core CT Scan Images. In order to capture the gray-level intensity variations of the CT scan images in a depth-by-depth basis, we computed the average of the gray-level values at each depth via

$$Avg_{GL} = \frac{\sum_{i=1}^{N} GL_i}{N}, \quad (1)$$

where GL_i is the gray-level value at each pixel of a particular depth, and N is the total number of pixels at each particular depth. The full matrix can be used, if computational time is not a concern, or if horizontal variations in gray-level intensity are not negligible and have a measurable impact on the outcome.

Color Features of Core Photos. Color is an important descriptor of lithofacies and can help distinguish between rock types that have a similar texture on grayscale. For instance, cemented sandstones can be easily distinguished from the noncemented ones using color information when compared to a case where only grayscale values are used. We used hue, saturation, and value (HSV) channels to extract the color information from the core photos. In the color space (HSV) used in this paper, hue refers to the pure color being described, saturation describes how "white" the color is, and value or intensity describes how dark the color is. Since the available core photos were encoded in red, green, and blue (RGB) channels, the core photos were first converted to HSV channels prior to extracting the color information. Finally, to get depth-tagged values for each channel, we averaged the pixel values across each row of the image. If computational time is not an issue, or if variations of color in the horizontal direction are not negligible and have a measurable impact on the outcome, the full matrix of the image can be used.

Textural Features of Core CT Scan Images. Texture is often defined as a region of an image in which a set of local statistics or other properties of the image are constant or vary slowly (Sklansky, 1978). However, there is no clear consensus in the definition of texture. Consequently, various approaches exist to describe the textural information contained in a given image. These approaches can be classified as statistical-, model-, and transform-based.

In order to describe the textural content of core CT scan images, we first employed a decomposition scheme using the Wavelet transform (Goupillaud et al., 1984). The wavelet transform has also been used in machine-learning-assisted segmentation tasks (Misra et al., 2019a). We decomposed the images using the Haar mother wavelet (Porwik and Lisowska, 2004) to obtain so-called detail images that enhance textural image information at specific orientations (i.e., horizontal, vertical, and diagonal). We specifically used the horizontal detail image to provide features in order to discriminate between vertically stacked rock classes. Then, we used a textural extraction algorithm termed gray-level co-occurrence matrix (GLCM) (Haralick et al., 1973), a statistical-based approach (Bharati et al., 2004), which is reported to outperform other approaches in classification tasks (Ohanian and Dubes, 1992). Other texture extraction algorithms, such as local binary patterns, have been used in workflows integrating machine-learning and image analysis techniques for the detection of relevant petrophysical attributes, such as organic matter (Wu et al., 2019).

The GLCM method quantifies the occurrence of pairwise pixel relationships between reference and neighboring pixels in a given image. These relationships are computed at a predefined offset distance and direction. Figure 4 shows the computation of the GLCM for one pixel of offset in the west-east direction for a simplified grayscale image. In the simplified grayscale image displayed in Fig. 4, each pixel is visited once and defined as the reference pixel. Then, according to the selected offset and direction, the relationship with the neighboring pixel is summarized in the GLCM (e.g., the occurrence of reference pixel 0 and neighboring pixel 1 occurs in the west-east direction twice when considering one pixel of offset; as such, the entry (0,1) in the GLCM matrix has a value of two).

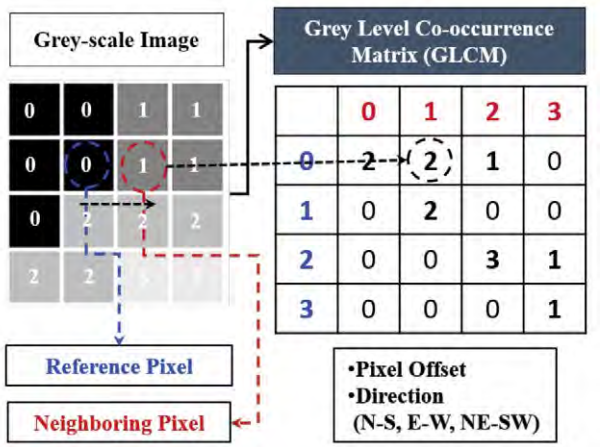

Fig. 4—GLCM computed for a simplified image with one pixel offset in the west-east direction.

GLCM is usually computed along four main orientations (horizontal, vertical, and two orthogonal diagonals). Computation of each one of these orientations is accomplished by the addition of GLCM in one direction and the transpose of the GLCM in the opposite direction (e.g., GLCM west-east and the transpose of GLCM east-west). Finally, the resultant GLCM is normalized by the number of pixels in the image. Once this is done, up to 14 textural features can be computed using the GLCM (Haralick et al., 1973). This method was originally developed for stationary grayscale texture images (i.e., images composed of a single texture).

In the case of nonstationary grayscale texture images (i.e., images that are composed of more than one texture), GLCM is computed over a small region (window) of the image. In order to fully describe the textural content of a nonstationary image, this window is placed at the center of each pixel, and the GLCM is computed. Then, the desired textural feature is derived from the previously computed GLCM, and the resultant value is assigned to the center pixel of the window. The window is then moved by one pixel, and the process is repeated until all the pixels of the image are covered. As a result, a new image representing the desired textural feature is obtained. In this paper, we computed contrast and energy via

$$Contrast = \sum_{(i,j=1)}^{N} (i-j)^2 \times G(i,j)\,, \tag{2}$$

and

$$Energy = \sum_{(i,j=1)}^{N} G(i,j)^2\,, \tag{3}$$

where $G(i,j)$ are the elements of the computed GLCM, N is the number of distinct gray levels in the input image, and i and j are the row and column number of the GLCM, respectively. Finally, after computing the textural images of the horizontal detail image, we transformed the textural image in a depth-by-depth basis via

$$Avg_{TF} = \frac{\sum_{i=1}^{N} TF_i}{N_p}\,, \tag{4}$$

where TF_i is the textural feature value corresponding to each pixel, and N_p is the total number of pixels at each depth.

GLCM/Window-Size Optimization. Window size is a critical parameter in texture feature extraction algorithms. Optimum window size should be large enough to capture the textural information of the textures present in the image. At the same time, an optimum window size should be small enough to produce features that allow a precise detection of the boundary between the different textures that compose the image. Optimum window-size estimation is typically done by trial and error and quality assessment of the expected outcome obtained from the extracted features. In this paper, we employed an approach proposed by Franklin et al. (1996) and Diehl et al. (2002) to automatically compute the optimum window size for textural feature extraction. The employed approach uses the spatial correlation concept by computing the experimental variogram of the gray-level values of the image and the estimated correlation length in the experimental variogram. The correlation length defines the distance at which a particular property is no longer correlated and can be used as a proxy for the optimum window size.

We computed the experimental variogram in the vertical direction of the image via

$$\gamma(h) = \frac{\sum_{i=1}^{NL(h)} (GL_i - GL_{i+h})^2}{2 \times NL(h)}, \quad (5)$$

where GL_i is the *i-th* pixel gray-level value, h is the lag distance, and NL is the number of pixel pairs at lag distance h. The variogram was computed for a maximum lag distance of half of the pixels in the vertical direction of an image covering one meter. The computation of the experimental variogram in the vertical direction was motivated by the relatively high variation commonly encountered in a sedimentary sequence in comparison to the horizontal variation. Then, we computed the first derivative of the experimental variogram. We used the first derivative to locate the lag distance at which the slope of the experimental variogram changed from positive to negative for the first time (correlation length). Finally, the estimated correlation length was employed as the dimensions of the optimum window size in the GLCM algorithm. Figure 5 shows the vertical experimental variogram, its first derivative for the displayed synthetic image, and the detected optimum window size. Additionally, Fig. 5 displays the effect of window size on the detected clusters for the displayed synthetic image when using the optimum window size and a fixed window size of 151 × 151 pixels. As observed in column 4 (detected clusters with a window size of 151 × 151 pixels) of Fig. 5, the size of the employed window for texture extraction can strongly impact the accuracy of the detected clusters resulting in misclassified intervals.

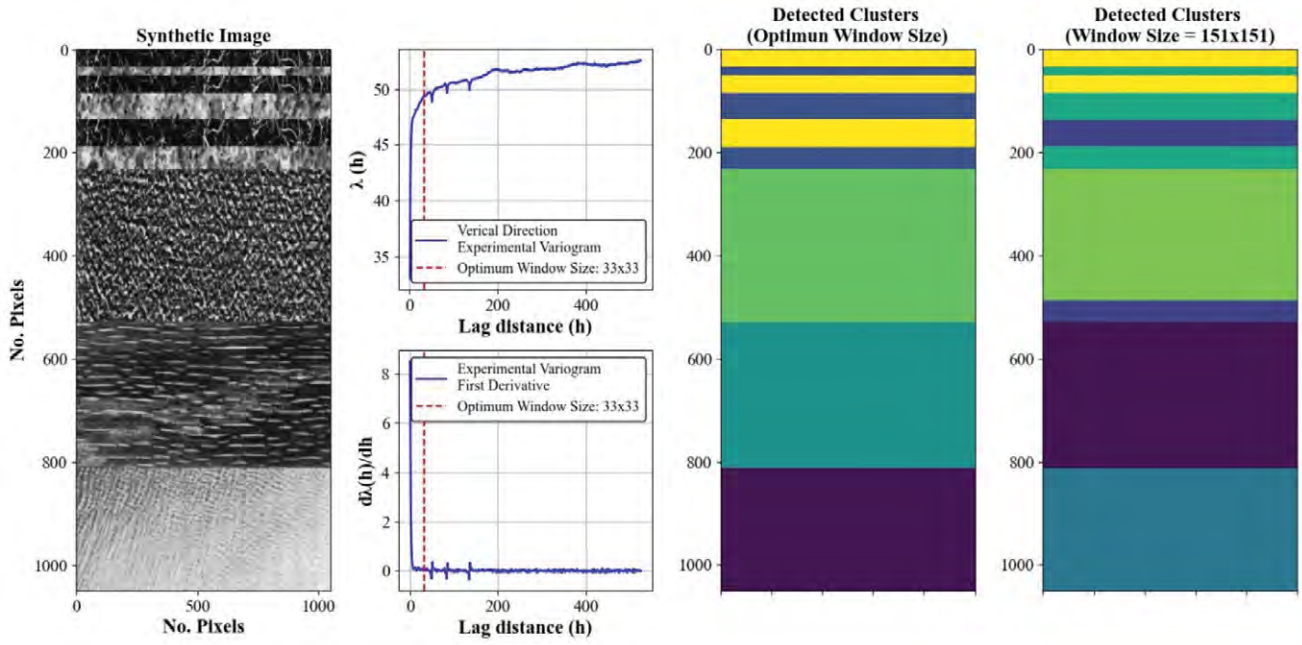

Fig. 5—Window-size optimization and detected clusters for a synthetic image, including five different texture from the Brodatz texture images (Brodatz, 1966). The first column displays a synthetic image composed of five different textures. The second column displays both the vertical direction experimental variogram and its first derivative. The last two columns display the detected clusters using the optimum window size and a fixed window size of 151 × 151 pixels, respectively.

Textural Features of Core Photos. Core photos have texture information at a higher resolution than the CT scan images. However, the higher resolution makes the calculation of GLCM features on long-interval core photos computationally expensive. The computation time of the GLCM for the CT scan image (4-bit) covering a 42-m depth interval (35,447 pixels in the *y*-direction and 384 pixels in the *x*-direction) using a window size of 21 × 21 pixels takes approximately 30 minutes, using a computer with a Core-i7 CPU @ 3.60 GHz and 32 GB of RAM. This can be mitigated by either reducing the resolution of the core photos or by using less computationally expensive techniques. Therefore, to preserve the resolution and, at the same time, optimize computation time, we used an entropy filter to estimate the roughness of texture. Entropy is defined by a base-2 logarithm of the range of gray-level distribution within a defined kernel. We used a 48 × 10 kernel to extract textural entropy. The rectangular kernel was chosen because a greater variation in texture is expected in the vertical direction than in the horizontal direction. Finally, to get entropy values corresponding to each depth, we averaged the entropy for each row of the image.

Detection of Rock Classes Using Image-Based Features

Before integrating the image-based rock-fabric features with conventional well logs and RCA data, we designed a workflow for automatic detection of rock classes from image data (Fig. 6). The objective of this workflow was to evaluate the capacity of the extracted image-based rock-fabric-related features to form clusters that reflect the visual content of the image data employed. We used a numerical approach to optimize the number of rock classes to avoid bias introduced by a user-defined number of rock classes.

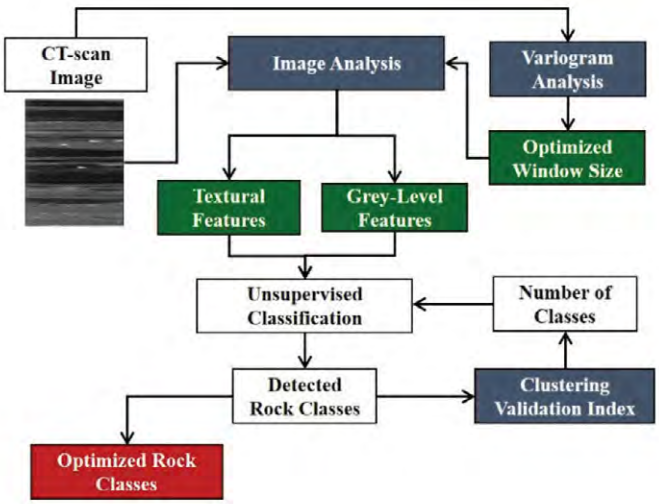

Fig. 6—Workflow for automatic detection of image-based rock classes.

First, we extracted the aforementioned features from core CT scan images covering one meter. Then, we used a data clustering algorithm (i.e., *k*-means) to determine the existing rock classes in the evaluated depth interval. Given that the number of rock classes in the evaluated depth interval was unknown, we employed a cluster validation index to estimate the optimum number of rock classes in the evaluated intervals. We used a cluster validation index, called the silhouette coefficient, which was introduced by Rousseeuw (1986). The silhouette coefficient per sample is estimated via

$$s_i = \frac{(b_i - a_i)}{\max(a_i, b_i)}, \tag{6}$$

where a_i is the average dissimilarity of the *i-th* sample with respect to the other samples of its own cluster and b_i is the dissimilarity of the *i-th* sample cluster with respect to the closest neighboring cluster. The dissimilarity measure used in the computation of the silhouette coefficient is the Euclidean pairwise distance. It should be noted that other pairwise distances (e.g., Manhattan, Citiblock, and Cosine) can also be used. In order to optimize the number of rock classes, first, we averaged the silhouette coefficient per sample for an increasing number of rock classes. Finally, we selected the optimum number of rock classes as the number of rock classes that gave us the highest average silhouette coefficient value.

Iterative Method for Improving Image-Based Rock Classification and Permeability Assessment

Integration of Image-Based Features With RCA Data and Well Logs. We performed image-based rock classification using features derived from core CT scan images and core photos as inputs for a *k*-means data clustering algorithm. We used average gray-level value, contrast, and energy derived from CT scan images, and hue, saturation, value, and entropy derived from core photos, as well as formation tops as inputs for image-based rock classification. We incorporated formation tops as numerical features by creating a synthetic log with integer numbers representing each encountered formation. Each formation was represented by an integer number ranging from one to the total number of encountered formations. Before clustering the input data, we removed data points from depth intervals flagged as missing core-depth intervals. Then, all the input data was scaled in the range of 0 to 1 to prevent biased results toward a specific feature. Once the data was scaled, we used principal component analysis (PCA) to generate a new set of independent features. PCA is commonly used in data clustering tasks to reduce the number of redundant features (Misra et al., 2019b). In this paper, we

used the minimum number of components that explain at least 95% of the variance of the original features. After using PCA, the four first principal components explained 95% of the variance of the original set of eight features. Finally, we iteratively clustered the input data for an increasing number of classes (i.e., from two to a maximum of ten classes).

Iterative Approach for Optimization of Number of Rock Classes. At each iteration, we generated porosity-permeability models using available RCA data on a class-by-class basis (i.e., one permeability model per detected class). The porosity-permeability model employed is the regression line obtained from a semilog crossplot of RCA porosity and permeability. At each iteration, we computed a permeability-based cost function defined by

$$C(x,k_{est}) = \frac{1}{N_{perm}} \sum_{1}^{N_{perm}} \left| \frac{k_{core,i} - k_{est,i}}{k_{core,i}} \right|, \quad (7)$$

where $k_{est,i}$ is the permeability estimate, $k_{core,i}$ is the core permeability, and N_{perm} is the total number of core permeability measurements. The employed cost function seeks to minimize the error between core-measured permeability and estimated permeability. Finally, we selected the optimum number of classes as the number classes for which the defined cost function converges below a threshold. It should be noted that the cluster validation index described in the previous section was not employed in the iterative approach herein described.

Propagation of Rock Classes to Offset Wells Without Image Data

We trained a supervised learning algorithm (quantitative classification) in a commercial formation evaluation software with conventional well logs as input data and image-based rock classes (from the well with image data) as labels to predict rock classes in an offset well (without using image data). The quantitative classification defines the label of each sample by computing the distance between the labeled sample (rock classes) and the unseen sample. The rock classes used in this step were obtained using the workflow introduced in the section "Integration of Image-Based Features With RCA Data and Well Logs." In this paper, we used gamma ray, bulk density, neutron porosity, and shear-wave slowness as input data for training the quantitative classification algorithm. Finally, we compared the permeability estimates in the offset well against the available RCA data. We also verified the reliability of the rock classes by comparing them against the available core description.

FIELD APPLICATION

We applied the proposed method to two wells, Well A and Well B. The depth interval of interest in this field data covers three formations: Formation 1, Formation 2, and Formation 3, from bottom to top. These formations represent three main lithologies: (i) Formation 1 constitutes a succession of coarse-grained sandstones; (ii) Formation 2 comprises spiculites, which is a biogenic rock predominantly composed of sponge silica spicules, and (iii) Formation 3 comprises an interval of marlstones and limestones. We used the extracted image-based features in Well A and the formation tops together for rock classification using an unsupervised clustering algorithm (i.e., *k*-means). We verified the reliability of the obtained rock classes against the visual description of the rock facies and also against available RCA data. Subsequently, we used the obtained rock classes in Well A to propagate rock classes to the offset well (Well B) using conventional well logs. We verified the reliability of the results obtained in the offset well with available RCA data.

Data Set Description

Well Logs. The available conventional well logs in both wells include gamma ray, bulk density, neutron porosity, array induction resistivity, photoelectric factor, compressional-wave slowness, and shear-wave slowness.

Image Data. We used dual-energy-acquired CT scan cross-sectional image cuts from raw 3D CT scan volume with a resolution of approximately 4.5 millimeters per pixel. These images were encoded in 8-bit format (i.e., 0 to 255 grayscale). Additionally, core photos at different resolutions were provided. Core photos were initially encoded in 8-bit RGB (i.e., red, green, and blue) format. We converted them to HSV format before the feature extraction step. Figure 7 shows examples of a core CT scan image and a core photo covering one meter of core.

Core Data. We used RCA information, such as total porosity, absolute permeability, and visual core description, with sampling rates as low as 0.1 m for two purposes. First, we used them as part of the iterative workflow for optimizing the number of rock classes. Second, they are used for verification of the estimated formation properties, such as porosity, permeability, and water/hydrocarbon saturation.

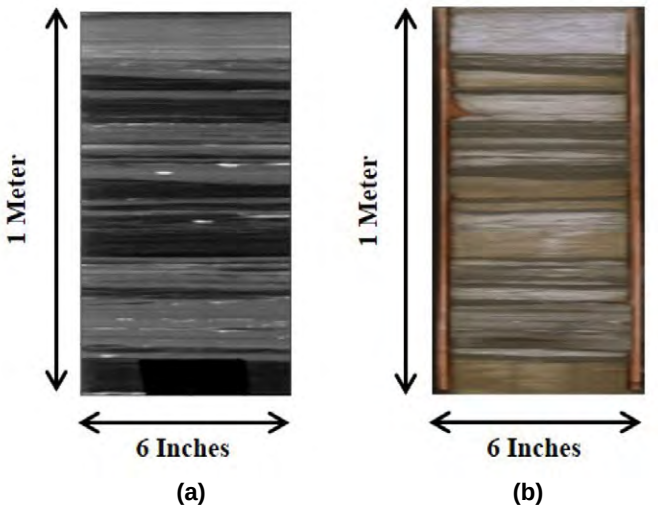

Fig. 7—Examples of image data used in this paper: (a) CT scan image (YZ cut) and (b) slabbed core photo.

Conventional Petrophysical Evaluation

In the first step, we performed formation evaluation to estimate the volumetric concentration of shale, water saturation, and total porosity. The aforementioned properties were estimated using gamma ray, bulk density, neutron porosity, and array induction resistivity. We estimated permeability assuming the same model parameters in the porosity-permeability model for the entire depth interval in each formation. Table 1 summarizes the input parameters for the initial formation evaluation. Results of formation evaluation were obtained at a resolution of one sample per half a foot, matching the sampling rate of the employed logs. However, it should be noted that the sampling rate does not reflect the actual vertical resolution of the well-logging tools, which is distinct for each tool. This vertical resolution can be orders of magnitude less than that of the images used for classification. Figure 8 shows the results of the initial formation evaluation for the interval of interest. The results of the conventional petrophysical evaluation are in good agreement with the RCA data. Part of the observed mismatch between conventional petrophysical evaluation and log data can be attributed to the imprecise depth match between well logs and core data, especially in the 2-m piece of poorly recovered core within Formation 1. Another cause of the mismatch can be rapid changes in the petrophysical properties, not captured by the resolution of the employed well-logging tools.

Image-Based Rock Classification Using the Detected Rock-Fabric Features

Core CT Scan Images. Figure 9 shows two examples of results for automatic rock classification obtained using core CT scan images. These images cover a depth interval of one meter. We used average gray-level, contrast, and energy as the inputs for the data clustering algorithm. The window size employed for the extraction of the textural features (i.e., contrast and energy) was automatically computed using the spatial correlation approach explained in the section "GLCM/Window-Size Optimization." Both intervals display commonly encountered visual geological features. Figure 9a shows a layered depth interval, while Fig. 9b shows a depth interval with a gradual textural variation. The automatically detected rock classes are in good agreement with the visual content of the core CT scan images. It should be noted how the occurrence of small fractures (Fig. 9b) and relatively disperse bright spots (Figs. 9a and 9b) do not result in the detection of additional rock classes. This comes as the result of using a cluster validation index to optimize the number of rock classes. The cluster validation index will favor dense and well-defined clusters and penalize disperse and small clusters. Consequently, a small noticeable response in the extracted features due to small fractures and relatively disperse bright spots will not significantly affect the detected rock classes.

Table 1—Assumed Input Parameters for Conventional Petrophysical Evaluation in the First Iteration

Parameters	Units	Fm. 1	Fm. 2	Fm. 3
Grain density	g/cc	2.65	2.65	2.71
Shale density	g/cc	2.45	2.45	2.45
Oil zone, flushed zone fluid density	g/cc	0.81	0.97	0.97
Water zone, flushed zone fluid density	g/cc	1.03	1.03	1.03
Archie's factor, *a*	-	1	1	1
Archie's porosity exponent, *m*	-	1.7	1.7	2
Archie's saturation exponent, *n*	-	2.25	2.25	2

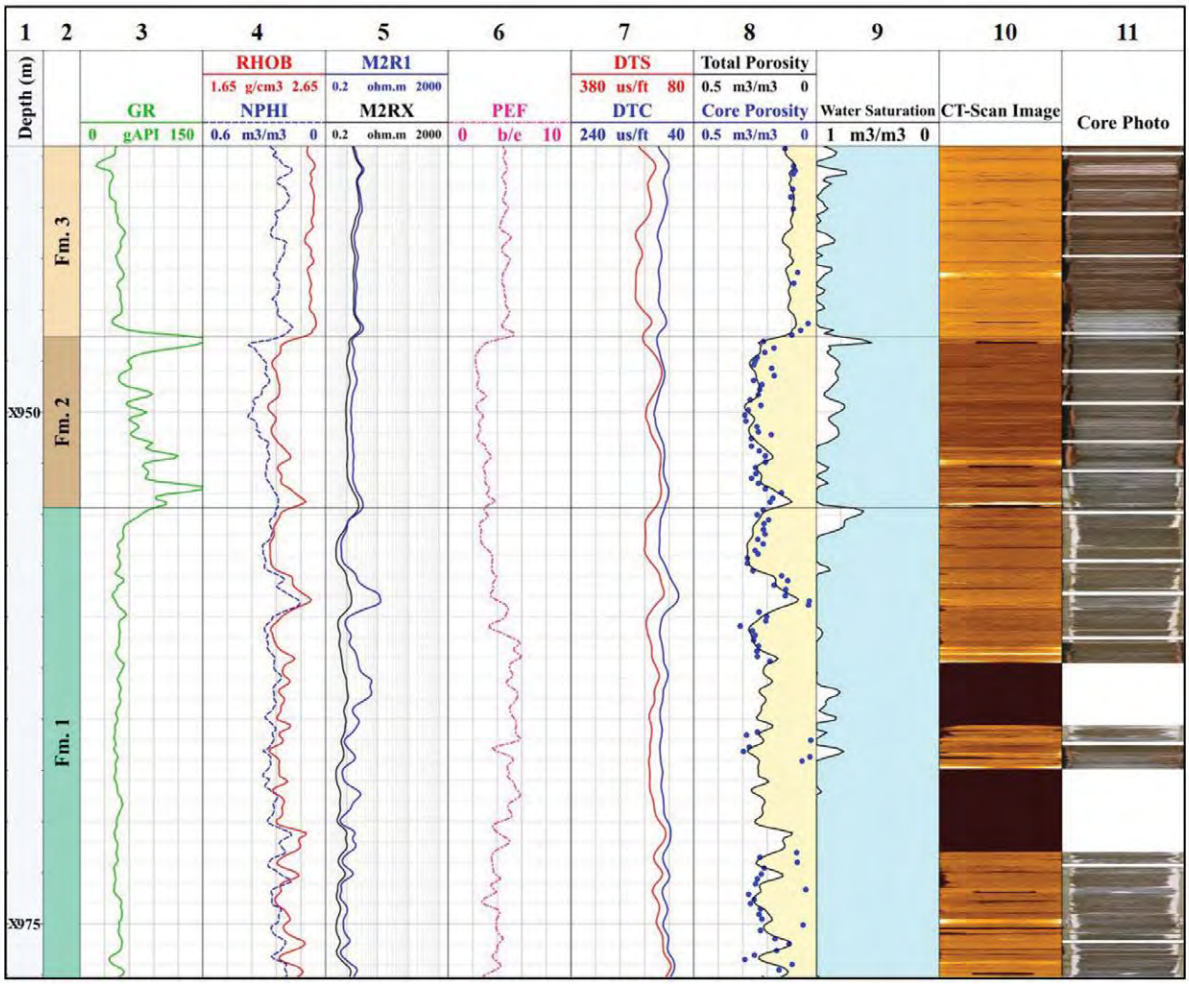

Fig. 8—Field example, Well A: Conventional formation evaluation. Tracks from left to right: track 1: depth; track 2: formations; track 3: gamma ray (GR); track 4: bulk density (RHOB) and neutron porosity (NPHI); tracks 5: shallow (M2R1) and deep resistivity (M2RX); track 6: photoelectric factor (PEF); track 7: shear-wave slowness (DTS) and compressional-wave slowness (DTC); track 8: estimated total porosity and core porosity measurements; track 9: water saturation; track 10: core CT scan image; and track 11: core photo.

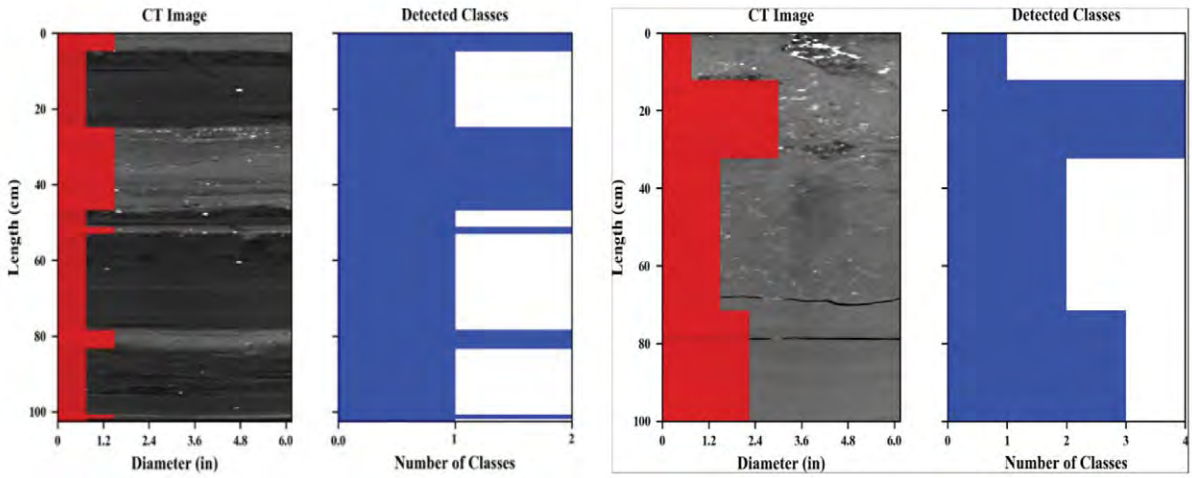

Fig. 9—Examples of automatic detection of rock classes in depth intervals with (a) layered rock texture and (b) a gradual textural variation. The red horizontal bars, superimposed to the CT scan image, represent the detected classes.

Integration of CT Scan Images and Core Photos. Figure 10 highlights the importance of the integration of multiscale and multiphysics image data for image-based rock classification. Core CT scan images capture changes in the density of the rock, while core photos display the interaction of the light spectrum with the core surface. The automatically detected rock classes using the CT scan image (Fig. 10, track 4) cannot differentiate between the gray limestone and the brown limestone present in the evaluated depth interval. On the other hand, automatically detected rock classes from core photos (Fig. 10, track 5) cannot distinguish between the brown limestone and the sandstone unit. However, the integration of image-based rock-fabric features improves the automatically detected rock classes by distinguishing all the present lithologies in the evaluated depth interval (Fig. 10, track 6). For instance, the discontinuous light-colored features from X945 to X945.7 are successfully captured in the integrated rock classification results.

Integration of Image-Based Rock-Fabric Features With Well Logs and RCA Data for Rock Classification

We used the workflow described in section "Image-Based Rock-Fabric Features" to extract both textural and gray-level/color features from the whole-core CT scan images and slabbed core photos. Figure 11 shows these features along with the corresponding images and the depth interval. Energy and contrast are the textural features obtained from core CT scan images, and entropy is the textural feature obtained from core photos. The color is described by the HSV features obtained from core photos. We observed that the extracted features respond to the visual variations in color as well as the texture of the core images.

Features derived from the core CT scan images (i.e., contrast and energy) respond to textural variations in the encountered lithology. Increase in contrast and decrease in energy aid in the distinction between coarse-grained and fine-grained lithologies. On the other hand, features derived

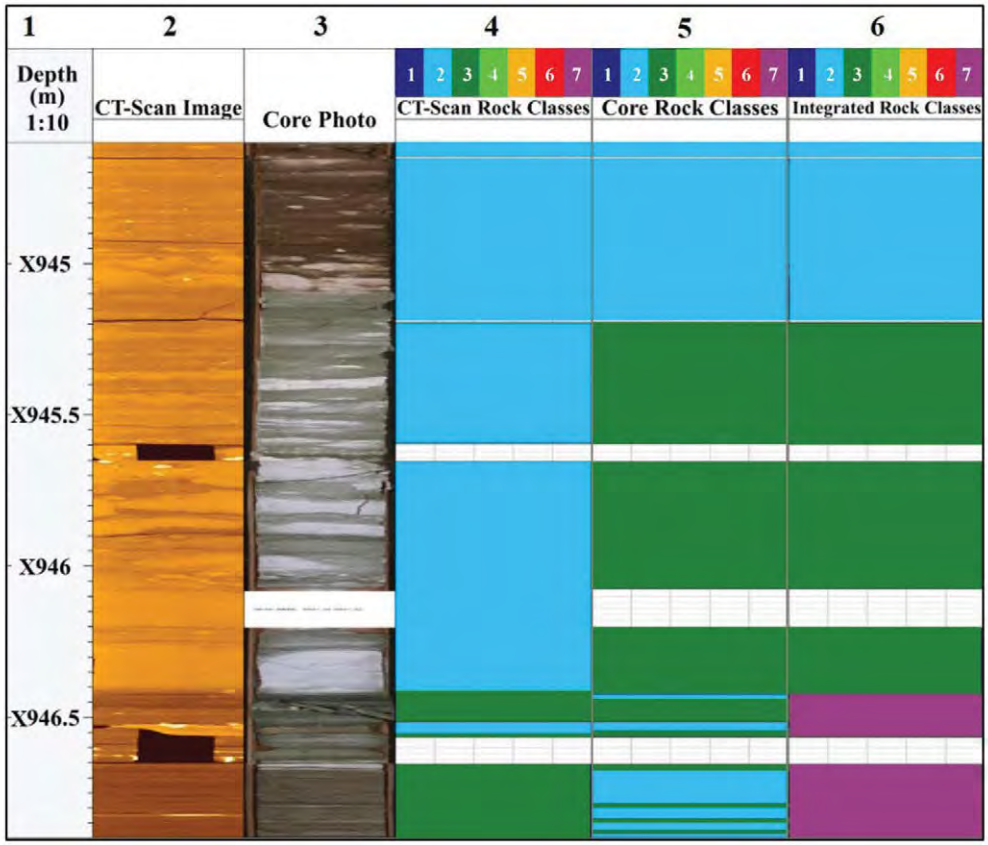

Fig. 10—Field example, Well A: Comparison of image-based rock classes obtained in a selected depth interval using core CT scan images, core photo, and integration of CT scan images and core photos. Tracks from left to right: track 1: depth; track 2: core CT scan image; track 3: core photo; track 4: rock classes obtained from core CT scan images; track 5: rock classes obtained from core photos; and track 6: rock classes obtained from integration of CT scan images and core photos.

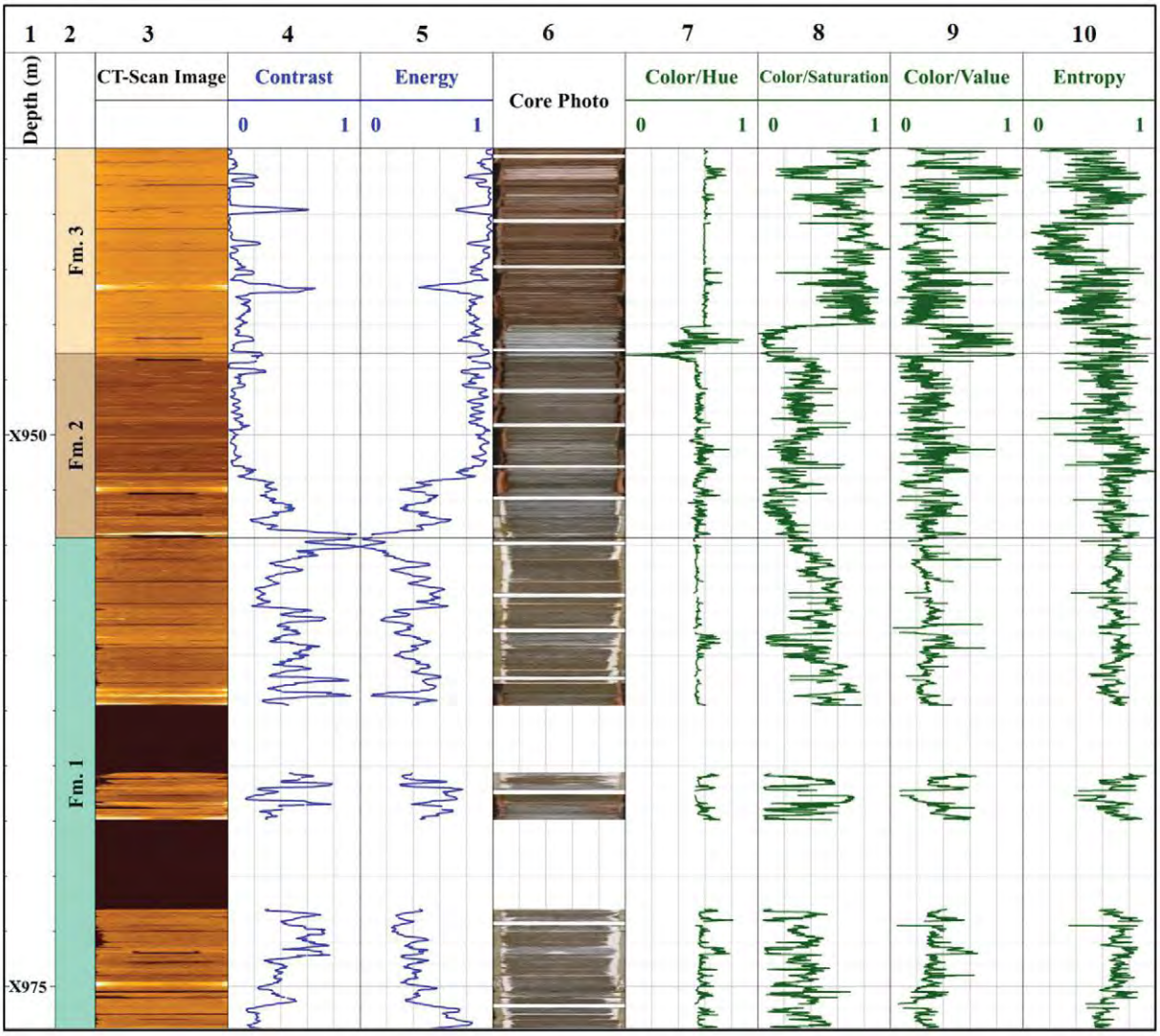

Fig. 11—Field example, Well A: Image-based rock-fabric features. Tracks from left to right: track 1: depth; track 2: formations; track 3: core CT scan image; track 4: textural contrast derived from core CT scan image; track 5: textural energy derived from core CT scan image; track 6: core photo; track 7: color hue derived from core photo; track 8: color saturation derived from core photo; track 9: color intensity (value) derived from core photo; and track 10: entropy derived from core photo.

from core photos, such as hue, saturation, and value, allow us to discriminate between lithologies with apparent similar textural properties.

Next, we used the extracted image-based features for rock classification using the *k*-means clustering algorithm. We iteratively increased the number of rock classes from two to ten. At each iteration, we constructed porosity-permeability models for each class using available core data and used the permeability-based cost function to optimize the number of rock classes. Figure 12 shows the plot of the calculated cost function against the number of rock classes ranging from two to ten. The cost function converges to a stable value in two steps. The first step-decrement at three rock classes is a result of the identification of three rock classes corresponding to the three different formations. The second step-decrement is at seven rock classes. It should be noted that the drop-in cost function from six to seven rock classes is minor (10% relative decrease in cost function) compared to other steps. It might lead to an interpretation of six optimum rock classes instead of seven. We decided to use seven as the optimum number of rock classes. The basis for this decision was the scarce permeability measurements taken in one of the identified rock classes, which cannot be accurately represented in the cost function and could

possibly cause a minor drop in cost function instead of possibly a larger drop. Figure 13 shows the results of the rock classification for the increasing number of rock classes from three to seven and the comparison of the well-log-based estimated permeability against measured permeability at each iteration. Figures 14a, 14b, 14c, 14d, and 14e compare core-measured permeability against class-based estimated permeability for the increasing number of rock classes from three to seven rock classes. Figure 14f shows the decrease in the mean relative error for the increasing number of rock classes using the case of three rock classes as the baseline. Figure 15 compares the integrated rock classes against different lithologies encountered in Well A, available from the core description.

Class-by-class estimated permeability models improve the agreement between core data and estimated permeability by 89% (decrease in mean relative error) when compared with formation-by-formation permeability models. We observed an absolute average error of less than 0.5 orders of magnitude between the core data and estimates of permeability, an acceptable error considering the overall variation observed in the core permeability measurements (i.e., over five orders of magnitude).

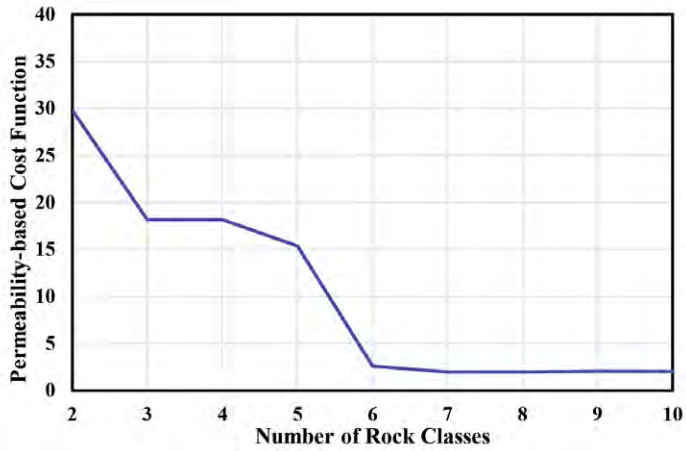

Fig. 12—The calculated cost function (Eq. 7) plotted as a function of the number of rock classes. This plot suggests seven rock classes as an optimum number of rock classes in the field example.

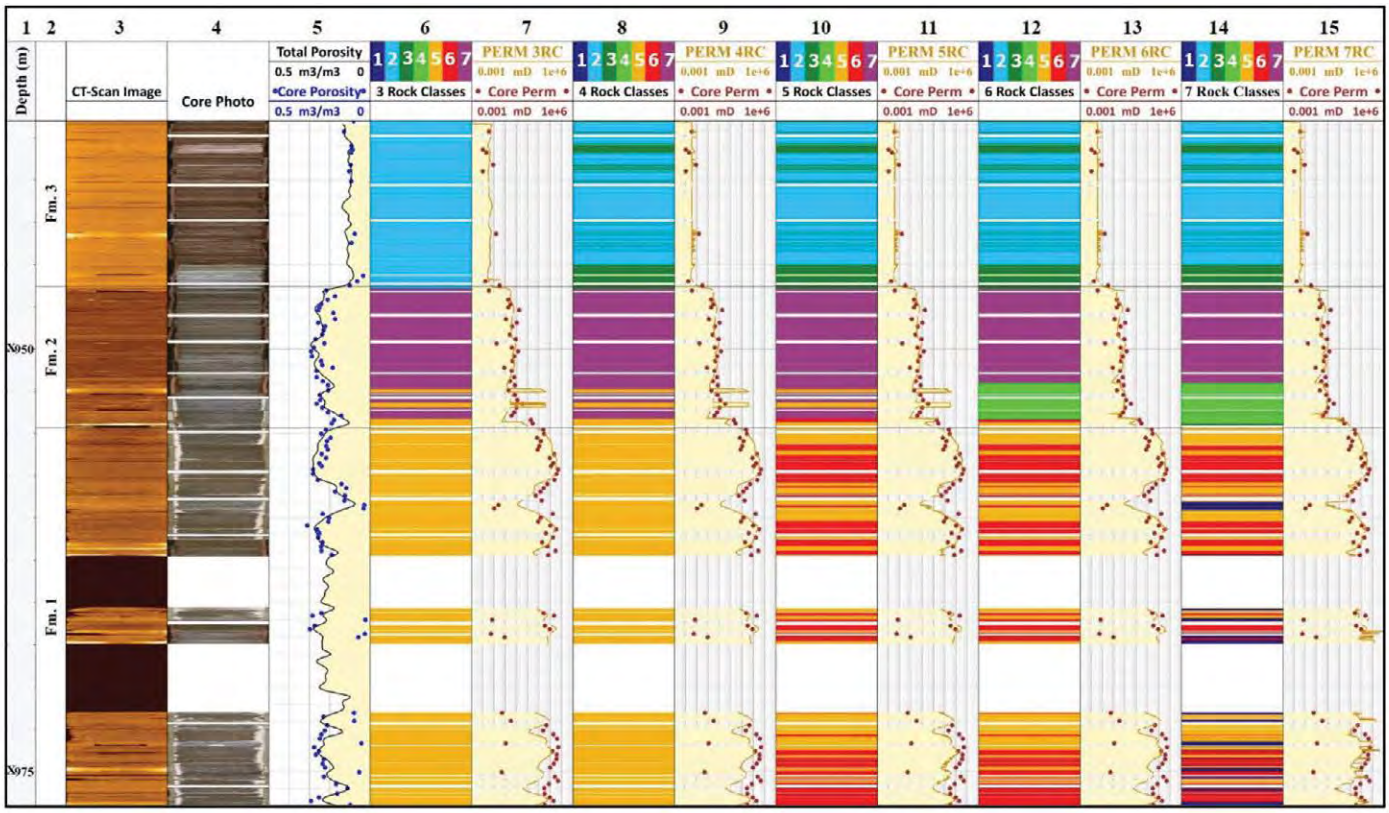

Fig. 13—Field example, Well A: Comparison of the rock classification results obtained with the number of rock classes ranging from three to seven. Tracks from left to right: track 1: depth; track 2: formations; track 3: core CT scan image; track 4: core photo; track 5: estimated total porosity and core porosity measurements; and tracks 5 to 15: rock classification results at each iteration and permeability estimates compared against core permeability measurements (Core Perm).

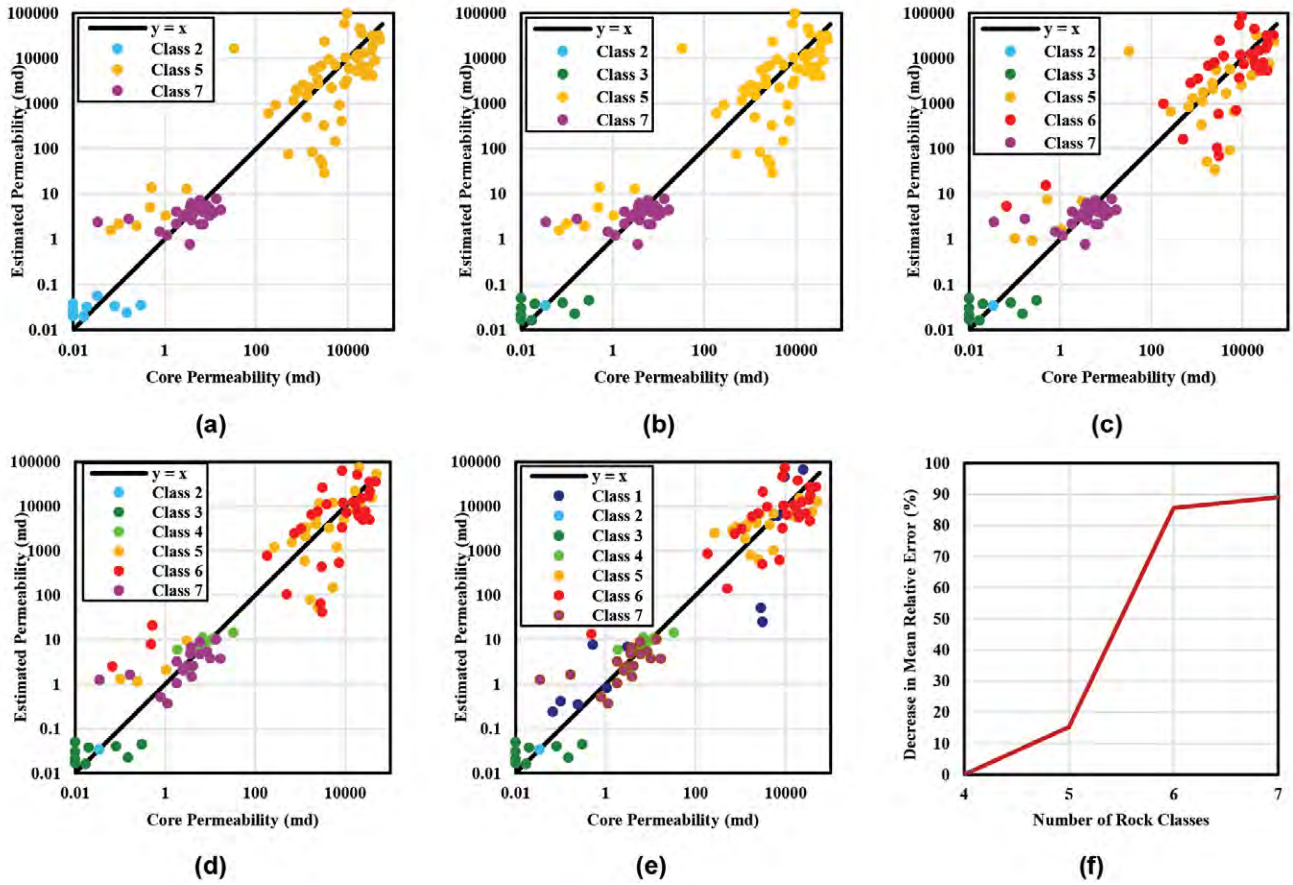

Fig. 14—Comparison of estimated permeability against core-measured permeability for (a) three rock classes, (b) four rock classes, (c) five rock classes, (d) six rock classes, and (e) seven rock classes, as well as (f) the decrease in the mean relative error against the increase in the number of rock classes. The decrease in the mean relative error is computed, taking three classes as the baseline.

Figure 16 shows the crossplot of porosity and permeability core data for all the seven identified classes. The permeability in the selected interval varies by several orders of magnitude across the rock classes. Few points appear in the middle of clusters that are formed by other classes (e.g., in Fig. 16, one point from Rock Class 6 is within the Rock Class 1 cluster and is possibly misclassified). Such misclassifications can be the consequence of the limitations of the features employed, the adopted clustering technique, lack of enough textural contrast, and/or poor-quality CT/core images. The adopted clustering technique (i.e., *k*-means) could be the most critical of the aforementioned factors due to the underlying assumptions and limitations of the technique. For instance, *k*-means is suited for spherical, well-separated, and similarly sized clusters, which in turn can penalize samples forming clusters of different shapes and sizes, resulting in misclassified samples. Figure 16 also shows a total of five points classified as RC1 that display high-permeability values, which does not correspond to the overall behavior of this class (i.e., low-permeability values due to the presence of cement material). Three of these points are correctly classified, and the visual appearance of both the whole-core CT scan and slabbed core photos agree with the visual appearance of the low-permeability points. A possible explanation for this observation can be the nonuniform cement distribution within the volume of core recovered (i.e., the side of the core slab from where the core plug was taken has lower cement concentration). The other two points were misclassified. The reason for the misclassification is an abnormal response in one of the extracted features from the whole-core CT scan images caused by bright regions originated by the presence of the couplings used to connect the coring barrels.

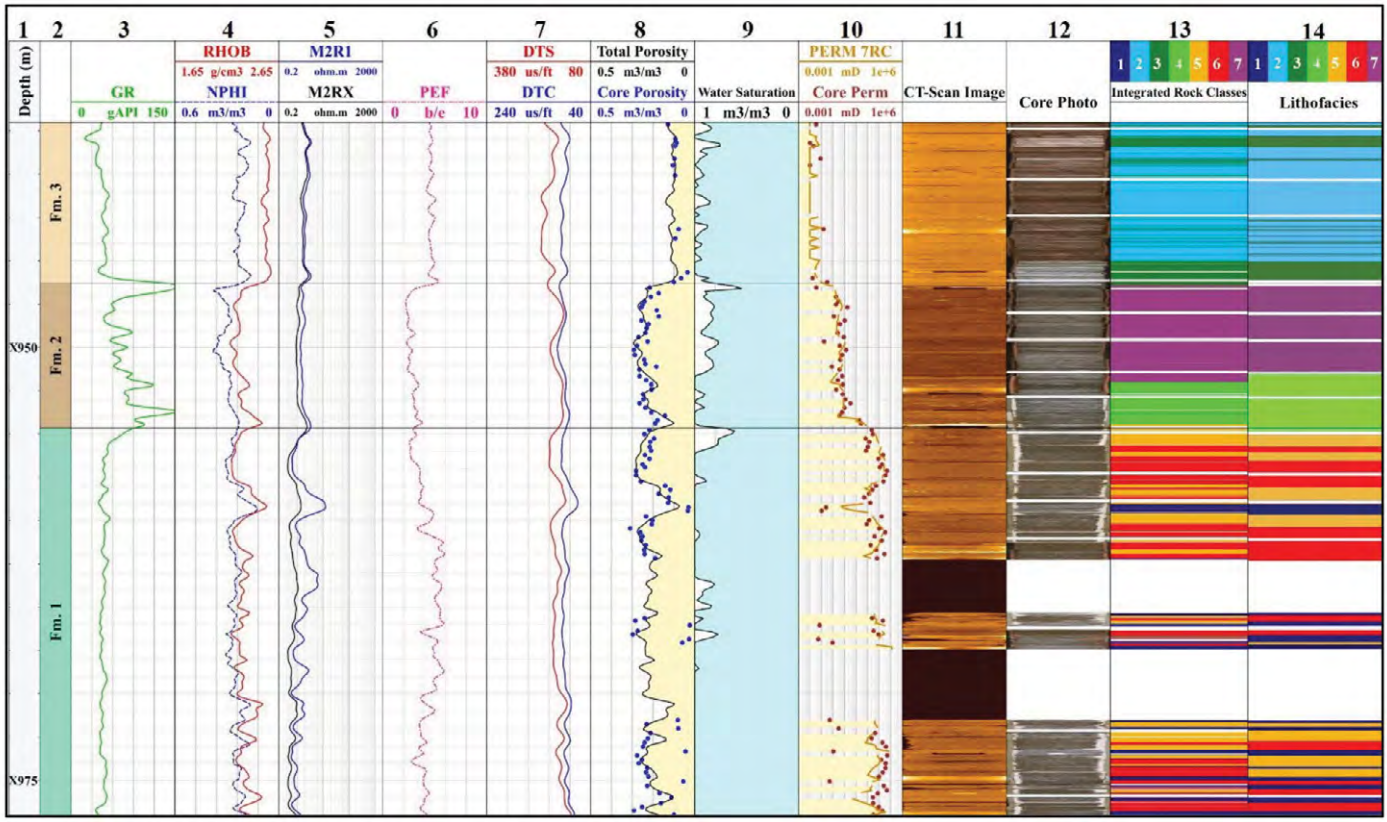

Fig. 15—Field example, Well A: Comparison of integrated image-based rock classes with lithofacies. Tracks from left to right: track 1: depth; track 2: formations; track 3: gamma ray (GR); track 4: bulk density (RHOB) and neutron porosity (NPHI); track 5: shallow (M2R1) and deep resistivity (M2RX); track 6: photoelectric factor (PEF); track 7: shear-wave slowness (DTS) and compressional-wave slowness (DTC), track 8: estimated total porosity and core porosity measurements; track 9: water saturation; track 10: comparison of permeability estimates (PERM 7RC) and core permeability (Core Perm); track 11: core CT scan image; track 12: core photo; track 13: integrated rock classes; and track 14: previously identified lithofacies.

The optimized rock classes are in agreement with the visual appearance of the rocks and with the core-derived lithofacies. Figures 17, 18, and 19 show examples of results of image processing and rock classification for selected depth intervals. Figure 17 shows how the extracted features help us to distinguish between three levels of cementation within the coarse-grained sandstones (Classes 1, 5, and 6). Figure 18 shows the transition from the spiculite (Class 7) at the bottom to the gray-green marly limestone (Class 3) in the middle, to the brown carbonate (Class 2) at the top. Figure 19 shows the contact between the coarse-grained sandstone (Class 5) and the condensed section with belemnite fossils (Class 4). Figure 20 shows the core photos of all the seven classes identified in the interval of interest.

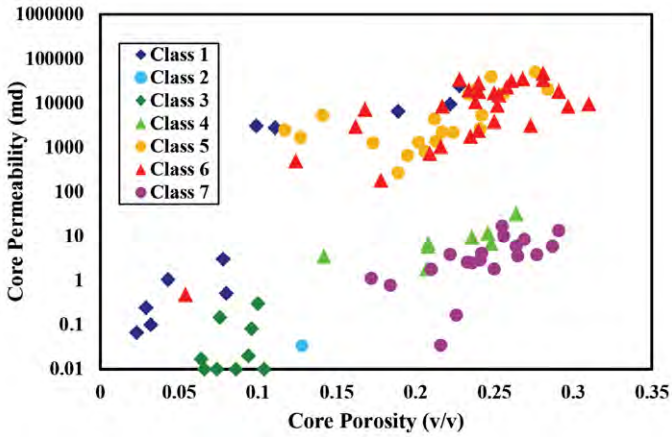

Fig. 16—Field example, Well A: Porosity-permeability crossplot for all the available classes from three formations. Different colors represent different rock classes identified through the introduced image-based rock classification methodology.

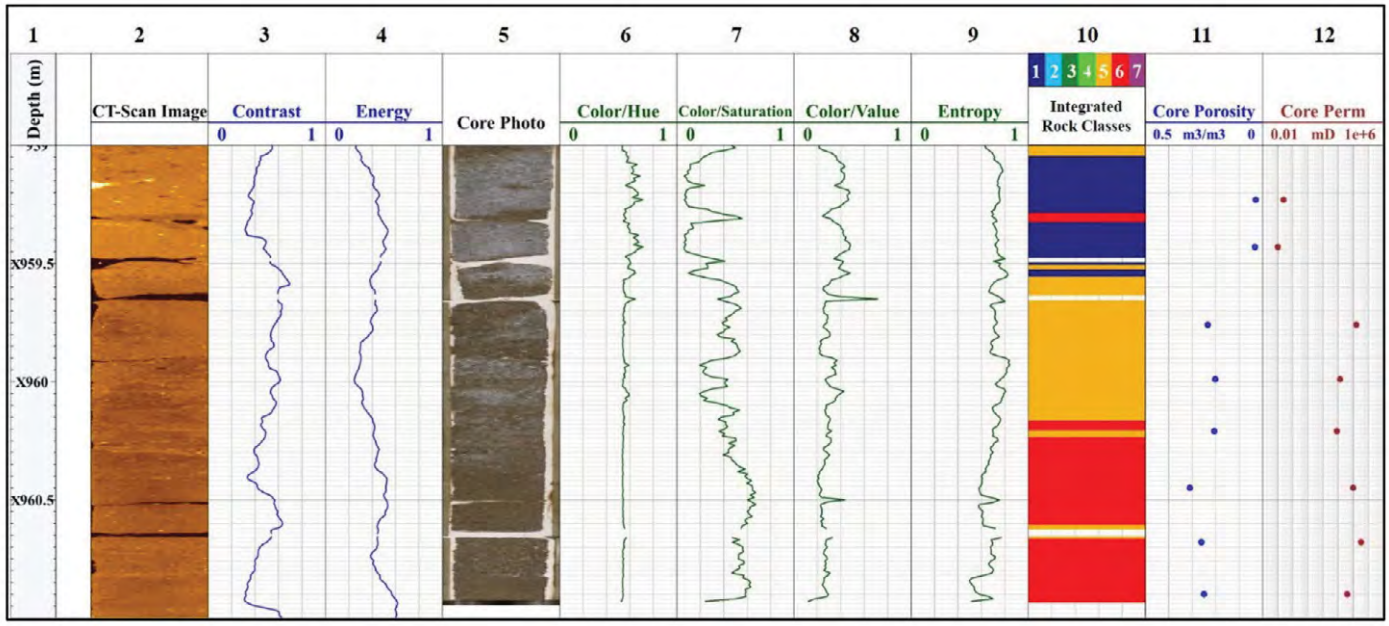

Fig. 17—Field example, Well A: Selected depth interval representing examples of image-based integrated Rock Classes 1, 5, and 6. Tracks from left to right: track 1: depth; track 2: core CT scan image; track 3: textural contrast derived from core CT scan image; track 4: textural energy derived from core CT scan image; track 5: core photo; track 6: color hue derived from core photo; track 7: color saturation derived from core photo; track 8: color intensity (value) derived from core photo; track 9: entropy derived from core photo; track 10: integrated rock classes; track 11: core porosity measurements; and track 12: core permeability measurements.

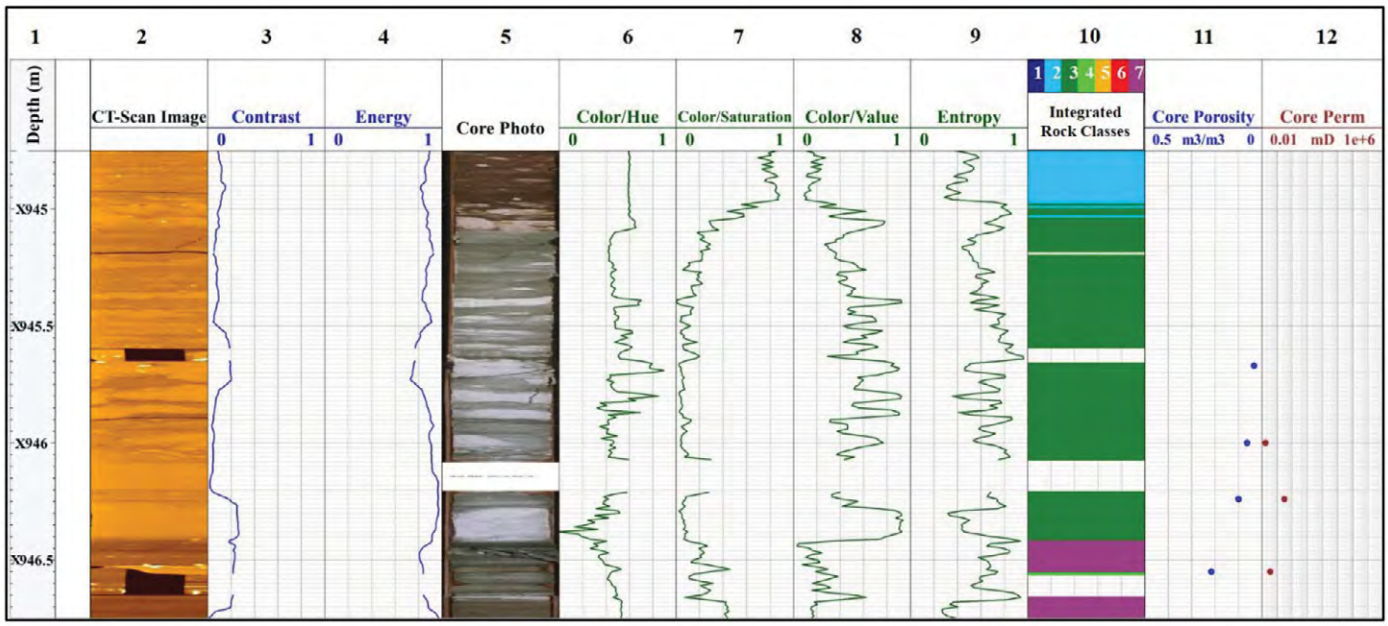

Fig. 18—Field example, Well A: Selected depth interval representing examples of image-based integrated Rock Classes 2, 3, and 7. Tracks from left to right: track 1: depth; track 2: core CT scan image; track 3: textural contrast derived from core CT scan image; track 4: textural energy derived from core CT scan image; track 5: core photo; track 6: color hue derived from core photo; track 7: color saturation derived from core photo; track 8: color intensity (value) derived from core photo; track 9: entropy derived from core photo; track 10: integrated rock classes; track 11: core porosity measurements; and track 12: core permeability measurements.

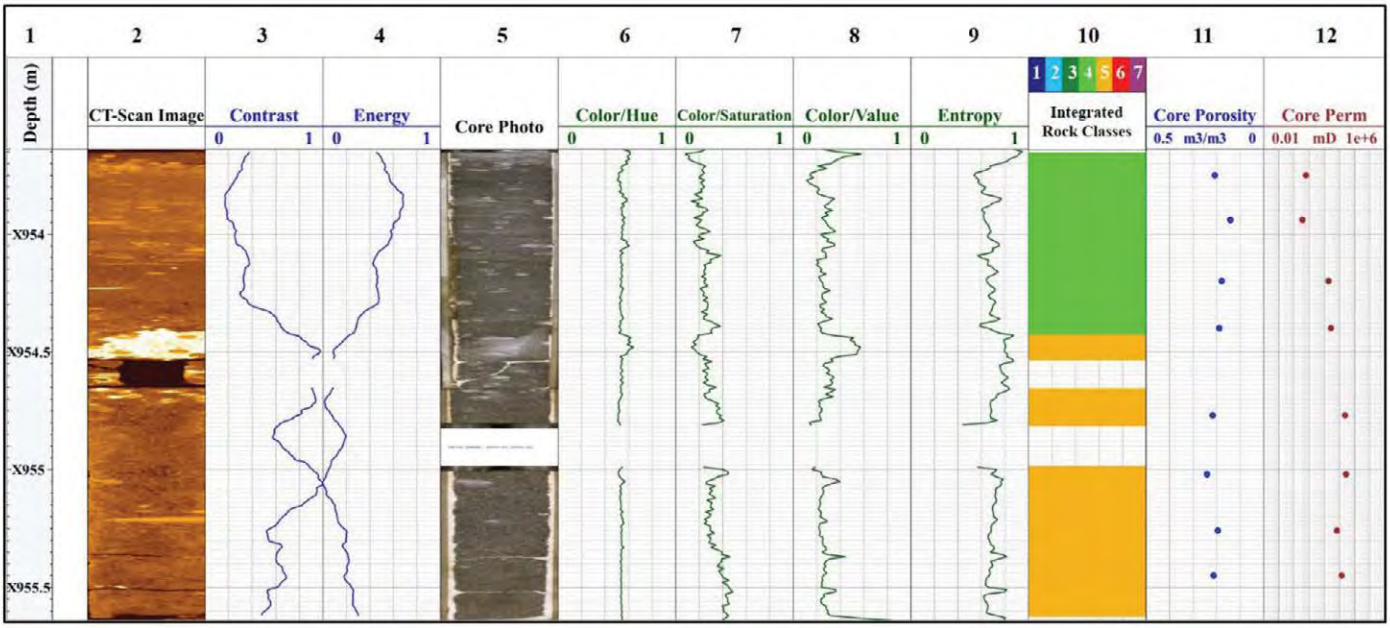

Fig. 19—Field example, Well A: Selected depth interval representing examples of image-based integrated Rock Classes 4 and 5. Tracks from left to right: track 1: depth; track 2: core CT scan image; track 3: textural contrast derived from core CT scan image; track 4: textural energy derived from core CT scan image; track 5: core photo; track 6: color hue derived from core photo; track 7: color saturation derived from core photo; track 8: color intensity (value) derived from core photo; track 9: entropy derived from core photo; track 10: integrated rock classes; track 11: core porosity measurements; and track 12: core permeability measurements.

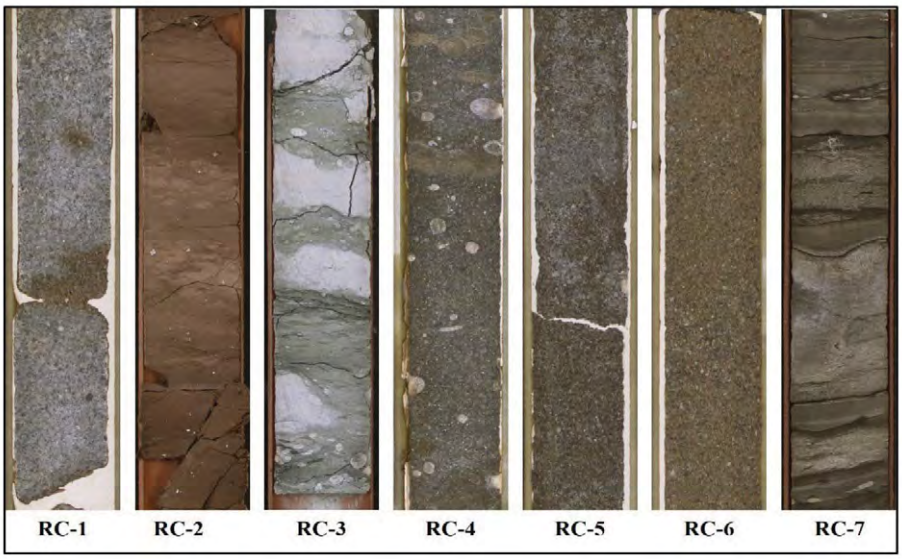

Fig. 20—Seven rock classes identified from integrated image-based workflow across three formations: RC-1: well-cemented sandstone; RC-2: brown limestone; RC-3: green-gray marly limestone; RC-4: condensed section with belemnite fossils; RC-5: sandstone with dispersed cementation; RC-6: coarse-grained poorly cemented sandstone; and RC-7: spiculite.

The detected classes are also in agreement with the lithofacies and have an 86% prediction accuracy (Fig. 15). Rock Classes 1, 5, and 6 all belong to the coarse-grained shore-face deposits, modified by differential diagenetic overprint, impacting their petrophysical properties. Rock Class 6 has 100-md to multi-Darcy permeability values for porosity values between 0.12 (v/v) to 0.30 (v/v). Rock Class 5 has dispersed cementation, but still has very high permeability of 100-md to multi-Darcy permeability values for porosity values ranging between 0.14 (v/v) to 0.30 porosity (v/v). In contrast, the well-cemented Class 1 has low porosity (less than 0.10 porosity) and low permeability. The

cement content was assessed through visual interpretation of available slabbed core photos (Fig. 17, track 5). The cement is displayed as light-gray material in core photos. In the intervals with high-cement content, the entire interval is light-gray colored, while as the cement content decreases, the light-gray material appears as speckles. The composition of the observed cement material is calcite, as described in the RCA report. Rock Class 7 is spiculites with porosity values ranging between 0.15 to 0.30. Rock Classes 4 and 7 belong to the same formation. However, Rock Class 4 has a 0.5 order of magnitude higher permeability than Rock Class 7 for the same porosity range between 0.15 and 0.30. Rock Classes 2 and 3 are the mudstone-wackstone carbonate deposits with permeability values less than 1 md and porosity values between 0.06 and 0.13 porosity. Figure 21 shows the confusion matrix results when comparing available lithofacies with the detected integrated rock classes in Well A. The sum of the values in each row of the matrix represents the number of samples of each lithofacies. The values in the main diagonal represent the number of samples correctly identified by the proposed automatic rock classification workflow. The sum offset values of each row represent the total number of samples incorrectly classified.

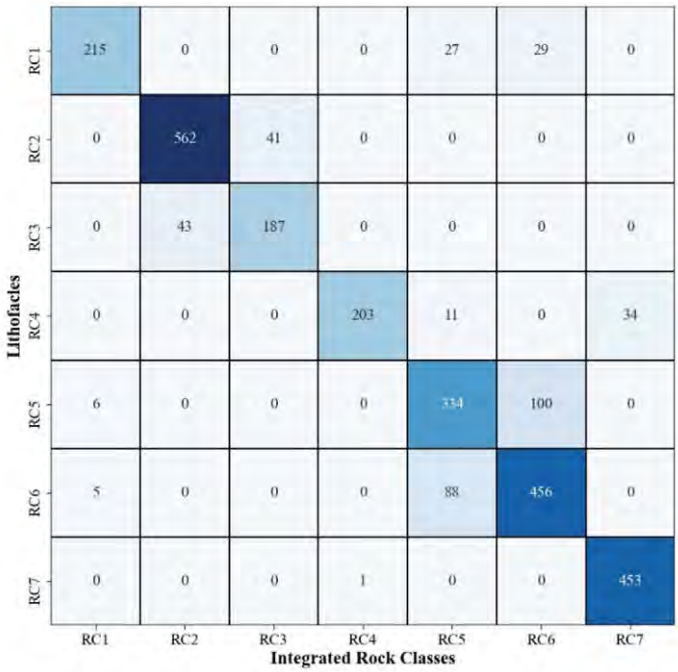

Fig. 21—Field Example, Well A: Confusion matrix of lithofacies and detected integrated rock classes. The main diagonal in the matrix represents the number of corrected identified samples. The offset values represent incorrectly identified samples.

Assessment of Rock Classes in Offset Well B

Figure 22 shows the result of rock classification in the offset Well B obtained from conventional well logs and the information obtained from Well A. The classes have been predicted using a quantitative classification algorithm trained with the obtained integrated rock classes and the well-log data available from Well A. Figure 22 also compares the estimated permeability values against available core data. Although the offset well has core data and core images, we did not use those for predicting rock classes or for deriving permeability models. We used core data available in the offset Well B to validate the predicted rock classes and estimated permeability. The permeability in Well B was estimated using the previously derived class-by-class permeability models of Well A. Propagation of the rock classes to Well B using the trained quantitative classification algorithm shows good agreement with the lithofacies found in Well A. The lower half of the interval is dominated with the coarse-grained facies belonging to Rock Class 6, and the upper half is dominated by the carbonate facies of Rock Classes 2 and 3. Class-by-class estimated permeability models improve the agreement between core data and estimated permeability by 20% (decrease in mean relative error) when compared with formation-by-formation permeability models.

DISCUSSION

The image-based rock-fabric-related features computed in this work were extracted from two-dimensional (2D) representations of the rock volume (i.e., slabbed core photos and YZ transversal cut CT scan images). Consequently, the changes in rock fabric captured by the extracted image-based rock-fabric-related features are limited to the dimensions displayed in the employed images. Therefore, if 3D variations in rock fabric are required to properly characterize directional properties such as permeability, CT scan image stacks should be employed rather than 2D image data.

Rock classification results obtained using a permeability-based cost function indicated a good correlation between image-based rock-fabric features and the measured permeability of the evaluated interval. However, the underlying physics of the employed images do not directly correlate to the physics of the fluid flow. Furthermore, the resolution of the employed images is not high enough to capture the pore structure of the evaluated interval. Nevertheless, variations in rock fabric captured by the image-based rock-fabric features helped us to identify coarse-grained intervals from fined-grained intervals

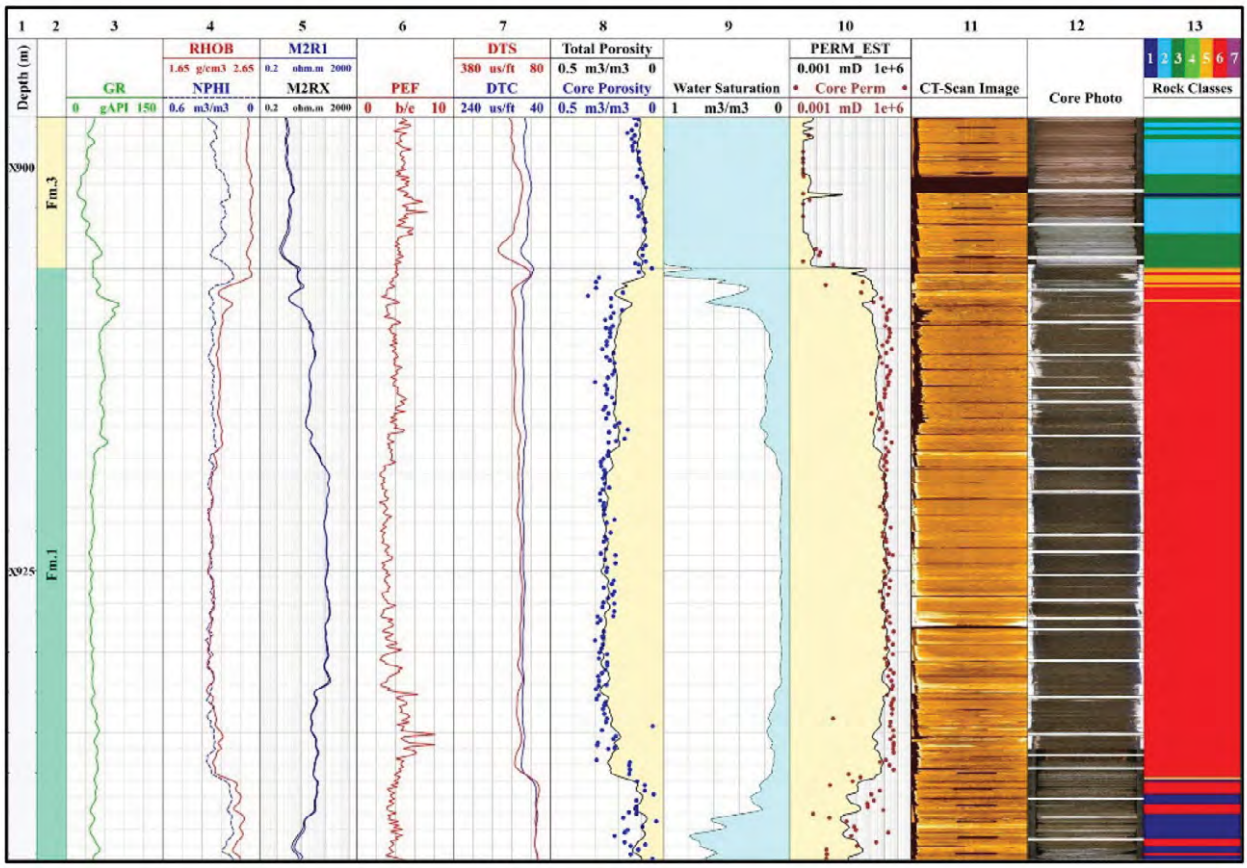

Fig. 22—Field example, Well B: Propagated rock classes and permeability estimation. Tracks from left to right: track 1: depth; track 2: formations; track 3: gamma ray (GR); track 4: bulk density (RHOB) and neutron porosity (NPHI); track 5: shallow (M2R1) and deep resistivity (M2RX); track 6: photoelectric factor (PEF); track 7: shear-wave slowness (DTS) and compressional-wave slowness (DTC), track 8: core porosity measurements and estimated total porosity; track 9: water saturation; track 10: comparison of permeability estimates (PERM EST) and core permeability (Core Perm); track 11: core CT scan image; track 12: core photo; and track 13: propagated rock classes.

(via energy and contrast from core CT scan images). Distinguishing these fabric features enabled the detection of contrasting values of measured permeability and helped to improve permeability assessment. Additionally, the image-based rock-fabric features, including color, saturation, and hue from core photos, allowed us to differentiate coarse-grained intervals with different degrees of cementation. The different degrees in cementation resulted in contrasting measured permeability values in the evaluated interval. Therefore, image-based rock-fabric features derived from core CT scan images and core photos contain significant information to identify different flow units.

The incorporation of formation tops as numerical features may cause biased results in certain circumstances, for instance, in the hypothetical case of having three Formations A, B, and C with assigned numerical values 1, 2, and 3, respectively. Formations A and C having similar petrophysical and geological properties will have a relatively large Euclidean distance. On the other hand, Formations A and B having dissimilar petrophysical and geological properties will have a relatively small Euclidean distance. A possible solution to this challenge, assuming conventional well logs accurately capture the similarities and dissimilarities in petrophysical and geological properties, is the inclusion of conventional well logs as inputs for the integrated rock classification step in addition to image-based rock-fabric-related features.

The use of conventional well logs for the training of the quantitative classification algorithm poses a challenge due to the differences in vertical resolution between the conventional well logs used to train the supervised algorithm and the core CT scan and core photos employed for the extraction of image-based rock-fabric features used for detection of the optimum number of rock classes. The rock classification results in Well B were in good agreement with the previously identified lithofacies in Well A. The

good agreement despite the resolution difference between the input data and the labels is a consequence of two main factors. First, the observed vertical variation in rock fabric in Well B was less compared to Well A. Second, it was possible to fine-tune the boundaries between rock classes by means of a self-organizing map (SOM) or Kohonen map. SOM is an unsupervised multivariate data analysis method employed in clustering and dimensionality reduction for high-dimensional data visualization (Kohonen, 2013). The SOM enables a 2D grid visualization of the classes along with the relative value of the features (a pie chart per each grid box) that define each class. This challenge can be further addressed by the integration of core CT scan images and core photos with image logs. The integration of image logs can help in the training of the supervised learning algorithm, providing an input with similar resolution as the core CT scan images and core photos.

The proposed workflow relies on the joint interpretation of both whole-core CT scan image data and slabbed core photos. However, other high-resolution wellbore/core image data could be used as an input to the proposed workflow. For instance, acoustic image logs of suitable resolution could be used instead of whole-core CT scan images. Although the physical principles honored by these two types of wellbore/core image data are different, both can be used as a proxy for formation density. In the case of the core photos, the use of an alternative wellbore/core image data is not straightforward. Other wellbore/core image data could be used, but it will not reveal the same information revealed by core photos. Therefore, the obtained rock classes are expected to be different than those obtained by the integration of whole-core CT scan images and slabbed core photos.

CONCLUSIONS

We introduced a workflow for automated identification of rock classes using CT scan images, core photos, RCA data, and conventional well logs. The workflow simultaneously optimizes the number and location of rock classes, as well as the permeability model for each class. The proposed approach reduces the time spent on visual rock classification from core image data. Furthermore, the proposed workflow incorporates physics through the use of a cost function, which minimizes the error between core-measured permeability (fluid flow) and class-based estimated permeability to optimize the number of rock classes. The workflow detected rock classes with 86% accuracy in the interval of interest compared against expert-derived lithofacies in Well A. The confusion matrix revealed that Rock Classes 5 and 7 have the lowest and highest classification accuracy, respectively. The use of class-based permeability models helped us to reduce the error in permeability estimates by 89% (decrease in mean relative error) compared to formation-by-formation permeability estimates. It should be noted that the optimization of the number of image-based rock classes can be affected by the sampling rate and biased sampling. For instance, rock classes for which scarce or negligible permeability measurements were taken cannot be accurately distinguished. This suggests that the proposed approach can be used for the optimization of the core-sampling procedure.

Results demonstrated that the image-based rock-fabric features derived from core photos and CT scan images capture textural and color variations in the evaluated depth interval. However, it should be noted that the use of an averaging window for textural features extraction can lead to smooth features, which in turn can cause poorly defined boundaries between different rock classes. Furthermore, the evaluated intervals can display gradual textural variation, making the definition of boundaries difficult, even for a human interpreter.

The proposed workflow provides a fast and accurate assessment of image-based rock-fabric-related features that can be employed for quick assessment of lithofacies. Additionally, the automatic optimization of integrated rock classes aids in the estimation of accurate petrophysical properties by means of class-based petrophysical models.

Furthermore, integrated rock classes obtained in wells with wellbore/core image data can be employed for training of supervised learning algorithms and subsequent estimation of integrated rock classes in noncored wells (or cored wells without image data). The advantages of the proposed workflow compared to the previously documented rock classification methods include: (a) it not only automatically extracts rock-fabric features from image data using image analysis, but also incorporates rock physics from well logs and RCA data in petrophysical evaluation, (b) it simultaneously improves permeability estimates and optimizes the number of rock classes, and (c) it integrates well logs and core-scale images for the propagation of rock classes to noncored wells.

ACKNOWLEDGMENTS

The research reported in this paper was funded by the Joint Industry Research Program on “Multi-Scale Rock Physics” sponsored by BHP, BP, Core Laboratories, Equinor, ExxonMobil, Occidental Petroleum, Petrobras, and Wildcat Technologies. Special gratitude goes to Equinor and partners for providing the data used in this paper, and the permission for publishing this work.

NOMENCLATURE

Abbreviations

3D =	three dimensional
BIC =	Bayesian Information Criterion
CT =	computed tomography
GLCM =	gray-level co-occurrence matrix
HSV =	hue, saturation, and value
RCA =	routine core analysis
RGB =	red, green, and blue
SOM =	self-organizing map

Symbols

a_i =	intracluster dissimilarity of the *i-th* sample
Avg_{GL} =	averaged gray-level value
Avg_{TF} =	averaged textural feature
b_i =	intercluster dissimilarity of the *i-th* sample
C =	cost function a x rock classes, md
$G(i,j)$ =	*i-th*, *j-th* element of the GLCM
GL_i =	gray-level value of the *i-th* pixel at a given row
h =	lag distance, pixels
k_{Core} =	core permeability, md
k_{est} =	estimated permeability, md
N =	total number of pixels per row
Nl =	total number of pixel pairs at lag distance h
N_{perm} =	total number of core permeability measurements
p_i =	gray-level value
s_i =	silhouette coefficient of the *i-th* sample
TF_i =	textural feature of the *i-th* pixel at a given row
γ =	experimental variogram

REFERENCES

Al-Obaidi, M., Heidari, Z., Casey, B., and Williams, R., 2018, Automatic Well-Log-Based Fabric-Oriented Rock Classification for Optimizing Landing Spots and Completion Intervals in the Midland Basin, Paper CCCC, *Transactions, SPWLA 59th Annual Logging Symposium*, London, United Kingdom, 2–6 June.

Bae, W., Jeon, E., Sung, W., and Kim, S., 2006, The Relationship Between Petrophysical Properties and Geological Facies of Carbonates, *Energy Sources, Part A*, **28**(6), 567–586. DOI: 10.1080/009083190928065.

Basu, T., Dennis, R., Al-Khobar, B.D., Al Awadi, W., Isby, S.J., Vervest, E., and Mukherjee, R., 2002, Automated Facies Estimation From Integration of Core, Petrophysical Logs, and Borehole Images, AAPG Annual Meeting, Houston, Texas, USA, 10–13 March.

Bharati, M.H., Liu, J.J., and MacGregor, J.F., 2004, Image Texture Analysis: Methods and Comparisons, *Chemometrics and Intelligent Laboratory Systems*, **72**(1), 57–71. DOI: 10.1016/j.chemolab.2004.02.005.

Brodatz, P., 1966, *Textures: A Photographic Album for Artists and Designers*, Dover Publications, New York. ISBN: 978-0486406992.

Chacko, S., Keskes, N., Hall, J.C., and Serag El Din, S., 2012, Textural Analysis of MCT Images: Measurements Beyond Rock Properties, Paper SPE-161383 presented at the SPE Abu Dhabi International Petroleum Conference and Exhibition, Abu Dhabi, United Arab Emirates, 11–14 November. DOI: 10.2118/161383-MS.

Delhomme, J.P., 1992, A Quantitative Characterization of Formation Heterogeneities Based on Borehole Image Analysis, Paper T, *Transactions, SPWLA 33rd Annual Logging Symposium*, Oklahoma City, Oklahoma, USA, 14–17 June.

Diehl, S.F., Budd, J.W., Ullman, D., and Cayula, J.F., 2002, Geographic Window Sizes Applied to Remote Sensing Sea Surface Temperature Front Detection, *Journal of Atmospheric and Oceanic Technology*, **19**(7), 1105–1113. DOI: 10.1175/1520-0426(2002)019<1105:GWSATR>2.0.CO;2.

Fitzsimons, D., Oeltzschner, G., Ovens, C., Radies, D., and Schulze, F., 2016, Integration and Data Analysis of Conventional Core Data With NMR and CT Data to Characterize an Evaporitic Carbonate Reservoir, Paper SPE-183145 presented at the SPE Abu Dhabi International Petroleum Conference and Exhibition, Abu Dhabi, United Arab Emirates, 7–10 November. DOI: https://doi.org/10.2118/183145-MS.

Franklin, S.E, Wulder, M.A., and Lavigne, M.B., 1996, Automated Derivation of Geographic Window Size for Use in Remote Sensing Digital Image Texture Analysis, *Computers & Geosciences*, **22**(6), 665–673. DOI: 10.1016/0098-3004(96)00009-X.

Georgi, D.T., Phillips, C., and Hardman, R., 1992, Applications of Digital Core Image Analysis to Thin Bed Evaluation, Paper 9206, *Transactions, Society of Core Analysts*, 14–17. http://www.ux.uis.no/~s-skj/ipt/Proceedings/SCA.1987-2004/1-SCA1992-06.pdf. Accessed August 12, 2020.

Gomes, J.S., Ribeiro, M.T., Strohmenger, C.J., Naghban, S., and Kalam, M.Z., 2008, Carbonate Reservoir Rock Typing–The Link Between Geology and SCAL, Paper SPE-118284 presented at the Abu Dhabi International Petroleum Exhibition and Conference, Abu Dhabi, United Arab Emirates, 3–6 November. DOI: 10.2118/118284-MS.

Goupillaud, P., Grossmann, A., and Morlet, J., 1984, Cycle-Octave and Related Transforms in Seismic Signal Analysis, *Geoexploration*, **23**(1), 85–102. DOI: 10.1016/0016-7142(84)90025-5.

Govert, A., Hall, B., and Jones, E., 2016, Unlocking Whole Core CT Data for Advanced Description and Analysis, AAPG Annual Convention and Exhibition, Calgary, Alberta, Canada, 19–22 June.

Hall, J., Ponzi, M., Gonfalini, M., and Maletti, G., 1996, Automatic

Extraction and Characterisation of Geological Features and Textures Front Borehole Images and Core Photographs, Paper CCC, *Transactions, SPWLA 37th Annual Logging Symposium*, New Orleans, Louisiana, USA, 16–19 June.

Haralick, R.M., and Shanmugam, K., 1973, Textural Features for Image Classification, *IEEE Transactions on Systems, Man, and Cybernetics*, **SMC-3**(6), 610–621. DOI: 10.1109/TSMC.1973.4309314.

Jungmann, M., Kopal, M., Clauser, C., and Berlage, T., 2011, Multi-class Supervised Classification of Electrical Borehole Wall Images Using Texture Features, *Computers & Geosciences*, **37**(4), 541–553. ISSN: 0098-3004.

Kherroubi, J., Maeso, C., Wang, Y., and Gamero-Diaz, H., 2016, Lamination Analysis From Electrical Borehole Images: A Quantitative Workflow, Paper BBBB, *Transactions, SPWLA 57th Annual Logging Symposium*, Reykjavik, Iceland, 25–29 June.

Kraaijveld, M.A., and Epping, W.J., 2000, Harnessing Advanced Image Analysis Technology for Quantitative Core and Borehole Image Interpretation, Paper VV, *Transactions, SPWLA 41st Annual Logging Symposium*, Dallas, Texas, USA, 4–7 June.

Kohonen, T., 2013, Essentials of the Self-Organizing Map, *Neural Networks*, **37**, 52–65. DOI: 10.1016/j.neunet.2012.09.018.

Linek, M., Jungmann, M., Berlage, T., Pechnig, R., and Clauser, C., 2007, Rock Classification Based on Resistivity Patterns in Electrical Borehole Wall Images, *Journal of Geophysics and Engineering*, **4**(2), 171–183. DOI: 10.1088/1742-2132/4/2/006.

Luthi, S.M, 1994, Textural Segmentation of Digital Rock Images Into Bedding Units Using Texture Energy and Cluster Labels, *Mathematical Geology*, **26**(2), 181–196. DOI: 10.1007/BF02082762.

Misra, S., Ganguly, E., and Wu, Y., 2019a, Generalization of Machine Learning Assisted Segmentation of Scanning Electron Microscopy Images of Organic-Rich Shales, Chapter 11, *in Machine Learning for Subsurface Characterization*, 315–338, Gulf Publishing. DOI: 10.1016/C2018-0-01926-X.

Misra, S., Chakravarty, A., Bhoumick, P., and Rai, C.S., 2019b, Unsupervised Clustering Methods for Noninvasive Characterization of Fracture-Induced Geomechanical Alterations, Chapter 2, *in Machine Learning for Subsurface Characterization*, 39–64, Gulf Publishing. DOI: 10.1016/C2018-0-01926-X

Ohanian, P.P., and Dubes, R.C., 1992, Performance Evaluation for Four Classes of Textural Features, *Pattern Recognition*, **25**(8), 819–833. DOI: 10.1016/0031-3203(92)90036-I.

Porwik, P., and Lisowska, A., 2004, The Haar-Wavelet Transform in Digital Image Processing: Its Status and Achievements, *Machine Graphics and Vision*, **13**(1/2), 79–98. URL: https://pdfs.semanticscholar.org/9b20/ddd6e8b08681a916b7b74b24994bcef31626.pdf. Accessed on August 25, 2020.

Purba, S.A., Garcia, A.P., and Heidari, Z., 2018, A New Hierarchical Method for Rock Classification Using Well-Log-Based Rock Fabric Quantification, *Petrophysics*, **59**(5), 720–734.

Rousseeuw, P.J., 1987, Silhouettes: A Graphical Aid to The Interpretation and Validation of Cluster Analysis, *Journal of Computational and Applied Mathematics*, **20**, 53–65. DOI: 10.1016/0377-0427(87)90125-7.

Salvador, S., and Chan, P., 2004, Determining the Number of Clusters/Segments in Hierarchical Clustering/Segmentation Algorithms, *16th IEEE International Conference on Tools with Artificial Intelligence*, Boca Raton, Florida, USA, 576–584. DOI: 10.1109/ICTAI.2004.50.

Serra, O.T., and Abbott, H.T., 1982, The Contribution of Logging Data to Sedimentology and Stratigraphy, *SPE Journal*, **22**(01), 117–131. DOI: https://doi.org/10.2118/9270-PA.

Sklansky, J., 1978, Image Segmentation and Feature Extraction, *IEEE Transactions on Systems, Man, and Cybernetics*, **8**(4), 237–247. DOI: 10.1109/TSMC.1978.4309944.

Suarez-Rivera, R., Edelman, E., Handwerger, D., Hakami, A., and Gathogo, P., 2012, Improving Geologic Core Descriptions and Heterogeneous Rock Characterization via Continuous Profiles of Core Properties, Paper 236, *Transactions, SPWLA 53rd Annual Logging Symposium*, Cartagena, Colombia, 16–20 June.

Tibshirani, R., Walther, G., and Hastie, T., 2001, Estimating the Number of Clusters in a Data Set via the Gap Statistic, *Journal of the Royal Statistical Society: Series B (Statistical Methodology)*, **63**(2), 411–423. DOI: 10.1111/1467-9868.00293.

Torres, D., Strickland, R.W., and Gianzero, M.V., 1990, A New Approach to Determining Dip and Strike Using Borehole Images, Paper K, *Transactions, SPWLA 31st Annual Logging Symposium*, Lafayette, Louisiana, USA, 24–27 June.

Wu, Y., Misra, S., Sondergeld, C., Curtis, M., and Jernigen, J., 2019, Machine Learning for Locating Organic Matter and Pores in Scanning Electron Microscopy Images of Organic-Rich Shales, *Fuel*, **253**, 662–676. DOI: 10.1016/j.fuel.2019.05.017.

Ye, S.J., Rabiller, P., and Keskes, N., 1997, Automatic High Resolution Sedimentary Dip Detection on Borehole Imagery, Paper O, *Transactions, SPWLA 38th Annual Logging Symposium*, Houston, Texas, USA, 15–18 June.

Ye, S.J., and Rabiller, P., 1998, Automated Fracture Detection on High Resolution Resistivity Borehole Imagery, Paper SPE-49300 presented at the SPE Annual Technical Conference and Exhibition, New Orleans, Louisiana, USA, 27–30 September. DOI: 10.2118/49300-MS.

ABOUT THE AUTHORS

Andres Gonzalez is a PhD student in the Department of Petroleum and Geosystems Engineering at the University of Texas at Austin. He holds a BSc degree in petroleum engineering from the Industrial University of Santander, Colombia. Andres has 6 years of experience in drilling engineering as well as in production engineering with several companies, such as Halliburton, Ecopetrol S.A., and Mansarovar, among others. Andres is currently a graduate research assistant at the University of Texas at Austin under

the supervision of Dr. Zoya Heidari. His research interests include the integration of multiscale image information in formation evaluation of conventional and unconventional reservoirs, multiscale petrophysics, and petrophysical laboratory measurements.

Lawrence Kanyan was a PhD student in the Department of Petroleum and Geosystems Engineering at the University of Texas at Austin when this paper was drafted. He holds an M-Tech degree in geological technology from the Indian Institute of Technology Roorkee. Lawrence has over 3 years of experience as a petroleum geologist in development and exploration. He has previously worked for Shell and Oil and Natural Gas Corporation (ONGC) Limited. His research interests include integrated reservoir characterization, multiscale formation evaluation, and applications of machine learning in image analysis for formation evaluation.

Zoya Heidari is an associate professor in the Hildebrand Department of Petroleum and Geosystems Engineering at the University of Texas at Austin. Before joining the University of Texas at Austin, she was an assistant professor at Texas A&M University in College Station from September 2011 to August 2015. Zoya was the founder and director of the Texas A&M Joint Industry Research Program on Multiscale Formation Evaluation of Unconventional and Carbonate Reservoirs from 2012 to 2015. She has been the founder and director of the University of Texas at Austin Industrial Affiliates Research Program on Multiscale Rock Physics since 2016. She holds a PhD degree (2011) in petroleum engineering from the University of Texas at Austin. She is one of the recipients of the 2019 EAGE (European Association of Geoscientists and Engineers) Arie van Weelden Award, the 2019 AIME Rossiter W. Raymond Memorial Award, the 2019 SPE Distinguished Membership Award, the 2017 SPE (Society of Petroleum Engineers) Cedric K. Ferguson Medal, the 2016 SPE Regional Formation Evaluation Award, the 2015 SPE Innovative Teaching Award, the 2014 TEES (Texas A&M Engineering Experiment Station) Select Young Faculty Fellows Award from the College of Engineering at Texas A&M University, and the 2012 SPE Petroleum Engineering Junior Faculty Research Initiation Award. Her research interests include petrophysics, borehole geophysics, rock physics, inverse problems, completion petrophysics, and reservoir characterization of unconventional and carbonate reservoirs.

Olivier Lopez is a leading researcher in geology and petrophysics in the Research and Technology department of Equinor ASA. His work mainly focuses on reservoir evaluation and characterization for siliciclastic, carbonate, and shale systems, and the integration of new technologies. Before joining Equinor ASA, Olivier was a project manager in Numerical Rocks ASA. Olivier holds a PhD degree (2006) in fundamental and applied geochemistry.